Deep-Space Exploration Enabled by CubeSats with Staged Electrospray Propulsion

by

Gustav M. Pettersson

B.Sc., KTH Royal Institute of Technology (2017)
M.Sc., KTH Royal Institute of Technology (2018)

Submitted to the Department of Aeronautics and Astronautics
in partial fulfillment of the requirements for the degree of

DOCTOR OF PHILOSOPHY IN AERONAUTICS AND ASTRONAUTICS

at the

MASSACHUSETTS INSTITUTE OF TECHNOLOGY

May 2024

Authored by:	Gustav M. Pettersson Department of Aeronautics and Astronautics May 17, 2024
Certified by:	Paulo C. Lozano M. Alemán-Velasco Professor of Aeronautics and Astronautics Thesis Supervisor
	Richard P. Binzel Professor of Planetary Sciences Thesis Committee Member
	Rebecca A. Masterson Johns Hopkins University Applied Physics Laboratory Thesis Committee Member
Accepted by:	Jonathan P. How R. C. Maclaurin Professor of Aeronautics and Astronautics Chair, Graduate Program Committee

Deep-Space Exploration Enabled by CubeSats with Staged Electrospray Propulsion

by

Gustav M. Pettersson

Submitted to the Department of Aeronautics and Astronautics
on May 17, 2024 in partial fulfillment of the requirements for the degree of

DOCTOR OF PHILOSOPHY IN AERONAUTICS AND ASTRONAUTICS

ABSTRACT

From their beginnings as an educational experiment, CubeSats have grown to a popular technology development platform and a capable tool for scientific missions. Deep-space CubeSats have been limited to rideshare launches thus far, acting as companions to enhance large missions or using propulsion to reach science orbits near the destination of the primary mission (e.g. to Mars or around the Moon). More CubeSat companions are planned on future high-profile missions and the concept is likely to continue to gain popularity, but is inherently limited by the primary mission. This thesis looks towards the next step: dedicated scientific deep-space CubeSat mission applications and technology development.

The asteroid belt contains unique scientific value as the small bodies in this region are remnants of solar system formation. Because there are over a million known bodies spread across dozens of types, however, it is infeasible to explore a representative sample with large missions. To solve this, swarm missions that explore the asteroids have been proposed, where a "mothership" is launched from Earth and transfers to a central location in the asteroid belt and releases a "swarm" of tens of smaller spacecraft to visit a sample of asteroids. So far, likely because of a combination of weak science motivation and poor technology readiness, no mission of this type has become reality. This thesis addresses the first part with two mission concepts that are strongly motivated by the decadal survey for planetary science and astrobiology: a swarm to visit the members of an asteroid family, and a swarm to visit a broad sample of the largest asteroids. The second part is addressed by leveraging the technologically mature CubeSat platform, which already solved many of the challenges of swarm missions, and making progress on some of the remaining limitations.

Two factors that challenge deep-space operations are the high propulsion capabilities (delta-v) required to impart meaningful orbit change and the falloff of available solar power away from the Sun, e.g. by a factor of five to ten in the main asteroid belt. Practical high delta-v CubeSat propulsion comes exclusively from electric propulsion, where the mass and volume of the propulsion system are reduced at the expense of higher power requirements compared to e.g. chemical propulsion. Unfortunately, the power demanded by state-of-the-art electric propulsion options make them infeasible for many deep-space missions. Electrospray propulsion systems overcome the power challenge thanks to their high efficiency, but are not mature enough to operate as long as necessary to deliver the requisite delta-v. This lifetime limitation can be overcome by dividing the propulsion system into a series of stages, creating a flexible system that scales to large delta-v and uses little power. In this thesis, the first complete CubeSat staged electric propulsion system is analysed, designed, implemented, and tested, to where it is ready for an in-space technology demonstration. The analysis shows that propulsion systems based on this new technology can enable deep-space CubeSats capable of several km/s of delta-v in the asteroid belt in the near future.

With propulsion well on its way to be solved, the main remaining limitation is the reliance of deep-space missions on ground resources, i.e. the deep-space network (DSN), for communications and navigation. With the number of satellites envisioned, either ground resources need significant expansion, or the method by which the CubeSats are operated requires change. By using the mothership as a communication and navigation relay the ground resource issue is eliminated. Some of the proposed missions are likely to be feasible with modifications of technology already available and demonstrated today, but the most ambitious mission variants shown in this thesis will require significant work. After a flexible mothership has been developed for the first mission, a wide range of exciting science missions in the asteroid belt will be possible, and the rapid technology development in the CubeSat sector can be leveraged in a new paradigm of scientific exploration.

Thesis supervisor: Paulo C. Lozano
Title: M. Alemán-Velasco Professor of Aeronautics and Astronautics

Acknowledgements

Foremost, I would like to thank my advisor Prof. Paulo Lozano who showed his belief in me from my first day at MIT and has supported every step of this thesis work. The research group that Paulo has built is a genuine family where every individual contributes ideas and selfless assistance to the broad range of projects that move the field of space propulsion ever forward. Paulo's enduring optimism sometimes stood in contrast to my less cheerful outlook, but having reached the end of this journey I must concede that there is always a way forward. I cannot imagine having a more supportive advisor and research group to grow with and I am deeply grateful for the opportunity to spend the past five years in their company.

I appreciate the commitment and vast experience that my committee members Dr. Becky Masterson and Prof. Rick Binzel have contributed to this work. For several years Becky was like a second advisor to me whose rigorous input on systems engineering and project management lifted the STEP-1 project above many roadblocks. Her forthright feedback was necessary to grow the quality of my work and her efforts to put me in contact with the right people at the right time were invaluable. Becky is not only a tremendous professional asset, but also a great friend to me and all her past students. Rick's knowledge of planetary sciences and enthusiasm towards teaching his students and the broader public was a critical source of inspiration to this work and defines the gold standard all academics should strive to. I especially want to thank Rick for our talks that helped fill in the gaps between the textbook-level description of asteroids and the latest research.

My acknowledgements go out to my thesis readers Prof. Oliver Jia-Richards, Dr. Bill Blackwell, and Dr. David Oh who took the time to read my work and provide important feedback and discussions that improved this work and helped me contextualise it. Some of the technology development in this thesis follows directly from Oliver's time as student at MIT so his feedback was especially pertinent in this area. Bill and David are both distinguished engineers and project leaders at Lincoln Labs and NASA JPL respectively and I sincerely appreciate them taking the time to read my thesis and feel especially buoyant after their positive comments.

There is not enough ink to properly give thanks to all members of the Space Propulsion Laboratory who were a part of my time here. Lab work is often a struggle that drags into a nightlong ghost hunt and ends in equal parts success, failure, and bewilderment. It takes character to come back the next day and try again, and it takes heart to do it to help someone else's project. Thankfully, the SPL is full of characters and hearts who make lab work rewarding and find amusement in the little things. For the avoidance of doubt, I explicitly include Prof. Carmen Guerra-Garcia and her students in the SPL family.

I want to thank the two-dozen or so undergraduate students who worked with me at some point during my time at MIT. I have learned a lot about leading a team of people through our interactions and appreciate the efforts they put towards the STEP-1 project. I wish them all the best in their respective future endeavours. I also want to thank Todd and Dave in the AeroAstro machine shop for teaching me about manufacturing and providing a lot of practical input and help during the project.

Before I joined MIT there were many influential people in academia and beyond who steered me in the right direction and helped me get to this point. Prof. Babak Hassibi and Dr. Anatoly Khina at Caltech gave me my first glimpses into academic research many years ago. Prof. Hjalmar Brismar and Dr. Sara Abrahamsson at KTH SciLifeLab and later UC Santa Cruz are great friends and supporters who helped me grow and build my first independent projects. Sara has been my principal advocate for many years and I fondly remember our many adventures in the past and hope for more in the future. Sven Grahn and Prof. Gunnar Tibert at the KTH Space Centre introduced me to working with CubeSats and were exceptional mentors during my Master's studies. Drs. Michael Dille, Uland Wong, and Terry Fong at NASA Ames are free spirits who taught me a great deal about working on research projects and having fun with it. Josep Perdigues and Dr. Zoran Sodnik at ESA trusted me with a lot of independence that allowed me to thrive and really jump in the deep end working on optical communications. I send my sincerest best with this thesis to all of them and anyone I regretfully have missed to mention by name.

Last but not least I thank my family and friends who have been by my side. My parents Bodil and Mikael let myself and my siblings grow up to be who we wanted and did everything in their power to help us find our ways. Their three baby hockey players ended up as an orthotist, an engineer, and a pilot, so I think they did all right even though none of us reached the NHL. I am so grateful to have been able to talk to my family openly during difficult times and miss them all dearly on the other side of the pond. My wife, Dr. Meg, is my favourite person and I look forward to what life has in store for us and where we end up. The past six months of writing this thesis have drained me completely and I don't know how I could have reached the end without her by my side.

This work was supported by grants from the NASA Smallsat Technology Partnership (STP) and NASA CubeSat Launch Initiative (CSLI). I especially want to thank Rudy De Rosee and Chris Baker for their technical advice and support in pushing the STEP-1 project forward. This work was supported in part by the Foundation Blanceflor.

Contents

List of Figures

List of Tables

Chapter 1

Introduction

1.1 Background

The Babylonians identified Mercury, Venus, Mars, Jupiter, and Saturn, and catalogued their motion across the sky at least as early as 750 BC [1]. While humans continued to study the stars and the occasional comet, it was not until the 1600s AD invention of the telescope that further solar system bodies were discovered. With the telescope as a tool, Gallieo discovered the main moons of Jupiter, Huygens found the rings and largest moon of Saturn, and not long after the modern view of the solar system emerged. The Sun is at the centre, large planets orbit on near-circular trajectories, and most of the planets have smaller moons orbiting them. As telescopes grew in capability in the 1800s, smaller and farther bodies were discovered in the solar system, rounding out the known planets and adding dozens of minor planets that would eventually be known as the asteroids [2], concentrated in the "main belt" orbital region between Mars and Jupiter. Today, we have identified 1.24 million asteroids in the main belt and an additional 77 thousand in other regions [3]. The asteroids are thought to be remnants from the solar system's formation that failed to congregate into the Sun or a planet and have therefore become a vital tool to study and understand the solar system [4]. Surveys of the asteroids have, primarily through telescope-based spectral analysis, identified several distinct types and revealed details about the composition of the solar system [5]. The distribution of asteroid types have also shown that the solar system has a chaotic past with sweeping planetary migrations whereby the asteroids have been jumbled up from their original formation locations [6]. The literature review in Section 2.1 provides further background on the asteroids' role in the solar system and how they are a key element to understanding our origins.

The age of space exploration began in 1957 when the first satellite, Sputnik, was launched into low Earth orbit. In the following decade, human-carrying and robotic spacecraft began to visit our solar system neighbours, including the Apollo programme to the Moon (1962–1972 [7]), and the Mariner programme to Venus and Mars (1962–1975 [8]). It took until 1996 before the first dedicated mission to explore the asteroids launched: the Near Earth Asteroid Rendezvous (NEAR) Shoemaker. The spacecraft studied the near-Earth asteroid (443) Eros in detail by high-resolution imaging and spectrometry [9], measuring gravitational [10] and magnetic [11] fields, and determining its shape [12] and elemental composition [13]. One key result of NEAR Shoemaker was to help resolve a longstanding issue in asteroid and meteorite studies: why do the spectral signatures of the most common asteroids (S-types) and meteorites (ordinary chondrites), which are asteroids that have fallen onto Earth, not match? As it turns out, ordinary chondrites and S-types are the same material but the surfaces of S-type asteroids have been "space weathered" and take on a different spectral signature [14]. A few asteroid exploration spacecraft have followed NEAR Shoemaker and have performed similar investigation of asteroids near Earth and in the main asteroid belt. A major milestone was the 2003 launch and 2010 sample-return of material from asteroid (25143) Itokawa by the Hayabusa spacecraft. Beyond performing in situ studies with the spacecraft, the returned materials were studied in the lab using e.g. electron microscopy and advanced spectroscopy methods and could directly confirm that the S-type asteroid Itokawa was an LL-group ordinary chondrite [15]. All past asteroid explorers have been large spacecraft, ranging in mass from 510 kg for Hayabusa [15] to 2747 kg for the recently launched Psyche spacecraft [16] to the homonymous main belt asteroid.

In the new millennium we have seen a sharp rise of a new class of satellites: the CubeSats. While this thesis focuses on CubeSats specifically, most of the results apply more broadly to small satellites (e.g. <100 kg) as a group. CubeSats were envisioned in the late 1990s as a tool for teaching students the process of developing and operating spacecraft based on a simple standard where a satellite is made up of one or a number of "unit cubes" with a side of 10 cm, placed inside a standardised canister and released into orbit by piggybacking on a large satellite's launch [17]. An important aspect of this idea was that the canister was designed to protect the launch vehicle and primary payload from any anomalies in the CubeSat, allowing the launch requirements to be relaxed compared to a traditional spacecraft. The strategy of protecting the primary mission allowed experimentation in CubeSat design and inclusion of abundant commercial off-the-shelf (COTS) electronics to rapidly evolve the capabilities within the small package [18]. Soon after, industry and governments picked up on the trend and the CubeSat market evolved to include single-unit (1U) satellites for education as originally envisioned, and larger triple-unit (3U) satellites targeting specific technology developments or applications, with over 100 CubeSats launched by 2012 [19]. In a 2016 report [20] by the National Academies of Sciences, Engineering, and Medicine the capabilities of

CubeSats for scientific applications were considered. The report concluded that CubeSats were a disruptive innovation that was already generating high-quality scientific data, and recommended supporting the development further to maximise scientific contributions. The report also identified several technology areas where special attention is needed, including propulsion which this thesis contributes towards. At the time of writing, CubeSats have grown to typically be 3U or 6U in size and number in the thousands in low Earth orbit [21]. The two MarCO 6U CubeSats have even flown by Mars where they successfully relayed data from the InSight lander back to Earth [22]. With CubeSat technology rapidly evolving we are on the precipice of a new era of deep-space exploration where small satellites will play an important role [23]. Since MarCO, a few more CubeSats have launched away from Earth orbit and this thesis intends to help with the next stages of technology development and scientific motivations to enable a wave of new CubeSat deep-space explorers in the near future.

Propulsion capability is a clear limitation of CubeSats since only 202 of the 2323 cumulative CubeSats that were launched by the end of 2023 had any kind of propulsion on-board [24]. As the interest and abilities of CubeSats grew in the mid 2010s the demand and rapid development of propulsion technologies followed [25]. For attitude control or small trajectory corrections a cold gas system is sufficient, as e.g. the MarCO mission to Mars used [22]. For long-term orbit maintenance, orbit changes, or deep-space transfers, however, higher specific impulse systems are required as the volume and mass available to a CubeSat propulsion system is small [26]. Of particular relevance to this thesis are electrostatic thrusters of electrospray, field-emission electric propulsion (FEEP), gridded ion, or Hall types. These are the only short-term options that can provide continuous thrust and specific impulse high enough to generate the several km/s of Δv a deep-space transfer requires [27].[*] A sufficient Δv capability alone is not enough to declare a propulsion technology suited to a mission; the mass and volume required by the propulsion system and its power draw during operation are fundamental properties to close a feasible mission design. The mass and volume of propellant are reduced by increasing the specific impulse, however the power required to generate thrust grows and therefore the mass and volume of solar panels and batteries. To reach the utopia point of large Δv, low mass and volume, and low power, the propulsion system must have a long lifetime *and* high specific impulse *and* high efficiency.[†] At present there is no system that meets all three on the CubeSat scale. State-of-the-art CubeSat electric propulsion systems with large Δv capability, i.e. FEEP and gridded ion thrusters, have effi-

---

[*] For this thesis the term "deep-space" refers to anything outside the Earth-Moon system.

[†] For systems engineering, the thrust-to-power ratio is the metric where efficiency comes in, scaling as efficiency over specific impulse. Efficiency is used here as it is more fundamental to technology maturity.

ciencies below 20%, while those that reach high efficiency, e.g. electrosprays, are limited to short lifetimes. As a comparison, full-size electric propulsion systems are routinely operated for several years through broad regimes of thrust and specific impulse at efficiencies over 50%, enabling many deep-space journeys. The state-of-the-art of propulsion is discussed in Section 2.4 of the literature review and includes a detailed discussion on using several stages to overcome lifetime limitations of propulsion systems that are still maturing.

In 2019 Krejci, Gomez-Jenkins, and Lozano introduced the concept of staged electrospray propulsion for CubeSats to expand their capabilities to deep-space [28]. They noted that the electrospray thrusters themselves only contributed a small fraction of the propulsion system's total mass, and thus the Δv of a spacecraft could be increased by stacking several stages of thrusters with individual tanks to eject dead weight as the propellant is used up. The idea of shedding unused structural mass as propellant depletes is not new; practically all chemically propelled launch rockets use multiple stages for the same reason, but is not beneficial to other electric propulsion systems. Beyond their inherent low mass and volume, electrospray thrusters are capable of high specific impulse and efficiency over 60% [29]; close to the utopia point of propulsion. Electrospray thrusters using ionic liquid propellant are, however, still maturing and unable to process the total propellant mass to reach large Δv, with lifetime limitations around 500 h in 2020 [30]. In a series of publications expanding on the staged electrospray concept, Jia-Richards et al., highlighted that the same staging concept can also enable sooner mission feasibility by overcoming the electrospray lifetime limitation [30–33]. Importantly, they showed that even with hard limits imposed on the lifetime of each stage this type of propulsion system would outperform all available systems on the market in terms of payload mass delivered to large Δv [33]. This means that the staging concept overcomes electrosprays' present disadvantage to fill the propulsion utopia-point for CubeSats as Figure 1.1 illustrates, and that as electrosprays mature the staging system scales towards very large Δv missions. The work by Jia-Richards et al., concluded with a proof-of-concept staging system that was demonstrated by firing thrusters on two subsequent stages in a vacuum facility [31] and is a direct predecessor to the technology development in this thesis. An introduction to staging and their work is given in Section 2.4.4 of the literature review.

1.2 Motivation and Purpose

This thesis exists to take a step towards broader deep-space exploration. The Earth-orbit revolution of CubeSats has not yet been replicated in deep-space, although a few trailblazers have been launched to lead the way and demonstrate that CubeSats as a cohort can operate

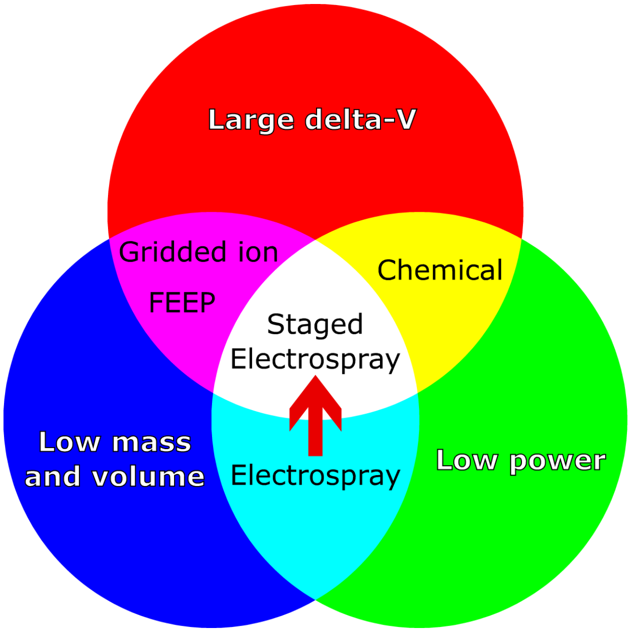

Figure 1.1: Venn diagram of state-of-the-art CubeSat propulsion technologies. The red arrow represents the technical push of this thesis: enhancing electrosprays to reach the utopia point in the centre.

and provide value in deep-space. All deep-space CubeSats so far have been companions piggybacking on a large mission that would probably not have happened independently. There are at least two reasons why: technological limitations and a lack of distinctive applications. The first reason is straightforward: make CubeSats more capable and more applications will call for them. The second reason requires musing: what applications are there in deep-space where CubeSats are not just a cheaper choice or a bonus mission, but the *best* or *only* feasible choice? In this thesis two applications are presented where the CubeSat excels as a solution to scientific inquiry. By focusing attention on these missions the benefits of CubeSats can be unlocked for deep-space exploration as well.

The present limitation of propulsion capability is a recurring (but not the only) hurdle for the identified scientific applications. In the last few years several impressive CubeSat electric propulsion systems have come to market, providing exciting opportunities for near-Earth applications. FEEP and gridded ion thrusters in particular are available and capable of several km/s Δv in compact packages, but their high power requirements make deep-space science missions difficult to close. Electrospray thrusters are compact and power efficient, and with the staging technology matured in this thesis their lifetime limitation is overcome to provide a propulsion system near the utopia-point and take us closer to the deep-space CubeSat revolution. By developing the staging with modularity in mind, the technology will continue to scale to ever higher Δv missions as the core electrospray technology matures.

1.3 Research Questions and Thesis Contributions

The themes of this thesis can be summarised by a few research questions covering the need for deep-space CubeSat explorers in general and staged electrospray propulsion as a technology in particular:

1. Are there applications where independent CubeSat-based missions in deep-space are scientifically motivated and feasible that cannot be reasonably addressed with traditional large missions?
2. How do such missions look and what are the technology readiness limitations?
3. Which properties of a staged electrospray propulsion system drives the overall performance and what performance can be expected of realistic future systems?
4. How do we practically implement staged electrospray propulsion systems within the CubeSat platform that are informed by the performance drivers?
5. Can staged electrospray propulsion systems survive and operate in the space environment? (Low Earth orbit in this thesis, deep-space operations are future work.)

This thesis opens with a literature review discussing relevant work on the research questions. A substantial portion of the literature review covers asteroid science as it is relevant for the mission motivations. Three chapters dedicated to each contribution follow and the thesis is concluded with a discussion of the outcomes and suggestions for future work. The thesis makes three main contributions:

1. Introduction of two novel main belt asteroid CubeSat swarm missions (Chapter 3).
    (a) Large asteroids explorer and asteroid family explorer motivated from decadal survey priority science.
    (b) Optimal selection of target asteroids based on propulsion constraints for both missions.
    (c) Architecture concepts introduced and feasibility shown for a subset of the targets with current technologies.
    (d) Discussion on the steps to enable feasibility of exploring all proposed targets in the future.
2. Analysis and development of the first staged electrospray CubeSat propulsion unit (Chapter 4).

    (a) Performance scaling model that shows improved performance over the state-of-the-art electric propulsion systems.
    (b) Sensitivity analysis to determine the driving design parameters.
    (c) Introduction of the staging loss factor Γ for practical mission analysis.
    (d) Implementation of staged electrospray in a flight-ready CubeSat form factor.

3. Technology Readiness Level of staged electrospray propulsion operating in low Earth orbit raised from 4 to 6 (Chapter 5).
    (a) Stage hold-down and release mechanism evaluated in low-gravity simulated by gravity offloading.
    (b) Engineering model propulsion unit demonstrated in a relevant environment via static load, random vibration, and thermal vacuum testing.

Chapter 2

Literature Review

This chapter provides relevant background for the scientific motivation of the proposed missions and an overview of the state-of-the-art for deep-space CubeSats. The scientific background summarises the modern understanding of solar system formation and evolution with a particular focus on asteroids. Asteroids were selected as the application focus area for deep-space CubeSats because they have clear scientific value and are so numerous that they can not be broadly explored by traditional large missions. Some important open questions are brought up throughout the background and a section is dedicated to the priority science questions in the most recent decadal survey for planetary science and astrobiology. The proposed mission are directly motivated by the decadal survey priority science in Chapter 3.

An overview of swarm missions and historical deep-space CubeSats are presented and used to anchor the feasibility and maturity of enabling technologies for the proposed missions. Extra focus is placed on propulsion with an overview of state-of-the-art systems in general and a detailed look at electric propulsion in particular. The review shows why electric propulsion systems are a key enabling technology for deep-space CubeSats and why the utility of the state-of-the-art is limited due to their high power consumption. Ionic liquid electrospray thrusters and staging systems are introduced and serve as the basis for the technology development in Chapter 4. This chapter concludes with some specific research gaps that are filled with this thesis.

2.1 The asteroids' role in the solar system

Asteroids are small solar system bodies orbiting the Sun primarily found in two regions: the main belt between Mars and Jupiter, and the Kuiper belt beyond Neptune (asteroids here are often called Kuiper belt objects [KBOs]). The largest asteroids are also known as dwarf planets, including (1) Ceres in the main belt, and Pluto in the Kuiper belt. The orbits of

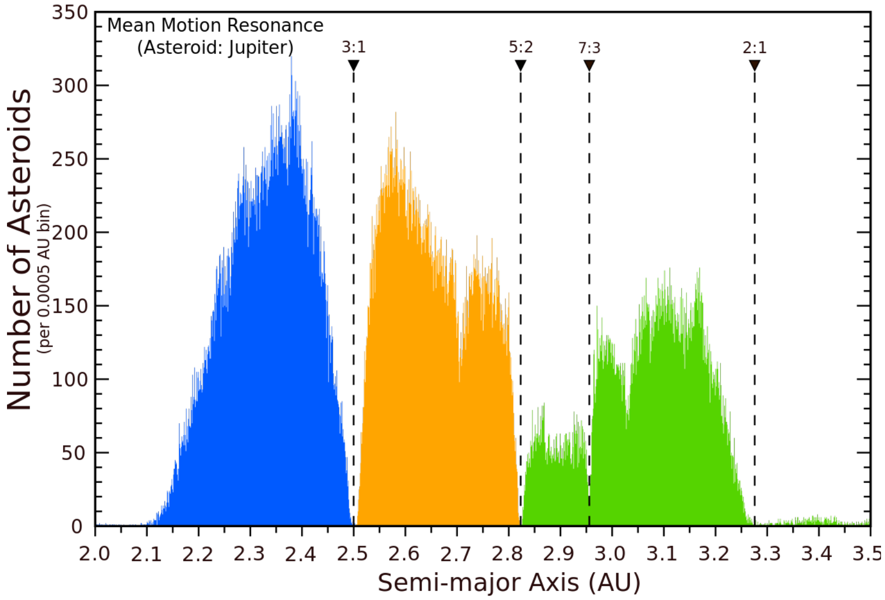

Figure 2.1: The distribution of asteroids in the main belt. The main belt is divided into the inner (blue), middle (orange) and outer (green) region by the Kirkwood gaps at the 3:1 and 5:2 Jupiter mean-motion resonances. The inner edge is due to the ν_6 secular resonance with Saturn. [Credit: Alan Chamberlain, NASA JPL/Caltech. Public domain.]

asteroids are strongly influenced by the gravity of the giant planets, where e.g. resonances with Jupiter carve gaps in the main belt distribution as shown in Figure 2.1. Asteroids in resonance with a giant planet will either be captured, as e.g. the Trojan asteroids, or have their orbits gradually pulled to higher eccentricity until they pass near a planet and collide or are ejected. Asteroids and other small bodies that fall on Earth are called meteorites and were previously disturbed onto an Earth-crossing orbit to become a near-Earth object (NEO). The dynamical processes that shape the distribution of the asteroids and continually deliver new meteorites are discussed in Section 2.1.3.

Different asteroids are distinguished by their reflectance spectra and divided into around 20 distinct types (also called classes) in four major groups: the S-type (stony), C-type (carbonaceous), X-type (includes the metallic M-type), and a broad category of “others” [5]. The unique appearances of different types suggest they were formed in different places or processes, however, virtually all types of asteroids are now found throughout the main belt, indicating a lively past of the solar system [6]. Thanks to the mixing of the main belt and continuous delivery of new NEOs to Earth, the meteorite record samples practically all types of bodies in the solar system but determining their origin is a major challenge [14]. Meteorites are broadly categorised as ordinary and carbonaceous chondrites, achondrites, iron meteorites, and stony-iron meteorites, with dozens of subgroups based on detailed traits.

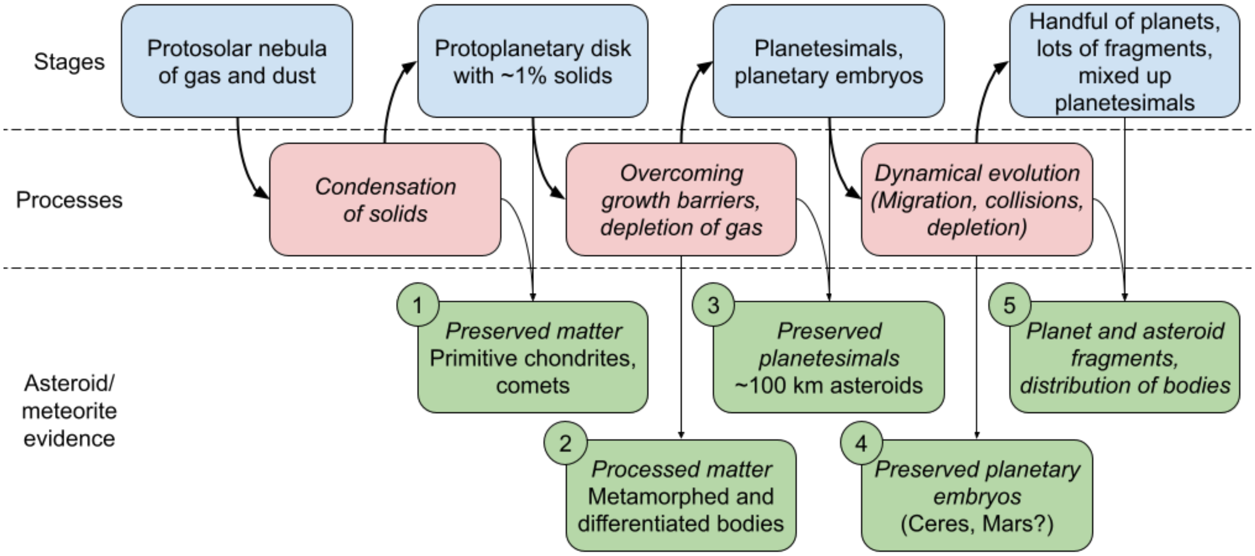

Figure 2.2: Illustration of the major steps of solar system formation and the sources of asteroidal and meteoric evidence of the past. The top row shows the major stages the solar system went trough and the second row shows the processes that transitioned from one stage to the next. At the bottom, five major sources of asteroids and meteorites originating from the stages and processes are shown.

For many meteorites this goes so far as to group them by unique putative parent bodies, of which there are only around 150 [34]. Using the “free sample return” of meteorites as ground-truth data is a great strength for studying asteroids and the solar system, and linking meteorites to their asteroid parent bodies is therefore a key scientific task [14]. Only a few clear links have been established. Broadly, ordinary and carbonaceous chondrites are related to S-type and C-type asteroids respectively, but it is unlikely that this is a one-to-one mapping. In some instances the specific parent body is known, e.g. the howardite, eucrite, and diogenite (HED) meteorites originate from the asteroid (4) Vesta [14]. Sections 2.1.1 and 2.1.2 present models of how the solar system and asteroids formed that are largely based on evidence from meteorites and their hypothesised links to asteroid parent bodies.

Comets, like asteroids, are small solar system bodies orbiting the Sun. Comets are traditionally distinguished by having a tail of gas and debris because their highly elliptical orbits pass close to the Sun causing volatile materials (e.g. water ice) to offgas. The distinction between comets and asteroids is fuzzy as they have related origins and comet-like active asteroids in the main belt and asteroid-like extinct comets have been discovered [35].

Asteroids and their cousins the comets and meteorites are remnants from the solar system’s formation and preserve its history and evolution, letting us peer into the past [36]. Figure 2.2 illustrates how asteroids originate from the major stages and processes of formation and will be referred to throughout this section. Much of the review materials here are based on chapters from the excellent book *Asteroids IV* published in 2015 [4] that collects the state-of-the-art knowledge in a roughly decadal series, with further detail and updated results added from other sources as necessary. This section is wrapped up with an overview of the major open questions in asteroid science today (Section 2.1.4).

2.1.1 Solar system formation

The solar system formed from a large cloud of gas and dust that became sufficiently dense to collapse under mutual attraction of gravity. The elemental composition at this time was similar to the present solar photosphere characterised by, in order of abundance, H, He, O, C, Ne, N, Mg, Si, and Fe [37]. Due to the gravitational release of energy the matter was heated and formed a dense protosolar nebula of gas and dust at an average temperature around 1400 K, rotating to preserve angular momentum, that cooled quickly in approximately 0.1 Myr [38]. The age of the solar system is defined by calcium-aluminium-rich inclusions (CAIs) that formed 4.567 Gyr ago and are the oldest preserved objects [39], consisting of several Ca-Al-O-based minerals condensing around 1600 K [37]. The oldest silicate rocks, chondrules, are millimetre sized spheres that primarily consist of the minerals olivine ($[\mathrm{Mg}, \mathrm{Fe}]_2\mathrm{SiO}_4$) and pyroxene ($[\mathrm{Mg}, \mathrm{Fe}, \mathrm{Ca}]\mathrm{SiO}_3$) [40] that condense around 1300 K [37]. The earliest chondrules started forming at the same time as CAIs, but they are typically 1 to 3 Myr younger than CAIs [39], forming throughout the period where most meteorite parent bodies also formed [41]. Chondrites are stony metorites that account for over 80% of all meteorite falls [14] and consist of chondrules stuck together with a matrix of dust as shown in Figure 2.3, sometimes with CAIs embedded within. Matter sampling the local environment and composition during formation are preserved in these primordial chondrites and their asteroid parent bodies as the first major asteroid evidence illustrated in Figure 2.2. In particular, CI-group carbonaceous chondrites and unequilibrated ordinary chondrites are among the most primitive material known [42].

The dust and gas of the nebula clumped together to form a protoplanetary disk with solids of varying sizes, ranging from microscopic to planetary, embedded in gas that eventually dissipated. In this environment gas and solids act differently, as the gas is supported against gravity by a pressure gradient and thus travels about 50 m/s slower than large objects that orbit at the Keplerian rate [34]. Whether a solid is coupled to the gas or orbits freely is a function of size: small objects (<1 mm) couple strongly to the gas and move with it, pebbles (c. 1 mm to 10 m) decouple from the gas and orbit faster but lose energy due to aerodynamic drag, and planetesimals (>1 km) orbit unencumbered at Keplerian speed [43]. Dust and ice particles coming into contact readily stick together to form fluffy particles up to around

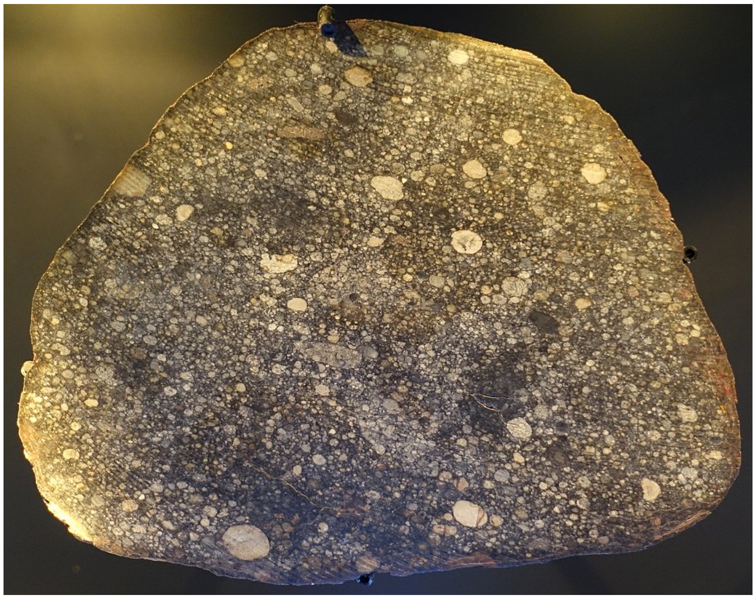

Figure 2.3: Cross section of the ordinary chondrite meteorite *Sahara 97210*, consting of many small spherical chondrules embedded in a fine matrix. [Credit: user *Daderot* on *Wikimedia Commons*. Public domain.]

0.1 mm in the nebula conditions, but at this size their impacts begin compacting the particles causing them to bounce off each other and stop growing [34]. How this "bouncing barrier" is overcome remains unclear, but studies of protoplanetary disks show large amounts of cm-scale pebbles so this barrier can not be a significant obstacle [44]. In principle, planetesimals could have formed from gradual clumping of pebbles into gravitationally bound bodies, however, even if they would clump together collisions will easily break them apart, an issue known as the "metre-size barrier" [36]. Models show that porous or icy objects are more sticky and could continue to slowly increase in mass from impacts, but the drift towards the Sun due to drag is faster than their growth rate, and this "drift barrier" also rejects models of slow accretion to planetesimal size [43]. These results mean that some mechanism must have enabled a jump in size from <1 m to >1 km; otherwise asteroids and planets are unlikely to form.

The leap from pebbles to planetesimals — bodies dense enough to be held together with gravity — is not entirely understood but modern models are illuminating the process. Studies of other solar systems being born show that planet formation starts early, as very young protoplanetary disks have structure; either they already have planets disrupting the disk, or they have the enhanced local density required to form planetesimals [43]. Two main models have emerged that can produce the required densities: turbulent concentration and streaming instabilities. Turbulent concentration occurs in gas vortex tubes that couple well to the size of chondrules and could potentially form 100 to 1000 km size bodies directly from chondrules [34]. The most recent turbulent concentration models yield smaller bodies than originally envisioned, 10 to 100 km, and notably require that the initial particles are not chondrules, but instead pebbles with a size of several cm to work effectively [45]. Streaming instabilities appear in models with lower turbulence where the aerodynamic drag between the gas and particles cause a feedback loop. If a region has a locally enhanced density of particles affected by drag they will speed up the gas around them and therefore reduce the local radial drift caused by drag. The reduced drift results in other particles catching up, enhancing the density further and creating positive feedback that exponentially increases the density in long thin filaments. With typical estimates for the conditions in the protoplanetary disk, streaming instabilities could efficiently form planetesimals of 100 km size if pebbles on the scale of 10 cm are already formed [34]. Because neither leading model supports direct chondrule-to-planetesimal formation it is generally accepted that pebbles formed of dust and/or chondrules (and significant amounts of water ice the outer solar system) were the precursors to planetesimals, with a jump in size from several cm to around 100 km. The size distribution of asteroids independently show that most asteroids in the main belt larger than 100 km could not have be formed by collisions of larger bodies, but rather were created at that size [46]. Thus the asteroid belt has dozens of preserved planetesimals waiting for us to study them closer, illustrated as the third major asteroid evidence in Figure 2.2.

The formation and abundance of chondrules present a number of challenges to modelling the details of planetesimal formation. There are two concepts with significantly different implications: chondrules are either the building blocks of planetesimals or the result of planetesimal formation. Some chondrules are known to have formed at the very beginning of the solar system [39], while others are known to be the result of planetesimal collisions [47], potentially supporting both paths. If planetesimals were formed in a sea of chondrule building blocks one would expect them to accrete chondrules and grow in layers over several million years [34]. However, all chondrules in a given chondrite are similar [34] and analyses of ordinary chondrites are consistent with a quick formation at the 100 km scale [48]. Recent advances in radiometric dating and isotopic studies have also shown that iron meteorites typically formed before chondrules, not from chondrules, so they can not be the precursors to all planetesimals [41]. If chondrules were formed in impacts between planetesimals and/or embryos then chondrites belong to a "second generation" of planetesimals and Vesta may be the only preserved example of the first generation [41]. The favoured view today is that chondrules are not the building blocks for early planetesimals and that there are several generations, where the rare and complex asteroid types belong to the older generations [49].

Once planetesimals have formed, a regime of runaway growth will produce a small number of planetary embryos that capture most of the mass in the local area. The largest planetesimals have the strongest gravity and readily accrete other planetesimals, increasing the strength of their gravity further and growing to a few thousand km (scale of the Moon or Mars) in less than 1 Myr [36]. The growth rate in the runaway phase is enhanced by also directly accreting pebbles, which is especially effective beyond the snow line* to form the embryos of giant planets [50]. Once the runaway growth phase has ended because the amount of matter in the local disk is dramatically reduced, the remaining planetesimals are inhibited from growing due to a phenomena coined “oligarchic growth”: the gravitational disturbance of planetary embryos make collisions between the remaining planetesimals to be of sufficiently high velocity to catastrophically break them apart, so they cannot grow significantly larger [43]. Because of oligarchic growth there are only four likely outcomes for planetesimals: 1) they are accreted onto a planetary embryo, 2) they break apart catastrophically in a collision, 3) they are ejected from the solar system, or 4) they remain preserved. The planetary embryos will continue to grow slowly and can reach a second runaway growth phase to form a gas giant when they become massive enough to retain a gas envelope if they form quickly enough that the gas in the disk has not dissipated [36]. The fourth evidence illustrated in Figure 2.2 shows how the largest not-quite-planets in our solar system, including large asteroids and possibly even Mars, could help explain the nature of planetary embryos.

At this point, there are giant planets in the outer solar system and a large population of planetary embryos and planetesimals in the inner solar system, forming what we would probably recognise as a solar system with massive asteroid belts. The planetary embryos and planetesimals in the inner solar system will evolve to form the terrestrial planets and asteroid belt; the timeline continues in Section 2.1.3.

2.1.2 Asteroid interiors and thermal evolution

Major outstanding questions about asteroid interiors complicate the view illustrated in Figure 2.2. As planetesimals and larger bodies are formed their materials evolve due to chemical interactions and increased pressure and temperature. How, when, and where the materials gravitationally collapse into a planetesimal will affect the internal structure primarily though heating, and any subsequent accretion may form secondary layers of materials from later epochs [34]. The preserved matter illustrated as the first major evidence in Figure 2.2 come from the most primitive materials known, including CI-group carbonaceous chondrites and unequilibrated ordinary chondrites. How materials interacted and evolved as bodies grew is the second major evidence in Figure 2.2 and depends on the local conditions in the protoplanetary disk and the accretion mechanisms.

---

*The minimum distance from the Sun where water can exist in ice form. Also called frost or ice line.

The decay of short-lived radioactive isotopes, mainly ^{26}Al with a half-life of 0.7 Myr and a smaller contribution from ^{60}Fe with a half-life of 2.6 Myr, are the primary sources for heating planetesimals [51]. Gravitational energy released from their sudden formation also heats planetesimals, however, this mechanism is not a major contributor as e.g. bodies forming with a diameter of 300 km would only see a temperature rise of around 10 °C [51]. Thermal alteration of a planetesimal with ice present proceeds by, in order of increasing temperature:

1. Ice melting: Formation of liquid water.
2. Silicate hydration: Water enters the mineral crystal structure.
3. Silicate dehydration: Water exits the mineral crystal structure.
4. Thermal metamorphism: Nearby minerals equilibrate and/or recrystallise.
5. Melting of Fe-Ni-S system: First melts are formed, possibly migrating to form a core.
6. Melting of silicates: Silicates start to flow. Core of Fe-Ni-S definitely formed. Several outcomes for the silicate melts can cause different internal structures.

where an ice-free planetesimal would skip the first three stages and the amount of heating determines where the process is cut off [42].

Changes to chondrites without melting is divided into aqueous alteration and thermal metamorphism. These effects are described on a scale from 1 to 6, where type 3 is neutral while higher numbers indicate more thermal metamorphism and lower numbers more aqueous alteration [42]. The most primitive meteorites are in the highly aqueously altered type 1 due to initially having a water-to-rock ratio over 60%, where the chondrules and dust matrix equilibrated and caused the former to vanish, but they may never have had chondrules at all [42]. The least altered chondrites (type 3, also called unequilibrated) were neither aqueously altered nor reached temperatures above 600 °C, and are therefore well preserved snapshots of the protoplanetary disk [52]. Thermal metamorphism will typically create a planetesimal with an onion-skin structure with the most processed (6) material in the centre, and the least processed (3) material at the surface, but without any significant compositional changes [48]. S-type asteroids show that ordinary chondrites were evenly metamorphosed with a thin outer layer of less processed material [52]. The peak temperatures measured for thermally metamorphosed meteorites are around 950 °C [42], as higher temperatures will lead to melting and thus the formation of achondrites. Primitive achondrites sit on the border between highly metamorphosed chondrites and achondrites, appearing as chondrites with partially melted chondrules [41].

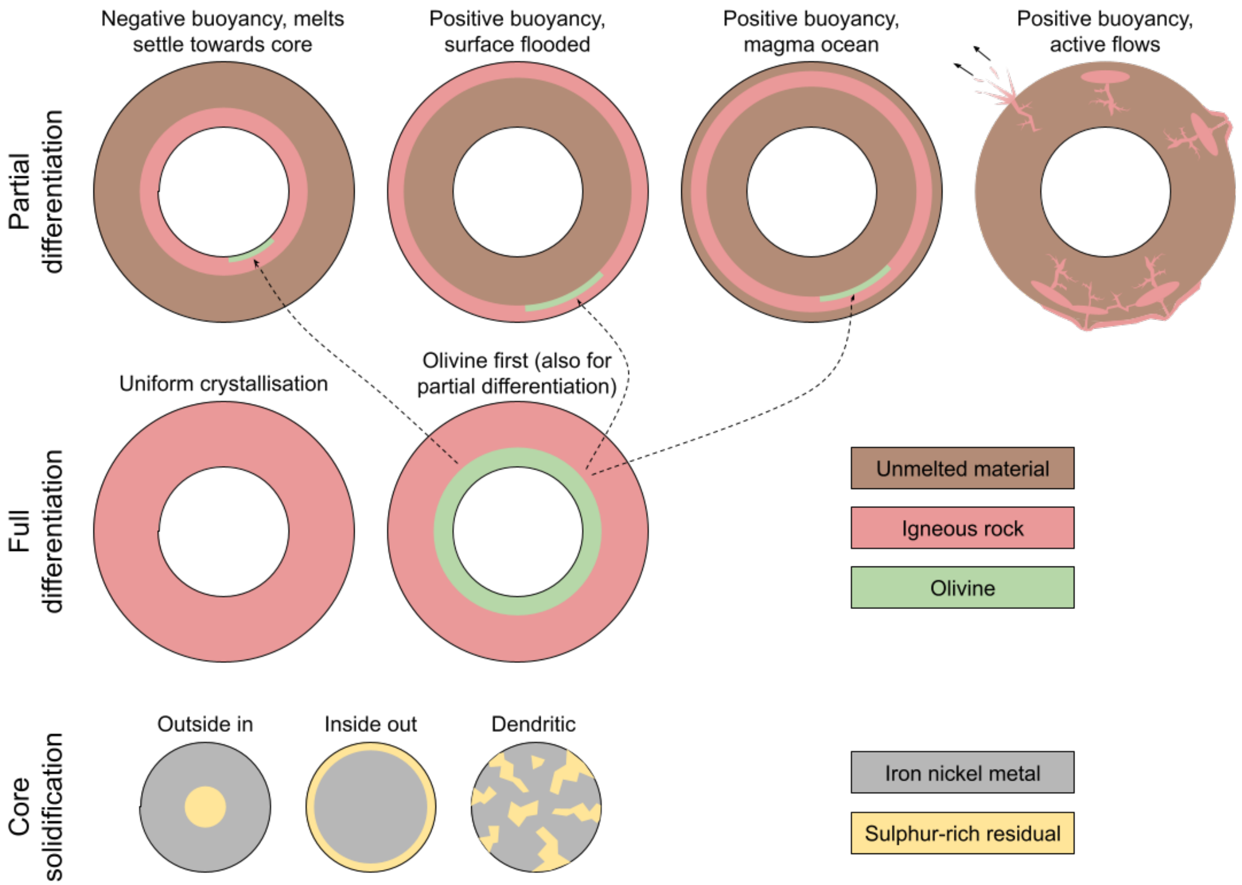

Figure 2.4: Illustration of possible outcomes for differentiated planetesimals, based on figures from [42, 51]. The core forms first and may be combined with any outcome for the mantle and crust, potentially including a core forming with an otherwise undifferentiated mantle.

When a planetesimal becomes hot enough to melt a significant part of its materials it may differentiate into a layered structure based on density as illustrated in Figure 2.4, with a dense metal-rich core surrounded by a mantle of leftover silicates and ice. To form a differentiated body a peak temperature of at least 950 °C is required, which is the lowest melting point for the Ni-Fe-S system [51]. With only a small fraction of melt the materials may remain in-place, however, recent models suggest that melts are capable of flowing to form a core in an otherwise solid planetesimal in around 1000 years [42]. The timing of formation and duration of accretion are more important for differentiation than the size of the planetesimal or planetary embryo due to the short half-life of ^{26}Al. Simulations show that 10 km bodies formed in the first 1.5 Myr would differentiate, as would 100 km bodies formed in the first 3 Myr, but even a 1500 km sized planetary embryo formed after 5 Myr would fail to reach sufficient temperatures to differentiate [51]. The timing of differentiation can be measured via the decay of ^{182}Hf to ^{182}W as the former is lithophile and the latter siderophile and thus will separate into the mantle and core respectively [53]. Dating of metal meteorites show that most core formation occurred 1.0 to 2.2 Myr after solar system formation, consistent with fast accretion models and ^{26}Al decay as the heat source [41].

Silicates, which make up most of the material in planetesimals, begin to melt around 1100 °C (complete melting at 1500 °C), at which time their buoyancy determines if they migrate towards the core or surface [51]. Due to variable initial conditions and the sensitivity of the silicate melt migration to factors such as gas content and body diameter several different surface features and interior structures are predicted for planetesimals as illustrated in the first row of Figure 2.4. If the silicate melts have negative buoyancy (predicted for carbonaceous chondrites) they will remain in the mantle and leave a primitive surface, whereas if they have positive buoyancy (predicted for ordinary chondrites) they will flow towards the surface and may flood it [51]. Flow towards the surface is complicated by the presence of a c. 10 km thick lithosphere where the temperature transitions from the hot interior to the cooler surface. The lower temperature can block the outwards flow and form "oceans" below the surface a few km thick for bodies smaller than 200 km, possibly leaving a primitive surface [42]. As flow paths emerge, however, any gas trapped in the body will try to escape and for small bodies (c. 60 km) even a small amount (c. 50 ppm) of gas would be sufficient to drive explosive eruptions of silicate melts to the surface or to escape velocity [42]. Highly buoyant silicate melts could also overcome the lithosphere's lower temperature and erupt as volcanoes that flood parts or the entire surface of the planetesimal where, thanks to rapidly radiating away their heat, they could encrust the planetesimal's primitive surface in one or multiple layers of igneous rocks [51]. As the aluminium heat source is lithophile it will preferentially join the melt and be transported away from the solid mantle and may limit the typical amount of silicates that are melted to around 30% [42]. With sufficient heating a fully differentiated body where all materials are melted may be formed as illustrated in the second row of Figure 2.4.

The cooling conditions after reaching peak temperature will also impact the internal structure of a planetesimal, especially the core. The molten core of Fe-Ni-S will crystallise into metallic FeNi, leaving behind sulphur-rich material (e.g. FeS) where the last parts of the core solidified [51]. The solidification may proceed concentrically from the outside or inside, or through dendritic growth to form complex structures [51] as illustrated in the bottom row of Figure 2.4. The cooling rates of iron meteorites vary widely and can be measured by the growth and diffusion of different metal crystals (the famous Widmanstätten pattern is an example) [54]. The diversity of cooling rates suggest that the parent bodies of many iron meteorites cooled after much of their insulating rocky mantle had been stripped off, probably from collisions with other large bodies [41]. If left intact, the molten mantle on a planetesimal

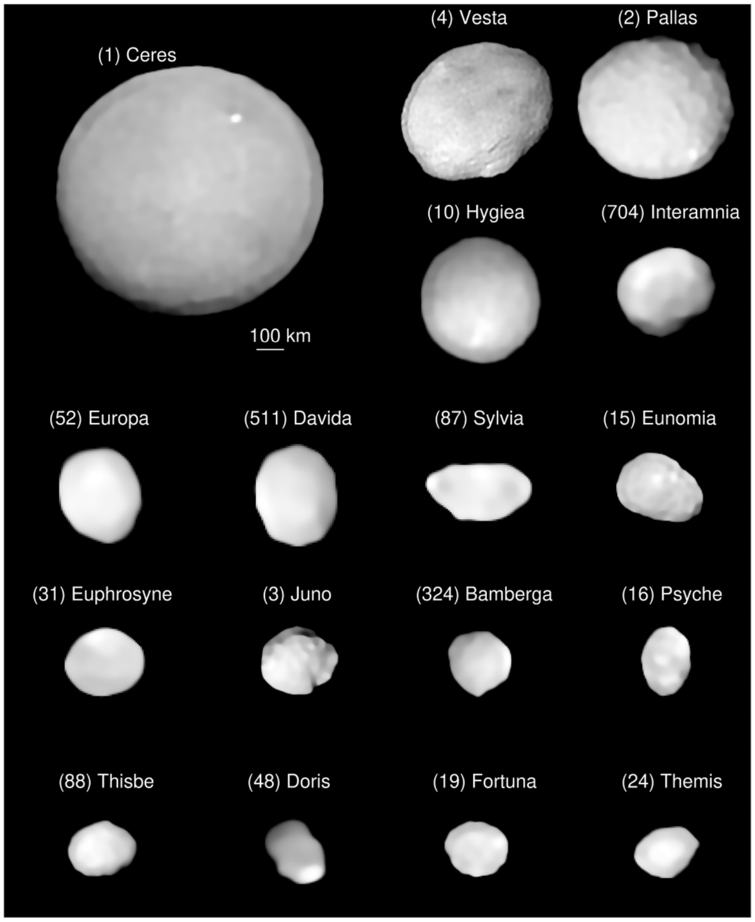

Figure 2.5: Shape reconstructions of most main belt asteroids >210 km from the SPHERE instrument at the Very Large Telescope [55]. [Credit: Vernazza et al. CC BY 4.0.]

would likely solidify as a bulk layer as the pressure differential is not sufficient to fractionally crystallise different minerals [51]. The sole exception is that olivine may precipitate first and sink to the core-mantle interface, which may the origin of the rare pallasite meteorites that show large pure olivine crystals embedded in metal [51]. The second row of Figure 2.4 shows the two solidification options for a fully differentiated planetesimal, but the same concept applies to e.g. the magma ocean on a partially differentiated body.

The orderly descriptions of planetesimal interiors are complicated by collisions in their early evolution, when there were many planetesimals and they were still warm and therefore "soft". The fast cooling rates of some iron meteorites point to several planetary embryos being stripped of their insulating mantle, leaving 100 to 300 km metal cores to cool quickly [41]. Studies of ordinary chondrites and their associated S-type asteroids also support collisions disturbing and rearranging them while still warm, without necessarily breaking them apart [48]. Modelling of hit-and-run impacts suggest that a gamut of outcomes for mantles ranging from nearly undisturbed to completely stripped should be expected, consistent with both the iron meteorite record and Vesta as a relatively undisturbed planetesimal [41]. Some of the battered and bruised putative planetesimals in the main asteroid belt are shown in Figure 2.5 with diverse shapes.

2.1.3 Dynamical processes

The solar system morphed from a collection of many planetary embryos and planetesimals to today though three major phases of dynamical evolution. In the first 100 Myr the embryos and planetesimals interacted to form the planets and asteroid belts under a strong influence of Jupiter, in the following 1 Gyr the solar system settled into its present form, and to this day slow dynamical processes keep the asteroids distributed in a quasi steady state. The low mass observed in the asteroid belt is a major constraint on dynamical processes as the protoplanetary disk should initially contain 1 to 2.5 Earth masses of matter in the main asteroid belt region, but today it only contains around 5×10^{-4} Earth masses [56]. The large reduction in population is typically attributed to a combination of several major processes discussed in this section: 1) planetary embryos accreting and disturbing smaller bodies, 2) giant planet resonances sweeping through the main belt, 3) drift mechanics feeding giant planet resonances, and 4) mutual collisions grinding away at the population. The fifth major asteroidal evidence in Figure 2.2 illustrates that the present distribution of bodies of all types are key evidence for understanding the dynamical evolution of the solar system.

By modelling the asteroid size distribution evolution due to collisions the primordial population and total amount of collisions can be uncovered. From these models it is clear that most large bodies (>100 km) are preserved planetesimals whereas small bodies (<30 km) are almost all collisional fragments, and that the initial population of asteroids were almost entirely in the 100 to 300 km size range [56]. Due to the large number of fragments produced, however, it is difficult to determine the primordial distribution and number of <100 km bodies from the present-day distribution [57]. The rate of collisions in the asteroid belt today is low, particularly for large bodies, where e.g. only four catastrophic disruptions per Gyr are expected among all >100 km bodies [57]. Furthermore, to match the present size distribution the asteroid belt has evolved for the equivalent of no more than 10 Gyr at the current rate, clearly insufficient to reduce the population by the several orders of magnitude required [56]. Asteroid families are formed when asteroids collide with sufficient energy to break apart and generate a debris field, of which over 120 have been discovered [58]. Due to a small force imparted on spinning asteroids from thermal radiation, dubbed the Yarkovsky effect, the family members spread out over time in inverse proportion to their size and allow the initial impact to be dated [59]. The number of families observed and their ages also constrain the collisional activity in the asteroid belt in agreement with the result that there have been only a few collisions breaking up large asteroids in the last several billion years [56].

Because the orbital regions of different asteroid types overlap significantly and cover a broad range of inclinations and eccentricities the solar system must have had a lively past [46]. In the 1990s, a model proposed by Wetherill [60] was able to reproduce the structure of the asteroid belt by embedding a population of planetary embryos with planetesimals in the asteroid belt and letting them co-evolve under the influence of Jupiter. His model showed that the embryos were effective at scattering the planetesimals' orbital elements, creating a distribution consistent with the main belt and ejecting a large fraction of the mass by crossing Jupiter's resonances. Modern simulations of the Wetherill model show that it can reproduce the observed asteroid belt well, including a radial mixing of the different types of asteroids by 0.5 to 1.5 au and a depletion of 98% of planetesimals and most planetary embryos [61]. While this model is successful in explaining the structure of the asteroid belt, it can not reproduce some of the broader constraints on solar system formation, in particular, the small mass of Mars [46].

To reproduce the small mass of Mars, models were proposed that cut off the protoplanetary disk at around 1 au, reducing the mass available for Mars to form [36]. To create this cutoff, Walsh et al. proposed the "grand tack" scenario in 2011 [62], which implemented contemporary work showing that that giant planets quickly drift inwards so long as gas remains in the protoplanetary disk. They showed that the migration of Jupiter in 0.1 Myr from its birthplace at the snow line (c. 3.5 au) to only 1.5 au would "shepherd" most planetesimals and planetary embryos inwards, creating the required cutoff in the protoplanetary disk at 1 au. While surprising from the perspective of our solar system, several giant exoplanets orbiting close to their host star have been observed and the newly discovered drifting mechanics provided a plausible explanation for why this could happen [36]. Today, Jupiter is found far away from the Sun, at 5.2 au, and the grand tack model explains this by Saturn also migrating inwards until it is captured in a 2:3 orbital resonance with Jupiter and these two giant planets jointly migrate outward towards their present orbits, stopping when the gas dissipated [62]. Critically for the validity of this model, simulations show that the in-then-out migration of Jupiter will not completely empty the asteroid belt, but leave around 0.1% of the original population and inject around 0.5% of the asteroids that formed between Jupiter and Neptune, plus a small number formed beyond Neptune [62]. Recent spectral surveys of the asteroid belt show that virtually all types of asteroids are present throughout the asteroid belt, consistent with the idea that the asteroids did not form near their present orbits but rather became mixed up during giant planet migration [6]. In addition to solving the small mass of Mars, the grand tack model naturally explains how the stony, dry, S-type asteroids and carbonaceous, wet, C-type asteroids in the main belt are so different: they may have formed on opposite sides of the snow line (and Jupiter) [46].

Irrespective of their early evolution, the giant planets should be in the outer solar system when the gas dissipates, but in a compact and mutually resonant configuration and with a disk of planetesimals beyond Neptune (i.e. the Kuiper belt) [46]. As the giant planets gradually accreted and scattered the outer disk their orbits would drift, eventually causing interactions between them resulting in “jumps” in orbital parameters that can reproduce the present giant planet orbits [63]. This model, dubbed the Nice model, also has the benefit of explaining the so-called late heavy bombardment (LHB). The LHB is a period derived from dating Moon craters that showed a large spike in crater production during in the period 0.5 to 0.8 Gyr into the solar system’s history [46]. If the giant planet instability occurred at the start of this period, it would also disrupt the asteroid belt and explain the origin of the LHB impactors [64]. Generally, around half of the main asteroid belt population would be removed (by collisions or ejection) and a few outer solar system asteroids would be injected during and immediately following the instability [46]. Recent work suggests that the giant planet instability occurred before the LHB and before the terrestrial planets were formed, because otherwise their orbits would be more inclined and eccentric than they are today [65].

While the timing and all implications are yet fully determined, the Nice model is generally accepted as the mechanism that set the giant planets’ final orbits and gave the asteroid belts their final shape [46]. While early timing does not explain the LHB, it opens an alternative scenario to explain the small mass of Mars, as the giant planet instability can disturb the formation of terrestrial planets in a compatible manner [66]. The dichotomy of stony and carbonaceous asteroids could also be explained without invoking the Grand Tack, where e.g. large changes in the frost line over the first few million years can produce two distinct planetesimal forming reservoirs for the two populations [67]. Testing these and future models relies on the observed distributions of asteroids and their fragments [46] and analysing craters on large asteroids [56].

2.1.4 Priority asteroid science

The state-of-the-art knowledge and priorities for research in planetary science and astrobiology are compiled in decadal surveys performed by the National Academies of Sciences, Engineering, and Medicine. Their reports provide independent analysis and strategy advice that are used as the primary sources to direct U.S. government funding for planetary science missions. The latest survey covers 2023-2032 and is titled “Origins, Worlds, and Life” [68] and is the sole source discussed in this section. Table 2.1 lists the 12 priority questions of the latest decadal survey, wherein four are most relevant to this thesis and discussed in this section.

Table 2.1: The priority science questions from the 2023-2032 decadal survey [68]. The questions in bold are most strongly related to the asteroid science discussed in this thesis.

Scientific Themes	Pritority Science Questions
(A) Origins	**Q1: Evolution of the protoplanetary disk.** Q2: Accretion in the outer solar system. **Q3: Origin of Earth and inner solar system bodies.**
(B) Worlds and Processes	**Q4: Impacts and dynamics.** **Q5: Solid body interiors and surfaces.** Q6: Solid body atmospheres, exospheres, magnetospheres, and climate evolution. Q7: Giant planet structure and evolution. Q8: Circumplanetary systems.
(C) Life and Habitability	Q9: Insights from terrestrial life. Q10: Dynamic habitability. Q11: Search for life elsewhere.
Crosscutting A-C linkage	Q12: Exoplanets.

The scope of this thesis is limited to spacecraft in situ observations of asteroids in the inner solar system, i.e. in the main belt or near Earth. The decadal survey also contains many other important research paths throughout our and other solar systems; this section is not intended as a complete summary. For the relevant priority science questions, only important research that may be carried out with in situ spacecraft observations of asteroids has been picked out.

Q1: Evolution of the protoplanetary disk

Major open questions remain about the formation and evolution of our solar system's protoplanetary disk. The processes that governed the disk's evolution were complex and coupled both to the evolution of the young Sun and possibly the surrounding star-forming region. Detailed analyses of primitive materials are an important avenue to make progress on this topic, especially through sample-return missions of primitive materials from comets. Most questions on this topic will be answered by detailed laboratory studies to constrain initial conditions and chemical evolution, combined with data from young exosolar systems. However, in situ spacecraft studies are suggested for some topics within this question in the decadal survey [68]:

- (Q1.2 and Q1.3) Different types of bodies were formed in the solar system, e.g. the many types of chondrites, differentiated bodies, and unique planets, that likely originated from distinct reservoirs in the protoplanetary disk. The timing and mechanisms that segmented reservoirs and the later mixing of bodies are poorly understood but important to understand the diversity and connections between bodies observed today. In situ satellite studies of the elemental and isotopic composition of bodies formed from different reservoirs are key to understand this topic. Isotopic measurements of H and N have proven especially useful as they can be distinguished with relatively low resolution in situ data.

- (Q1.3) It is now well established that planetesimals were formed in gravitational collapses to 100 km scale bodies, instead of slowly growing by particles sticking together. Several barriers limiting the slow growth path are known, but in the outer solar system it is possible that these are overcome in specific conditions. Bodies formed by gravitational collapse should initially be weak and porous, so studying the interior structure of large asteroids could illuminate their formation and the effect of growth barriers.
- (Q1.4) The timing and mechanisms of gas removal from the protoplanetary disk is poorly known but locally likely proceeded quickly and lead to a chaotic epoch as the gas' damping effect on orbits vanished. The magnetisation strength of bodies can be a measurement of the gas density when they were formed because the gas is necessary to retain the nebular magnetic field. In situ measurements of the magnetic properties of different types asteroids would constrain the nebular magnetic field as a function of space and time to close this gap in our understanding of the protoplanetary disk.

Q3: Origin of Earth and inner solar system bodies

The processes that formed the the terrestrial planets and asteroids have implications for understanding our origins, but also the study of extraterrestrial Earth-like planets and the search for life. How random or deterministic the outcome of our solar system is, assuming we know the initial conditions, remains a fundamental uncertainty in if we should view our solar system as a typical outcome or unique example. It is established that giant planet migration (of Jupiter in particular) had strong effects on shaping the inner solar system by the relocation of their disruptive orbital resonances, but the timing and extent of these effects remain open. The timing and mechanics of initial differentiation, as well as the origin of volatile elements that are fundamental to organic chemistry, remain uncertain but drive the diverse characteristics of the terrestrial planets. To understand how the earliest bodies in the inner solar system became the planets and asteroids a mixture of modelling work and broad exploration is required. The decadal survey's strategic research goals include detailed studies of Mercury and Venus, and important in situ spacecraft observations of the asteroids to help resolve several of the open questions [68]:

- (Q3.1) The diverse set of asteroid types observed and the diverse set of meteorites recovered need to be reconciled to advance our understanding of both. In situ measurements of the composition and nature of the large asteroids in the main belt, that potentially include samples formed across the solar system, are necessary. This should especially focus on rare or underexplored asteroid types, however, spectral classification of asteroids may be unreliable as partially differentiated asteroids may present a primitive surface and space weathering may mask the true composition.

- (Q3.1) Asteroid thermal metamorphism and complete or partial differentiation may be important in the diversity of asteroids and planetary building blocks. In situ geochemical, petrological, and geophysical studies of large asteroids could clarify these processes and also help determine the mechanisms of planetary accretion by constraining the nature of the accreted materials.

- (Q3.2) The formation locations of different types of asteroids in the main belt must be determined to understand how the giant planets reshaped the solar system. The presumed most primitive bodies, including P and D asteroids, should be studied and compared to bodies thought to originate from beyond the giant planet forming region, e.g. comets, Kuiper belt objects, and the Trojan asteroids. In situ measurements of asteroids' volatile content and temperature at formation are especially valuable.

- (Q3.2) In situ studies of multiple large asteroids can provide their impact history and therefore determine the timing of bombardment caused by the giant planet instabilities. This data will help resolve if the instability occurred early and could be the cause for a small Mars and the mixing of asteroids, or if it occurred late and could be the cause for the late heavy bombardment of the Moon. If early, the extensive migrations in the grand tack model may not be necessary to explain the outcome of our solar system.

- (Q3.5) Differentiation mechanisms are key to the outcomes of planetary formation but are loosely constrained in terms of outcomes based on initial conditions. Large and small body differentiation are likely driven by different primary mechanisms, where short-lived radionuclides are especially critical to small body differentiation. The nature and degree of differentiation of solar system bodies as a function of their size and formation location, especially for planets but also large asteroids, needs to be studied.

- (Q3.5 and Q3.6) There is conflicting evidence on if volatile elements (e.g. H, C, N, O) that are fundamental to organic chemistry and life were included in the initial planetary accretion or are primarily an enrichment by later accretion of outer solar system materials. The range of compositions and elements available on bodies formed in the outer solar system, including comets and primitive asteroids, needs to be measured to determine where the volatiles on the terrestrial planets originated.

Q4: Impacts and dynamics

Dynamical modelling of the solar system has made strides to convincingly reproduce the orbits and sizes of the planets and small body reservoirs, including e.g. the main asteroid belt and Kuiper belt. Present work is focused on the dynamical evolution of the small body reservoirs and the effects of their bombardment of the planets over the last several billion years. Three main sources of bombardment have been established but their relative importance over time remains to be determined: 1) icy bodies from the Kuiper belt that are disrupted by the giant planets, becoming comets, 2) leftover bodies from planet formation on highly inclined and eccentric orbits that eventually collide, 3) asteroids in the main belt on stable orbits that are disrupted by planet migration or giant planet resonances. Crater counting is the only method available to date a body's surface without sample return, and therefore fundamental to all planetary science. Crater chronology is significantly limited, however, since only a narrow region of lunar craters have been independently dated and these are used to extrapolate ages across the inner solar system with unknown accuracy. The challenge of understanding bombardment is amplified by a relatively poor understanding of the nature and physics of impacts, and the decadal survey suggests several in situ studies to reduce the uncertainties in impact physics and the solar system's dynamical evolution [68]:

- (Q4.1) Several small asteroid reservoirs, e.g. Jupiter's Trojans, are captured in stable resonances with the planets and have likely remained undisturbed since they were captured during giant planet migration. In situ studies of the size distribution and composition of asteroids in these reservoirs could constrain the early dynamical history of the solar system and the nature of the bodies that bombarded the planets.

- (Q4.1) Active asteroids are bodies in the main belt that show cometary activity near perihelion, suggesting they are rich in volatiles. The active asteroids may be icy asteroids formed in nearby regions that have been disturbed by impacts, or comets captured during giant planet migration. In situ studies of these bodies could illuminate the relationship between comets and asteroids.

- (Q4.1 and Q4.4) Asteroid families provide unique opportunities to study both the collisional disruption of asteroids and the dynamical evolution of their fragments. By in situ observations of family members their nature and ages can be determined and compared to model results. The Yarkovsky and YORP effects are major drivers of asteroid evolution in general, and families allow these effects to be studied directly.

- (Q4.2) The large asteroids may preserve surface features that have been erased on larger bodies with more geological activity. In situ observations of their craters could determine the nature of early bombardment of the inner solar system, and would be especially powerful if coupled with absolute dating of basins with known samples, e.g. meteorites from Vesta.

- (Q4.4) If the properties of the projectile and target (e.g. strength, porosity, and size) are combined with the parameters of the impact (e.g. velocity and angle) the outcome of an impact should be well determined. However, the knowledge of both initial parameters and impact processes remain limited. In situ studies of how porous asteroids and comets are compacted in collisions by precision density measurements of craters would help to improve modelling.

Q5: Solid body interiors and surfaces

After initial accretion and differentiation, the interiors and surfaces of solid bodies, ranging from asteroids to Earth in size, continue to evolve. Internal materials are deposited on the surface through eruptions and liquid layers inside the body can cause large movements of the crust or induce magnetic fields. External effects are significant, especially on airless bodies, where small impacts cause the surface materials to be ground down and spread around the body, and large impacts can cause global changes including internal melting or alteration of convective flow patterns. Micrometeorite and energetic particle bombardments cause a slow "space weathering" effect, where nanoparticles are generated on the surface of rocky bodies that typically darken and flatten their spectra, while icy bodies are brightened by changes to the water phase. How the surface evolves, and how the interior affects it, is critical to understand as the vast majority of data available only studies the surface. The decadal survey therefore includes several strategic research goals where in situ observations are performed to better understand the meaning of body surfaces [68]:

- (Q5.1 and Q5.5) How magmatism and other internal processes affect planetesimals is poorly understood, but as the building blocks of the planets they are key to improving accretion and evolution models. Planetesimals vary from primitive porous aggregates to highly processed and differentiated bodies, and studying the large asteroids and dwarf planets by in situ imaging, spectroscopy, and topography measurements would help us understand their interior composition and structure.

- (Q5.5) Space weathering is a challenge for interpreting remote sensing data as it masks the true surface properties on a body, and the conditions and timescales are difficult to reproduce in the lab. In situ high-resolution imaging and spectroscopy of rocky and icy bodies can observe the surface of a body at several stages of weathering (due to impacts or internal processes revealing fresh material) and therefore improve our understanding of space weathering. If well characterised, space weathering could also become an effective tool to date asteroids from remote observations.
- (Q5.5) Small bodies formed in the outer solar system contain volatile elements, including water ice. How volatiles are stored and to what degree they are ejected from sublimation and collisions is poorly understood. The loss of volatiles seems to affect the surface, as e.g. Jupiter family comets appear different than the Kuiper belt objects they are thought to originate as. In situ studies of the volatile materials on active asteroids, icy moons, and comets would illuminate the behaviour of these bodies.

2.2 Swarm missions

Swarm missions are defined in this thesis as distributed missions where several satellites work together to meet a goal. In some cases the whole swarm is controlled to fly in a controlled formation and in other cases the swarm members have more independence in their trajectories. There are several challenges with implementing swarms, such as building capable small satellites, deploying many small satellites from a single vehicle, and operating large groups of satellite. These challenges align with the philosophy and experience in developing CubeSats, and the resilient nature of many swarm missions also allow a higher risk tolerance in the individual swarm members [69]. Swarm-type missions have gained significant traction in Earth orbit, starting with series of Earth observation platforms and navigation systems (i.e. GPS), and developing into scientific investigations such as ESA's Cluster and Swarm missions investigating Earth's magnetic field [70]. Recently, CubeSats have become common in Earth swarm missions, including the TROPICS CubeSat mission where a group of satellites collaborate to track tropical cyclones [71], and Planet's constellation of CubeSats that image the Earth every day and sell their data for science and other purposes [72].

Exploring the asteroids is a natural target for deep-space swarm proposals due to the large number of targets interesting for exploration. The NASA Autonomous NanoTechnology Swarm (ANTS) [73] was a concept from the early 2000s for highly autonomous picosatellites to prospect the main asteroid belt and characterise at least 1000 asteroids per year. The concept relied on biologically inspired reconfigurable spacecraft weighing only 1 kg with large solar sails and nuclear batteries [74] and was expected to be feasible around 2020. Much of the work on ANTS focused on modelling the autonomy and controls of this type of mission where some spacecraft would serve as a a "ruler" to guide a subset of "workers" in the swarm with individual instrument nodes [75]. A mission with a similar goal, to visit 100 main belt asteroids, was proposed in 2006 as the Asteroid Population Investigation and Exploration Swarm (APIES) mission in response to an ESA call [76]. The APIES architecture introduced a "mothership" that would transfer to a central location in the asteroid belt and release the swarm members to formation fly around the mothership and visit asteroids that passed nearby. APIES was planned to use mature technologies and was enabled thanks to the mothership platform because the communication distances and propulsion requirements on each swarm member became relatively small. Each swarm member would have a mass of 43 kg and Δv capability of 2 km/s from an arcjet electric propulsion system. Both the interest and practical challenges of asteroid belt swarm exploration missions are emphasised by the fact that several iterations of the Global Trajectory Optimisation Competition (GTOC) has concerned “asteroid hopping” swarm missions, including the 2015 edition which is discussed in detail by Izzo et al. [77].

CubeSat-based swarm missions have been studied as concepts to replace large missions and as novel investigations. Blocher performed a case study on replacing the Cassini mission to Saturn with a CubeSat swarm [78]. They assumed a mothership transferring to Saturn orbit to reduce the propulsion needed on the CubeSats and protect from radiation until release. Architectural choices were compared where Cassini’s instrumentation was moved onto one or several CubeSats. Their system would use heritage from MarCO and the Artemis 1 CubeSats and could provide similar or better science return at a lower cost. Blocher recommended further work on instrumentation miniaturisation and found that the power available was a major limiting factor for observations. Garrick-Bethell et al. proposed the NanoSWARM to the Moon to measure near-surface magnetic fields and trapped particles by dozens of nanosatellites [79, 80]. The mission was designed to uncover mechanisms of space weathering on airless bodies and the sources of water and magnetism on solar system bodies. The nanosatellite probes would flyby the lunar surface at a low altitude, down to 500 m, simultaneously with a carrier mothership at around 10 km.

2.3 CubeSats for deep-space science

The CubeSat was introduced in the early 2000s and has grown into a popular platform for scientific applications in Earth orbit. With recent technological advances and focused support by space agencies we are on the verge of a new exploration era in the solar system where the CubeSat will play an important role [23]. The *CubeSat Handbook* published in 2021 [81] gives a complete historical overview and introduction to the applications and development of CubeSats, including for scientific applications and deep-space. This section provides an overview of past deep-space CubeSats and a survey of technology challenges and maturity. For a broader look at the state of CubeSat technology see e.g. the annual *State-of-the-Art Small Spacecraft Technology* report published by NASA [82].

CubeSats have already found roles in scientific missions in Earth orbit and are generally acknowledged as a valuable platform that deserves continued investment, as e.g. the National Academies of Sciences, Engineering, and Medicine found in their 2016 report on the topic [20]. Missions can generally be classified as a mission of opportunity, where a rideshare launch makes a science orbit accessible to a CubeSat at low cost, or a dedicated mission, where one or several scientific CubeSats are the primary payload launched. Both types occur, but the former is far more common, with respective examples such as the Dynamic Ionosphere CubeSat Experiment (DICE) that was on a rideshare to LEO [83] and the TROPICS CubeSats that were launched to dedicated orbits [71].

2.3.1 Missions

All CubeSat missions to deep-space so far have been missions of opportunity, starting with the famous technology demonstrations of MarCO-A/B in 2018 that flew by Mars and relayed landing data from the primary mission, InSight, in real time [84]. The conceptualisation and core technology development for MarCO began with the INSPIRE project in the early 2010s, which itself built on experience from several previous NASA Jet Propulsion Laboratory and university projects [85]. Since MarCO, a series of deep-space and lunar CubeSats have been launched and are listed in Table 2.2, of which all but LICIACube and Lunar Flashlight were launched as secondary payloads on the Artemis 1 mission. It is evident that the success rate after MarCO has been poor, but it may have been exacerbated by long delays of the Artemis 1 launch. Little has been published about the ArgoMoon, LunIR, and Team Miles missions after launch so they are presumed failed. A few pictures from ArgoMoon were shared on social media, but none of the Artemis 1 upper stage which was the goal of the mission.

Table 2.2: List of all past deep-space and lunar CubeSats and their status.

Name	Date	Destination	Propulsion	Status
MarCO-A [86]	2018	Mars flyby	Cold gas	Success, ended [84]
MarCO-B [86]	2018	Mars flyby	Cold gas	Success, ended [84]
LICIACube [87]	2021	NE asteroid	Cold gas	Success, ended [88]
NEAScout [89]	2022	NE asteroid	Solar sail	Failure, spacecraft [90]
BioSentinel [91]	2022	Heliocentric	Cold gas	Success, ongoing [92]
CuSP [93]	2022	Heliocentric	Cold gas	Failure, spacecraft [90]
EQUULEUS [94]	2022	Earth-Moon L2	Resistojet	Success, ongoing [95]
LunaH-Map [96]	2022	Moon orbit	Gridded ion	Failure, thruster [97]
Lunar IceCube [98]	2022	Moon orbit	Gridded ion	Failure, spacecraft [90]
Lunar Flashlight [99]	2022	Moon orbit	Monoprop.	Failure, thruster [100]
OMOTENASHI [101]	2022	Moon orbit	Solid rocket	Failure, spacecraft [90]
ArgoMoon [102]	2022	Moon orbit	Monoprop.	Partial failure?
LunIR [103]	2022	Moon orbit?	?	Failure?
Team Miles [103]	2022	Heliocentric?	Ion?	Failure?

Despite recent failures, the heritage of MarCO and some of the subsequent deep-space CubeSats makes mature systems broadly available for all subsystems necessary to operate a mission. Maturity is often measured by the Technology Readiness Level (TRL) scale from 1 to 9, where TRL 9 are “flight proven” systems that have successfully operated in practice. See [104] or Chapter 5 for a more detailed discussion on TRL. It is important to consider the environment a system will be exposed to in flight to determine the TRL, as e.g. a deep-space mission is exposed to more radiation but spared from frequent thermal cycling compared to a common low Earth orbit (LEO) mission. All systems successfully used on MarCO and other deep-space CubeSats (incl. lunar missions) will be considered TRL 9 for deep-space operation, and commercial off-the-shelf (COTS) components that are regularly used in LEO (i.e. are TRL 9 there) will be considered as prototype demonstrations giving a TRL of 7 for deep-space. In the following subsections the maturity of enabling technologies, including propulsion, are presented.

2.3.2 Technology maturity

Five publications dated from 2013 to 2021 [105–109] that explicitly consider deep-space CubeSat technology development were reviewed to define the key enabling technologies which were and are important. Technologies that three or more of the publications characterised as enabling are discussed further in this section. The enabling technologies and state-of-the-art are summarised in Table 2.3.

Table 2.3: Overview of deep-space CubeSat technologies including the references which identify the given technology as enabling. The second column summarise their status.

Enabling technology	State-of-the-art
Radiation tolerance [105–107, 109]	Rad-hard and COTS batch testing electronics
Power generation [106–108]	Deployable sun-tracking solar arrays >100 W/kg
Communications [105–109]	X-band reflectarray and DSN transponder
Attitude control [107–109]	Integrated star tracker, reaction wheels, thrusters.
Navigation [105, 107–109]	DSN tracking standard, optical emerging.
Autonomy [105–107, 109]	Automatic trajectory corrections
Propulsion [105, 107–109]	*See Section 2.4*
Instrumentation [105, 107, 109]	Several types available as TRL 9

Radiation tolerance and lifetime

The CubeSat revolution in LEO was enabled by low-cost high-performance COTS electronics. However, by operating outside Earth's protective magnetosphere and for long duration, deep-space CubeSats are subjected to more radiation than their LEO counterparts [106].[*] By carefully selecting components, testing batches for their radiation tolerance, and implementing localised shielding, the use of COTS electronics in deep-space CubeSats is feasible [105]. Additionally, several radiation-tolerant CubeSat avionics systems have been developed recently that employ radiation hardened components [93, 105, 106]. Beyond hardware, the software for deep-space CubeSats must also be robust against radiation-induced events [109].

Based on these developments, radiation tolerance is no longer a fundamental challenge for deep-space, but remains an important engineering consideration. Radiation induced damage can be cumulative and limited experience in long-term operation remains. The MarCO satellites operated for around seven months (and did not fail due to electronics issues) [84] and there are several CubeSats currently operating outside Earth orbit. As an example, BioSentinel which is based on similar hardware as MarCO has operated for over a year in deep-space without any significant issues [92]. By invoking successful past examples, general electronics (e.g. computers, power systems) are considered TRL 9 for deep-space CubeSats and are readily available.

Power generation and storage

The demands for power on deep-space CubeSats can be high due to demanding communications and propulsion systems [109] and large solar arrays and battery capacities are therefore enabling technologies. 100 W-class solar arrays have been demonstrated on several

---

[*] Note that radiation is worse in Earth's radiation belts than most deep-space destinations [105].

6U CubeSats, including LunaH-Map [96], and therefore reach TRL 9. MMA Design, who delivered the solar arrays for MarCO, lists off-the-shelf solar arrays with a specific power of over 130 W/kg with up to 191 W and 235 W of power in 6U and 8U CubeSats respectively [110]. No demonstrations of 200 W-class CubeSat solar arrays have been published, but because they are listed as available versions of COTS product series where other specifications are TRL 9 they are estimated at TRL 6-8. The reduction in sunlight intensity away from the Sun is especially challenging for some deep-space CubeSats because the available power is reduced by a factor of six in the asteroid belt (2.5 au). As an example, nominally 200 W solar arrays would only produce 33 W, which is low especially for missions using electric propulsion. A combination of improved maximum solar array size and efficient use of power will be important for deep-space missions in the asteroid belt or beyond.

Missions often have multiple pointing requirements, e.g. keeping the solar arrays pointed at the Sun while a propulsion unit is pointed in the correct direction for a burn. In some cases the nature of the mission allows these requirements to be met with a fixed relative angle, but in general either the solar panels or thrusters need to be adjusted in flight. During a burn the thrust vector must to pass through the centre of mass of the spacecraft to avoid accumulating excess momentum, and therefore the body of the spacecraft typically needs to be reoriented to achieve the desired thrust direction. The solar array angles then need to be adjusted relative to the spacecraft body to point towards the Sun. Several solar array drive assemblies (SADAs) are available as COTS components, see e.g. [111] and were used on LunaH-Map [96] and are therefore considered TRL 9.

High-capacity COTS battery cells were used on the MarCO CubeSats and were found to be suitable for high-density low-cost deep-space energy storage. Compared to specialised battery packs for large missions, the MarCO batteries provided higher energy density at lower cost, but with reduced low-temperature performance [112]. In general, energy storage availability is not a concern for deep-space CubeSats and is considered TRL 9.

Other power sources, i.e. radioisotope thermoelectric generators (RTGs), have historically been an enabling technology for deep space missions [113] but are unlikely to see CubeSat adoption due to high costs and risks.

Communications

Due to the long distances involved it is not surprising that communications are a challenge for deep-space. Large parabolic antennas on Earth, e.g. those of the NASA Deep Space Network (DSN), are used to communicate at acceptable data rates for most missions. The DSN-compatible and radiation-tolerant Iris X-band transponder for the INSPIRE project [85], and large deployable reflectarray high-gain antenna [114] were used on the MarCO mission and therefore reach TRL 9. MarCO communicated with Earth at a distance of 1.07 au and a data rate of 8 kbit/s during the InSight landing and orbit determinations were performed regularly during cruise to update the spacecraft trajectories [115]. The third generation Iris transponder can output 3.8 W RF power on X-band in a 1.1 kg and 0.8 L total package and consumes 34 W during full transmit and receive [116]. The reflectarray high-gain antenna for MarCO covers one of the large faces of a 6U CubeSat when stowed and deploys into an aperture of 0.2 m^2, providing a gain of 29 dBi at 8 GHz [114]. Reflectarray CubeSat antennas for Ka-band frequencies [117] and up to 1 m^2 [118] have also been demonstrated. From a practical perspective, the allocation of a CubeSats surface area can become limiting if both large solar arrays and a large high-gain antenna are required to perform a mission. A potential solution is to place solar cells on the backside of the reflectarray as was demonstrated on the ISARA CubeSat mission [117]. Ka-band and larger area reflectarrays are considered TRL 7 and 4 respectively based on these publications.

Proliferating deep-space CubeSats adds significant challenges on ground systems. The DSN currently operates near maximum capacity, and the experiences of operating the Artemis 1 CubeSats show that strides are required to support more missions at once [119]. Work is ongoing to optimise the scheduling and improve the DSN's multiple-spacecraft-per-antenna capabilities and to increase capacity through cross-support with other large antennas [109, 120]. Because the DSN typically only supports a few tens of missions at a time [119] major investments would be necessary to support further tens of individual CubeSats. Some proposed missions, such as the two CubeSats piggybacking on Hera, will utilise a mother-daughter communications architecture with short inter-satellite links instead of directly communicating with Earth [121]. Architectures of this type can relax requirements on both CubeSat and Earth communications capabilities, especially for missions that employ several satellites, i.e. swarms. Short inter-satellite links are considered TRL 8 due to their implantation on the Hera mission scheduled for launch in 2024.

Optical communications can enable high data-rate deep-space satellite links, especially for large human and robotic exploration [122]. Optical communication systems are also actively developed for CubeSats but are primarily motivated by requirements of high data rates in the crowded LEO environment [123]. In the long-term, deep-space CubeSat optical communications will also become available and may increase the available data rates [109].

Attitude determination and control

Star trackers and reaction wheels are used for high precision attitude determination and control systems (ADCS) on Earth-orbiting CubeSats. For example, the ASTERIA space telescope achieved attitude control to within a few arcseconds using an integrated COTS

ADCS [124]. A modified version of the same system, the Blue Canyon XACT, was used on the MarCO CubeSats [125] and several subsequent deep-space CubeSats. A challenge for attitude control in deep-space is the absence of Earth's magnetic field which is typically used to manage accumulated momentum on the spacecraft and must be replaced with some form of propulsion [109]. As an example, MarCO and BioSentinel used cold gas thrusters [84, 91], while e.g. Lunar IceCube was planned to use its electric propulsion system with thrust vectoring for the same purpose [98]. On MarCO the cold gas thrusters were controlled directly by the ADCS and autonomously managed momentum buildup during flight [126] and thus deep-space ADCS and momentum management are considered TRL 9.

Deep-space navigation

Knowing the position of a satellite is critical for operations and to manage the orbit or trajectory of the spacecraft. For Earth orbiting CubeSats, a popular source of position are the NORAD satellite tracking data tables supplied as two-line elements (TLEs), providing position accuracy on the order of a few km [127]. GPS receivers are commonly used for missions where higher position (and/or time) accuracy is required, and COTS components readily afford independent position knowledge to within tens of metres in CubeSat form factors [128]. Navigation is closely related to communications for deep-space missions. Developed since the late 1970s, delta differential one-way ranging (delta-DOR) is the workhorse navigation method for deep-space. It is performed by transmitting a sequence of tones from the spacecraft that are received on several DSN antennas to determine the range to the spacecraft and triangulate its position and velocity with exceptional accuracy [129]. The Iris transceiver is fully compatible with this method and was used in flight on the MarCO CubeSats with an estimated accuracy of 300 m and 0.1 mm/s in position and velocity respectively [130]. The same system was also used on later missions, resulting in TRL 9 for Earth-supported deep-space navigation.

Independent on-board navigation techniques reduce the need for Earth communication sessions and therefore reduce operational cost and are important to scale the use of deep-space CubeSats. Three prominent forms of independent navigation are possible based on data from optical, x-ray pulsar, or intersatellite crosslink sources [131]. In optical navigation, solar system objects with known positions (i.e. planets and asteroids) are observed against background stars to independently determine the position of the spacecraft [132] and was first demonstrated on the NASA Deep Space 1 mission launched in 1998 [133]. The Deep Space 1 demonstration showed best-case errors of 150 km and 0.2 m/s in position and velocity respectively, although the authors note significant issues with the camera system that was used to capture the navigation data. The ESA M-ARGO deep-space CubeSat is planned to demonstrate optical navigation in a CubeSat form-factor but can only observe bright planets due to the miniaturised sensors and has a predicted accuracy of 1000 km and 1 m/s [134]. Optical navigation is considered TRL 7 from the Deep Space 1 demonstration as the hardware required is readily available for CubeSats. For swarm missions, crosslink radiometric ranging can be used to improve accuracy, either by adding intersatellite ranges as extra constraints or by letting some swarm members specialise in navigation determination that they share with nearby satellites [135].

Further in the future, x-ray pulsars may be used for deep-space navigation that works independently of any solar system objects and could provide sub-km position accuracy [136]. The SEXTANT experiment on the International Space Station demonstrated position accuracy better than 10 km using x-ray navigation and a relatively compact 6 kg and 6 L x-ray navigation detector is planned to fly on the CubeX small satellite [137]. Due to the large size of present x-ray navigation demonstrators optical navigation is likely to be preferred for CubeSats in the foreseeable future.

Autonomy

Primarily due to infrequent and low-bandwidth communications a deep-space CubeSat requires significant advances in autonomy to handle anomalies and process data without human intervention [109]. Responses must be implemented both in software and hardware to ensure the system is always reset when necessary and that faults are managed in a safe and measured manner. Additionally, command sequences and data downloads must be planned ahead and executed on the spacecraft [106]. Advances in autonomy is also recognised as a key technology for future large planetary science missions to meet performance requirements and reduce operational costs [138]. The ESA LUMIO 12U CubeSat will operate near the Earth-Moon L2 point and is designed specifically to test autonomy strategies for limited communications via a mothership relay and therefore represents a deep-space mission well [139]. LUMIO must survive up to ten days without communication and rely on only 16 h of communications per month during science operations. For deep-space missions, autonomy is especially relevant in combination with autonomous navigation to control long duration transfer orbits [131]. Effective techniques must also be developed to determine which science data is most valuable to transmit within limited data budgets, where e.g. artificial intelligence may play a role [140]. Earth orbit CubeSat constellations face some of the same challenges and could be a potential source of development, however at present such systems rely heavily on complex ground networks and frequent communications [141].

As the number of CubeSats in deep-space grow and available ground support time per satellite diminishes autonomy will only grow in relevance. All areas of operations are covered by autonomy, including spacecraft health, navigation and trajectory management, instrument operation and data product selections, and it is therefore difficult to define a numerical TRL value and the scope of autonomy will vary broadly by mission. A lot of effort is required in this area and methods must be developed where advances can be reused in the future to support the ethos of the CubeSat, where new generations rapidly evolve based on flight experiences.

Instrumentation

Capable instrumentation is key for useful missions. With the rapid expansion of CubeSats in Earth orbit new miniaturised science instruments have been developed and are now in regular use [142]. It is clear that CubeSats already provide high quality science, and will continue to grow in this role [20]. For a near-Earth asteroid mission as an example, visible and thermal imagers, spectrometers, laser altimiters, magnetometers, and radars are all feasible and valuable options on a CubeSat [108]. Particle detectors and plasma instruments are also available for CubeSats [106]. With the strong interest for CubeSats as scientific platforms in Earth orbit the availability of instrumentation is broad, and the CubeSats now piggybacking to deep-space will further adapt instrumentation for relevant applications [142].

Several of the "second generation" deep-space and lunar CubeSats that flew on Artemis 1 implemented advanced instrumentation driven by science objectives. Due to their poor success rate the in-space experience gained is limited, but the instrument development for the Artemis 1 satellites is poised to influence many future deep-space CubeSats. As an example, neutron and gamma-ray spectrometers are workhorse advanced instruments for composition measurements on asteroids that were used on Dawn [143], will be used on Psyche [144], and were developed for CubeSat platforms with the Artemis 1 cohort. The Miniature Neutron Spectrometer on LunaH-Map was designed to achieve twice the count rate of the instrument on Lunar Prospector, which was launched in 1998 to map the elemental composition of the Moon [145], in a package of 3.4 kg and 2 L [146]. Despite the thruster failure on the spacecraft the instrument was operated successfully and showed to meet its performance requirements and is considered TLR 9 [97].

As scientific spacecraft fundamentally are platforms to host instruments the integration between the instruments and the spacecraft bus are important to consider. The already launched Artemis 1 cohort and the Juventas [147] and Milani [148] CubeSats that have been integrated for launch with the large Hera mission show integration feasibility but the scientific return in practice remains unknown. As several relevant instruments have been integrated in 6U CubeSats and tested, but operational performance is lacking, instrumentation is considered TRL 7.

2.4 CubeSat propulsion

Propulsion can serve three major purposes on a deep-space CubeSat: attitude control (especially momentum management), trajectory corrections, and primary propulsion for transfer to a desired orbit [26]. The four major types of propulsion: cold gas, chemical, electric, and propellantless, are suited to a subset of these tasks and will be discussed in this section. CubeSat are generally limited in terms of volume and mass and therefore having a small propellant fraction is essential to fit the other systems and instruments to perform a mission. The importance of propulsion to deep-space CubeSats is evident from Table 2.2, as all prior missions have used propulsion at minimum for attitude control, but also for trajectory correction and orbit transfers. As discussed in this section, cold gas systems are ideal for simplicity and agility at low Δv, i.e. for attitude control or small trajectory corrections. For larger corrections or as primary propulsion for missions with moderate Δv requirements (up to c. $100\,\mathrm{m/s}$), monopropellant chemical thrusters are a good choice while retaining many of the benefits of cold gas systems. For larger Δv requirements, electric propulsion or propellantless solar sails are required. Especially for missions away from the Sun the practical use of the latter is limited and solar sails will not be discussed further.

In-space propulsion is based on conservation of momentum where a propellant is ejected at high velocity from the spacecraft to give a reaction thrust in the opposite direction. If a propellant mass flow of $\dot{m}$ is ejected at a velocity c the ejected momentum rate is $\dot{m}c$ and the spacecraft will experience an instantaneous acceleration $\dot{v}$ by Newton's 2nd law:

$$m\dot{v} = \dot{m}c = F \tag{2.1}$$

where m is the instantaneous mass and F is the thrust force. The propellant mass is lost from the spacecraft mass so the acceleration will grow over time if the thrust is constant. By considering an initial mass m_0 and a total expelled propellant mass m_p the cumulative change in velocity Δv of a spacecraft in an inertial frame is:

$$\Delta v = c \ln \frac{m_0}{m_0 - m_p} \quad \Rightarrow \quad m_p = m_0 \left(1 - e^{-\frac{\Delta v}{c}}\right) \tag{2.2}$$

which is Tsiolkovsky's famous rocket equation. The inverse form of the rocket equation allows the required propellant mass to perform a mission to be calculated, and it is clear that the exhaust velocity c is an important factor. The exhaust velocity c measures the amount of impulse delivered per mass of propellant expelled, and is therefore called the specific impulse. Specific impulse is often given in units of seconds with the convention

$I_{\text{sp}} = c/g$ where $g = 9.81\,\text{m/s}^2$ is the acceleration due to gravity on Earth. The rocket equation limits the practical Δv that is achievable in a CubeSat to $\Delta v < 0.7c$ if at most half of the spacecraft by mass is propellant.

Typical missions in deep-space require 0.7 to 9.5 km/s of Δv [109] to be completed and therefore require a minimum specific impulse of 1 to 14 km/s (100 to 1400 s) for feasibility. On the lower end, these missions may be possible with chemical propulsion but in general electric propulsion is required. For this reason, only a brief summary of the state-of-the-art in deep-space cold gas and chemical propulsion is provided and the focus on this section is on electric propulsion.

2.4.1 Cold gas

In a cold gas propulsion system a stored high-pressure propellant is released through a nozzle to generate thrust. The propellant is typically a refrigerant and these systems are simple and suitable to miniaturisation [26]. Many cold gas systems have successfully flown on CubeSats, including a 3.5 kg system on the MarCO satellites for attitude control and trajectory corrections that had a specific impulse of 40 s and could deliver around 60 m/s of total Δv [130, 149]. A more compact thruster system was developed for BioSentinel to provide detumbing and momentum management in a package less than 1.4 kg with a similar specific impulse and total Δv capability of around 6 m/s [150]. The cold gas thrusters on MarCO and BioSentinel both operated successfully in deep-space [84, 92] (but did have some valve issues) and therefore the TRL is 9.

2.4.2 Chemical

In a monopropellant chemical rocket an energetic propellant is decomposed to produce a hot gas and generate thrust, with a hydrazine propellant decomposing on a catalyst bed as the classical example [26]. Despite its heritage and popularity as in-space propulsion, hydrazine thrusters are prohibitively expensive for CubeSats due to the highly toxic propellant and risk for auto-combustion [25] and therefore safer “green” monopropellants have been developed as a replacement [26]. A 5.5 kg green monopropellant system using ASCENT* was developed for Lunar Flashlight with a specific impulse of 210 s and a total Δv capability of 230 m/s [151]. The Lunar Flashlight system was fired in orbit but did not perform correctly due to debris in the propellant lines [100]. ArgoMoon used a smaller 2.1 kg system with similar propellant that delivered 190 s specific impulse and was capable of c. 57 m/s Δv. The on-orbit performance of the system on ArgoMoon has not been reported, which, in combination

---

*Formerly AF-315E.

with the partial success on Lunar Flashlight places monopropellant systems at TRL 8 or lower in deep-space.

Other chemical propulsion modes are possible, i.e. bipropellant systems where a fuel and oxidiser are stored separately and combined in the thruster, or solid rockets which don't require plumbing. However, bipropellant systems are too complex and solid propulsion is impractical for most CubeSat applications [26].

2.4.3 Electric

In electric propulsion the energy used to accelerate the propellant is primarily supplied from electricity, instead of tank pressure or chemical bonds. Because the energy supply is decoupled from the propellant, more energy can be supplied per mass of propellant to increase the exhaust velocity and therefore Δv capability with the same mass of propellant. A wide range of electric propulsion technologies have been proposed for CubeSat applications and can be classified by their acceleration method into electrothermal, electrostatic, or electromagnetic systems [27]. Electric propulsion systems have important system-level implications because the power required is generally high and set a lower bound on the amount of electricity that must be generated on board. The overall efficiency of the propulsion system, η, can be defined as the ratio of exhaust jet power to input power $\mathbb{P}$:

$$\eta = \frac{\frac{1}{2}\dot{m}c^2}{\mathbb{P}} = \frac{Fc}{2\mathbb{P}} \qquad \Rightarrow \qquad \mathbb{P} = \frac{Fc}{2\eta} \tag{2.3}$$

where the simplification applies Eq. 2.1. To perform a given mission the propulsion system needs to generate sufficient acceleration and therefore thrust such that the desired Δv is delivered in a reasonable time. The practical lower limit on thrust means that specific impulse is a direct tradeoff between the amount of propellant carried and the size of the power system on the spacecraft. Consider the combined propellant mass m_p and power system mass $\alpha\mathbb{P}$:

$$m_{\text{comb}} = m_p + \alpha\mathbb{P} \tag{2.4}$$

and assume the thruster is operated continuously for a time T. Then the propellant mass is $\dot{m}T$ and we can minimise the total mass with respect to specific impulse by invoking Eqs. 2.1 and 2.3:

$$m_{\text{comb}} = \dot{m}T + \alpha\frac{Fc}{2\eta} = \frac{F}{c}T + \alpha\frac{Fc}{2\eta} \tag{2.5}$$

$$0 = \frac{dm_{\text{comb}}}{dc} = -\frac{F}{c^2}T + \alpha\frac{F}{2\eta} \tag{2.6}$$

$$\Rightarrow \qquad c_{\text{opt}} = \sqrt{\frac{2\eta T}{\alpha}} \tag{2.7}$$

Note that the optimal specific impulse c_{opt} does not depend on the Δv required for the mission under the assumption that the spacecraft mass and propulsion parameters are approximately constant, and that the propellant mass and power system mass are equal in the optimal case. Increasing the specific impulse above the value given by Eq. 2.7 reduces the overall mass that can be delivered which, with some typical values of $\eta = .5$, $T = 1\,\text{yr}$, and $\alpha^{-1} = 100\,\text{W/kg}$ (at Earth), sets an upper limit to specific impulse of 5700 s. For deep-space missions the available solar power drops off as $1/R^2$ and therefore the upper limit of specific impulse is reduced linearly with distance to the Sun. With F prescribed by the mission and α determined by the destination, an electric propulsion system's efficiency is the factor that limits the maximum useful specific impulse. As an example, electromagnetic propulsion systems such as pulsed plasma thrusters have inherently poor efficiency ($< 10\%$ [152]) and are therefore not useful for deep-space CubeSats and will not be discussed further. State-of-the-art electric propulsion systems are discussed below and their basic performance parameters are summarised in Table 2.4 for convenience.

Table 2.4: Summary of performance parameters for electric propulsion systems.

System	Technology	F	I_{sp}	$\mathbb{P}$	η
AQUARIUS [95]	Resistojet	5.9 mN	87 s	20 W	13%
Busek BIT-3 [153]	Gridded ion	1.0 mN	1960 s	70 W	14%
ThrustMe NPT30 [154]	Gridded ion	0.9 mN	2450 s	60 W	18%
Spaceware nL [155]	Hall	2 mN	800 s	53 W	15%
Enpulsion Nano [156]	FEEP	0.35 mN	2500 s	45 W	10%
MIT iEPS [152]	Electrospray	12 µN	760 s	0.13 W	36%
Accion TILE [29]	Electrospray	9 µN	2400 s	0.16 W	66%

Electrothermal systems supply energy in the form of heat from an arc discharge or a resistor to a gas that is released to generate thrust. This type of system is conceptually simple and was among the earliest electric propulsion technologies developed, however, due to inherently limited specific impulse they are not common in small satellites [26]. Systems that use water vapour as the propellant are an exception thanks to exceptional practicality and low-cost. The EQUULEUS CubeSat successfully demonstrated a 2.5 kg resistojet propulsion system with a specific impulse of 87 s that carries 1.2 kg of water and generates 5.9 mN of thrust with 20 W of input power [95]. For a 12 kg CubeSat the Δv capability is 90 m/s which demonstrates that resistojets are similar in performance and therefore suits similar applications as monopropellant systems.

Electrostatic systems is a broad and popular category of electric propulsion systems that includes gridded ion thrusters, Hall thrusters, and electrospray-family thrusters [27]. Gridded ion and Hall thrusters are two-stage systems where a gaseous propellant is ionised and subsequently accelerated by electric fields to produce thrust. These types of electrostatic thrusters are popular in large spacecraft applications and were used on the Dawn and Psyche main asteroid belt missions respectively. Gridded ion thrusters have successfully been miniaturised for CubeSat applications and can use iodine as propellant which is solid at room temperature and therefore can be packaged very efficiently. The ThrustMe NPT30 [154] thruster is an example of a TRL 9 system for LEO CubeSats available in a 1.2 kg and 1 L package that can deliver around 1 km/s of Δv to a 3U CubeSat. The Busek BIT-3 [153] system uses similar technology but in a larger package of 2.9 kg and 1.6 L and can deliver around 2 km/s of Δv in 6U CubeSats. BIT-3 was used on two Artemis 1 missions, LunaH-Map and Lunar IceCube (see Table 2.2), however the propulsion unit failed on the former due to a corroded valve [97] and the latter spacecraft never made contact [90]. Due to the failed demonstration BIT-3 is considered TRL 8 or less, but thanks to its performance compared to other state-of-the-art systems (see Section 4.1.3) it is likely to soon fly again. The Exotrail Spaceware nanoL [155] is a miniaturised Hall thruster using xenon gas propellant that was successfully demonstrated in LEO [157] and comes in a 3.4 kg and 2.3 L package (excl. "tuna can") [158]. As is typical for Hall thrusters the specific impulse is lower than for comparable gridded ion thrusters [26] at 800 s [155] and the Δv that can be delivered is around 400 m/s in a 6U CubeSat, but the thrust to power ratio is high compared to other electric propulsion as seen in Table 2.4. The generally low efficiency of CubeSat-scale gridded ion and Hall thrusters (below 20%) is a fundamental result of miniaturisation [26] and can be compared to the Dawn and Psyche thrusters that have efficiencies of 55% and 50% respectively [159, 160] calculated by Eq. 2.3.

The electrospray family of electrostatic thrusters operate on liquid propellants by directly extracting and accelerating particles to produce thrust as shown in Figure 2.6. The liquid forms a Taylor cone in the presence of a sufficiently strong electric field and emits a jet of charged droplets, small ionic clusters, or a mixture of both in a steady-state. The geometry of the emitter and propellant feed and the properties of the liquid, including its viscosity, conductivity, and surface tension, strongly alter the nature of the emission [161]. Electrospray, field-emission electric propulsion (FEEP), and colloid thrusters are all names

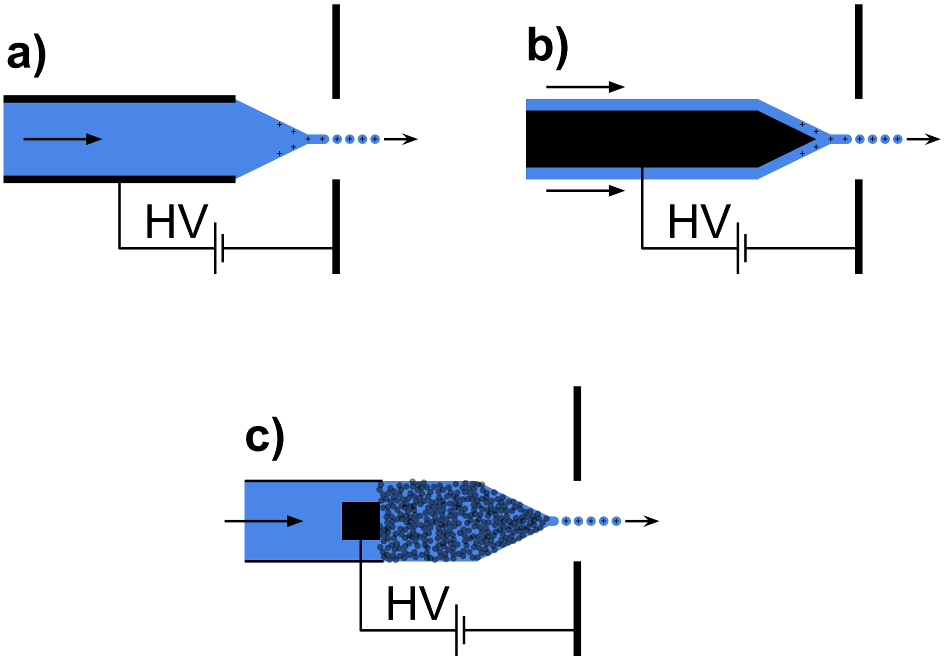

Figure 2.6: Illustration of electrospraying techniques. a) Capillary emitter. b) Externally wetted emitter. c) Porous emitter with distal electrode.

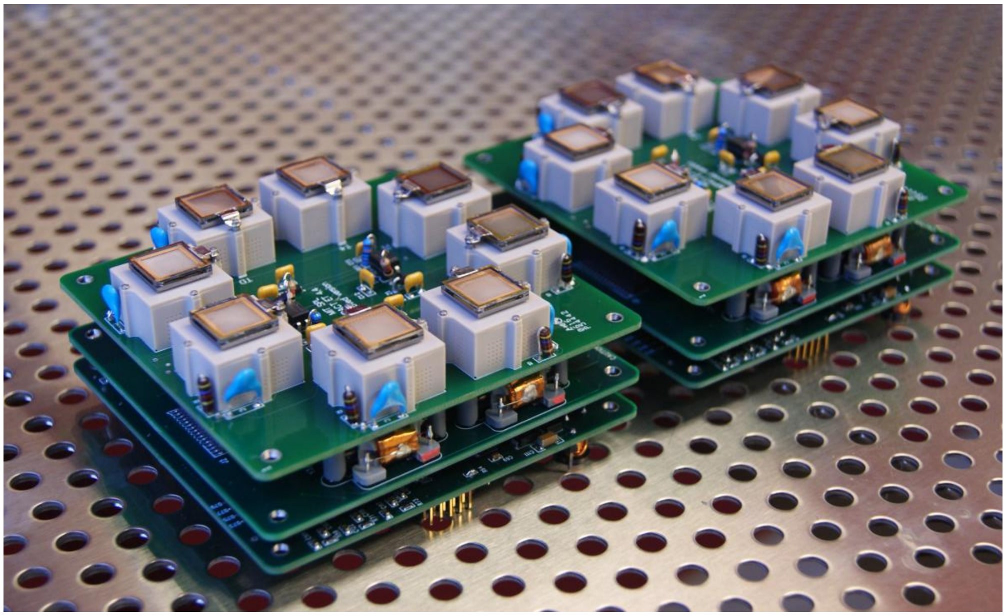

Figure 2.7: Picture of integrated 0.3 L CubeSat electrospray propulsion systems with eight thrusters and a power processing unit (PPU). [Credit: MIT Space Propulsion Laboratory.]

for thrusters in the electrospray family that rely on the same physical phenomena but are not used interchangeably because the designs are dissimilar in practice. The name used typically varies by the propellant, where electrosprays* use ionic liquids, FEEPs use liquid metals, and colloid thrusters use liquids with solvated ions [27]. Electrospray family thrusters lend themselves uniquely to CubeSat thrusters because they produce their thrust on the microscale and therefore are not impacted by challenges with miniaturisation [26]. The Enpulsion Nano FEEP thruster uses indium liquid metal as propellant and was demonstrated in LEO in 2018 [162] and was therefore among the earliest COTS electric propulsion systems available for CubeSats. The current "R3" version is available in a 1.4 kg and 1.0 L package and has a specific impulse ranging from 1500 to 5000 s [156]. The thrust and efficiency are low compared to other systems as seen in Table 2.4, but thanks to the high specific impulse a Δv of over 1 km/s is possible in a 3U CubeSat.

Ionic liquids have emerged as a practical propellant for electrospray thrusters because it is possible to extract both positive and negative species from the propellant to preserve spacecraft neutrality and omit a separate neutralisation mechanism [163] and because pure ion emission is possible to yield high specific impulse and efficiency [164]. Due to the low mass of the emitted species and limited current output the thrust per emitter is low, and therefore arrays are machined from porous materials to package dozens to hundred of emitters in a macroscopic package. Such clustered emitters have been manufactured as linear arrays [165], stacks of linear arrays [166], and fully planar two-dimensional arrays [167] using different micromachining techniques. Krejci and Lozano demonstrated a small ($1\,\mathrm{cm}^2$) 480-emitter ionic liquid electrospray thruster in laboratory testing that produced 13 µN of thrust at a specific impulse of 760 s using only 0.13 W of power [152]. Multiple ionic liquid electrospray thrusters on individual propellant tanks are typically mounted together to further scale up the overall performance as shown in Figure 2.7. A commercial evolution of the same thruster has been developed by Accion Systems as the TILE and was demonstrated in the lab to produce 9 µN of thrust and 2400 s specific impulse with 0.16 W of power [29]. Ionic liquid electrospray thrusters have high power efficiency, reaching 36% for the MIT model and 66% for the Accion model as seen in Table 2.4 and are therefore especially interesting for deep-space missions as they raise the maximum specific impulse given by Eq. 2.7 as discussed in Section 2.5. The specific impulse of ionic liquid electrospray thrusters is uncertain in practice because the fraction of propellant that is lost without contributing to thrust, called anomalous mass loss, may be significant. Natisin et al. [168] found that only 39% of the propellant was utilised in their testing, while testing at MIT showed that 80%

---

[*] Sometimes specified as ionic liquid ion source (ILIS) thrusters to distinguish from the family.

of the propellant was used [169].* All data available so far relies on indirect ion mass flow estimates and the causes and extent of anomalous mass loss are an active area of research.

Despite excellent scalability, high efficiency, and good specific impulse, ionic liquid electrospray thrusters are not yet a panacea for CubeSat propulsion. An ionic liquid electrospray thruster was demonstrated in 2017 to operate for over 300 h [170] and it is generally accepted that the current iteration of electrosprays can operate reliably for about 500 h at nominal thrust. Staging has been proposed as a method to overcome the lifetime limitation of electrospray thrusters [30] and is discussed in the following section.

2.4.4 Staging

The rocket equation (Eq. 2.2) places an upper limit on the possible Δv as a function of the maximum practically attainable specific impulse and propellant mass fraction. Taking a typical chemical lift rocket as an example, let $c = 3\,\mathrm{km/s}$ ($I_{\mathrm{sp}} = 306\,\mathrm{s}$) and assume $\gamma = 0.09$ is the ratio of structural mass to propellant mass and $\beta = 0.01$ is the ratio of payload mass to propellant mass (i.e. the rocket starts out as roughly 90% propellant, 9% structure, 1% payload). Then the initial mass m_0 and maximum Δv is:

$$m_0 = m_p + \gamma m_p + \beta m_p \tag{2.8}$$

$$\Rightarrow \quad \Delta v = c \ln \frac{m_0}{m_0 - m_p} = c \ln \frac{1+\gamma+\beta}{\gamma+\beta} = 7.2\,\mathrm{km/s} \tag{2.9}$$

which is less than the orbital velocity of 7.8 km/s in LEO and the given single-stage rocket could never make orbit, even before losses to fight gravity and air resistance are accounted for. If a fraction ϵ of the propellant mass m_p is given to a second stage it has a propellant mass of $m_{p,2} = \epsilon m_p$ which leaves $m_{p,1} = (1-\epsilon) m_p$ for the first stage. Assuming both stages retain the same c and γ the launch mass remains as in Eq. 2.8 and the Δv for each stage becomes:

$$\Rightarrow \quad \Delta v_1 = c \ln \frac{1+\gamma+\beta}{1+\gamma+\beta-(1-\epsilon)} = c \ln \frac{1+\gamma+\beta}{\epsilon+\gamma+\beta} \tag{2.10}$$

$$\Rightarrow \quad \Delta v_2 = c \ln \frac{(1+\gamma)\epsilon+\beta}{(1+\gamma)\epsilon+\beta-\epsilon} = c \ln \frac{\epsilon+\gamma\epsilon+\beta}{\gamma\epsilon+\beta} \tag{2.11}$$

---

[*] Calculated for the second test (Fig. 9b in [169]) from the average mass flow with time-of-flight and the actual mass loss. The first thruster leaked significantly and the third thruster did not operate nominally so they are excluded.

The total Δv reaches 10.6 km/s at the optimum value of $\epsilon = 0.09$, i.e. the second stage should be around 1/10 of the size of the first stage and the rocket can now place the payload in LEO. If a third stage is added the Δv increases again but the returns diminish with each additional stage so two or three stages has become ubiquitous for launch vehicles.

Staging can increase the performance of in-space electric propulsion systems by the same mechanisms as for launch rockets but only for certain types of systems. If the thrusters themselves contribute a significant fraction of the structural mass, which is the case in electric propulsion where the propellant mass is vastly reduced, γ increases as the stages get smaller and the gains due to staging are quickly erased. Krejci and Lozano showed that thanks to the small mass of electrospray thruster arrays, staging can increase the Δv capability of a CubeSat over a single stage, however the amount of payload mass was reduced [28]. In derivative works Jia-Richards et al. [30–33] noticed that the staging system can also overcome the lifetime limitations of electrospray thrusters and make large Δv propulsion systems feasible with current technology. A modest penalty of larger propulsion system wet mass and volume are paid compared to a hypothetical single stage system, but e.g. if the system were sized as the MarCO cold gas system the Δv for a 6U CubeSat could still reach a game-changing 3.5 km/s [32]. Jia-Richards and Lozano developed an analytical framework for calculating the performance of CubeSats with staged electrospray propulsion [33] that is presented and extended in Section 4.1 and developed a proof-of-concept propulsion model [31] that is the basis for the work in Section 4.3.

It should be noted that lifetime limitations for deep-space electric propulsion are not limited to electrospray thrusters. Many recent deep-space missions required more than one thruster due to lifetime and redundancy considerations. For example, Dawn carried three thrusters [171], and Psyche [172] and BepiColombo [173] carry four each. In these examples the extra thrusters are carried all the way to the end of the mission.

2.5 Research gaps

Previously proposed swarm missions to the asteroid belt have not had any strong scientific motivations. In both APIES and ANTS, the missions are proposed for the generic purpose of visiting a certain number of asteroids in the main belt. While they certainly would have scientific value, the authors fail to argue why and the missions are therefore also not optimised for science return. To make a swarm mission to the asteroid belt a reality in the near future at least one strong scientific case must be found and motivated and the mission must be optimised for that case. The APIES and ANTS studies are now around 20 yr old and therefore technologically obsolete. Revisiting the feasibility of a main asteroid belt swarm while leveraging the strides made in small spacecraft capabilities in the past two decades is necessary to revitalise the mission concept.

CubeSat propulsion is an exciting field where major advances have been seen in the past few years, especially on high Δv electric propulsion systems operating in LEO. However, to perform a deep-space mission in the asteroid belt or other destinations away from the Sun poses new challenges because solar power generation is heavier. If Eq. 2.7 is calculated with the state-of-the-art power generation in the asteroid belt of $\alpha^{-1} = 21\,\mathrm{W/kg}$ and a thrusting duration of 1 yr, an efficiency of at least 46% is required to optimise near a typical electric propulsion specific impulse of 2500 s. The actual efficiencies of <20% that have been realised for CubeSat COTS electric propulsion are so low that operations in the asteroid-belt are always suboptimal and the large solar arrays will negate much of the mass savings that motivate electric propulsion in the first place. Staged electrospray propulsion systems have been proposed previously in recognition of this limit because their efficiencies are so high that they provide an optimal balance of propellant and power system mass in the asteroid belt, but need work to expand analysis and implement and test a real propulsion system.

Previous analysis of staged electrospray propulsion systems have two major limitations: a poor parameter anchoring to reality and no guidance for how to measure or improve the propulsion system implementation. The lack of parameter anchoring is evident from the assumptions made in previous analyses as shown in Table 2.5, where the propellant mass fraction of each stage ranges from 0.17 to 0.72 and dramatically changes the mass and volume of the final propulsion system. Prior work also lacks a sensitivity analysis to show the impact of different design parameters and does not define any figure of merit to measure the efficacy of a staging implementation. The propellant mass fraction could serve as a figure of merit, but has a clear drawback in that it measures overall performance instead of the performance impact of a staging system compared to hypothetical single stage design and therefore is mostly sensitive to the base assumptions.

Table 2.5: The assumed dry mass, propellant capacity, and resulting propellant mass fraction of electrospray stages used in previous analyses.

Analysis	Dry mass	Prop. capacity	Prop. mass fraction
3U CubeSat in [28]	0.5 kg	0.1 kg	0.17
3U CubeSat in [30]	0.075 kg	0.12 kg	0.61
6U Target CubeSat in [32]	0.29 kg	0.75 kg	0.72
3U CubeSat in [33]	0.1 kg	0.12 kg	0.54

Chapter 3

Deep-Space Science Applications for CubeSats

Thanks to MarCO it is clear that CubeSats are capable of deep-space operations and can survive the environment for months or even years. A group of scientific CubeSats were launched as secondary payloads on the Artemis 1 Moon mission in 2022, where three were intended for deep-space, and a few more CubeSat companions have been flown or planned for large deep-space missions, as discussed in Section 2.3.1 of the literature review. Deep-space missions of opportunity, as all CubeSats so far have been, are an important platform to increase the value of large missions and a practical path for technology development. In the coming years we will almost certainly see CubeSat companions become common additions on large deep-space missions for enhanced science return, as e.g. on ESA's Hera mission [147] launching this year to (65803) Didymos. By their nature, however, companion-type missions have a limited scope due to the small number of large deep-space missions that are launched in a given year. To overcome this limitation, a new type of mission is becoming prevalent: rideshare launches of CubeSats with large on-board propulsion capabilities. By enabling significant independent manoeuvring, a deep-space CubeSat may launch to e.g. a generic Earth escape (as on Artemis 1) or geostationary orbit (GEO) and complete its mission independently from there to a different destination than the primary launch payload. Several CubeSats to near-Earth asteroids (NEAs) have been attempted or planned with a rideshare to Earth escape followed by significant independent propulsion, including the NEAScout mission that launched on Artemis 1 (but never made radio contact [174]), and the future M-ARGO mission [108]. Starting from a rideshare to GEO, where many communications satellites are added each year, has been proposed for CubeSat NEA missions and shown to be feasible with a spacecraft based on MarCO if sufficiently high performance propulsion is realised [32]. Related, but not central to this thesis, are scientific CubeSats to the Moon that use the same type of rideshare opportunities.

This chapter shows applications with strong science value that can motivate ambitious independent deep-space CubeSat missions and discusses the feasibility and technology readiness of concept missions. The inherent strengths and weaknesses of the CubeSat as a scientific platform are considered by evaluating the decadal survey for planetary science and astrobiology for questions where a broad exploration at less depth is an important path to further our understanding of the solar system. The topic was narrowed down to asteroids because of their combination of deep scientific value and vast numbers that make it infeasible to explore a significant fraction of them with large spacecraft. The missions considered here are of the swarm type, where many CubeSats are operated to perform an investigation as a collective. In all cases a mothership architecture is assumed because it considerably reduces the propulsion and communication requirements on the individual swarm members.

3.1 Missions for CubeSat exploration

The priority science questions in the planetary science and astrobiology decadal survey [68] are defined to focus scientific research on the most important questions. The questions related to asteroids near Earth and in the main belt are summarised in Section 2.1.4 of the literature review and show how asteroid missions are key to understanding the formation and evolution of our solar system. Potential applications must be reconciled with the inherent properties of CubeSats that are ideal where the instrumentation complexity is low but the breadth of sampling required to get a complete picture is wide. As an example, surveying the magnetic properties of asteroids is suitable because it requires a broad sampling to be representative and can be performed with simple instrumentation. From the priority science in the decadal survey, three categories of missions ideal for CubeSat swarms are discussed further in this section:

1. Studying several members of an asteroid family (questions 3.1, 4.1 and 4.4).
2. Studying the nature of large asteroids (questions 3.1, 3.2, 3.5, 4.2, and 5.1).
3. Measuring remnant magnetism on different types of asteroids (question 1.4).

Studies of near-Earth asteroids (NEAs) sought by the decadal survey are excluded for three reasons: 1) NEA targets are ideal for missions of opportunity because a general rideshare to an escape or lunar trajectory may be used, 2) meteorites serve as “free sample-return” of NEAs that, in combination with recent NEA sample-return missions, may reduce the need for in situ studies over time, and 3) due to their proximity to Earth, they are the easiest to study with ground-based instrumentation.

Other asteroid missions sought by the decadal survey are less suited to the CubeSat platform as they require advanced instrumentation or have a specific target of interest. Mission studying the composition and chemistry of primitive asteroids, and the study of asteroids in small reservoirs respectively, are examples where large missions are suitable. The study of space weathering falls into the large mission category as well and may require sample return for major advances, however, high resolution images and spectroscopy which are a typical product of any asteroid mission may be helpful byproducts of the missions discussed here to characterise space weathering.

Two missions are proposed in this section and motivated by direct quotes from the decadal survey. Both missions focus on understanding the nature of the initial small body population that was the feedstock for the planets and evolved into the present asteroids. The first mission studies an asteroid family to better understand small body dynamics and therefore what the present day asteroids can tell us about the past. The second mission characterises the large asteroids, which are thought to be remnant planetesimals, to directly learn about the bodies that are preserved from the beginning of our solar system. Because the large asteroid mission aims to visit a diverse set of asteroids, it is also ideal for surveying the magnetic properties of asteroids and will incorporate the third investigation. The engineering and feasibility of the missions are discussed later in Section 3.2.

3.1.1 In situ studies of asteroid families

Asteroid families are created when nature performs a grand experiment for us to observe: smashing together solar system bodies. Understanding the present dynamical evolution of the solar system is key to model the past as we can then virtually turn back the clock billions of years. The originally formed planetesimals have collided and broken apart into smaller bodies, which go on to collide and break apart further, and give a quasi steady-state distribution of bodies in the solar system today [57]. Additionally, materials previously hidden inside are excavated by the collisions, providing a unique opportunity to look inside solar system bodies. In situ studies of asteroid families therefore contribute to two priority science questions in the decadal survey: how did the inner solar system bodies form (Q3) and how have they evolved (Q4)?

In Question 4.1 of the decadal survey it is stated that:

> Many questions and gaps in our knowledge [...] still obscure our understanding of [the] fundamental planet-building processes. For example, the initial size dis-

> tributions of planetesimals across the solar system are poorly understood, as are the physical processes that govern small body disruption. [68, p. 184]

and notes that asteroid families are a key tool for understanding the dynamical evolution of the solar system:

> Collisions are a primary geologic process for small body populations. They break down worlds and create new fragments that can also be disrupted by subsequent impacts. [...] Major collisions also create swarms of fragments on similar orbits, called families, that can tell us about the nature of large-scale impact events occurring in the past. Using models, these kinds of constraints can be used to glean insights into how individual bodies and populations have evolved from their primordial states. [68, p. 186]

The outcomes for small bodies are complicated by non-gravitational forces dubbed the Yarkovsky and YORP effects, that alter both the orbit and spin-state of small asteroids. The orbit drift due to the Yarkovsky effect causes family members to spread out after a collision and makes it possible to determine when the family-forming collision took place [59]. The outcomes of the spin-state changes due to the YORP effect are more subtle, but determine the long-term evolution of small bodies:

> There are hypothetical stable end states that such bodies may evolve to, preserving their mechanical structure and dynamical state over long-time spans. Conversely, there are other hypothesized effects which ultimately cause rubble piles to disaggregate into their constituent boulders and grains, which would then further evolve as monolithic bodies. The existence and efficiency of these different processes are unknown, yet are crucial to understanding the nature and age of the small bodies in the solar system, and the current rate at which they are created through catastrophic impacts. [68, p. 186]

Because of their significance to the dynamical evolution of the solar system, the decadal survey explicitly calls for an in situ study of asteroid family members that the proposed mission meets [68, p. 188]:

- Question 4.1 Strategic Research: “Benchmark the ages of asteroid families and the nature of family-forming events by observing asteroid family members in situ, counting craters on their surfaces, and comparing their model ages to dynamical evolution models of how the family members evolve.”

Beyond directly studying solar system dynamics, a mission to an asteroid family will also yield important insights to the formation of solar system bodies. The planets were formed though collisions and accretion into the vast objects we see today, whose properties are linked to the mixing and alteration of materials that took place as summarised in Question 4.3 of the decacal survey:

> Collisional and accretional events were an integral aspect of the formation of planetary bodies and exercised a controlling influence on their physical and chemical states throughout their evolution. In the context of modern-day Earth, collisions and impacts are often viewed as destructive events. Yet collisions have had a profoundly constructive role in the formation and evolution of planetary bodies, beginning with their bulk composition and extending through to the timing and duration of differentiation and exogenous delivery of chemical ingredients essential to life. [68, p. 195]

Furthermore, the building blocks of the planets, i.e. the planetesimals, are the ultimate source of the asteroid families and present a unique opportunity to directly observe the inside of a planetesimal:

> In the asteroid belt and TNO [Trans-Neptunian Object] populations, many bodies have been shattered, disrupted, and scrambled by large impacts. In the process, interior materials normally hidden away at depth are now potentially accessible, some on small bodies that may eventually approach Earth. Accordingly, by interpreting the jigsaw puzzles created by impacts, and placing their samples into geologic context, we can probe the origin and evolution of planetesimals to a much greater extent than would be possible with intact bodies. [68, p. 196]

The proposed mission can therefore contribute to our understanding of planetesimals directly if the family is carefully selected to have been formed by a large, previously undisturbed, body and therefore meet two further research directions explicitly called for in the decadal survey [68, p. 162]:

- Question 3.1 Strategic Research: "Determine the diversity of compositions and nature of remnant planetesimals residing in the inner solar system and establish links between the small body taxonomy and meteorite types through Earth-based and spacecraft-based remote sensing, in situ measurements, and laboratory analyses of meteorites and returned samples."

- Question 3.1 Strategic Research: “Determine the mechanisms of planetary accretion by developing and evaluating physical models that link dynamics and chemistry coupled with observational constraints on compositions and distributions of material and planetesimal structures comprising the solar system.”

Observables

In situ missions need to produce data that can not realistically be produced with easier methods and that are relevant to the priority science questions. The porosity and density of the family members are important physical properties that are poorly understood [175] and should naturally be measured by any in situ mission.

Recent work on catastrophic family-forming collisions suggest that all members are gravitationally reaccumulated rubble-piles made up of small fragments, i.e. that the parent body was completely shattered [176]. This result should extend to all small asteroids (as they are almost certainly collisional fragments), but the results from (433) Eros by NEAR Shoemaker suggest it is a mostly coherent body [177]. The contradiction between models and measurements may be resolved by observing if collisional family members include monolithic bodies or if they are all rubble-piles. The latter case may suggest that rubble-piles become stronger over time, by e.g. internally rearranging and consolidating the boulders [176].

The spectral type of asteroids is traditionally a parameter used to determine if asteroids are family members or unrelated interlopers. This presumes that family members are homogeneous, however, that assumption has not been tested. If all members are rubble-piles they may appear homogeneous because each member contains a similar mixture of different materials within the parent body. Models suggest that for strong bodies the materials that reaccumulate originated nearby in the parent body, whereas for weak parents it is practically random [176]. The original composition and strength of the parent can thus be constrained by observing compositional variation among the boulders that make up family members.

In summary, the important observables are:

1. What is the mean density and porosity of the family members?
2. Are the family members rubble-pile or monolithic (including fractured) bodies?
3. Are there compositional variations among the blocks that make up the family members? If yes, is the ratio of constituents the same or different among the family members?

The smallest resolution that is required when observing the structure and composition of the asteroids can be determined by taking the near-Earth asteroid (25143) Itokawa results by Hayabusa as a typical reference. The boulder size-frequency distribution follows a simple power-law below 20 m on Itokawa [178], and therefore a resolution limit of 10 m should be sufficient to capture all large blocks and the size-frequency distribution on the family members.

To ensure that the results are testable against models the asteroid family must also be young (recently formed), because non-gravitational forces, e.g. the Yarkovsky and YORP effects, will scatter the orbital elements over time. As an example, the family members of the 8 Myr old family of (490) Veritas have orbital elements that have been shown to closely preserve the parameters of the impact [176].

The range of sizes among family members is typically narrow and therefore the minimum number of bodies that need to be visited is relatively low. Model outcomes suggest that a collision should result in a handful of large fragments plus a group of small members that are within an order of magnitude in size [176]. A mission of 10 swarm members should be sufficient, where the targets include the largest member, one or two more of the large fragments, and the rest sampling evenly among the smaller members.

For missions with the alternative motivation of studying the breakup of a large complex asteroid the set of observables and number of spacecraft are also suitable, because the structure and compositional variation of the family members are the key properties that can be used to determine the composition and interior of the parent body.

Target selection

The Nesvorny HCM family database compiled in 2020 [179], which contains a total of 119 families, was used to define the available asteroid families and designate their membership. Families that were recently formed are ideal for this mission as they have been altered less by further collisions or space weathering and are less spread out by dynamic forces. Table 3.1 lists the available families that have at least 100 members and have an estimated age of less than 100 Myr. Additionally, the family of (15) Eunomia is included as it is thought to originate from a cratering event on an at least partially differentiated body [180] that may have been fractured previously but was certainly not a rubble pile [181]. Due to the rare occurrence of catastrophic breakup of large bodies, on the order of one per Gyr [57], a younger or more disruptive breakup of a preserved differentiated planetesimal is unlikely to be available to study.

The propulsion requirements to explore the asteroid families were calculated by finding optimal one-impulse flyby and two-impulse orbit insertion trajectories between the mothership and all asteroids in the family. Lambertian trajectories were calculated in ESA's pykep [188] software where the release time and time of flight were optimised for each asteroid. The CubeSats were released starting on Jan 1st 2030 and up to six years later to ensure the

Table 3.1: Young asteroid families in [179] with $N \geq 100$ members and the Eunomia family sorted by family number (FID). The families in bold were selected for further study.

FID	N	Largest member	a	e	i	Age
502	5670	(15) Eunomia	2.64	.15	13.1	910 to 2380 Myr [182]
508	296	(396) Aeolia	2.74	.17	3.5	64 to 131 Myr [182]
511	195	(606) Brangane	2.59	.18	9.6	33 to 58 Myr [182]
517	354	(342) Endymion	2.57	.14	8.3	37 to 65 Myr [182]
520	150	(1547) Nele	2.64	.27	12.2	4.4 to 7.2 Myr [183]
608	579	(1521) Seinajoki	2.85	.12	15.0	82 to 459 Myr [182]
609	1294	(490) Veritas	3.17	.07	9.2	8.0 to 8.6 Myr [184]
610	541	(832) Karin	2.86	.04	2.1	5.7 to 5.8 Myr [184]
617	376	(778) Theobalda	3.18	.26	14.4	4.6 to 9.2 Myr [185]
620	148	(90) Antiope	3.15	.15	1.3	<10 Myr [186]
621	246	(158) Koronis	2.87	.05	2.2	<15 Myr [187]

whole orbit period was considered. The time of flight was allowed to be up to two years. The mothership was assumed to be at the position of the largest member of the family, as this member is approximately central and should certainly be studied in the mission. Trajectories were initially calculated with a time step of 10 weeks and all solutions with $\Delta v < 3\,\text{km/s}$ for flyby or $\Delta v < 6\,\text{km/s}$ for orbit insertion were kept and refined to a 1-week time step in both release time and time of flight. All asteroid positions and velocities were retrieved from the JPL Horizons system [189].

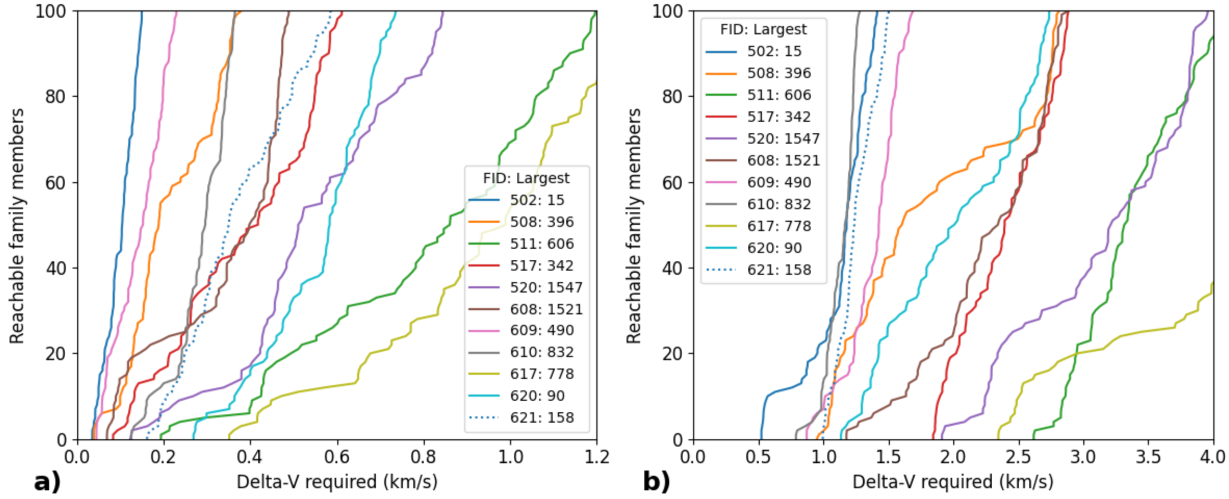

Figure 3.1: Δv required to reach a given number of asteroid family members starting at the largest member. a) For flyby. b) For orbit insertion.

Figure 3.1 shows the Δv required to reach the nearest 100 members of each family, where the families of (15) Eunomia, (490) Veritas, and (832) Karin stand out with small requirements in both cases. Because it is easily accessible and possibly the best chance to directly study the results of a collision on a differentiated body, Eunomia is a prime candidate for this mission. The Karin family is known to be a secondary family resulting from a collision within in the larger Koronis family [181], and therefore it does not suit the investigation of planetesimals. On the other hand, a mission to the Karin family is ideally suited to constrain collisional models for rubble-piles because it has already been used to make detailed predictions about the parent body, impactor, and nature of the collision [176, 190] that can be tested. The Veritas family is also an intriguing target because early spectroscopic results indicated that it came from the breakup of a large differentiated body [191], however, more recent modelling instead proposes that the namesake may be an interloper and the parent body was porous and not differentiated [176]. The case of the Veritas family is discussed further in [190] and references therein and remains open for interpretation and in need of more measurements. In the middle main belt the families of (396) Aeolia and (342) Endymion are accessible but little is published about them. The Aeolia family may be an interesting target because an active asteroid could be a member and some variance in albedo and spectral type has been observed among the members [192], but it is not considered further here. The families of (606) Brangane and (1547) Nele are certainly interesting targets to study. Brangane is a small (36 km) so-called Barbarian asteroid that displays unique spectral properties and is expected to be a rare fragment of a first-generation planetesimal [193]. Barbarian asteroids are the subject of intense research and an in situ study of this family may more directly investigate the dynamical evolution of materials that accreted the terrestrial planets. The Nele family is one of the youngest known and in an isolated orbit where its members are easily distinguished from interlopers [183], and is therefore ideal to study the breakup of small asteroids and Yarkovsky/YORP evolution of the resulting bodies. The families that were selected as interesting targets for this investigation are shown in bold in Table 3.1.

Figures 3.2 and 3.3 show the Δv required to reach the family members plotted against two important properties for mission engineering: the distance to the Sun, which determines the amount of sunlight available for power, and the distance to the mothership, which determines the radio link distance. For each asteroid family, the Δv was cut off when half of the members, up to a maximum of 100, were reachable. For the Veritas and Karin families on near-circular orbits the results are closely clustered and the requirements on Sun and mothership distance were determined to the values in Table 3.2 such that almost all members are reachable. The other families are on eccentric orbits and show a large spread in Sun distance where a clustering around perihelion and aphelion is apparent. In these cases, the missions are made less challenging by assuming the CubeSats are launched from the

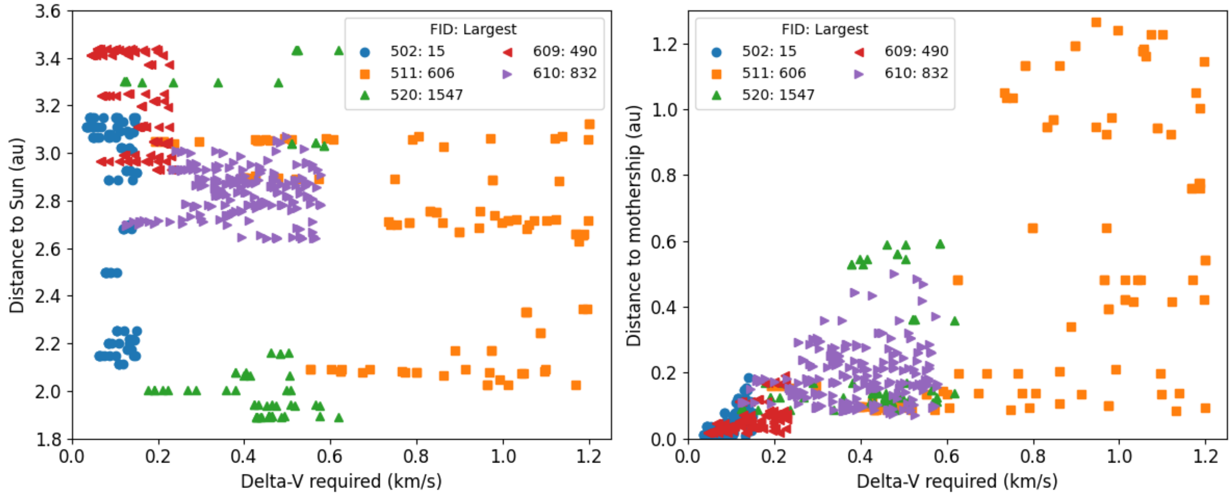

Figure 3.2: Distance to the Sun and mothership on arrival for flyby trajectories to the selected asteroid families.

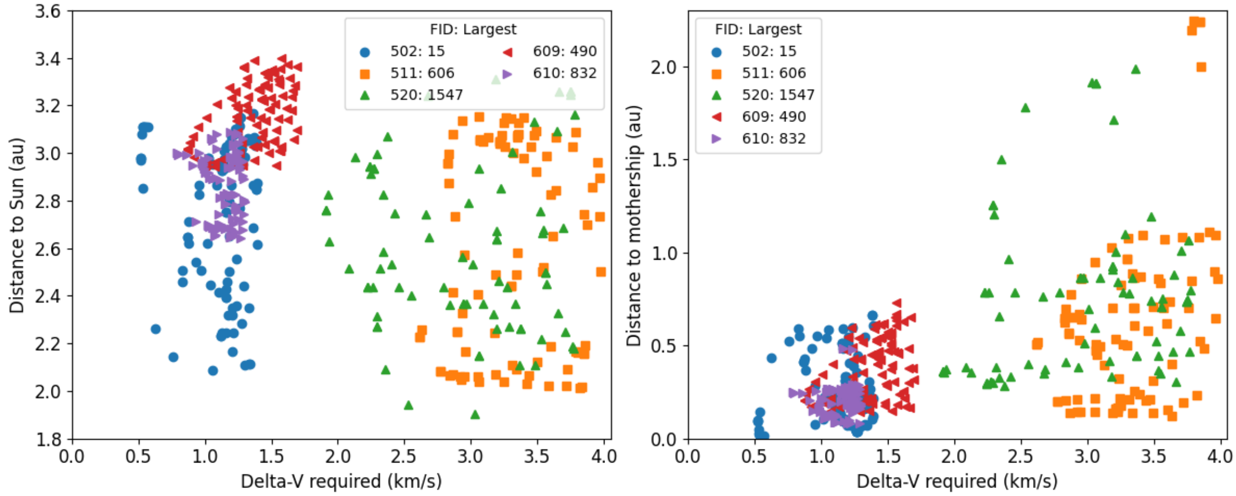

Figure 3.3: Distance to the Sun and mothership on arrival for orbit insertion trajectories to the selected asteroid families.

Table 3.2: Required maximum distance to the Sun ($R_{\max}$), mothership ($d_{\max}$) and propulsion capability ($\Delta v_{\max}$) required of the CubeSats to explore each family.

		Flyby mission			Orbiting mission		
FID	Largest member	$R_{\max}$	$d_{\max}$	$\Delta v_{\max}$	$R_{\max}$	$d_{\max}$	$\Delta v_{\max}$
502	(15) Enuomia	2.3 au	0.1 au	0.15 km/s	2.5 au	0.5 au	1.4 km/s
511	(606) Brangane	2.2 au	0.2 au	1.2 km/s	2.2 au	0.3 au	4.0 km/s
520	(1547) Nele	2.2 au	0.2 au	0.15 km/s	2.4 au	0.5 au	3.8 km/s
609	(490) Veritas	3.5 au	0.1 au	0.23 km/s	3.4 au	0.6 au	1.7 km/s
610	(832) Karin	3.0 au	0.3 au	0.58 km/s	3.1 au	0.3 au	1.3 km/s

mothership and visit asteroids near perihelion. With the requirements of Table 3.2 imposed there are approximately 50 to 100 accessible targets for each family, which is sufficient for the science goals and will allow further downselection to the final targets based on desired population properties such as size distribution and range of release times.

3.1.2 In situ survey of the large asteroids

The large asteroids, around 100 km and larger, are known to mostly be remnant planetesimals because their population can not be explained by collisions of larger bodies and modern formation models suggest that gravitational collapse forms bodies at this scale [56]. Planetesimals are a key step in solar system formation and their evolution through thermal or aqueous processing and partial or complete melting can produce a wide range of outcomes. The interior structures of large asteroids are not well known; after gravitational collapse they should be weak and porous, but they may evolve as far as resembling mini-planets with a core and mantle. The effects of composition, size, and formation timing and location on their evolution is poorly known and therefore our understanding of the materials that formed the planets is limited. The existence of multiple generations of planetesimals, ranging from ones that formed early and were the primary feedstock for the planets, and ones formed late as a result of planetary formation or from leftover material, complicate the story [49]. In situ studies of the large asteroids are important to several priority science questions in the decadal survey to understand planetesimals themselves, and because their old age may preserve clues to the earliest days of our solar system.

One reason why meteorites and asteroids are important to study is explained in Question 3.1 of the decadal survey:

> Some of the best constraints on the building blocks of the terrestrial planets come from meteorite samples and asteroid studies. Asteroids display considerable diversity in spectral properties (e.g., color, albedo), size, and geophysical characteristics, and may include materials that originated across both the inner and outer solar system. While there are a multitude of asteroids, their total mass is small, 0.04 percent of Earth's mass, and the extent to which their compositions are fully representative of materials that formed the terrestrial planets remains unclear. [68, p. 159]

The question further states that linking asteroids with their associated meteorites are key to moving solar system science forward, but it is difficult in practice, especially as the surfaces of the large asteroids may be misleading:

> Spectral observations of asteroids have identified a wide range of classifications, a few of which have been linked to meteorite types by spacecraft exploration. For example, Hayabusa's sample return from (25143) Itokawa has demonstrated a link to ordinary chondrite meteorites, and Dawn's exploration of (4) Vesta has confirmed that (4) Vesta is the parent-body of the howardite, eucrite, and diogenite (HED) meteorites. Other associations between meteorite types and asteroid classes remain to be tested. For example, the spectral signatures of some partially differentiated asteroids may have exteriors that resemble more primitive bodies. [...] Linking the diversity observed in meteorite samples to the large-scale diversity observed in the asteroid population is fundamental to advancing our knowledge of both types of objects. [68, p. 161]

Studying the solar system via the asteroids is helped by their chaotic past, because the main asteroid belt likely contains bodies formed far away from their present locations:

> According to planet formation and giant planet migration models, the main asteroid belt is a collection zone for planetesimals formed from across the solar system. While some asteroids may have originated in the main belt region, the majority likely came from the terrestrial planet zone (predominately the Mars region), the giant planet zone, and the primordial Kuiper belt. This wide variety of source regions means that the asteroids and meteorites potentially reflect a broad range of planetesimal compositions. [68, p. 161]

The large asteroids are, however, not frozen in their initial state. Instead, they have evolved physically and chemically though the processes discussed in Section 2.1.2 of the literature review and may be highly complex objects. Virtually all bodies show some evidence of alteration that have affected their properties:

> Even primitive chondritic meteorites—thought to best reflect the initial, unaltered composition of the protoplanetary disk—show evidence of parent-body processes that have affected their properties and mineralogy. Hydrothermal alteration, thermal metamorphism, shock heating, and compaction occurred early in the solar system, prior to complete accretion of the terrestrial planets. All these processes played important roles in determining the physical characteristics of chondritic materials and contributed to the variability of the building blocks of terrestrial bodies. [68, p. 161]

Some bodies may be heavily altered from their initial materials due to melting. However, our knowledge of small body differentiation requires further measurements and model work as explained in Question 3.5 of the decadal survey:

> While differentiation ages of planetesimals and asteroids have not been as well determined, the observation that basaltic samples from Vesta crystallized within a few million years of the beginning of the solar system indicates that differentiation was very early. [...] Overall, small bodies appear to have differentiated earlier than large bodies, perhaps reflecting a combination of the size of these bodies and their proclivity to lose heat, and the preponderance of 26Al in the early solar system that provided an important heat source during early times and stages of accretion. [...] Fundamental questions remain as to how the timing and style of primordial differentiation was linked to a body's size and the physical environment and chemical conditions in which it formed. Additional samples, more detailed thermal modeling, and more thorough understanding of the surface geology and interior structure of differentiated bodies are required to make further progress. [68, p. 171]

The importance of the large asteroids and the limitations of remote surveys that only measure their large-scale characteristics, which may not be representative of what lies beneath, motivates several in situ studies in the decadal survey [68, pp. 162, 173, 213]:

- Question 3.1 Strategic Research: "Determine the diversity of compositions and nature of remnant planetesimals residing in the inner solar system and establish links between the small body taxonomy and meteorite types through Earth-based and spacecraft-based remote sensing, in situ measurements, and laboratory analyses of meteorites and returned samples."

- Question 3.1 Strategic Research: "Determine what secondary processes have led to the diversity of asteroids and planetary feedstocks by conducting geochemical, petrological, and geophysical investigations of meteorites, asteroids, and samples returned from asteroids."

- Question 3.5 Strategic Research: "Determine the contribution of outer solar system materials to the inventory of the inner solar system planets through measurements of the volatiles and refractory components of water-rich asteroids and comets by telescopic observations, in situ measurements, and/or analysis of returned samples."

- Question 5.1 Strategic Research: "Investigate magmatism, and the effects of interior processes on surface compositions of planetesimals (specifically large asteroids and dwarf planets) via high-resolution imaging, spectroscopy, and topography."

The locations and nature of the large asteroids are also evidence for the evolution of the giant planets' orbits, as they strongly affect small bodies with their resonances (see Section 2.1.3 of the literaure review). The intact large asteroids may retain the oldest cratering records, required to study the timing of early bombardment as explained in Question 3.2 of the decadal survey:

> Giant planet encounters with one another may also allow a small fraction of comets ejected from the primordial Kuiper belt to be captured in stable orbits across the solar system. This might explain why primitive, comet-like asteroids (D- and P-types) are found in the central and outer main belt as well as in the Hilda and Trojan populations associated with Jupiter, and would imply that the asteroid belt contains planetesimals from the furthest reaches of the solar system. As the giant planets moved to their present-day orbits, dynamical resonances associated with them also moved to their current locations, perhaps depleting or eliminating portions of the primordial inner main belt while perhaps creating the innermost asteroid population, the Hungaria asteroids. The instability would have also driven impacts within the belt; this could be assessed by studying the impact history of asteroids large enough to have resisted disruption, as well as by identifying evidence for any common shattering/disruption times from meteorite shock degassing ages. [68, p. 163]

A particularly intriguing possibility is that there were more giant planets in the young solar system that at some point were ejected. If this is the case, the main asteroid belt's structure and members may hold a record that can be used to test models:

> An overall goal is to find evidence for or against these dynamical set pieces through missions to small bodies and/or meteorite analysis. We need to determine precisely how the signatures of post-nebula giant planet migration are recorded in small body populations and whether the nature of the asteroid belt can tell us how many giant planets existed prior to the giant planet instability. We want to determine whether dormant comet-like asteroids were implanted in the main belt, Hildas, and/or Trojans by the giant planet instability and whether the primordial asteroid belt interacted with an "extra Neptune". [68, p. 164]

Cratering records also hold a broader significance as they are used as a tool to date features across the solar system, as explained in Question 4.2 of the decadal survey:

> The history of impacts on different bodies varies across the solar system and is dependent on impactor populations that evolved over time. The fingerprints of these different impactor populations are recorded in the cratering record of planetary surfaces, so interpreting these crater populations can tell us about

> small body populations that might no longer exist. Additionally, untangling the temporal evolution of impact bombardment on different bodies has scientific value beyond impact studies, because the accumulated crater populations on landforms is the only way of estimating their age without returning samples and analyzing them in laboratories on Earth. [68, p. 189]

The locations and cratering records of the large asteroids therefore motivate in situ studies in the decadal survey [68, pp. 164, 195]:

- Question 3.2 Strategic Research: "Determine whether C- and B-type asteroids within the main asteroid belt originated within the giant planet region by assessing their volatile content, using in situ methods or sample return, and identifying whether any provide evidence of parent body origin at low temperatures beyond Jupiter."
- Question 3.2 Strategic Research: "Determine the timing of the giant planet instability through evidence of early comet bombardment of the asteroid belt (e.g., impact history of large asteroids that resisted disruption, identification of common shattering/disruption times for asteroids from meteorite shock degassing ages) and constraining the ages of the oldest lunar impact basins."
- Question 4.2 Strategic Research: "Determine the nature of early bombardment and the primordial asteroid belt by observing large intact asteroids that may still have some record of impacts/craters from early bombardment phases, counting craters, and modeling their crater size distributions."

Finally, Question 1.4 of the decadal survey explains why asteroids may retain a magnetic record of the presence of gas when they were formed. The dispersal of the gaseous nebula has important implications, as it may have both halted planetesimal formation and initiated the giant planet instability:

> One interpretation of meteorite constraints is that planetesimal formation came to an end when the solar nebula dispersed. With that said, the solar nebula is big enough that this could mean modestly different timescales for the endgame of planetesimal formation in the inner and outer solar systems, and perhaps within those regions as well. [...] The end of the solar nebula also means the termination of gas processes that can damp planetary eccentricities and inclinations. This could set the stage for a period of violent upheaval for the orbits of the giant planets. The dispersal time of the nebula also affects the final composition of planetary objects by truncating the condensation and accretion sequence at a particular location-dependent temperature and pressure. [68, p. 117]

Remnant magnetism has been observed in several meteorite types that correspond to some source of magnetic fields, including a potential convecting metal core [51]. Uniform remnant magnetism in some meteorites (and therefore possibly asteroids) is correlated to their formation age, and suggests magnetism may be a direct way to measure the dispersal time of the nebular gas:

> Because the sustenance of magnetic fields requires the existence of a conducting medium, the dispersal of the nebula would have led to dissipation of the nebular field. Therefore, under the assumption that the field is present whenever there is gas (and this might not necessarily be the case), the dispersal time of the nebula could be estimated by establishing when the solar nebula magnetic disappeared as inferred from the absence of paleomagnetism in meteorites younger than a certain age. [68, p. 119]

Another important investigation that the decadal survey calls for and can be carried out at the large asteroids is therefore to measure the remnant magetism (or absence thereof) [68, p. 120]:

- Question 1.4 Strategic Research: "Measure the intensity of the solar nebula magnetic field as a function of space and time with return of asteroid and comet surface samples; in situ magnetic measurements at asteroids, comets, Centaurs, and Kuiper belt objects; and laboratory paleomagnetic measurements of returned and terrestrially collected samples."

Observables

For a mission to the large asteroids there are observables that focus on the body itself and observables that focus on the story the body tells in a broader context. The spectra of the large asteroids have already been measured globally in telescopic surveys, so an in situ mission concerns the details. There are also typically mass estimates for large asteroids (derived from mutual close encounters) but the uncertainties can be large [194] and therefore direct mass measurements are valuable in situ data.

The internal structure and composition is of chief interest for this class of mission, where especially evidence of differentiation or other complex processes are interesting. Irregularities in the gravity field, evidence of a past magnetic core, and surface features offer insights. Because the targets have experienced crater-forming impacts, interior materials are exposed and excavated and therefore high-resolution spectroscopy can detect composition to some depth. To support investigations of early bombardment a large fraction of the surface should be mapped for the large-scale cratering record smaller patches may be mapped to count the more recent small-scale craters.

In summary, the following observables should be targeted:

- What is the mean density, and are there denser regions (e.g. a core) inside?
- Are there compositional variations on the surface? If there are deeply excavated materials, what are their compositions?
- Do the surface features say anything about the interior structure?
- Is the asteroid magnetised? If yes, is it dipole (i.e. core dynamo) or uniform (i.e. remnant nebular field)?
- What is the crater size-frequency distribution? Is it uniform across the surface?

The smallest resolution required in both cases is driven by the smallest craters that need to be mapped, either directly for their size or for the composition in their basin. Small craters of the km scale were used to date larger basins on Vesta [195] so a resolution limit of 100 m is sufficient for the large asteroid investigation. To measure the magnetic field and distinguish between dipole or uniform magnetisation a very low pass is required, as the dipole field strength falls of with distance to the third power and higher orders even more aggressively. With the high risk tolerance of a CubeSat mission an orbiter can get very close during late science operations which also suits gravity sensing, but may be restricted on certain asteroids if they are deemed especially important for planetary protection.

Understanding the diversity of the large asteroid population is a fundamental motivation for this mission and therefore it is important to select targets for breadth of discovery. As a minimum goal, half of the unique large asteroid spectral classes should be visited and the total number of asteroids visited should be double that number. Multiple individuals in the most common spectral classes will naturally be explored by this strategy which makes it possible to determine how uniform the populations of common large asteroids are.

Target selection

The JPL small body database [196] was used to find all main belt asteroids with a diameter larger than 100 km and with a defined SMASS-II or Tholen spectral type, yielding 202 bodies after (1) Ceres, (4) Vesta, and (16) Psyche were excluded as they are or will be well characterised by other missions. The SMASS-II spectral type took precedence, however, for 51 bodies only the Tholen classification was available. The first type listed was used for bodies with several Tholen types listed and the Tholen types M, P, and F, which do not exist

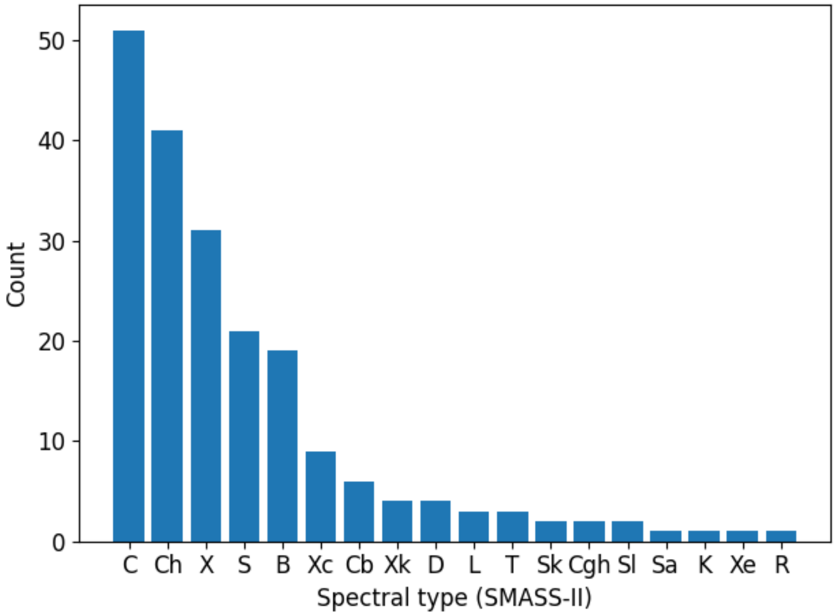

Figure 3.4: Large asteroids (>100 km) in the main belt sorted by spectral type.

in SMASS-II, were placed in X, X, and B respectively to group them with similar objects. Five asteroids with diameters larger than 100 km were not included as neither spectral type was defined: (227) Philosophia, (303) Josephina, (424) Gratia, (780) Armenia, and (788) Hohensteina. The large main belt asteroids considered are distributed into 18 spectral types as shown in Figure 3.4.

Optimal one-impulse flyby and two-impulse orbit insertion trajectories between the mothership, where the CubeSat is released, and all other large asteroids were calculated using lambertian trajectories in ESA's pykep [188] software. The CubeSats were released starting on Jan 1st 2030 and up to three years later, and their time of flight was allowed to be up to two years. The mothership was assumed to orbit adjacent to one of the large asteroids which will be referred to as the source asteroid for the mission. Thanks to the small number of targets, the search could be performed as a brute-force combinatoric search in approximately 5 min with an initial time step of 10 weeks where each solution was refined to a time step of 1 week in both launch time and time of flight. All asteroid positions were retrieved from the JPL Horizons database [189]. The number of unique spectral types visited and the total number of targets reachable will be used as metrics to capture both the breadth and depth of each option.

For the one-impulse flyby case the results are shown in Figure 3.5, where a nearly linear relationship between the number of reachable targets and Δv capability is apparent. The number of unique spectral types visited also increases linearly but plateaus at 15/18 spectral

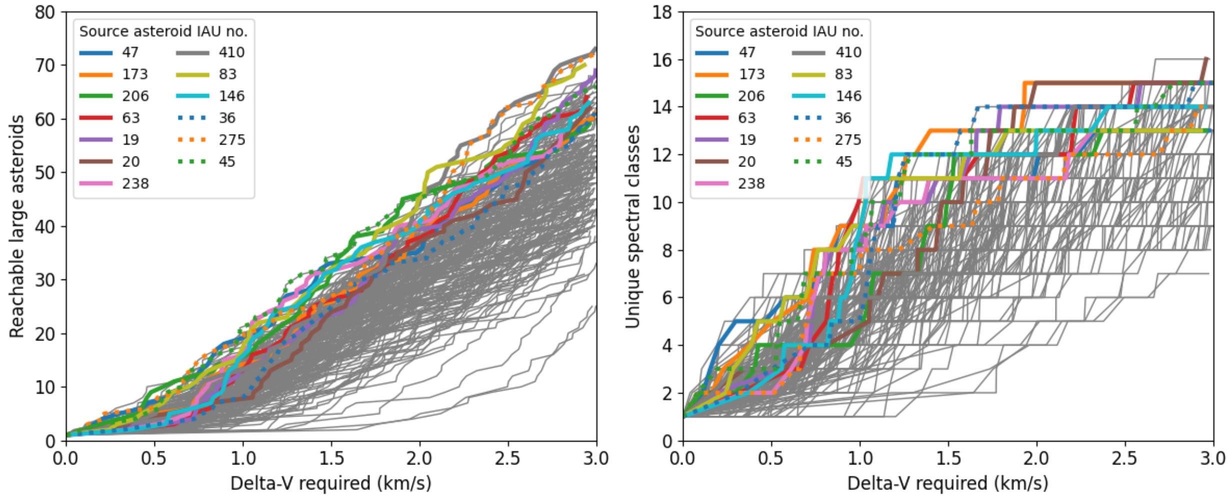

Figure 3.5: Reachable asteroids for flyby as a function of the Δv capability of the CubeSat swarm when all asteroids are trialled as the source. The thick coloured lines show the source asteroids that have the highest number at some point between 1 to 2.5 km/s and the thin grey lines show all others.

types when $\Delta v \approx 2$ km/s. Between 1 to 2.5 km/s there are a set of 14 source asteroids that have the highest number of reachable targets or unique spectral types visited and therefore are the Pareto-optimal set of targets for flyby missions and the only ones that will be considered further. With the goal to visit at least half of all spectral types the required Δv for flyby is around 1 km/s. Figure 3.6a shows the Pareto front in detail at 1 and 1.5 km/s Δv for flybys, where a strong scaling is seen at the higher Δv. The same set of mission options are shown in Figure 3.7 with the range to the Sun and the mothership where it is clear, and not unexpected, that all target options end up spreading across much of the asteroid belt and far from the mothership to reach the few large asteroids. A mission originating at (47) Aglaja is most tractable and gives the minimum requirements in Table 3.3, which also shows the maximum requirements to reach all asteroids considered.

The results for the two-impulse orbit insertion case are shown in Figure 3.8 where, as expected, larger Δv is required to reach a substantial number of targets compared to flyby. A Δv of at least 3 km/s is required to reach 10 asteroids and around 4.5 km/s is required to visit a majority of the unique spectral types. In the orbiting mission case there are 12 source asteroids in the Pareto-optimal set for further consideration, shown in Figure 3.6b at 4 and 5 km/s Δv. The range to the Sun and mothership required for the same set of missions are shown in Figure 3.9 and tells a similar story to the flyby case. If the outliers are excluded, a mission originating at (62) Erato has the lowest requirements and is chosen as the minimum

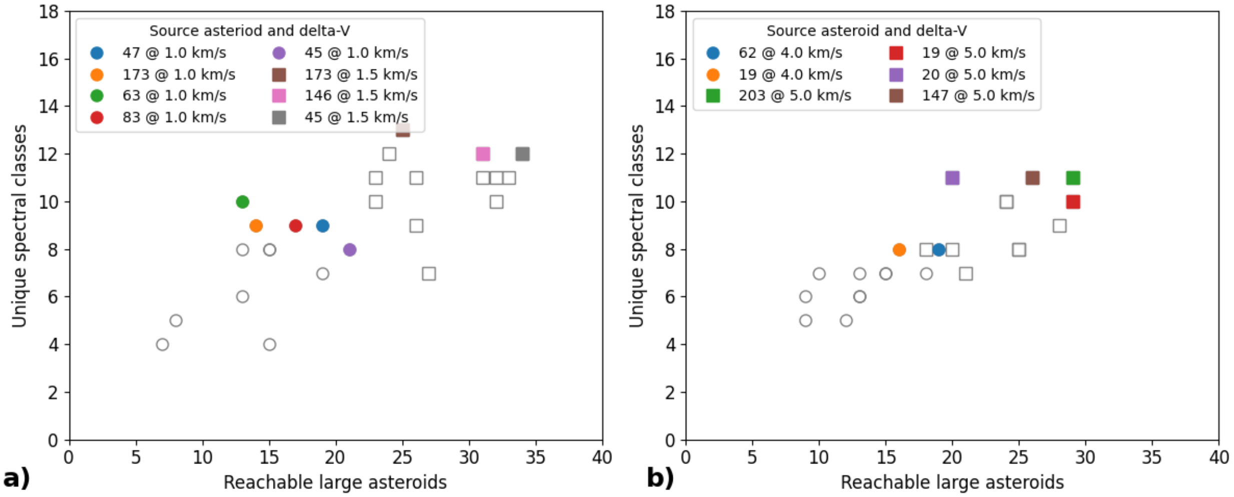

Figure 3.6: Pareto frontier of targets at specific Δv capabilities. The open symbols show all solutions that are on the Pareto front at some Δv and the filled symbols show the Pareto front at specific Δv. a) For flyby. b) For orbit insertion.

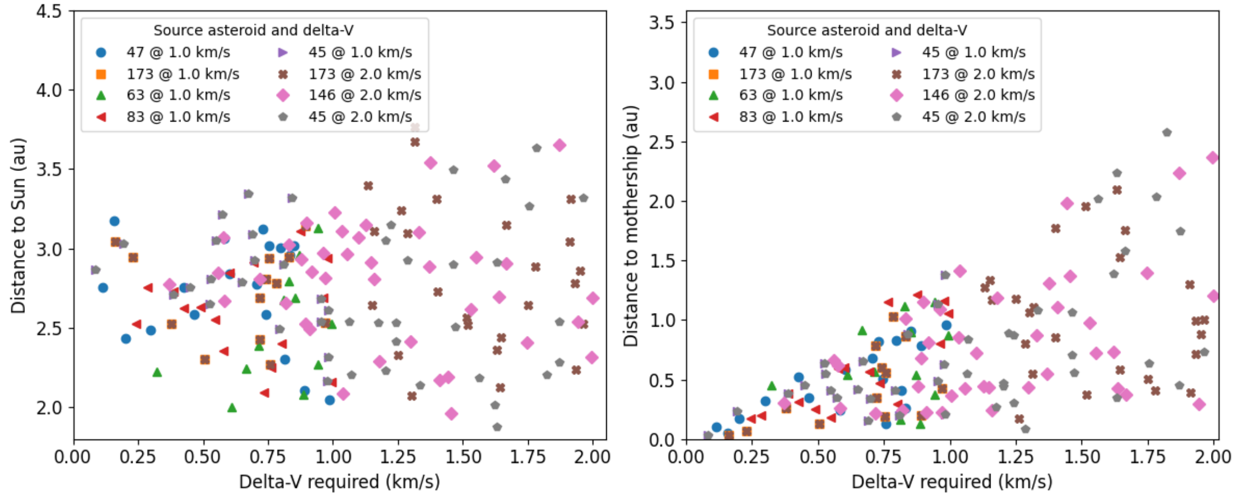

Figure 3.7: Pareto frontier of targets at specific Δv capabilities. The open symbols show all solutions that are on the Pareto front at some Δv and the filled symbols show the Pareto front at specific Δv. a) For flyby. b) For orbit insertion.

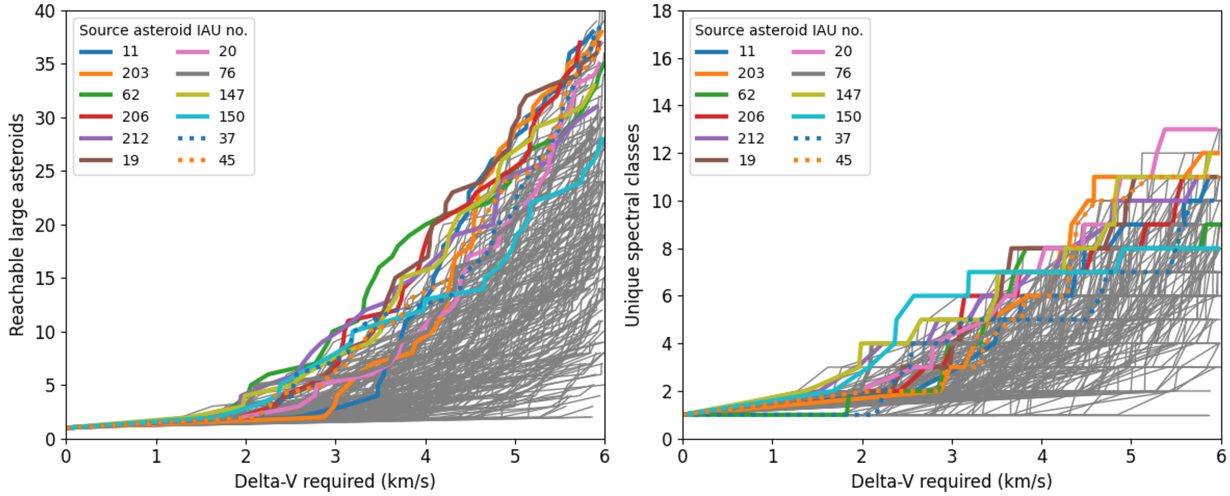

Figure 3.8: Reachable asteroids for orbit insertion as a function of the Δv capability of the CubeSat swarm when all asteroids are trialled as the source. The thick coloured lines show the source asteroids that have the highest number at some point between 2 to 5 km/s and the thin grey lines show all others.

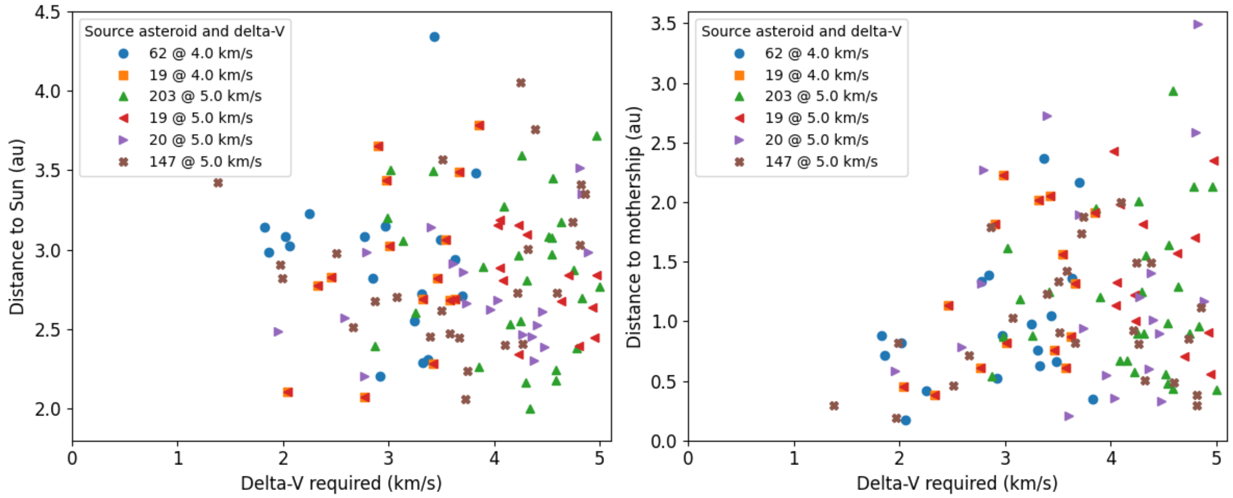

Figure 3.9: Reachable asteroids for orbit insertion as a function of the Δv capability of the CubeSat swarm when all asteroids are trialled as the source. The thick coloured lines show the source asteroids that have the highest number at some point between 2 to 5 km/s and the thin grey lines show all others.

with the four most remote targets excluded in Table 3.3. The maximum case was set at the lowest limit where at most one asteroid was excluded for each mission.

Table 3.3: Required maximum distance to the Sun (R_{max}), mothership (d_{max}) and propulsion capability (Δv_{max}) required of the CubeSats to explore the large asteroids. The "min" and "max" options are the requirements to reach the easiest group of target and almost all large asteroids respectively.

Mission	R_{max}	d_{max}	Δv_{max}
Flyby min [(47) Aglaja only]	3.2 au	1.0 au	1.0 km/s
Flyby max	3.8 au	2.6 au	2.0 km/s
Orbit min [(62) Erato only]	3.3 au	1.4 au	3.9 km/s
Orbit max	3.8 au	2.8 au	5.0 km/s

3.2 Engineering deep-space science CubeSats

This section evaluates the feasibility of the proposed science missions and shows that they range from feasible in the short term to requiring significant work. The future work required to enable the missions are discussed in Section 3.3 and include realising the full-scale staged electrospray propulsion systems developed in this thesis and some further work on power generation, communications, and autonomy.

3.2.1 Architecture concept

In principle a swarm of CubeSats could be launched to Earth-escape and explore different main belt asteroids from there, however, in practice it is either infeasible or requires heavy and complex CubeSats; contrary to their idea. Because all CubeSats need to travel from Earth to the asteroid belt, a mothership that travels from Earth to a centralised location in the asteroid belt and releases the swarm there is a suitable concept. Mothership-swarm concepts to the asteroid belt have been proposed earlier, see e.g. [76], but with the advent of CubeSats are nearing practicality. Because the swarm members are released in the asteroid belt already, their lifetime and propulsion requirements are significantly reduced compared to a trajectory starting at Earth. Similarly, the range of distances to the Sun that the CubeSats need to be designed to operate at is reduced, and therefore their thermal and power systems are simplified. A deep-space swarm is further challenged by the load it would put on Earth-based resources, especially the Deep Space Network (DSN) that services deep-space missions with communications and navigation. As discussed in the literature review Section 2.3.2, the DSN is already laden and cannot support a large influx in deep-space missions. The mothership provides a solution to this issue as well, as it can serve as a data relay and navigation reference for the CubeSat swarm whereby the mission can be operated as if it were a single spacecraft.

All investigations presented here require a similar mothership, whereby the design effort of one flexible spacecraft could enable dozens of CubeSat mission in the asteroid belt. With the mothership design fixed, the cost to continue exploring the asteroid belt after the first mission is complete can fall dramatically and the rapid technology development in the CubeSat field can be fully utilised. Designing deep-space spacecraft and their associated trajectories is a nuanced and complicated task that is avoided in this thesis by building on prior examples. The mothership will be based on combining the properties of the two main-belt asteroid missions thus far designed: Dawn and Psyche. Fortunately, Dawn was a relatively small spacecraft (launch mass of 1218 kg) with a very high Δv capability to visit both (1) Ceres and (4) Vesta in one mission [159], and Psyche is a relatively large spacecraft (launch mass of 2747 kg) with a lower Δv requirement as it only visits one target [16]. Thanks to the large propulsion capability of Dawn it can perform the Earth to main belt leg with significant additional mass to account for the CubeSats. A mission will be considered feasible if the launch mass is less than Psyche's launch mass and if the Dawn spacecraft can generate the same Δv as Psyche at the given mass. Table 3.4 shows that this is possible if up to 486 kg of mass is added to Dawn. By assuming that the 47 kg of instruments [171] are removed a mass limit of 533 kg is determined for the CubeSat swarm and its infrastructure on the mothership. Approximately 32 CubeSat deployers fit on one exterior panel on the Dawn spacecraft and 50% of the mass of the CubeSats will be added to account for the deployers and other components required on the mothership to harbour the CubeSats during the transit to the asteroid belt.

Table 3.4: Comparison of spacecraft capabilities showing the maximum launch mass of a Dawn-based mothership to reach the asteroid belt. The Δv shown is the maximum capability of the propulsion system without margins.

Spacecraft	Specific impulse	Wet mass	Propellant mass	Δv_{max}
Dawn [159]	3100 s	1218 kg	425 kg	13.1 km/s
Psyche [16, 160]	1770 s	2747 kg	1085 kg	8.7 km/s
Mothership limit	3100 s	1704 kg	425 kg	8.7 km/s

The CubeSats will be based on the 6U MarCO platform that were launched in 2018 and operated for approximately 8 months on a journey from Earth to slightly past Mars [84]. A breakdown of the mass and volume of the MarCO spacecraft is given in Table 3.5 and accounts for all of the major components of the spacecraft. MarCO's radio system for receiving data from InSight and smaller items such as diagnostic cameras and harnessing are not included but appear to add up to approximately 10% of the spacecraft mass. A significant fraction of the volume is unaccounted for, which is consistent with MarCO having empty space inside (see e.g. Figure 4 in [125] and Figure 2-4 in [115]). For the swarm CubeSats, the attitude determination and control system (ADCS), command and data handling (CDH), electrical power system (EPS), X-band reflectarray antenna, and batteries from MarCO will be carried over as-is, and the latest version of the X-band Iris radio will be assumed. The basic system components add up to 4.7 kg and 2.1 L as shown in Table 3.6, to which the propulsion system, power system, instruments, and 20% margin to account for the structure and miscellaneous items are to be added for each application.

Table 3.5: The mass and volume budgets of MarCO estimated from public data sources.

Component	Mass	Volume (internal)
Tungsten ballast [84]	2.5 kg	0.1 L
Cold gas propulsion [149]	3.5 kg	2.5 L
Solar panels (36 W) [197]	0.4 kg	~ 0
Iris radio 2.0 [115]	1.4 kg	0.9 L
X-band antenna [114]	1.0 kg	~ 0
ADCS [198]	0.9 kg	0.5 L
Batteries*	0.8 kg	0.3 L
CDH + EPS†	0.9 kg	0.5 L
Launch total [84]	14 kg	7.5 L (6U)
Structure (10%)	1.3 kg	0.7 L
Unaccounted	1.3 kg	2.0 L

*Estimated as 12 typical 18650 cells plus 30% for structure and electronics from [112].

†Estimated to be the same size and weight as the ADCS system.

Table 3.6: Assumed mass and volume of base components derived from the MarCO estimates in Table 3.5.

Component	Mass	Volume (internal)
Iris radio 2.2 [116]	1.1 kg	0.8 L
X-band antenna	1.0 kg	~ 0
ADCS	0.9 kg	0.5 L
Batteries	0.8 kg	0.3 L
CDH + EPS	0.9 kg	0.5 L
Total	4.7 kg	2.1 L

3.2.2 Instruments

The instrumentation suite is based on previous deep-space and lunar CubeSat missions to meet the observables with TRL 8-9 components and is summarised in Table 3.7. The primary observable for all mission varieties is high resolution imaging and spectroscopy of the surface at a 10 m resolution for the asteroid families and 100 m for the large asteroids. The ASPECT multispectral imager covers the spectral range of 0.5 to 2.5 µm with a resolution of 20 to 40 nm and an angular resolution of 0.01 °/px (10 m sampling at 50 km) [199]. ASPECT measures 1.3 kg and 1.2 L, has flight heritage, and is planned for several deep-space missions including the Milani CubeSat (with ESA's Hera) to (65803) Didymos [200]. The flyby missions will also require a monochromatic long-range imager to guide the trajectory and capture surface features on approach. The LEIA long-range imager on the LICIACube flyby of Didymos (with NASA's DART) with a large aperture and an angular resolution of 0.014 °/px (10 m sampling at 400 km) will be assumed [87]. The detailed design of LEIA has not been published, but the size and mass were estimated from [201] to 1.0 kg and 1.5 L. The orbiting missions will have a nagivation camera for proximity operations instead of the long range imager, which is assumed to be the same camera as the MarCO star tracker camera, that weighs 0.4 kg and requires 0.3 L [198].

Table 3.7: Instrumentation selection for the four mission types under consideration. All missions have a multispectral (MS) imager, the flybys have a long-range (LR) imager, and the orbiters have a navigation camera (NavCam) and laser rangefinder. A low-frequency (LF) radar and magnetometer are added to the family and large asteroid orbiters respectively.

	Asteroid family		Large asteroids			
Instrument	Flyby	Orbit	Flyby	Orbit	Mass	Volume
MS imager	Yes	Yes	Yes	Yes	1.3 kg	1.2 L
LR imager	Yes	No	Yes	No	1.0 kg	1.5 L
NavCam	No	Yes	No	Yes	0.4 kg	0.3 L
Rangefinder	No	Yes	No	Yes	0.1 kg	0.1 L
LF Radar	No	Yes	No	No	1.3 kg	1.0 L
Magnetometer	No	No	No	Yes	0.5 kg	0.5 L
Total	2.3 kg, 2.7 L	3.1 kg, 2.6 L	2.3 kg, 2.7 L	2.3 kg, 2.1 L		

To directly measure the mass of the asteroids the orbiters will carry a laser rangefinder measuring the distance to the asteroid on low orbits and thus characterising their gravity. A commercial-off-the-shelf rangefinder with a maximum range of 1.5 km is planned to be space qualified for the M-ARGO deep-space CubeSat and fits within 0.1 kg and 0.1 L [108]. The large asteroid orbiters also carry a magnetometer to simultaneously characterise the magnetic properties of the body. Small, light, high precision magnetometers are broadly available and common on spacecraft [202] and 0.5 kg and 0.5 L is allocated for this purpose. The flyby missions are unlikely to pass close enough to measure higher-order gravity terms or any magnetic field and therefore the instruments are excluded.

A key question for the asteroid family investigations are the structures within the members, i.e. porosity and boulder size. The JuRa low-frequency synthetic aperture radar for the Juventas CubeSat (also with ESA's Hera to Didymos) is planned for a similar study of Dimorphos [147]. The mass of JuRa is 1.3 kg and it requires 1 L of internal space, plus a set of external antennas [203]. The interiors of the large asteroids will be indirectly investigated through their gravity, spectroscopy of excavated regions due to collisions, and their magnetic properties.

A neutron and gamma ray spectrometer (NGRS) would be an ideal instrument for composition measurements on a large asteroid orbiter but is not included in any investigation because the flight-heritage model developed for LunaH-Map requires 3.4 kg and 2 L of space and therefore doubles the size of the instrumentation suite. This type of instrument may be included in future, smaller, iterations or if the size of the swarm members are made larger.

For flyby missions the relative velocity of the spacecraft and target asteroid during closest approach is an important metric to determine the instrumentation requirements and feasibility. Figure 3.10 shows the flyby velocities for the considered trajectories, reaching up to 12 km/s in the worst case. The majority of the flybys are performed at lower relative velocities than recent large missions and at a similar velocity as LICIACube (7 km/s) [204] so there are no feasibility concerns.

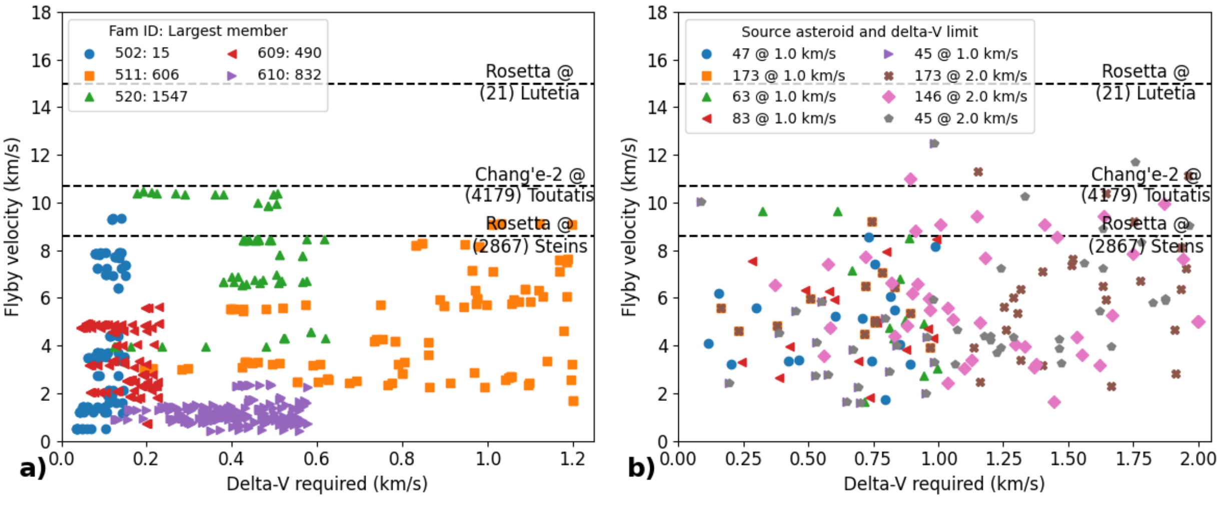

Figure 3.10: Flyby velocities for each asteroid in the selected missions. The horizontal lines show recent flybys by the Rosetta and Chang'e-2 missions [205] for comparison. a) For asteroid families. b) For large asteroids.

3.2.3 Propulsion and power

The CubeSat swarm's propulsion and power needs are driven by the trajectories for each use case. The total Δv and launch mass of the spacecraft sizes the propulsion system and the distance to the Sun combines with the average power to size the solar arrays. As with the other components, the solar arrays will be based on those used on MarCO, which are available in a wide range of sizes [110] at an estimated TRL 6-8. The specifications at 1 au are assumed to be a specific power of 130 W/kg with up to 191 W in a 6U CubeSat and up to 235 W in an 8U CubeSat (using two wings of four panels each) with a solar array drive always pointing the panels towards the Sun. For operations at 2.5 au, sufficient for three of the asteroid families, these numbers fall to 21 W/kg, 31 W, and 38 W respectively. (For the other missions the available power is even lower.) Due to the distance to the Sun all missions are expected to be power limited and the surface area is maximised by assuming an 8U CubeSat form factor (total volume limit of 10 L) for the analyses. Two staged electrospray propulsion systems are included in this analysis, the "target" and "reach" systems, corresponding to the short-term and medium-term performance expectation respectively of the propulsion systems developed in this thesis. The state-of-the-art electric propulsion system that can deliver the highest Δv on the market, Busek's BIT-3, is used as a point of comparison. The details of the propulsion systems are given in Section 4.1.3. An average system power requirement of 5 W is added to the propulsion system power to account for operating the base components and any thermal control.

As power is a major limiting factor, the thrust of the propulsion systems will be reduced where possible. The required Δv was calculated for impulsive manoeuvres but the CubeSats use low-thrust electric propulsion and therefore the actual Δv requirement will be higher. The acceleration due to gravity in the main belt is around $10^{-3}\,\mathrm{m/s^2}$ (at 2.5 au) which is approximately one order of magnitude higher than the acceleration produced on an 8U CubeSat with a 1 mN-class electric propulsion system. Gravity losses may therefore be significant if the impulsive Δv has a radial component but other losses should be small as the relative changes in orbital elements are small in all trajectories. The details of low-thrust transfers are beyond the scope of this analysis. To make the impulsive trajectories generally feasible with low-thrust propulsion a requirement is set that at least half of the trajectory is coasting, i.e. the acceleration of the spacecraft is sufficient to produce the impulsive Δv in half the time of flight. The required thrust can be found by comparing the time of flight to the Δv as shown in Figure 3.11 for the missions to asteroid families. For all flyby missions and the orbit insertion missions to the families of (15) Enuomia, (490) Veritas, and (832) Karin the staged electrospray propulsion systems (both target and reach) at half thrust (0.8 mN)

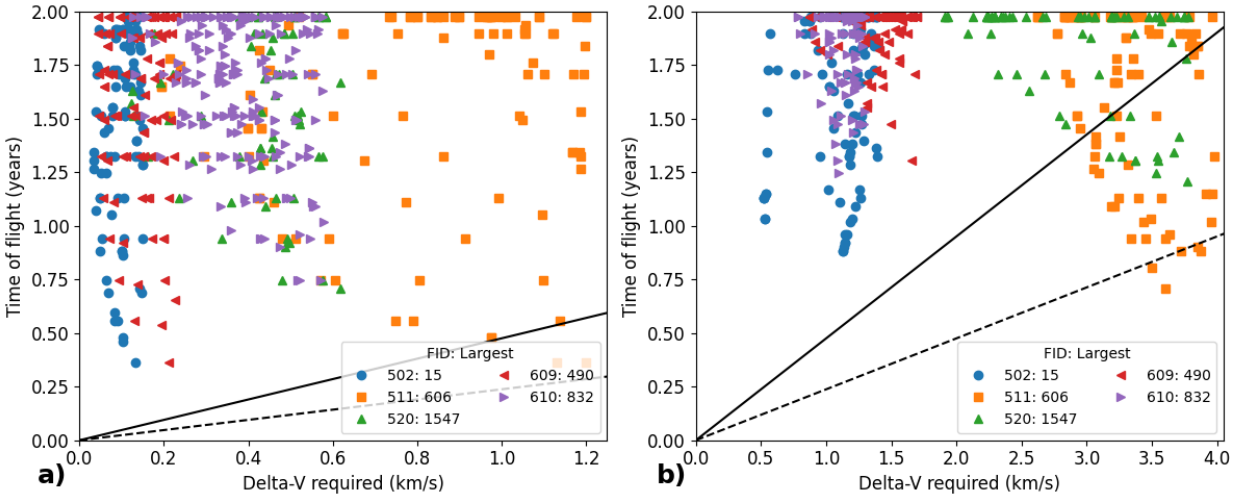

Figure 3.11: The flight time of the trajectories to each family member reachable in the proposed missions. The solid and dashed lines correspond to half (0.8 mN) and full (1.6 mN) thrust respectively for a 12 kg constant-mass spacecraft with the target staged electrospray propulsion system. a) For flyby. b) For orbit insertion.

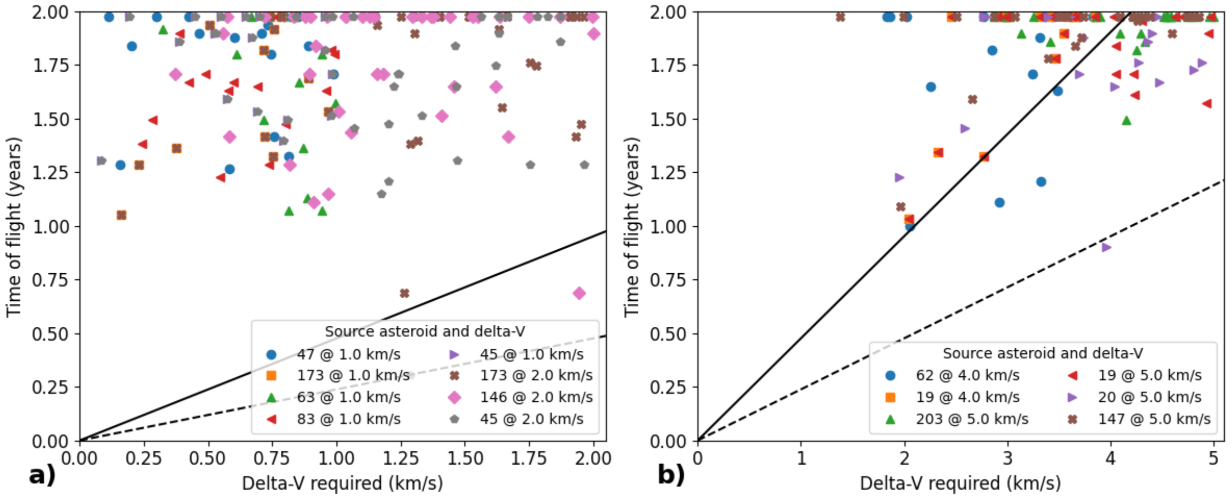

Figure 3.12: The flight time of the trajectories to the nearby large asteroids starting at the given source asteroid. The solid and dashed lines correspond to half (0.8 mN) and full (1.6 mN) thrust respectively for a 12 kg constant-mass spacecraft with the target staged electrospray propulsion system. a) For flyby. b) For orbit insertion.

and the BIT-3 system at minimum thrust (0.66 mN) are sufficient. (The full 5 W of auxiliary power is still assumed for the electrosprays at half thrust.) The orbit insertion missions to the families of (1547) Nele and (606) Brangane require the full thrust of the propulsion systems, 1.6 mN and 1.1 mN for the staged electrosprays and BIT-3 systems respectively, but are also feasible and meet the impulsive approximation. Overall, the limitations on thrust do not affect the asteroid family missions significantly.

The thrust required for the large asteroid exploration missions can be seen from Figure 3.12. Practically all destinations for flybys are feasible at half thrust and should approximate well to the impulsive trajectories. The orbit insertion missions to the large asteroids typically require the full thrust of the propulsion systems. When combined with the distance to the Sun, orbit insertion missions around the large asteroids are challenging with current technology. With thrust limitations included with the prior requirements of Table 3.3, the set of reachable large asteroids are given in Table 3.8. In the "minimum" requirement for an orbiter half-thrust is assumed because while it does not meet the science goals, such a mission is nearly feasible with current technology.

Table 3.8: The combined number of unique reachable large asteroids and spectral types for the missions in Figure 3.6 when constrained by CubeSat performance requirements on maximum distance to the Sun ($R_{\max}$) and mothership ($d_{\max}$), and propulsion capability ($\Delta v_{\max}$) and thrust ($F_{\max}$).

Mission	$R_{\max}$	$d_{\max}$	$\Delta v_{\max}$	$F_{\max}$	Asteroids	Types
Flyby min [(47) Aglaja only]	3.2 au	1.0 au	1.0 km/s	0.8 mN	19	9
Flyby max	3.8 au	2.6 au	2.0 km/s	0.8 mN	99	18
Orbit min [(62) Erato only]	3.3 au	1.4 au	3.9 km/s	0.8 mN	12	4
Orbit max	3.8 au	2.8 au	5.0 km/s	1.5 mN	71	16

Tables 3.9 to 3.13 show the system mass and volume calculations for the asteroid family exploration CubeSats in Table 3.2 when accounting for all systems, including propulsion and power. Missions are marked as feasible when the total system power is below the worst case generation, sufficient Δv is available, and the system volume is within the 8U CubeSat 10 L limit. In cases where an improvement of 20% or less is required the feasibility is marked as close and may be resolved with more detailed study or near-future technology improvements. The feasibility of each mission in terms of propulsion and power requirements is illustrated in Figure 3.13 for both the staged electrospray systems and the state-of-the-art reference. The figure shows that no missions are feasible with the state-of-the-art but that the majority of missions are feasible with the staged electrospray systems developed in this thesis. If a 50% improvement in maximum power generation is realised all of the asteroid family exploration missions are feasible with staged electrosprays in regards to power and propulsion

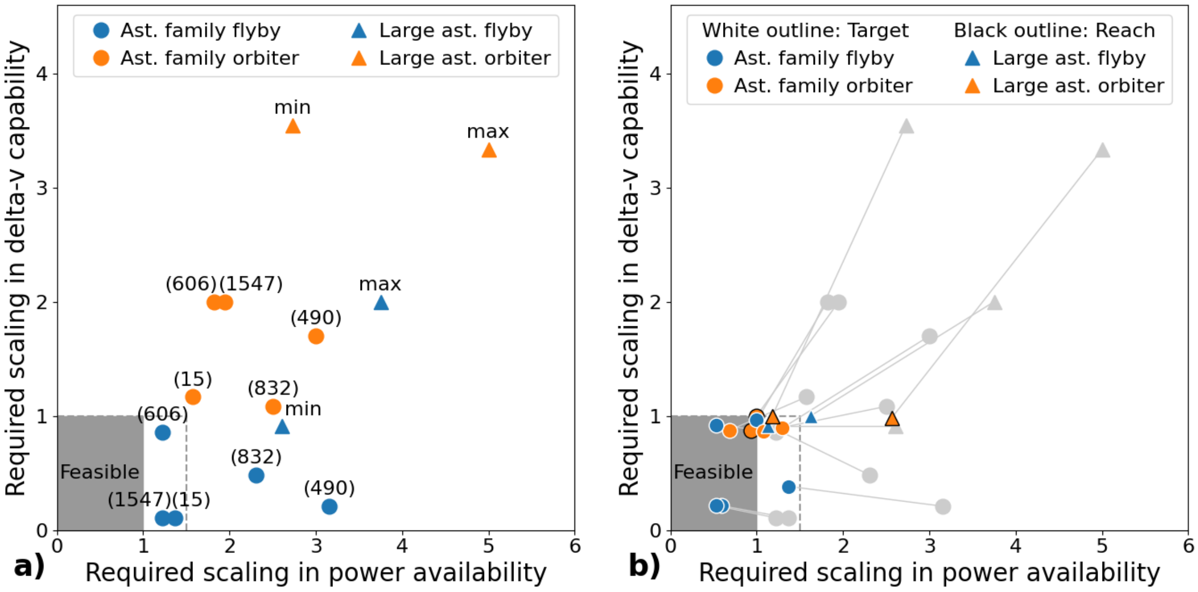

Figure 3.13: Visualisation of the feasibility of all proposed missions. The horizontal axis shows the required power compared to state-of-the-art solar panels and the vertical axis shows Δv of the propulsion system compared to the Δv the mission requires. Numbers denote the largest members for asteroid family missions while min and max refer to the large asteroid exploration missions. a) For the state-of-the-art BIT-3 gridded ion thruster. b) For the staged electrospray propulsion systems, where the outline colour denotes if the target or reach system was assumed.

requirements. The flyby and orbiter missions to the family of Enuomia (Table 3.9) are both feasible with the target staged electrospray propulsion system and presently available power systems. The CubeSats for the orbiter mission have a launch mass of 14.2 kg and therefore a swarm of up to 25 CubeSats is available in the total mass allocation. The flyby missions to the families of Brangane (Table 3.10) and Nele (Table 3.11) are also feasible with the target propulsion system and swarms up to 29 and 32 CubeSats respectively are available. Due to the high Δv requirements for orbiters to the Brangane and Nele family members, the target staged electrospray propulsion system is not feasible due to the volume limit. To reduce the volume the reach propulsion system is specified instead, after which the volumes are still above the maximum but are considered close. Swarms up to 19 and 20 CubeSats are available respectively in the mass allocation. Missions to the outer main belt families of Veritas (Table 3.12) and Karin (Table 3.13) are more challenging due to their distance to the Sun. The Karin flyby and orbiter missions can be made feasible with a slight restriction in the available targets, but the Veritas mission is difficult to reconcile as the power available needs to increase by 30%.

Due to the power available no asteroid family missions are feasible with the state-of-the-art BIT-3 comparison system. A flyby mission to the family of Brangane is possible to perform with the BIT-3 system if the available power is improved by around 22%, while all other missions require larger technology steps. For the flyby missions to the families of Enuomia and Nele the Δv requirements are low enough that a state-of-the-art chemical propulsion system may be able to perform the mission. In all cases, the launch mass of the CubeSats will be higher compared to using the electrospray systems, resulting in a commensurate reduction in the number of swarm members.

The propulsion and power calculations for the large asteroid exploration mission are given in Tables 3.14 and 3.15 and do not show feasibility with available technology. Their feasibility in terms of propulsion and power is also illustrated in Figure 3.13. The minimum requirement missions, originating at (47) Aglaja and (62) Erato for flybys and orbiters respectively, are feasible with small improvements in power availability and allow 26 and 21 CubeSats in the mass allocation respectively. The minimum flyby mission is feasible with the target staged electrospray system but the volume restriction demands the reach system for orbiters. The flyby mission originating at Aglaja meets the science goals by visiting 19 unique large asteroids across nine spectral types (B, C, Ch, D, S, Sa, T, X, and Xk), as seen in Table 3.8. While having similar feasibility constraints, the minimum orbiter mission can only reach 12 unique large asteroids across four unique spectral types (C, Ch, S, and X).[*] Significant advances in solar power technology are required for feasibility of CubeSat orbiters to a broad population of large asteroids, with more than a doubling of the maximum power available.

With the state-of-the-art BIT-3 propulsion system comparison the road to feasibility for large asteroid exploration is long, as both power technology and the overall Δv deliverable require leaps forward. A factor of three improvement in power available is necessary for the minimum requirements and for all except the easiest flyby mission the Δv needs to increase by a factor of two to four. Thanks to the dense propellant these hypothetical systems likely fit well within the volume constraints, but the mass of the CubeSat will be over 20 kg, and therefore a smaller number of swarm members fit in the mass allocation.

---

[*] As an alternative, a mission with the same requirements originating at (19) Fortuna can visit an Sk-type asteroid in addition to these, but only reaches nine large asteroids overall.

Table 3.9: CubeSat feasibility for missions to the family of (15) Enuomia. Both flybys and orbiter missions are feasible with the target staged electrospray propulsion system.

Mission	Flyby Enuomia family		Orbit Enuomia family	
Δv_{max}	0.15 km/s		1.4 km/s	
R_{max}	2.3 au		2.5 au	
α_{min}	25 W/kg		21 W/kg	
$\mathbb{P}_{\text{min}}$	44 W		38 W	
Base comp.	4.7 kg, 2.1 L		4.7 kg, 2.1 L	
Instruments	2.3 kg, 2.7 L		3.1 kg, 2.6 L	
Propulsion	**Target**	BIT-3	**Target**	BIT-3
Stages	1	-	3	-
Thrust	0.8 mN	0.66 mN	0.8 mN	0.66 mN
Total power	26 W	60 W	26 W	60 W
Prop size	1.1 kg, 1.3 L	2.9 kg, 1.6 L	2.8 kg, 2.5 L	2.9 kg, 1.6 L
Power mass	1.1 kg	2.4 kg	1.3 kg	2.9 kg
Margin 20%	1.8 kg, 1.2 L	2.5 kg, 1.3 L	2.4 kg, 1.4 L	2.7 kg, 1.3 L
Totals	11.0 kg, 7.3 L	14.8 kg, 7.7 L	14.2 kg, 8.6 L	16.3 kg, 7.6 L
Δv	0.7 km/s	1.4 km/s	1.6 km/s	1.2 km/s
Feasible	**Yes**	No ($\mathbb{P}$)	**Yes**	No ($\mathbb{P}$, Δv)

Table 3.10: CubeSat feasibility for missions to the family of (606) Brangane. Flybys are feasible with the target staged electrospray propulsion system but the orbiters require the reach system and are close to the volume limit.

Mission	Flyby Brangane family		Orbit Brangane family	
$\Delta v_{\max}$	1.2 km/s		4.0 km/s	
$R_{\max}$	2.2 au		2.2 au	
$\alpha_{\min}$	27 W/kg		27 W/kg	
$\mathbb{P}_{\min}$	49 W		49 W	
Base comp.	4.7 kg, 2.1 L		4.7 kg, 2.1 L	
Instruments	2.3 kg, 2.7 L		3.1 kg, 2.6 L	
Propulsion	**Target**	BIT-3	**Reach**	BIT-3
Stages	2	-	5	-
Thrust	0.8 mN	0.66 mN	1.5 mN	1.1 mN
Total power	26 W	60 W	41 W	80 W
Prop size	2.0 kg, 1.9 L	2.9 kg, 1.6 L	6.0 kg, 4.9 L	2.9 kg, 1.6 L
Power mass	1.0 kg	2.2 kg	1.5 kg	3.0 kg
Margin 20%	2.0 kg, 1.3 L	2.4 kg, 1.3 L	3.1 kg, 1.9 L	2.7 kg, 1.3 L
Totals	12.0 kg, 8.0 L	14.6 kg, 7.7 L	18.4 kg, 11.5 L	16.4 kg, 7.6 L
Δv	1.3 km/s	1.4 km/s	4.6 km/s	2.0 km/s
Feasible	**Yes**	No ($\mathbb{P}$)	**Close (Vol.)**	No ($\mathbb{P}$, Δv)

Table 3.11: CubeSat feasibility for missions to the family of (1547) Nele. Flybys are feasible with the target staged electrospray propulsion system but the orbiters require the reach system and are close to the volume limit.

Mission	Flyby Nele family		Orbit Nele family	
$\Delta v_{\max}$	0.15 km/s		3.8 km/s	
$R_{\max}$	2.2 au		2.4 au	
$\alpha_{\min}$	27 W/kg		23 W/kg	
$\mathbb{P}_{\min}$	49 W		41 W	
Base comp.	4.7 kg, 2.1 L		4.7 kg, 2.1 L	
Instruments	2.3 kg, 2.7 L		3.1 kg, 2.6 L	
Propulsion	**Target**	BIT-3	**Reach**	BIT-3
Stages	1	-	4	-
Thrust	0.8 mN	0.66 mN	1.5 mN	1.1 mN
Total power	26 W	60 W	41 W	80 W
Prop size	1.1 kg, 1.3 L	2.9 kg, 1.6 L	4.8 kg, 4.1 L	2.9 kg, 1.6 L
Power mass	1.0 kg	2.2 kg	1.8 kg	3.5 kg
Margin 20%	1.8 kg, 1.2 L	2.4 kg, 1.3 L	2.9 kg, 1.8 L	2.8 kg, 1.3 L
Totals	10.9 kg, 7.3 L	14.6 kg, 7.7 L	17.3 kg, 10.6 L	17.1 kg, 7.6 L
Δv	0.7 km/s	1.4 km/s	3.8 km/s	1.9 km/s
Feasible	**Yes**	No ($\mathbb{P}$)	**Close (Vol.)**	No ($\mathbb{P}$, Δv)

Table 3.12: CubeSat feasibility for missions to the family of (490) Veritas. The target staged electrospray propulsion system is sufficient for both flybys and orbiter missions, but the available power is insufficient with available technology.

Mission	Flyby Veritas family		Orbit Veritas family	
$\Delta v_{\max}$	0.23 km/s		1.7 km/s	
$R_{\max}$	3.5 au		3.4 au	
$\alpha_{\min}$	11 W/kg		11 W/kg	
$\mathbb{P}_{\min}$	19 W		20 W	
Base comp.	4.7 kg, 2.1 L		4.7 kg, 2.1 L	
Instruments	2.3 kg, 2.7 L		3.1 kg, 2.6 L	
Propulsion	**Target**	BIT-3	**Target**	BIT-3
Stages	1	-	4	-
Thrust	0.8 mN	0.66 mN	0.8 mN	0.66 mN
Total power	26 W	60 W	26 W	60 W
Prop size	1.1 kg, 1.3 L	2.9 kg, 1.6 L	3.6 kg, 3.2 L	2.9 kg, 1.6 L
Power mass	2.5 kg	5.7 kg	2.3 kg	5.3 kg
Margin 20%	2.1 kg, 1.2 L	3.1 kg, 1.3 L	2.7 kg, 1.6 L	3.2 kg, 1.3 L
Totals	12.7 kg, 7.3 L	18.7 kg, 7.7 L	16.5 kg, 9.5 L	19.2 kg, 7.6 L
Δv	0.6 km/s	1.1 km/s	1.9 km/s	1.0 km/s
Feasible	No ($\mathbb{P}$)	No ($\mathbb{P}$)	No ($\mathbb{P}$)	No ($\mathbb{P}$, Δv)

Table 3.13: CubeSat feasibility for missions to the family of (832) Karin. The target system is capable of both flyby and orbiter missions, but the power requirement is close for the orbiters.

Mission	Flyby Karin family		Orbit Karin family	
$\Delta v_{\max}$	0.58 km/s		1.3 km/s	
$R_{\max}$	3.0 au		3.1 au	
$\alpha_{\min}$	14 W/kg		14 W/kg	
$\mathbb{P}_{\min}$	26 W		24 W	
Base comp.	4.7 kg, 2.1 L		4.7 kg, 2.1 L	
Instruments	2.3 kg, 2.7 L		3.1 kg, 2.6 L	
Propulsion	**Target**	BIT-3	**Target**	BIT-3
Stages	1	-	3	-
Thrust	0.8 mN	0.66 mN	0.8 mN	0.66 mN
Total power	26 W	60 W	26 W	60 W
Prop size	1.1 kg, 1.3 L	2.9 kg, 1.6 L	2.8 kg, 2.5 L	2.9 kg, 1.6 L
Power mass	1.8 kg	4.2 kg	1.9 kg	4.4 kg
Margin 20%	2.0 kg, 1.2 L	2.8 kg, 1.3 L	2.5 kg, 1.4 L	2.9 kg, 1.3 L
Totals	11.9 kg, 7.3 L	16.9 kg, 7.7 L	15.0 kg, 8.6 L	17.2 kg, 7.7 L
Δv	0.6 km/s	1.2 km/s	1.5 km/s	1.2 km/s
Feasible	**Yes**	No ($\mathbb{P}$)	**Close ($\mathbb{P}$)**	No ($\mathbb{P}$, Δv)

Table 3.14: CubeSat feasibility for flyby missions of the large asteroids. The feasibility for the minimum mission originating at (47) Aglaja is limited by the power available, but the difference is small and may be overcome. The power gap for the maximum mission is large. The target staged electrospray propulsion system is sufficient for both flyby and orbiter missions.

Mission	Flyby large asteroids min		Flyby large asteroids max	
$\Delta v_{\max}$	1.0 km/s		2.0 km/s	
$R_{\max}$	3.2 au		3.8 au	
$\alpha_{\min}$	13 W/kg		9 W/kg	
$\mathbb{P}_{\min}$	23 W		16 W	
Base comp.	4.7 kg, 2.1 L		4.7 kg, 2.1 L	
Instruments	2.3 kg, 2.7 L		2.3 kg, 2.7 L	
Propulsion	**Target**	BIT-3	**Target**	BIT-3
Stages	2	-	4	-
Thrust	0.8 mN	0.66 mN	0.8 mN	0.66 mN
Total power	26 W	60 W	26 W	60 W
Prop size	2.0 kg, 1.9 L	2.9 kg, 1.6 L	3.6 kg, 3.2 L	2.9 kg, 1.6 L
Power mass	2.0 kg	4.7 kg	2.9 kg	6.7 kg
Margin 20%	2.2 kg, 1.3 L	2.9 kg, 1.3 L	2.7 kg, 1.6 L	3.3 kg, 1.3 L
Totals	13.3 kg, 8.0 L	17.6 kg, 7.7 L	16.2 kg, 9.6 L	19.9 kg, 7.7 L
Δv	1.1 km/s	1.1 km/s	2.0 km/s	1.0 km/s
Feasible	**Close ($\mathbb{P}$)**	No ($\mathbb{P}$)	No ($\mathbb{P}$)	No ($\mathbb{P}$, Δv)

Table 3.15: CubeSat feasibility for orbiter missions to the large asteroids. The feasibility for the minimum mission originating at (62) Erato is limited by the power available, but the difference is small and may be overcome. The power gap for the maximum mission is large. The reach staged electrospray propulsion system is required in both cases and meets the volume constraint for flybys but not orbiters.

Mission	Orbit large asteroids min		Orbit large asteroids max	
$\Delta v_{\max}$	3.9 km/s		5.0 km/s	
$R_{\max}$	3.3 au		3.8 au	
$\alpha_{\min}$	12 W/kg		9 W/kg	
$\mathbb{P}_{\min}$	22 W		16 W	
Base comp.	4.7 kg, 2.1 L		4.7 kg, 2.1 L	
Instruments	2.3 kg, 2.1 L		2.3 kg, 2.1 L	
Propulsion	**Reach**	BIT-3	**Reach**	BIT-3
Stages	4	-	7	-
Thrust	0.8 mN	0.66 mN	1.5 mN	1.1 mN
Total power	26 W	60 W	41 W	80 W
Prop size	4.8 kg, 4.1 L	2.9 kg, 1.6 L	8.2 kg, 6.7 L	2.9 kg, 1.6 L
Power mass	2.2 kg	5.0 kg	4.6 kg	8.9 kg
Margin 20%	2.8 kg, 1.7 L	3.0 kg, 1.2 L	4.0 kg, 2.2 L	3.8 kg, 1.2 L
Totals	16.8 kg, 10.0 L	17.9 kg, 7.0 L	23.7 kg, 13.1 L	22.5 kg, 7.0 L
Δv	3.9 km/s	1.1 km/s	5.1 km/s	1.5 km/s
Feasible	**Close ($\mathbb{P}$)**	No ($\mathbb{P}$, Δv)	No (Vol., $\mathbb{P}$)	No ($\mathbb{P}$, Δv)

3.2.4 Communications and navigation

Deep-space communications are challenging due to the extraordinary distances involved between the transmitter and receiver. High output power and sensitive receivers are combined with large antennas operating at high frequencies to focus the transmitted energy and make the links feasible. The link budget for Dawn to the DSN is shown in Table 3.16, which achieves a 124 kb/s downlink at a distance of 2 au. For comparison, a hypothetical case of MarCO communicating to Dawn at the same distance is shown in the table, resulting in approximately 50 dB lower received power and no possible data transmission possible. To close a useful link two things must be true: 1) sufficient power is received that the carrier can be tracked, and 2) the power to noise ratio is high enough to decode the amount of data that is being transmitted. The MarCO receiver has a specified sensitivity of −147 dBm [116] to track the carrier, which compared to the receive power from Dawn at 2 au of −183 dBm means that at least 36 dB need to be found to close a link at all and even more to have a high data rate. The gap is easily reconciled for the asteroid family flyby missions that can be performed with a maximum link range of 0.2 au (Table 3.2) and therefore reduces the space loss by 20 dB. To make up the rest with at least TLR 7 technologies the mothership can be fitted with a 3 m diameter antenna instead of the 1.5 m antenna on Dawn (+6 dB) and the frequency can be increased from X to Ka-band (+12 dB) as shown in Table 3.17. The resulting data rates are low, but because the mothership is used as a communications relay the amount of time available to transmit data is large and the science phase will already be over in a flyby.

Optical navigation (using cameras already available in the ADCS and/or payload suite) is TRL 7 and provides position and velocity accuracy on the order of 1000 km and 1 m/s based on work for M-ARGO. This accuracy should be sufficient to navigate the majority of the thrusting arc and relative optical navigation to the target asteroid is commonplace for the final segment. The optical navigation will be supplemented by periodic ranging to the mothership to calibrate any biases, where the mothership itself is assumed to be navigated using traditional Earth-based resources. If the accuracy of the optical navigation is insufficient on approach to the target asteroid it may be briefly supplemented by ranging or delta-DOR with Earth as well, where the losses due to a link distance of up to 5 au is easily compensated by the capabilities of the DSN antennas. Because the mothership is in a well determined position far away from Earth, simple ranging and Doppler measurements from the CubeSat to both sources can determine the position to high accuracy.

Table 3.16: Simplified link budgets for Dawn to the deep-space network at 124 kb/s downlink and 31 b/s uplink and between Dawn and MarCO. Values taken from Dawn and MarCO link budgets in [115, 206]. The inter-spacecraft link assumes Dawn has been reconfigured to both transmit and receive with its high-gain antenna.

Link	Dawn to DSN	DSN to Dawn	MarCO to Dawn	Dawn to MarCO
Transmit power	50 dBm	72 dBm	36 dBm	50 dBm
Transmit gain	40 dBi	67 dBi	29 dBi	40 dBi
Space loss (2 au)	−280 dB	−280 dB	−280 dB	−280 dB
Receive gain	68 dBi	7 dBi	40 dBi	7 dBi
Receive power	−122 dBm	−134 dBm	−175 dBm	−183 dBm
Noise	−185 dBm/Hz	−174 dBm/Hz	−174 dBm/Hz	−172 dBm/Hz
Power/noise	63 dBHz	40 dBHz	−1 dBHz	−11 dBHz
Data rate	51 dBHz	15 dBHz	-	-
Eb/No	12 dB	25 dB	-	-

Table 3.17: Simplified link budget for a TRL 7+ asteroid family flyby mission taking advantage of a switch to Ka-band (32 GHz) and a larger antenna on the mothership, allowing a 400 b/s link to mothership, 40 b/s link to swarm.

Link	Swarm to m-ship	M-ship to swarm
Transmit power	36 dBm	50 dBm
Transmit gain	41 dBi	58 dBi
Space loss (0.2 au)	−272 dB	−272 dB
Receive gain	58 dBi	19 dBi
Receive power	−137 dBm	−145 dBm
Noise	−174 dBm/Hz	−172 dBm/Hz
Power/noise	37 dBHz	27 dBHz
Data rate	26 dBHz	16 dBHz
Eb/No	11 dB	11 dB

3.3 Technology readiness discussion

The overall technology readiness for a CubeSat swarm to the asteroid belt ranges from high for a subset of missions, to moderate for most missions, to poor for the most difficult missions. The work in this thesis makes a major contribution towards feasibility as the target staged electrospray propulsion system based on demonstrated technology enables flyby and orbiter missions to several asteroid families that were previously infeasible. If the reach system is realised then a broad array of asteroid family orbiter missions to the inner and middle asteroid belt become feasible. If small improvements (+20%) in maximum solar array size are realised in parallel, at least one outer asteroid belt family (Karin) is feasible to explore and missions to the large asteroids are also possible. The large asteroid flyby mission originating at (47) Aglaja only requires the target propulsion system and can visit 19 asteroids across nine spectral types. A limited large asteroid orbiter mission originating at (62) Erato also becomes feasible with the reach system and the increased solar array size, but can only visit 12 asteroids across four classes and therefore does not meet the science goals.

To enable more of the large asteroid missions either the propulsion needs improvements beyond the reach system in this thesis, which are not likely anytime soon, or the constraints need to be reconsidered. The large asteroid missions are strongly limited by the maximum time of flight, so as more enduring CubeSats and longer communications ranges are enabled they become closer to reality. The trajectory optimisation is also very important, as the mothership by necessity will traverse the asteroid belt to get to the designated destination but is assumed to be static. For the asteroid families which are closely spaced the effect of this simplification is probably small, but as the large asteroids are broadly spaced it can become important. By adding the trajectory of the mothership as additional degrees of freedom the CubeSats may be dropped off closer to a large asteroid destination, but to be realistic the launch from Earth and gravity assists along the way must be considered and therefore the complexity of the analysis grows beyond the scope of this thesis.

The largest limitation is the communications distances between the mothership and CubeSats that need to be supported. For several missions the distances exceed 1 au, and therefore it is more difficult to talk to the mothership than with systems on Earth that employ huge antennas and advanced electronics. Depending on how the capacity of the DSN and associated systems evolve it may be preferred to use the mothership primarily as a means of transportation and navigation beacon, while science data is dumped directly back to Earth. To enable a 1 au link between the CubeSat and mothership with the assumptions of Table 3.17 an additional 14 dB must be found, which would require a combination of a much larger antenna, higher transmit power, and more sensitive receiver on the mothership. Such advances are both technologically difficult and would add mass to the mothership that reduces its capability as a transporter. More likely, enabling au scale links between the mothership and swarm in the future will have to come from using higher frequencies, i.e. taking the step to optical communication. Regardless of the architecture choices, autonomy will be important to reduce the frequency of interactions due to the large number of swarm members.

Chapter 4

Analysis and Design of Staged Electrospray Propulsion

Staged propulsion systems have several benefits and drawbacks compared to single-stage systems. With staging, unused mass can be shed over the duration of a mission and thrusters can be replaced to increase the total impulse and improve reliability. Simultaneously, multiple stages will increase the initial mass, volume, and complexity of a propulsion system compared to a single stage carrying the same amount of propellant. Analysing the characteristics of staged propulsion systems is therefore important to weigh the benefits and drawbacks and optimise the design towards suitable applications. Therefore, staged systems are targeted towards high Δv applications where the mass shedding becomes significant, and/or applied to core propulsion technologies where the penalty mass and volume per additional stage can be kept low. CubeSats are typically built from off-the-shelf building blocks, and staged propulsion systems can provide a further benefit here because a single design can be adapted by varying the number of stages to the required mission.

In this chapter the first complete CubeSat staged electric propulsion system is presented in detail and analysed as a part of the Staged Electrospray Pathfinder 1 (STEP-1) CubeSat project. STEP-1 aims to develop and demonstrate staged electrospray propulsion and the testing of the implementation is shown in Chapter 5. The analysis in Section 4.1 shows that scaling to the highest Δv ever in CubeSats (beyond 5 km/s) is possible and reveals which parameters are important to reach even higher performance with future work. In power-limited applications (e.g. operation in the main asteroid belt) the propulsion technology developed in this thesis also requires lower total mass than any state-of-the-art propulsion systems available for $\Delta v > 1\,\text{km/s}$ applications. The design and implementation of the system was driven by the analysis results and is detailed in Section 4.3 with validation via finite element analysis in Section 4.4 and the testing described in Chapter 5.

4.1 Analysis

This section analyses staged electrospray propulsion to calculate the performance and scaling, provide useful approximations for missions analysis, and guide future development. The staging system is described by a set of parameters, including e.g. the volume and mass fraction of each stage that is actively used for propellant and thrusters, whereby the number of stages, wet mass, and volume of the propulsion system required to meet a certain Δv can be calculated. Previous work by Jia-Richards et al. [32, 33] provide methods to estimate the system-level performance that are extended here. A sensitivity analysis unveils that the area utilisation and thruster performance are key to reduce the penalty of staging compared to a hypothetical single-stage system, which are also key to improve single-stage systems and therefore a symbiotic development path. The relatively complex expressions for the number of stages, wet mass, and volume are simplified with approximate forms that intuitively link parameters to performance and allow the staging loss factor Γ to be defined. The staging loss factor is a single-parameter characterisation of a staging system's performance relative to an idealised single-stage system and is a practical metric to define staging performance requirements and evaluate the merits of a design. With this new factor, staged electrospray systems can be evaluated to close approximation by the same methods as other propulsion systems by using an effective specific impulse ΓI_{sp}.

The performance of a baseline, target, and reach staged electrospray propulsion system is derived and compared to state-of-the-art propulsion systems available for 6U CubeSats. The baseline system assumes electrospray thruster performance readily available today and can provide large Δv capability but lags the other systems in wet mass and volume requirements. The reach system assumes that state-of-the-art demonstrated electrospray thruster performance is used and equals the state-of-the-art in wet mass for high Δv applications. Thanks to the high thrust-to-power ratio of electrospray thrusters they clearly surpass the state-of-the-art when the power system's mass is included, especially for deep-space missions where the intensity of sunlight drops.

4.1.1 Staged electrospray system mass and volume

The wet mass and total volume of a propulsion system are key high-level parameters for a propulsion system, that together with the Δv capability and operational support (e.g. electrical power) determine mission feasibility. In this section the mass and volume are considered as functions of a given mission Δv and spacecraft initial mass, m_0. The rocket equation relates Δv to the required propellant mass, m_p, depending only on the specific impulse, c, which is also the effective exhaust velocity:[*]

$$\Delta v = c \ln \frac{m_0}{m_0 - m_p} \approx \frac{c m_p}{m_0 - \frac{1}{2} m_p} \tag{4.1}$$

$$\Rightarrow \quad m_p = m_0 \left(1 - e^{-\frac{\Delta v}{c}}\right) \approx \frac{m_0 \Delta v}{c + \frac{\Delta v}{2}} \tag{4.2}$$

where the approximations come from applying the total impulse, $c m_p$, to the average mass of the spacecraft. If $\Delta v < 0.3c$ the error is a less than 1% overestimate of m_p. If N identical stages are used that have a dry mass of m_s and a propellant mass of m_p/N each the Δv capability is higher since an extra m_s of mass is removed at each staging event. For stage i the initial mass is $m_{0,i} = m_0 - (i-1)(m_s + m_p/N)$ and the Δv and propellant mass are related by:

$$\Delta v' = c \sum_{i=1}^{N} \ln \frac{m_0 - (i-1)(m_s + \frac{m_p}{N})}{m_0 - (i-1)(m_s + \frac{m_p}{N}) - \frac{m_p}{N}} \tag{4.3}$$

$$\approx \frac{c m_p}{m_0 - \frac{N-1}{2} m_s - \frac{1}{2} m_p} \tag{4.4}$$

$$\Rightarrow \quad m_p \approx \frac{m_0 \Delta v'}{c + \frac{\Delta v}{2}} \left(1 - \frac{N-1}{2} \frac{m_s}{m_0}\right) \tag{4.5}$$

where the approximation is again given by the average mass method [33]. Quantities with a prime are used to differentiate the staged case from the single stage case where they are different. If the total propellant mass in the staged case is reduced to m_p' to give the initial propulsion capability of Δv, the propellant required is given by:

$$m_p' \approx \frac{m_0 \Delta v}{c + \frac{\Delta v}{2}} \left(1 - \frac{N-1}{2} \frac{m_s}{m_0}\right) \tag{4.6}$$

which for a stage dry mass of 500 g on a 12 kg spacecraft reduces the amount of propellant required by 2% for each additional stage compared to a single large stage. Due to the extra dry mass of each stage the lowest overall mass and volume is typically achieved with a single stage system; alas N can not be selected freely. Since electrospray thrusters are still maturing the maximum impulse deliverable is limited. The maximum impulse per thruster of a given active area is $j_{\text{max}} = FL/A_{\text{em}}$, where F is the nominal thrust, L is the lifetime at nominal thrust, and A_{em} is the emitter area. Typical values of $F = 12\,\mu\text{N}$, $L = 500\,\text{h}$,

---

[*] c denotes the mass-specific impulse with units of m/s, and $I_{\text{sp}} = c/g$ will be used to denote the weight-specific impulse with units of s. The conversion factor is $g = 9.81\,\text{m/s}^2$.

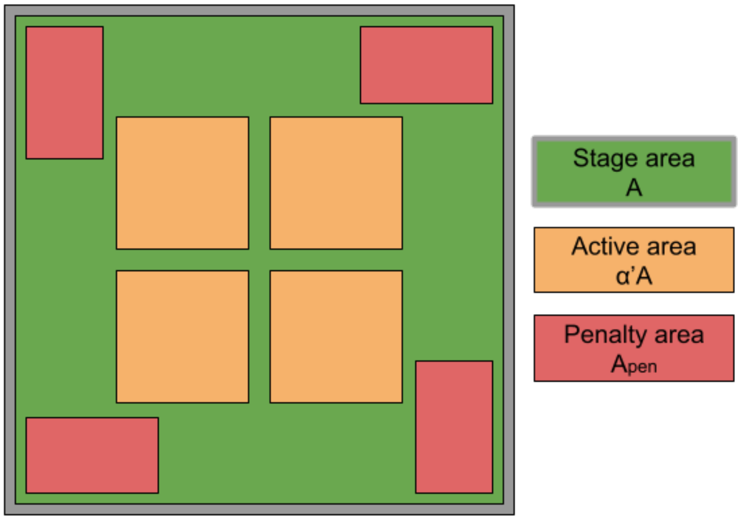

Figure 4.1: Illustration of the face area A of the thruster stage. The active area is the portion of the stage used for propellant storage and thruster emitters. The penalty area is the amount of area lost to fit the staging system, i.e. the HDRM and electrical interconnects.

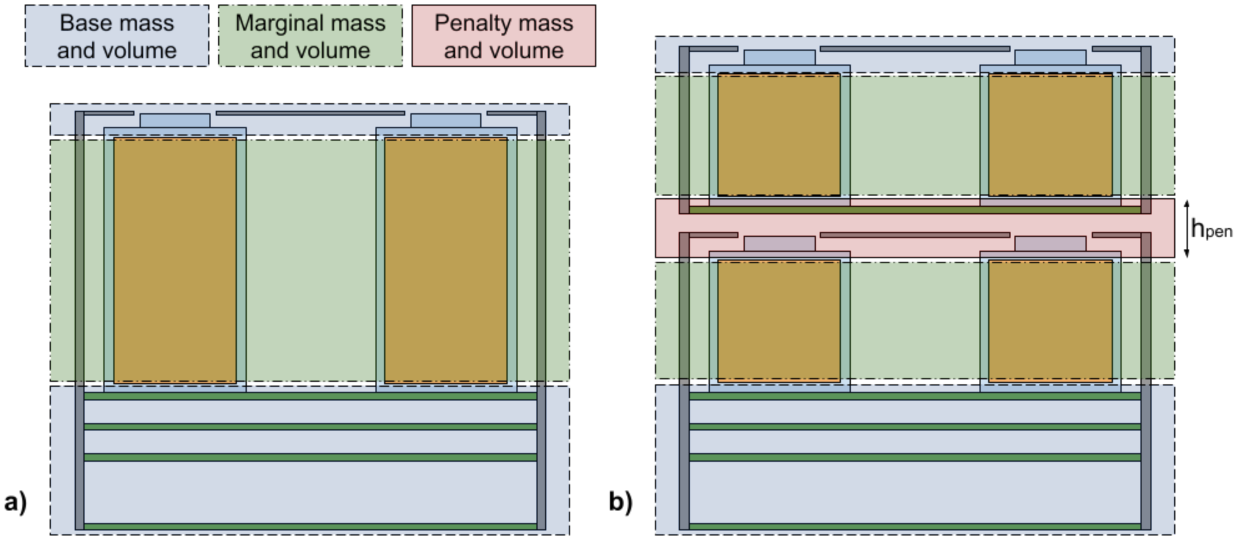

Figure 4.2: Illustration of the cross-section of two electrospray propulsion systems showing the base, marginal (propellant and related structure), and penalty mass contributions. a) A single stage system. b) A two-stage system with the same amount of propellant.

and $A_{\text{em}} = 1\,\text{cm}^2$ give $j_{\max} = 22\,\text{N}\,\text{s}/\text{cm}^2$, limiting the impulse of a $50\,\text{cm}^2$ emitter area to $1.1\,\text{kN}\,\text{s}$ (several hundred m/s on 3U CubeSat with a single stage). With a hard limit on impulse the number of stages required is given by [33]:

$$N \approx \left\lceil \frac{2m_0 + m_s}{m_s + j_{\max}\alpha' A\left(\frac{2}{\Delta v} + \frac{1}{c}\right)} \right\rceil \tag{4.7}$$

where α' is the active area fraction and A is the total face area of the stage as illustrated in Figure 4.1. The dry mass of a stage depends on how much propellant it needs to carry and therefore m_s is itself a function of N. If we assume that the stage is designed to carry the propellant mass that corresponds to the maximum impulse the thrusters on the stage can deliver, then:

$$\left(\frac{m_p'}{N}\right)_{\max} = \alpha' A \frac{j_{\max}}{c} \tag{4.8}$$

and the dry mass of each stage designed to carry the maximum amount of propellant is [32]:

$$m_{s,\max} = \gamma' \alpha' A \frac{j_{\max}}{c} + m_{\text{pen}} \tag{4.9}$$

where γ' is the structural to propellant mass fraction of the stage and the mass penalty, m_{pen}, accounts for the extra mass of e.g. the hold-down and release mechanism (HDRM) and thrusters that are repeated on each stage as shown in Figure 4.2. Restricting the analysis to cases where the stages are always the maximum size is slightly sub-optimal for intermediate cases but has a major practical benefit because a suite of optimal propulsion systems with different number of stages become available to meet a variety of needs. If we introduce the area penalty A_{pen} that accounts for the area occupied by staging hardware on each stage and the linear structural density of the stage's marginal mass λ, the marginal mass and volume fractions can be written as:

$$\gamma = \frac{\lambda}{\alpha A \rho_p}, \qquad \alpha' = \alpha \frac{A - A_{\text{pen}}}{A}, \qquad \gamma' = \frac{\lambda}{\alpha (A - A_{\text{pen}}) \rho_p} \tag{4.10}$$

where ρ_p is the propellant density and the stage dry mass becomes:

$$m_{s,\max} = \frac{\lambda}{\rho_p} \frac{j_{\max}}{c} + m_{\text{pen}} \tag{4.11}$$

The overall wet mass of a propulsion system, m_{wet}, can be expressed as the sum of a base mass m_{base}, the propellant mass, and the marginal structural mass as shown in Figure 4.2a:

$$m_{\text{wet}} = m_{\text{base}} + m_p + \gamma m_p \tag{4.12}$$

If N stages that share the propellant equally are used their dry mass and penalty terms are added [32]:

$$m'_{\text{wet}} = m'_{\text{base}} + m'_p + N\frac{\lambda}{\rho_p}\frac{j_{\max}}{c} + (N-1)m_{\text{pen}} \tag{4.13}$$

where the propellant loading per stage m'_p/N is allowed to vary to meet a desired Δv exactly but the stages are designed for the maximum propellant that the thrusters can process. The total volume of the propulsion system can analogously be expressed as a function of propellant mass though a base volume V_{base}, the propellant density ρ_p, and the marginal volume fraction α. The staged system adds a penalty volume Ah_{pen} where h_{pen} is the wasted space between each stage shown in Figure 4.2b. The volume of propulsion systems can then be expressed as [32]:

$$V_{\text{tot}} = V_{\text{base}} + \frac{m_p}{\alpha\rho_p} \tag{4.14}$$

$$V'_{\text{tot}} = V'_{\text{base}} + N\frac{A}{\rho_p}\frac{j_{\max}}{c} + (N-1)Ah_{\text{pen}} \tag{4.15}$$

where notably the volume of the staged system does not depend on the area utilisation because the added propellant is cancelled by an equal increase in thruster area to process the propellant. Using the expressions in Eqs. 4.10 and 4.11 the propellant mass and number of stages are given by:

$$(4.6) \Rightarrow \quad m'_p = \frac{\Delta v}{c + \frac{\Delta v}{2}}\left[m_0 - \frac{N-1}{2}\left(\frac{\lambda}{\rho_p}\frac{j_{\max}}{c} + m_{\text{pen}}\right)\right] \tag{4.16}$$

$$(4.7) \Rightarrow \quad N \approx \left\lceil \frac{2m_0 + \frac{\lambda}{\rho_p}\frac{j_{\max}}{c} + m_{\text{pen}}}{\alpha(A - A_{\text{pen}})\frac{j_{\max}}{c}\left(\frac{2c}{\Delta v} + 1\right) + \frac{\lambda}{\rho_p}\frac{j_{\max}}{c} + m_{\text{pen}}} \right\rceil \tag{4.17}$$

The performance of staged electrospray propulsion systems are compared to idealised single-stage systems with unlimited lifetime in Figure 4.3 using the parameters in Table 4.1. The parameters $\Delta m_{\text{base}} = m'_{\text{base}} - m_{\text{base}}$ and $\Delta V_{\text{base}} = V'_{\text{base}} - V_{\text{base}}$ account for any change in base mass to include e.g. staging control electronics. The starting point for the parameters is the STEP-1 system as implemented with the baseline system having the propellant load optimised for the thruster lifetime and a modest assumption of $\alpha = 0.5$, i.e. half of the free

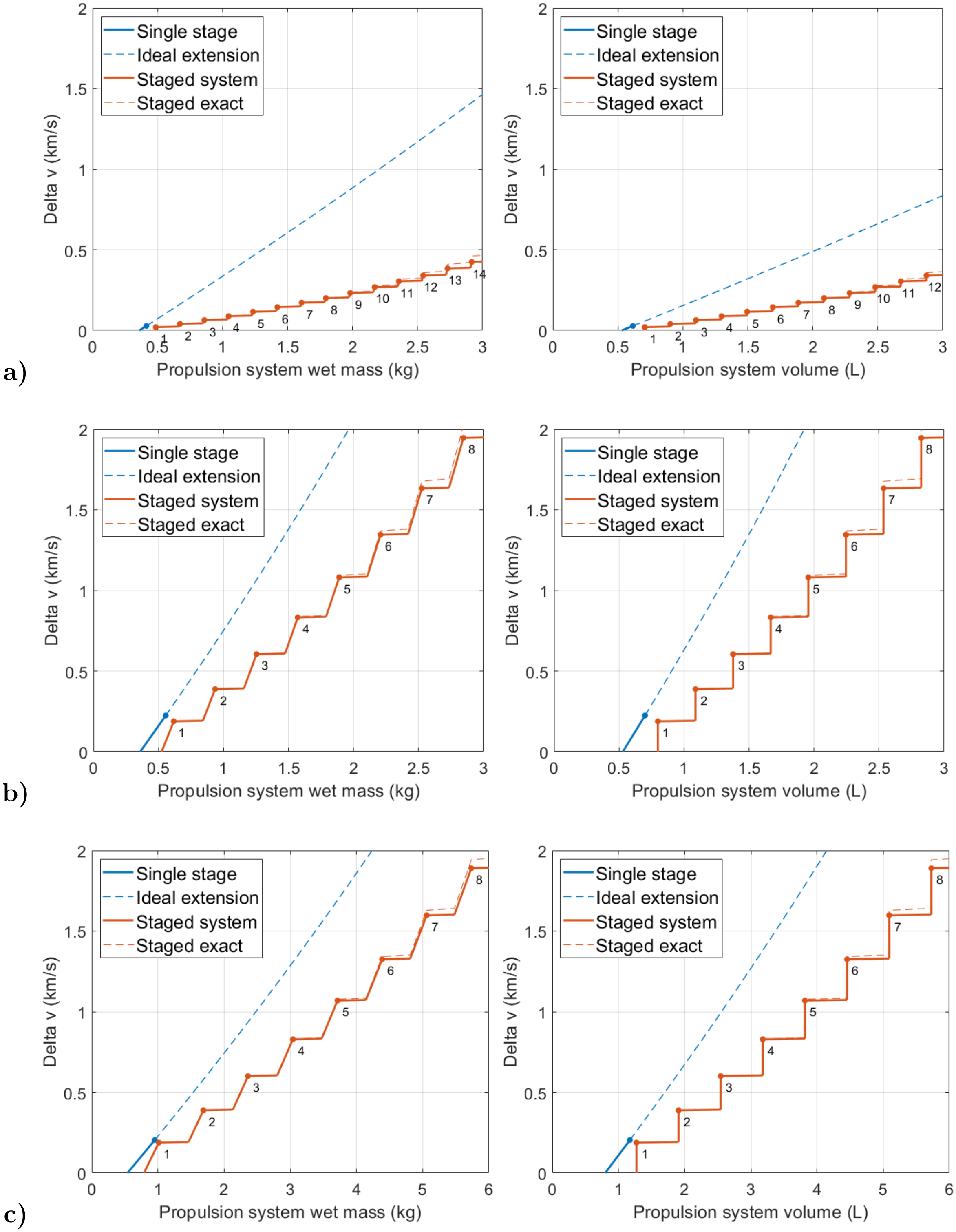

Figure 4.3: Wet mass and volume of staged electrospray propulsion systems using baseline parameters. Single-stage systems with an idealised extension assuming unlimited lifetime and the actual Δv of the staged systems from Eq. 4.3 are shown for comparison. a) 3U STEP-1 as implemented. b) 3U Baseline. c) 6U Baseline.

Table 4.1: System parameters for the staged electrospray propulsion cases separated into categories.

Category	Parameter	STEP-1 3U	Baseline 3U	Baseline 6U
Mission properties	m_0 (kg)	4	5	12
	A (cm^2)	100	100	220
	ρ_p (g/cm^3)	1.3	1.3	1.3
Structural efficiency	α	0.1	0.5	0.5
	λ (g/cm)	50	50	100
	m_{base} (g)	360	360	540
	V_{base} (cm^3)	530	530	800
Thruster properties	c (km/s)	10	10	10
	$j_{\max}$ (N s/cm^2)	10*	22	22
Staging penalties	Δm_{base} (g)	80	80	80
	ΔV_{base} (cm^3)	100	100	100
	m_{pen} (g)	140	140	280
	h_{pen} (cm)	1.2	1.2	1.2
	A_{pen} (cm^2)	15	15	15

* Limited by tank size, not thruster lifetime.

face area of each stage is actively used. These baseline parameters are selected to represent the performance capabilities of staged electrospray systems that can be built today with little effort. The scaling from 3U (A=10×10 cm^2) to 6U (A=10×22 cm^2) doubles the stages' structural and penalty masses, λ and m_{pen}, to account for the larger size and increases the base mass and volume, m_{base} and V_{base}, by a factor of 1.5 to allow a higher power PPU. The baseline 3U system compares well with the idealised single stage case, where e.g. a four-stage system capable of 0.83 km/s has a mass and volume that is around 45% more than a hypothetical single-stage system. The 6U baseline also compares well, with a four-stage system capable of 0.83 km/s requiring approximately 40% more wet mass and volume than the idealised single-stage system. The poor-performance of the STEP-1 system as implemented is expected as the development was focused on maturing staging as a technology and optimising the staging penalties in a compact and low cost package as explained in Section 4.3.

4.1.2 Sensitivity of mass and volume to parameters

To guide future development of staged electrospray propulsion the aspects of the design that have the largest impact on systems-level performance are determined with a sensitivity analysis. The parameters related to structural efficiency and thruster properties in Table 4.1 are especially interesting as they determine the performance of single stage systems and will

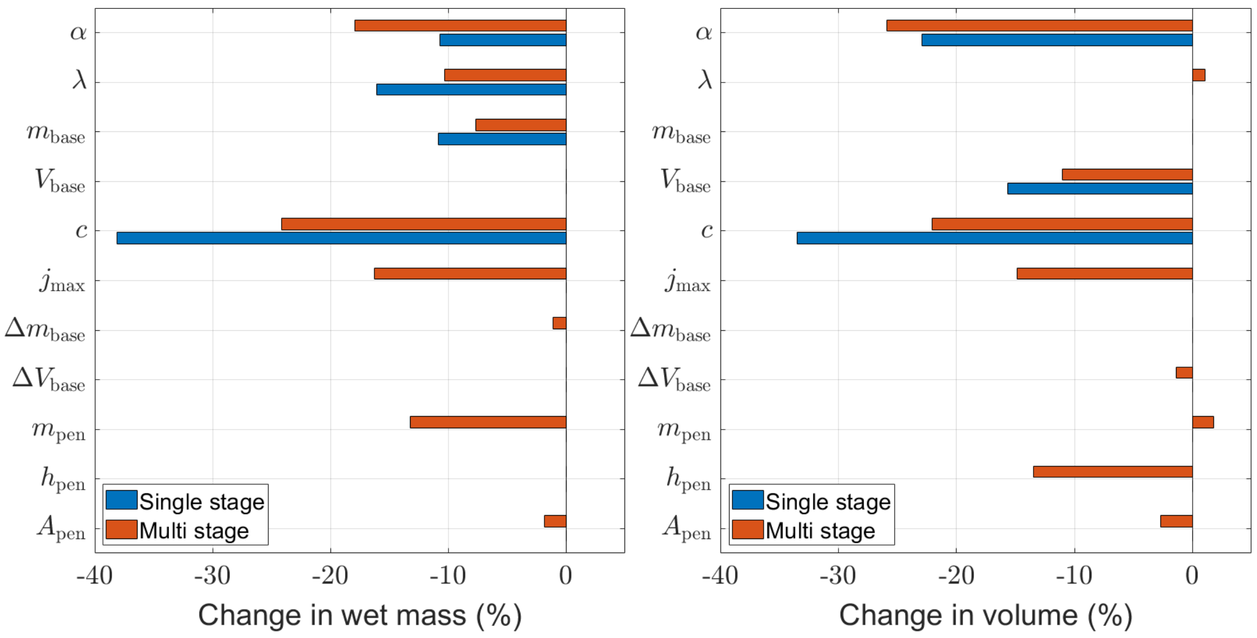

Figure 4.4: The change in wet mass and volume of the 6U baseline staged electrospray propulsion system and the idealised single stage system at $\Delta v = 1\,\text{km/s}$ when each listed parameter is improved by a factor of two.

progress without effort on the staging technology. To represent likely applications, the 6U baseline parameters are used as the starting point and the comparison is performed where Δv is fixed at $1\,\text{km/s}$. The number of stages N is allowed to be fractional to make the analysis results stable (the ceiling function of Eq. 4.17 is omitted) and for single stage systems $j_{\max}$ is assumed to be infinite to get a feasible solution. Figure 4.4 shows the change in mass and volume of hypothetical staged and single stage propulsion systems where each factor has been improved by a factor of two. All parameters were halved except for the thruster properties c and $j_{\max}$ that were doubled and α was improved to 0.75, such that the unused free face area was halved. It is clear that the most important factor for both staged and single stage systems is to improve the specific impulse, although there is a trade-off because the thrust-to-power ratio is reduced as discussed in Section 4.1.3. In two cases, λ and m_{pen}, improving the parameters cause a small increase in the propulsion system volume because each additional stage becomes less cumbersome and therefore the optimal N is larger. The volume increases are no more than a few percent when the parameters are halved and can be neglected. Note that a halving of the staging mass and height penalties is approximately equivalent to doubling the lifetime ($j_{\max}$) of the thrusters, but may be easier to implement in practice because long duration thruster testing would not be required.

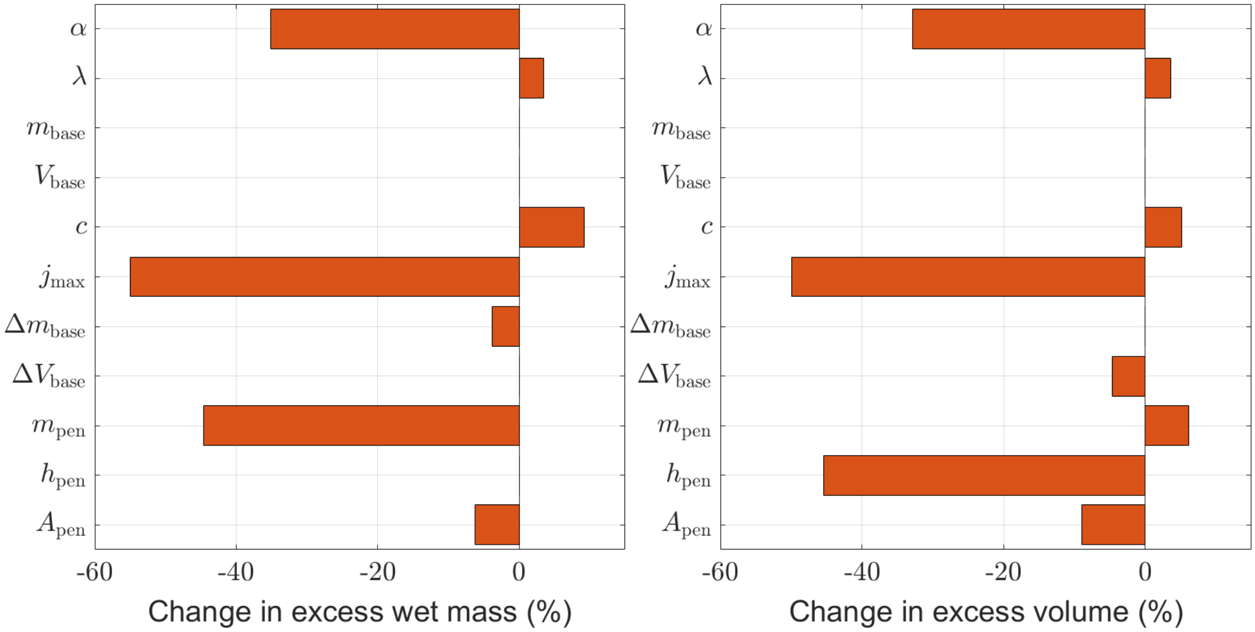

Figure 4.5: The change in excess wet mass and volume of the 6U baseline staged electrospray propulsion system over the idealised single stage system at $\Delta v = 1\,\mathrm{km/s}$ when each listed parameter is improved by a factor of two. The vertical dashed lines show the baseline mass and volume for each system.

How well staging technology itself performs can be measured by the difference in mass and volume of a staged compared to a hypothetical single-stage system that delivers the same Δv. In Figure 4.5 the mass and volume changes are given relative to the single-stage system. If the specific impulse c, which previously was shown to be the most impactful parameter, is doubled the gap between the staged and single-stage system widens by around 10%. On the other hand, improvements in thruster lifetime j_{max}, which are necessary to realise single-stage systems, close the gap aggressively and therefore as electrospray thrusters mature the excess wet mass and volume caused by the staging architecture will diminish. The figure also shows that to ensure that the gap closes over time in both mass and volume there are three important parameter to focus on: the mass and height staging penalties and the area utilisation. The mass and height penalties, m_{pen} and h_{pen}, are the primary contributors to the wet mass and volume excess, and the excess is approximately halved when the parameters are halved. The area utilisation α, which was shown to be important for overall performance, also closes the gap significantly because the number of stages required is reduced.

By developing approximations for mass and volume as a function of the system parameters a more nuanced understanding of the sensitivity can be developed. Let the number of stages in Eq. 4.17 remain fractional and keep only the leading terms in the numerator and

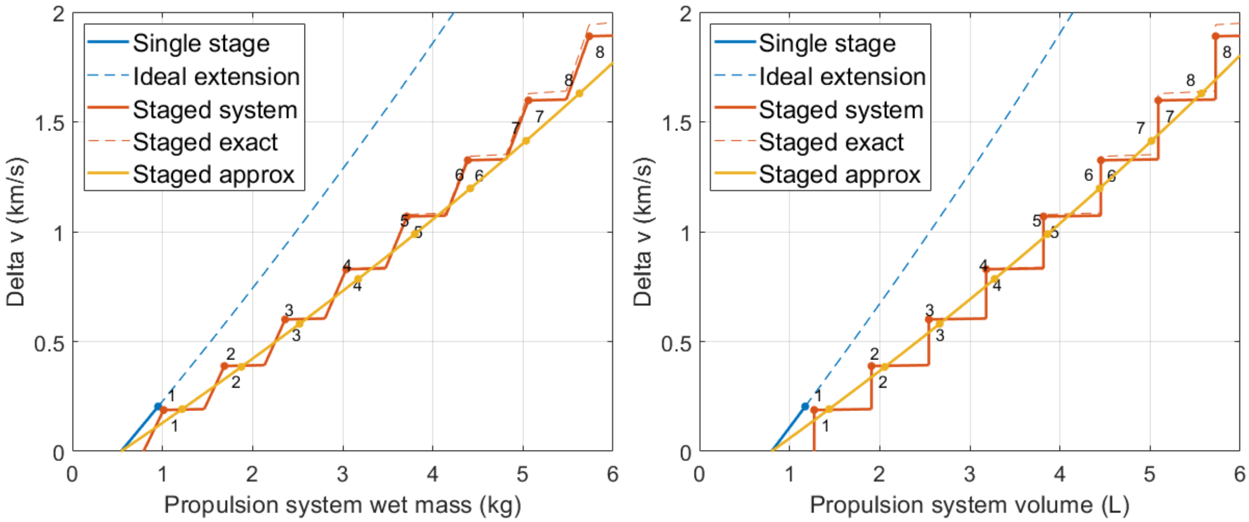

Figure 4.6: The actual wet mass and volume of the 6U baseline system and the approximate mass and volume when the effective specific impulse is used. The stage number markings for the approximation show where N takes an integer number.

denominator, then:

$$N \approx \frac{c}{\alpha(A - A_{\text{pen}})j_{\max}} \frac{m_0 \Delta v}{\left(c + \frac{\Delta v}{2}\right)} = \frac{c m_p}{\alpha(A - A_{\text{pen}})j_{\max}} \tag{4.18}$$

If this approximation is applied to Eqs. 4.13 and 4.15 and we let $m_p' \approx m_p$ the wet mass and volume can be rearranged into forms similar to exact expressions of the idealised single-stage system:

$$m_{\text{wet}} = m_{\text{base}} + m_p \left[1 + \frac{\lambda}{\alpha A \rho_p}\right] \qquad (= m_{\text{base}} + m_p \left[1 + \gamma\right]) \tag{4.19}$$

$$m_{\text{wet}}' \approx m_{\text{base}} + m_p \left[1 + \frac{\lambda}{\alpha A \rho_p} \frac{A}{A - A_{\text{pen}}} \left(1 + \frac{\rho_p m_{\text{pen}}}{\lambda} \frac{c}{j_{\max}}\right)\right] - m_{\text{pen}} + \Delta m_{\text{base}} \tag{4.20}$$

$$V_{\text{tot}} = V_{\text{base}} + \frac{m_p}{\alpha \rho_p} \tag{4.21}$$

$$V_{\text{tot}}' \approx V_{\text{base}} + \frac{m_p}{\alpha \rho_p} \frac{A}{A - A_{\text{pen}}} \left(1 + \rho_p h_{\text{pen}} \frac{c}{j_{\max}}\right) - A h_{\text{pen}} + \Delta V_{\text{base}} \tag{4.22}$$

where the two additive terms are negligible for any reasonably sized propulsion system but are included for completeness. The overall performance of the staging system can now be reduced to a single parameter, the staging loss factor Γ, by noting that the approximate wet mass and volume in Eqs. 4.20 and 4.22 only differ from the single-stage case by the factor that scales the propellant mass m_p. To account for the mass and volume effects separately, introduce the respective loss factors Γ and Γ_V:

$$\Gamma = \frac{\alpha A \rho_p + \lambda}{\alpha A \rho_p + \frac{A}{A - A_{\text{pen}}} \left(\lambda + \rho_p m_{\text{pen}} \frac{c}{j_{\text{max}}} \right)} \tag{4.23}$$

$$\Gamma_V = \frac{1}{\frac{A}{A - A_{\text{pen}}} \left(1 + \rho_p h_{\text{pen}} \frac{c}{j_{\text{max}}} \right)} \tag{4.24}$$

and write:

$$m_{\text{wet}} \approx m_{\text{base}} + \frac{m_p}{\Gamma} \left[1 + \frac{\lambda}{\alpha A \rho_p} \right] \qquad \left(= m_{\text{base}} + \frac{m_p}{\Gamma} \left[1 + \gamma \right] \right) \tag{4.25}$$

$$V'_{\text{tot}} \approx V_{\text{base}} + \frac{m_p}{\alpha \rho_p \Gamma_V} \tag{4.26}$$

to reduce the staging case to the single stage case. Since $m_p \propto 1/c$ the effect of the staging loss factor can be fully accounted for by introducing the effective specific impulse $c' = c\Gamma$ and using known propellant capacity scaling parameters of a singe-stage electrospray. The validity of the approximation is shown by a comparison at the 6U baseline in Figure 4.6. The approximations always overestimate N and neglect the gain from $m'_p < m_p$ and are therefore a slight underestimate on the actual performance.

By using the effective specific impulse the staged electrospray propulsion systems can be treated as any other during first-pass missions analysis, which reduces the threshold for infusing staged electrospray technology in the future. The two versions of effective specific impulse correct for the mass and volume of the propulsion system respectively and should be selected based on the driving design constraint. Mass is traditionally the driving constraint in spacecraft design, which is why the version without subscript applies to mass. The loss factor Γ is becomes a single parameter by which the merits of a staging design can be measured practically and requirements can be defined with. Inspecting the staging loss factors allow the results in the sensitivity analysis to be naturally understood and summarised:

1. As in the single-stage case, wet mass and volume scale linearly with the propellant mass, which itself is an exponential function of $\Delta v/c$ and is the greatest single factor that determines the size of the propulsion system.

2. The thruster parameter c/j_{max} appears in the denominator of both staging loss factors. Therefore, if the lifetime of the thrusters are improved the same amount as the specific impulse the relative gap between the staged and idealised single-stage system will be constant.

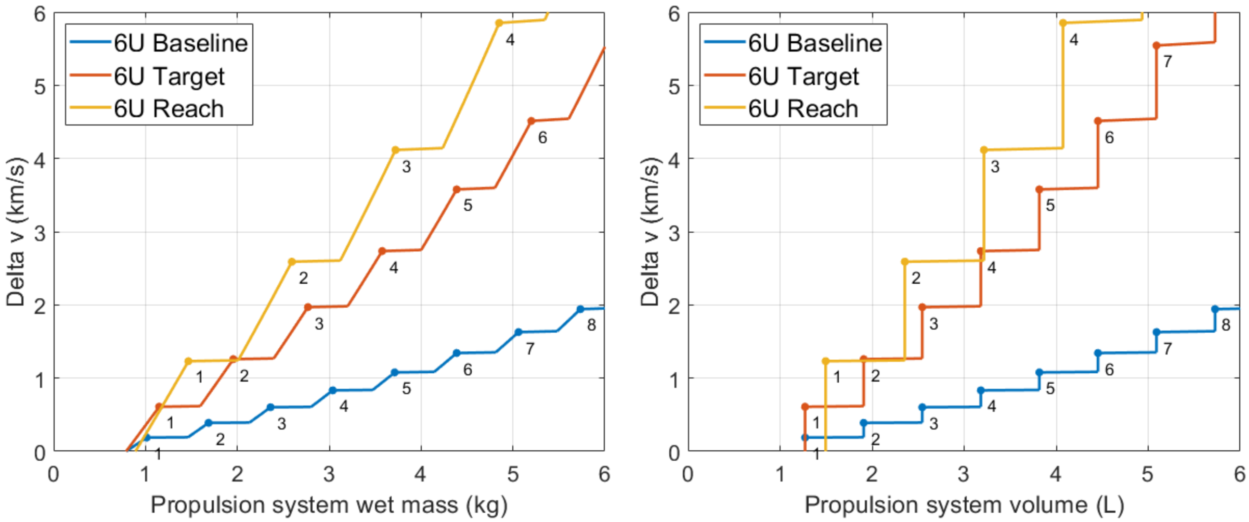

Figure 4.7: The wet mass and volume of three different 6U staged electrospray propulsion systems with the parameters given in Table 4.2. The exact Δv from Eq. 4.3 is shown.

3. The area utilisation α weakly impacts the staging loss factors, however, it scales the total contribution of structural mass and is therefore a key parameter to improve the overall performance and to close the gap between staged and idealised single-stage systems if the thrusters are unchanged.

4. The staging mass and height penalties m_{pen} and h_{pen} scale their respective loss factors directly and are key parameters to improve the design, whereas the area penalty A_{pen} only appears as a fraction of the total area and has a smaller effect.

With the sensitivity analysis complete the future development direction and potential for staged electrospray systems becomes clear. Figure 4.7 shows the system performance for the three cases given in Table 4.2 where the baseline represents the performance that is immediately available at the time of writing this thesis. Future engineering should focus on improving the area utilisation which is assumed to reach 80% in the target and reach systems. The thruster performance assumes an increase in specific impulse to the state-of-the-art demonstrated values in electrosprays [29] in the reach system, and slightly below as the target. Additionally, the lifetime is doubled as the target and quadrupled as the reach goal compared to the 500 h baseline. From these results it is clear that the staged electrospray propulsion concept can scale aggressively to a short-term target system that provides over 500 m/s Δv per stage and a longer term view towards more than 1 km/s per stage. In all cases the volume loss factor is worse than the mass ditto, so future engineering effort on the staging system should consider reducing the staging penalty height h_{pen}. The

Table 4.2: System parameters for the baseline case that is available today, and the short-term scaling target and reach systems.

Category	Parameter	Baseline 6U	Target 6U	Reach 6U
Mission properties	m_0 (kg)	12	12	12
	A (cm^2)	220	220	220
	ρ_p (g/cm^3)	1.3	1.3	1.3
Structural efficiency	α	0.5	0.8	0.8
	λ (g/cm)	100	100	100
	m_{base} (g)	540	540	540
	V_{base} (cm^3)	800	800	800
Thruster properties	c (km/s)	10	20	25
	$j_{\max}$ (N s/cm^2)	22	44	88
Staging penalties	Δm_{base} (g)	80	80	80
	ΔV_{base} (cm^3)	100	100	100
	m_{pen} (g)	280	280	280
	h_{pen} (cm)	1.2	1.2	1.2
	A_{pen} (cm^2)	15	15	15
Staging loss factors	Γ	0.57	0.64	0.74
	Γ_V	0.55	0.55	0.65

specifications of the 6U systems are summarised in Table 4.3 where additional assumptions on thruster performance for further analysis are included.

4.1.3 Comparison to state-of-the-art systems

In this section the wet mass and volume of the proposed staged electrospray systems are compared to the state-of-the-art commercially available options listed in Table 4.4. The comparison focuses on mature electric propulsion systems as they are ideal for large Δv CubeSat applications. One chemical (monopropellant) and one cold gas system are included for comparison. See the Section 2.4 of the literature review for a broader discussion of the state of propulsion for deep-space CubeSats. Figure 4.8 shows the wet mass and volume for the different systems and their Δv capability in a 12 kg 6U CubeSat. In the mass comparison all electric propulsion systems perform similarly at low Δv but the BIT-3 and staged electrospray propulsion are the only systems capable of Δv above 2 km/s and do so with comparable wet masses below 3 kg. The scalability of staged electrospray systems to even higher Δv is also seen in the figure, where almost 6 km/s is attainable with the four-stage reach system at less than 5 kg of wet mass. As expected, the chemical and cold gas systems are not competitive for high Δv applications as e.g the three-stage target system can provide over 1.4 km/s of Δv in the same volume and with 1 kg less mass than the MarCO cold

Table 4.3: Summary of specifications for the 6U staged electrospray system cases where the upper half is the outcome of the parameters in Table 4.2. In the lower half, the assumed thrust density and efficiency have been added and the system thrust and power is calculated.

Parameter	Symbol	Baseline 6U	Target 6U	Reach 6U
Active area	$\alpha(A - A_{\text{pen}})$	103 cm^2	164 cm^2	164 cm^2
Unstaged dry mass	-	810 g	810 g	910 g
Per stage dry mass	m_s	450 g	450 g	550 g
Stage prop. capacity	m'_p/N	230 g	360 g	580 g
Unstaged volume	V_{base}	1270 cm^3	1270 cm^3	1500 cm^3
Per stage volume	-	640 cm^3	640 cm^3	860 cm^3
Thrust per area	F/A_{em}	12 µN/cm^2	10 µN/cm^2	9 µN/cm^2
Total thrust	F	1.2 mN	1.6 mN	1.5 mN
Power efficiency	$\eta_{\mathbb{P}}$	30%	50%	60%
Auxiliary power	$\mathbb{P}_{\text{aux}}$	5 W	5 W	5 W
Total power	$\mathbb{P}$	25 W	37 W	36 W

Table 4.4: Specifications of state-of-the-art CubeSat propulsion systems. The minimum and maximum operating point are shown for the electric propulsion systems. All are TRL 8-9.

System	Type	m_{wet}	V_{tot}	I_{sp}	m_{p}	F	$\mathbb{P}$
Busek BIT-3 [153]	RF iodine	2.9 kg	1.6 L	1290 s	1.5 kg	0.66 mN	55 W
				2150 s		1.1 mN	75 W
ThrustMe NPT30-I2 [154]	RF iodine	1.2 kg	1.0 L	1200 s	230 g*	0.4 mN	38 W
				2450 s		0.9 mN	60 W
Enpulsion Nano R3† [156]	FEEP indium	1.4 kg	0.95 L	3500 s	220 g	0.16 mN	25 W
				2500 s		0.35 mN	45 W
Lunar FL [151]	Monoprop.	5.4 kg	2.5 L	210 s	1.5 kg*	400 mN	-
Vacco MarCO [126, 149]	Cold gas	3.5 kg	2.5 L	40 s	1.9 kg	100 mN	-

* Estimated from maximum specified I_{sp} and total impulse.

† Assuming a "gamma class" emitter for maximum performance.

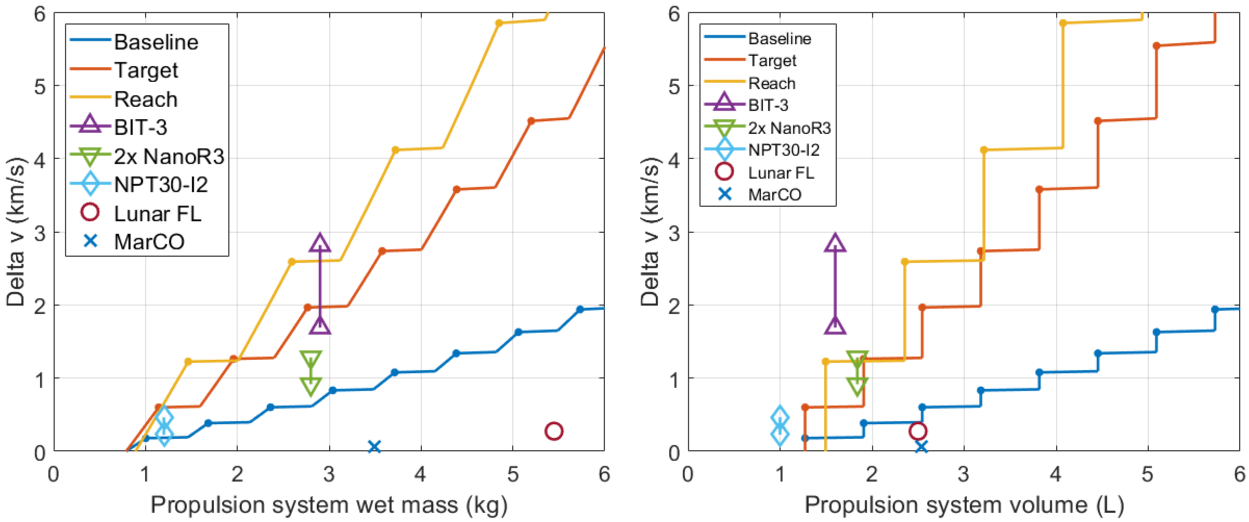

Figure 4.8: The wet mass and volume of the three 6U staged electrospray propulsion systems compared to state-of-the-art systems where the minimum and maximum operating points are connected with lines. Due to its small size and low thrust the Nano R3 system is shown where two units are used.

gas system. When the volumes are compared a weakness of the staged electrospray system is revealed as they are physically larger than the other electric propulsion options. Because the density of ionic liquid propellants are around 1.3 g/cm^3, but solid iodine and indium that are used in the other CubeSat electric propulsion systems have densities of 4.9 g/cm^3 and 7.3 g/cm^3 respectively, the larger volume is a fundamental limitation. The sensitivity analysis showed that the path towards lower volume for staged electrospray propulsion is to increase the area utilisation and thruster lifetime while reducing the staging penalty height, but it is unlikely to close the gap fully without a denser propellant.

The power required to operate electric propulsion typically drives the power system design on missions where the thrusters are planned to operate for long periods of time, as e.g. in a deep-space transfer. The power is typically generated with solar panels that are characterised by their specific power which is up to 130 W/kg is the state-of-the-art (see Section 2.3.2 of the literature review). For deep-space trajectories away from the Sun the power requirements become even more important as the incident light intensity falls as $1/R^2$. In the main asteroid belt at 2.5 au from the Sun, the state-of-the-art specific power therefore falls to 21 W/kg. Table 4.3 shows the power requirements of the staged electrospray propulsion systems, which are significantly lower than the state-of-the-art systems at comparable thrust. The reach parameters assume that the state-of-the-art thrust, specific impulse, and efficiency demonstrated for a single electrospray thruster in [29] is realised in the integrated system while the baseline roughly corresponds to the results in [152]. The power of electric propulsion

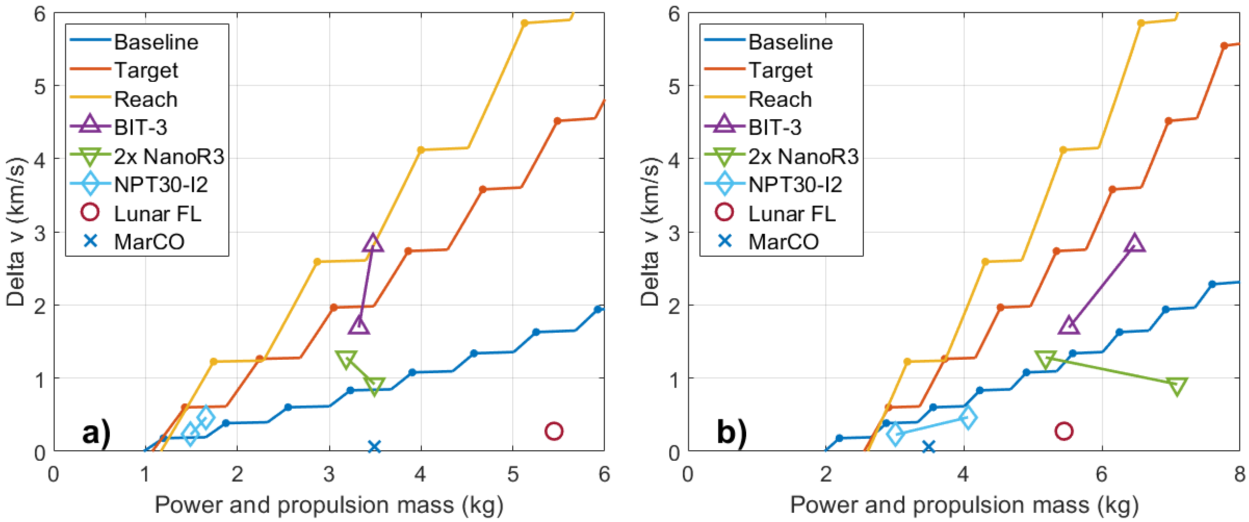

Figure 4.9: The combined wet mass and power system mass for the three 6U staged electrospray propulsion systems compared to state-of-the-art propulsion systems. a) In near-Earth operations with specific power 130 W/kg. b) In main asteroid belt operations with specific power 21 W/kg.

systems are given by $\mathbb{P} = Fc/2\eta$ where η is the efficiency and an auxiliary power draw of 5 W was added to the staged electrospray systems to account for control electronics and thermal management.[*] For reference, the STEP-1 propulsion unit draws 2.1 W of auxiliary power with the heaters at maximum power and 0.3 W without the heaters.

Figure 4.9 shows the required mass when the power system for each propulsion system is accounted for. In near-Earth operations the mass advantage of the other electric propulsion systems is reduced to roughly equal the 6U target staged electrospray propulsion system. When deep-space operations in the asteroid belt are considered the staged electrospray target and reach systems require around 1 to 2 kg less mass respectively than the best performing state-of-the-art system. Additionally, Figure 4.9b demonstrates how staged electrospray propulsion provides a broad suite of propulsion options for 0.5 to 6 km/s Δv or beyond for deep-space CubeSats with a single design implementation. Note that the power requirements for the solid propellant electric propulsion systems may increase further when cold deep-space operations are considered. The electrospray thrusters operate nominally down to around 15 °C without heaters while e.g. the BIT-3 needs 15 to 20 W to keep the propellant flowing when the chassis temperature is 30 °C, and needs more at lower temperatures [153].

---

[*] Note that if the effective specific impulse $c' = c\Gamma$ is used the efficiency must also be scaled by Γ.

4.2 Debris concerns

As staging systems release parts of the spacecraft in orbit they generate more debris than a typical mission, which may limit the practical use of the technology to regimes where the debris is either insignificant or quickly diminished. In the intended application of deep-space missions in e.g. the asteroid belt the released debris does not pose any threat due to the vast space between objects. Any planetary protection cleanliness requirements applying to the spacecraft remain regardless of the propulsion system and therefore staging does not add to the burden. Due to the number of objects released, however, the probability of unplanned impacts by components of the mission is higher. The intrinsic collision probability for objects in the main belt has been estimated to range from 10^{-18} to $10^{-17}/(\mathrm{km}^2\,\mathrm{yr})$ and the total area of the asteroid belt is estimated to be around $10^{11}\,\mathrm{km}^2$ [207], yielding a total random collision probability of 10^{-7} to $10^{-6}/\mathrm{yr}$ for the released stages. Therefore, it will take around one to ten million years for each stage to collide with another object in the asteroid belt, and much longer still before colliding with anything significant.

Using staging systems is also desired in Earth orbit for technology demonstrations or future missions but comes with clear debris limitations. A significant amount of work may be required to use staging technology safely and stay below the 5-year guideline on total orbit lifetime per mission. The empty stages generally have a poor ballistic coefficient due to mostly being empty space and deorbit in less than half the time of a typical CubeSat. Therefore, at a starting altitude below 400 to 500 km depending on the solar activity, a typical staged electrospray mission will meet the 5-year requirement.

To safely perform staging in Earth orbit the release must be controlled so that the orbit of the released stage is predictable and does not pose a collision hazard. A practical method to ensure the latter is to require that the released stages remain close to the main bus and slowly drift away. The position tracking and prediction capabilities of space surveillance systems are not published, but publicly released data suggests positions can be predicted with an accuracy of 0.5 to 2 km [127]. The relative position $\mathbf{r}(t)$ of the released stage can be calculated with the Clohessy–Wiltshire equations of motion for a release velocity of $\Delta\mathbf{v}$ as [208, p. 89]:

$$\mathbf{r}(t) = \begin{bmatrix} \frac{1}{n}\sin nt & \frac{2}{n}(1-\cos nt) & 0 \\ \frac{2}{n}(\cos nt - 1) & \frac{4}{n}\sin nt - 3t & 0 \\ 0 & 0 & \frac{1}{n}\sin nt \end{bmatrix} \Delta\mathbf{v} \tag{4.27}$$

where $n \approx 4\,\mathrm{rad/h}$ is the mean motion of the spacecraft bus and the coordinates in order are radially outward, along track, and orbit normal. Here, the effect of drag is ignored and the separation is periodic with a maximum of $\Delta v/n$ when released in the orbit normal direction, which occurs after a quarter orbit and recurs every subsequent half orbit. To keep the released stage within 1 km of the spacecraft bus with an orbit-normal release direction the maximum release velocity becomes $\Delta v \leq 1.1\,\mathrm{m/s}$. Due to the periodic nature of the relative position, however, the released stage risks impacting the spacecraft bus so some amount of along-track separation is desirable.

The difference in drag determines the minimum along-track separation drift and is given by [209]:

$$\Delta s(t) = \frac{3}{2}(a_{\mathrm{bus}} - a_{\mathrm{stage}})t^2 \tag{4.28}$$

where t is the elapsed time since separation and a_{bus} and a_{stage} are the accelerations due to drag for the bus and released stage respectively. The magnitude of drag is given by:

$$a = \frac{1}{2}\frac{\rho v^2}{b} \tag{4.29}$$

where ρ is the atmospheric density, v the orbital velocity, and b the ballistic coefficient which is approximately $200\,\mathrm{kg/m^2}$ and $40\,\mathrm{kg/m^2}$ for the STEP-1 bus and stage respectively. At a typical atmospheric density of $10^{-11}\,\mathrm{kg/m^3}$[*] the difference in acceleration is $5.7\,\mathrm{\mu m/s^2}$ (circular Earth orbit with $n = 4\,\mathrm{rad/h}$) and the separation is around 250 m after one orbit and 64 km after 24 h (c. 0.5° separation in mean anomaly). If a faster separation is desired the attitude of the spacecraft can be adjusted to give an along-track component to the initial separation velocity.

---

[*] Corresponding to 280 to 440 km altitude depending on solar activity in the 2012 COSPAR atmosphere.

4.3 Design and Implementation

The results of the sensitivity analysis in Section 4.1.2 determined the design drivers for the implementation presented here, dubbed the Staged Electrospray Pathfinder 1 (STEP-1). The thrusters' specific impulse and lifetime are the two most important parameters, followed by how efficiently the available area of each stage is used (i.e. the tank design and thruster packaging). These parameters are also key to single-stage systems and therefore requirements were imposed that ensure the thruster interfaces are identical in the staged system. With this selection, the thruster and tank development is decoupled from the staging system and parallel advances can contribute immediately to overall system performance. Thanks to the decoupling there is also no need for the staging demonstrator to maximise the capabilities of each stage, instead, the cost and timeline for developing STEP-1 was reduced by using a thruster design, configuration, and power processing unit (PPU) from a previous generation single-stage system similar to what is shown in Figure 2.7. Additionally, to implement the desired scalability and practicality, requirements are added so that the number of stages is unlimited and all intermediate stages are identical:

1. The staging shall be "invisible" to the thrusters and power processing unit.
2. The stages shall use standard thruster mechanical and electrical interfaces.
3. The number of stages possible shall be unlimited.
4. All stages shall be identical, except for the fixed last stage and the first stage.

The mass and height penalties per stage were found to be the most important parameters in the staging analysis that are not directly related to the thrusters. Therefore, the selection of the hold-down and release mechanism (HDRM) and detailed design focus on minimising these parameters. To meet requirement 2 the basic design of each stage is fixed to having a standard 1.6 mm printed circuit board (PCB) for thruster mounting and a grounded shield between the thruster heads. To ensure no ambient plasma "leaks" in to the high-voltage electronics the maximum distance between grounded areas on the stages is set to 2 mm, which is smaller than the Debye length in low Earth orbit [210]. A simple hard-anodised aluminium frame with a 2 mm wall thickness designed for easy manufacturing was selected to connect the PCB and the shield and act as the external structure, shown in Figure 4.10. To meet requirement 3 a three-stage design was implemented where the middle stage can be repeated any number of times. All stages are implemented on the same PCB design with different components populated and all stage frames are identical except for the mounting

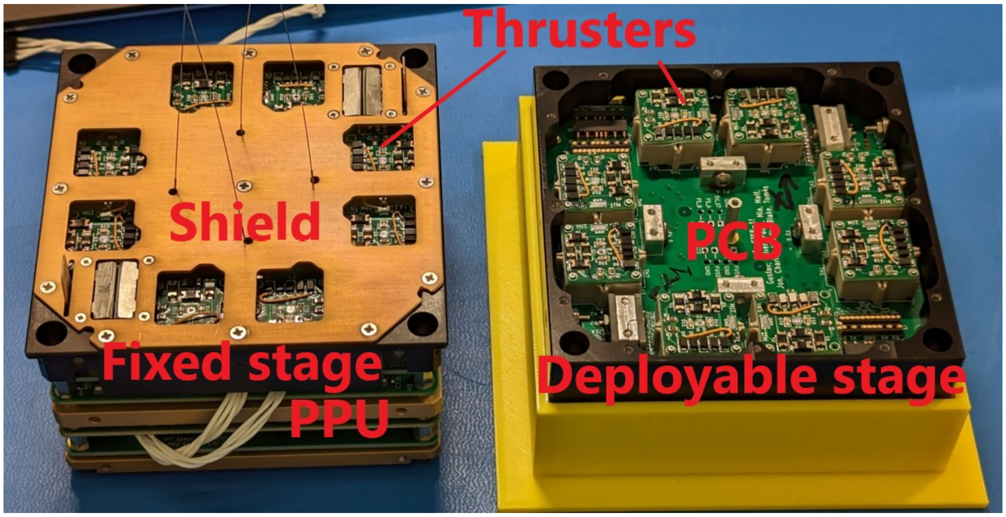

Figure 4.10: Picture of the fixed third stage with the PPU stack mounted below and the deployable second stage with the shield removed for visibility. Thruster emulators are mounted on the stages. Actual thrusters fill the shield apertures with their extractor grids flush to the bottom of the shield.

interface to the spacecraft bus on the fixed stage and the CubeSat "feet" on the first stage, exceeding requirement 4.

The staging system also needs to be compatible with the CubeSat specifications and implement sufficient safety and redundancy to be approved for flight. The following set of requirements were derived in the STEP-1 flight project to be allowed to fly the system:

5. The HDRM shall be redundant, such that two or more actions or faults are required for separation.
6. The staging system shall have a method to test the integrity of the HDRM.
7. The separation speed of the released stage shall be no more than 1.1 m/s (see Section 4.2).
8. A visual method shall be provided to confirm that the HDRM is inert before integration.

With the base design of the stages set and the carried-over thruster design several parameters of the staging system in Table 4.1 are constrained before the design details are considered. The thrusters fix the thruster properties, propellant density, ρ_p, and area utilisation, α', while the PPU and stage design set the base mass, volume and linear density, m_{base}, V_{base}, and λ. Additionally, by accounting only for the mass of the PCB, a thin shield, and the thruster tops and bottoms the mass and height penalties are unavoidably at least $m_{\text{pen}} \geq 100\,\text{g}$ and $h_{\text{pen}} \geq 8\,\text{mm}$. The primary goal of the design of the staging system is

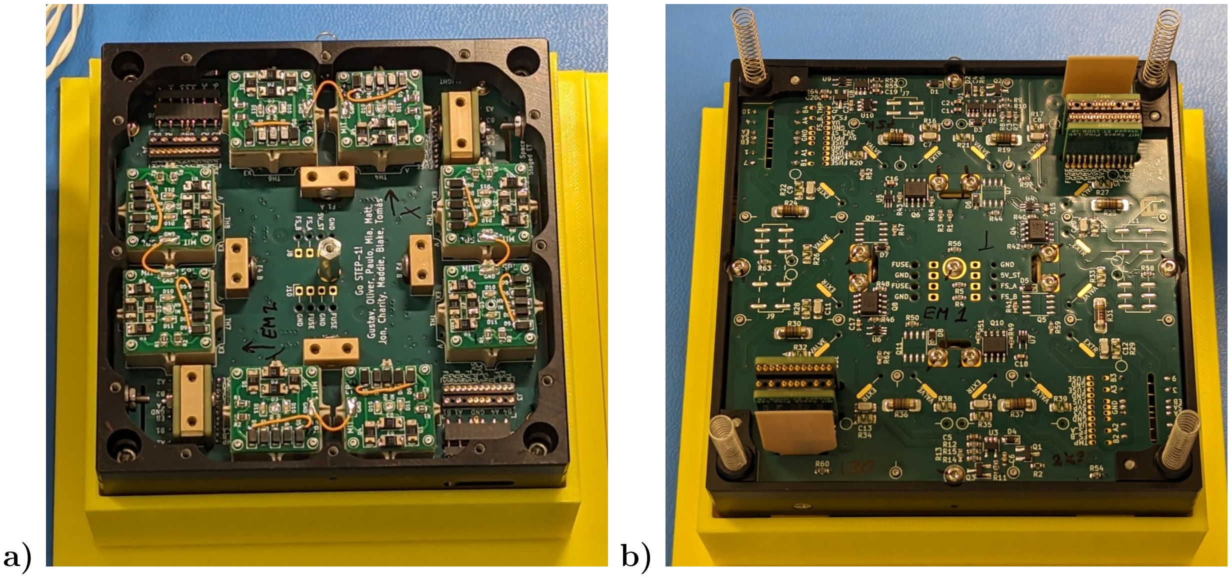

Figure 4.11: Photographs showing the mating interface between the stages. a) Top side of a stage with the shield removed for visibility. The four small blocks near the middle are the attachment points for the hold-down wires. The corner pockets have a shallow conical angle and a pocket to house the separation springs. b) Bottom side of a stage. The mating conical interfaces and the bonded separation springs are clearly visible in each corner.

therefore to minimise the excess in these two penalties, with secondary goals to minimise the area penalty and base mass deltas: A_{pen}, Δm_{base}, and ΔV_{base}.

The design of the staging system is separated into four sections: the HDRM that mates and releases the stages, the electronics that route signals and controls the separation, an analysis of cold welding risks, and the thermal control. The final design was validated with finite element analysis in Section 4.4 and tested in Chapter 5. The contributions to the staging penalty terms for the implemented design are summarised in Table 4.5.

Table 4.5: Contributions to the staging penalty terms in Table 4.1 for the STEP-1 design.

Penalty	m_{pen}	h_{pen}	A_{pen}	Δm_{base}	ΔV_{base}
Unavoidable	100 g	0.8 cm	-	-	-
HDRM	20 g	0.4 cm	$3\,\text{cm}^2$	-	-
Electronics	20 g	-	$12\,\text{cm}^2$	80 g	$100\,\text{cm}^3$
Total	140 g	1.2 cm	$15\,\text{cm}^2$	80 g	$100\,\text{cm}^3$

4.3.1 Hold-down and release mechanism

The HDRM concept selection was previously studied [30] and demonstrated as a proof-of-concept in a vacuum environment [31] by Jia-Richards and Lozano. A simple miniature

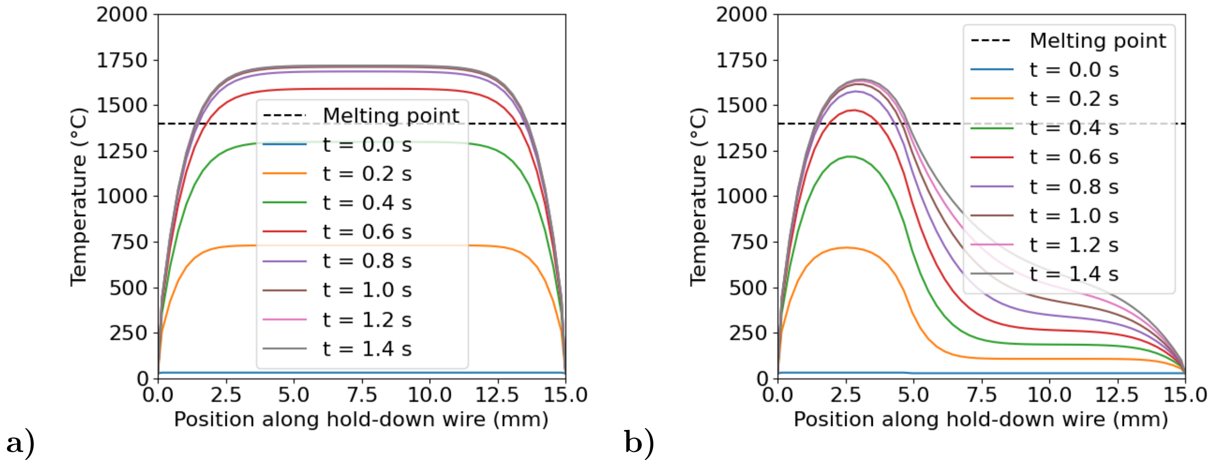

Figure 4.12: Simulated temperature rise of the hold-down wire with a current of 7 A. a) With the whole wire exposed. b) With a sleeve covering everything except 5 mm.

fuse wire mechanism [211] using 304 stainless steel was selected because of its compactness and high load carrying capacity, while avoiding potentially hazardous technologies such as pyrotechnics. The first generation design in [30] was based on a set of ceramic standoffs connecting each stage PCB with a separation spring and fuse wire nested inside that would separate when a current was passed through them. The STEP-1 design kept the overall concept but made several improvements to the design, with the new interface shown in Figure 4.11. First, the hold-down wires were moved from inside standoffs to independent blocks on the stage PCBs to allow a smaller stage height and a stronger metal-on-metal interface between the stages. The total of four wires were kept to spread the load and meet requirement 5 for redundancy, adding 3 cm^2 to the staging area penalty. Second, the standoffs were replaced with mating features directly integrated with the external walls creating a strong single-piece frame. Third, the mating interface was made conical to resist horizontal forces. Other HDRM options were also considered for the second-generation staging system, but all were determined to have a larger stage mass penalty than the fuse wire approach which adds no more than 10 g to the stages between the four small blocks, integrated mating features, and control electronics. The load put on the PCB by mounting the hold-down wires inboard caused excessive deflection when the initial design was analysed. To stiffen the structure the shield was made thicker and connected to the PCB as discussed in Section 4.4.2, adding another 10 g for a total of 20 g in staging penalty due to the HDRM design. 4 mm of dead space is added between the stages to the height penalty to fit the thicker shield and mating cones on the bottom side of the PCB.

The components of the HDRM were dimensioned by considering the loads that are experienced in a launch and the dynamics of separation. The hold-down wire diameter of

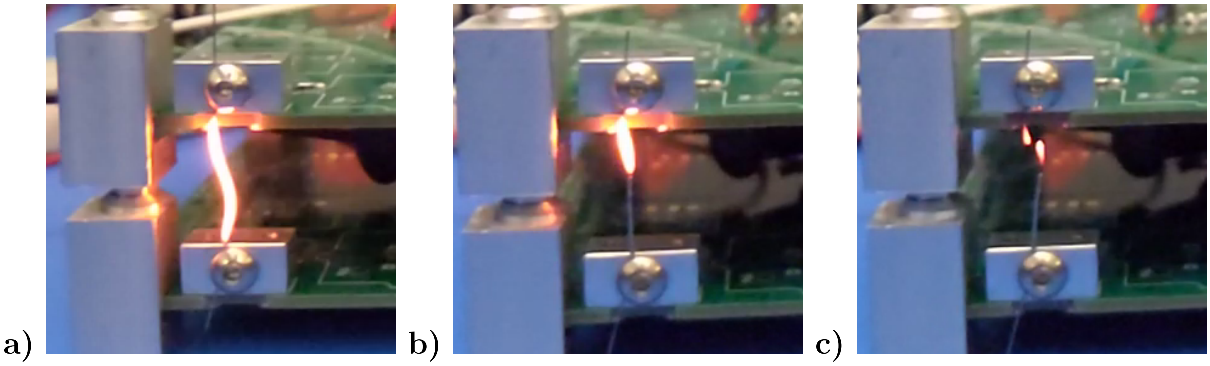

Figure 4.13: Photographs of untensioned hold-down wires fusing at 6 A current. a) 15 mm long wire without a sleeve. b) Same wire with 9 mm sleeved. c) Sleeved wire after breaking.

0.25 mm was selected by performing finite element analysis on the staging system with a worst-case loading, see Section 4.4. The heating of the hold-down wire with radius r due to a current I can be modelled by the one-dimensional heat equation, where the temperature $u(t, x)$ evolves due to diffusion, radiation, and Joule heating as:

$$\rho_m c_p \frac{\partial u}{\partial t} = k \frac{\partial^2 u}{\partial x^2} - \frac{2\sigma}{r}\left(u^4 - u_0^4\right) + \frac{\rho_R I^2}{\pi^2 r^4} \tag{4.30}$$

with mass density $\rho_m = 8000\,\mathrm{kg/m^3}$, heat capacity $c_p = 500\,\mathrm{J/(kg\,K)}$, conductivity $k = 16\,\mathrm{W/(m\,K)}$, resistivity $\rho_R = 7.0 \times 10^{-7}\,\Omega\,\mathrm{m}$, and the Stefan-Boltzmann constant $\sigma = 5.67 \times 10^{-8}\,\mathrm{W/(m^2\,K^3)}$. The initial condition and boundary conditions were set to $u_0 = 300\,\mathrm{K}$ but the results are insensitive to the chosen temperature. The current gives the steady state temperature as:

$$u_{\max}^4 = \frac{\rho_R I^2}{2\pi^2 \sigma r^3} + u_0^4 \tag{4.31}$$

which was set to 2000 K to guarantee the wire is heated above the melting point of steel, yielding a required current of 7 A per wire. The thermal mass of the wire determines the time to reach the melting point, which is approximately 0.5 s as shown in Figure 4.12a. The location along the wire that heats up and separates can be controlled by the strong inverse dependence on radius in Eq. 4.30, which also reduces the energy expenditure. In [211] the heating location was controlled by selectively thinning the wire, but we instead add a sleeve to the wire where heating should be reduced. A thin tube of stainless steel that approximately triples the cross-sectional area is crimped to the hold-down wire and the segment to be heated is left exposed. The final exposed length was set to 5 mm as it was the shortest exposed segment that did not significantly impact the peak heating, shown in Figure 4.12b. Figure 4.13 demonstrates the effect of adding the sleeve and shows how, with only the desired segment heated, the wire is severed cleanly in a predictable location.

Note that a tensioned wire will break suddenly when is begins to yield in the heated region as the wire is stretched, which reduces the radius r and causes runaway heating according to Eq. 4.30. To ensure the hold-down on the stages remains approximately symmetric the wires are fused in pairs, requiring a total of 14 A. The resistance for a pair of sleeved wires, including PCB traces and harnessing, is up to 200 mΩ and the staging control electronics are required to be able to supply the output current for 1 s to give margin.

The separation springs were selected to guarantee a separation speed of less than 1 m/s to meet requirement 7. The final stage mass was estimated to be at least 180 g and therefore the total separation energy was limited to 90 mJ. The spring-loaded electrical connectors add 15 mJ, see Section 4.3.2, leaving a budget of 75 mJ of stored energy in the separation springs. To ensure the springs are the last point of contact between the stages the stroke was set to 16 mm. Off-the-shelf springs with a rate of 110 N/m and a relaxed length of 25 mm were selected, for a stored energy of 56 mJ. The total stored energy is (71 ± 9) mJ when an uncertainty in the separation spring rate of 10% and an uncertainty in the electrical connector compression of 20% is assumed. The total separation energy when accounting for the highly uncertain drag of the electrical interrupter (see Section 4.3.2) is (54 ± 21) mJ as shown in Table 4.6 and the expected separation velocity is 0.59 to 0.89 m/s for a 190 g stage. To keep the springs from buckling they are constrained in pockets and to avoid unnecessary debris they are bonded with epoxy to the bottom side of each stage as shown in Figure 4.11.

Table 4.6: Estimate of the total separation energy with uncertainties for the STEP-1 HDRM.

Component	Separation energy
Separation springs	$+(56 \pm 6)$ mJ
Electrical connector	$+(15 \pm 3)$ mJ
Interrupter drag	$-(17 \pm 12)$ mJ
Total	(54 ± 21) mJ

The conical interface of the stage has a risk of sticking when forced together as the shallow angle θ creates a large normal force due to mechanical leverage, potentially acting as a wedge. If the interface is deformed or the friction arising from the normal force cannot be overcome the stage may fail to separate. Figure 4.14 illustrates the forces that arise in the interface when an externally applied force F (e.g. from the wires of the HDRM or acceleration during launch) pushes the interface together:

$$F = N\sin(\theta) + \mu N\cos(\theta) \quad \Rightarrow \quad N = \frac{F}{\sin(\theta) + \mu\cos(\theta)} \tag{4.32}$$

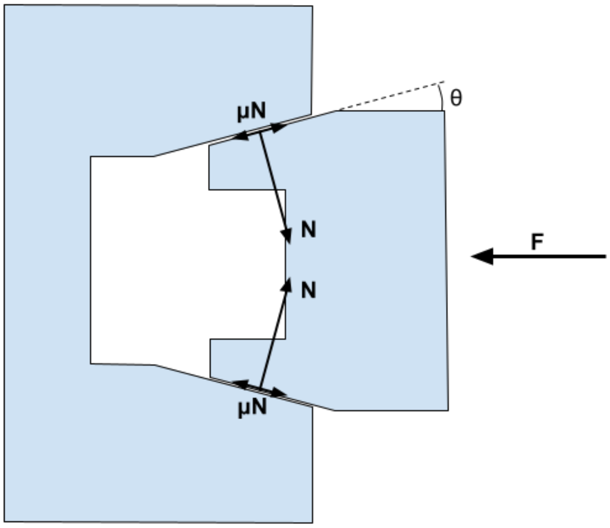

Figure 4.14: Illustration of the forces acting on the stage mating interface.

If the applied force is reduced, the interface will slide apart again if:

$$F < N\sin(\theta) - \mu N\cos(\theta) \quad \Rightarrow \quad \mu < \tan(\theta) - \frac{F}{N\cos(\theta)} \tag{4.33}$$

where $\mu < \tan(\theta)$ is required to guarantee that the stage will separate when the external force is removed ($F = 0$, i.e. the HDRM is released). This is recognised as the condition for the critical angle of an inclined plane where an object will slide, $\theta_c = \arctan(\mu)$. The hard anodised mating interface has a low coefficient of friction of 0.1 to 0.2 [212] (measured dry against steel, friction data against itself was not found) yielding a θ_c of 6° to 11° which determines the minimum cone angle. The maximum cone angle and cone depth were determined to ensure the electrical contacts can not cross due to lateral movement during separation to 26° and 1.5 mm respectively, see Section 4.3.2. 15° was selected as the cone angle as appropriate cutting tools (30° included angle) are readily available and fall within the two values to guarantee no interface sticking and keep the electrical signals in order. Section 4.5 includes two measurements of the actual friction on the manufactured parts resulting in critical angles of $(14.2 \pm 2.2)°$ and $(9.6 \pm 1.8)°$, which was unexpectedly high and thus the margin for frictional sticking is smaller than desired or possibly non-existent. During the extensive testing reported in Chapter 5 and prior prototyping no sticking was ever observed, but it may be wise to increase the cone angle to 22.5° (45° included angle) for any derivative designs to give adequate margin. A possible remedy without adjusting the geometry is to coat one side of the interface with a thin layer of polytetrafluoroethylene (PTFE) or another low-friction coating to reduce the coefficient of friction and restore the margin. However, detailed testing and analysis would be required as e.g. the cold flow properties of PTFE may cause the coating itself stick the parts together over time.

The large normal force or wear from thermal cycling may also cause failure and sticking of the interface. With $\theta = 15°$ and a coefficient of friction $\mu = 0.15$ the normal force is $N \approx 2.5F$. The design static load is 320 N, which in addition to the HDRM tension of 120 N yields $N \approx 1.1$ kN spread over the 140 mm^2 total mating area. The resultant interface pressure of 8 MPa is significantly lower than the hardness of hard anodised aluminium of 4.5 GPa [212] and therefore there is no concern that the static load could deform the interface causing it to stick. Thermal cycling could induce the sticking phenomena with the same condition in Eq. 4.33 as for an external force when the parts grow or shrink. Because the parts are the same material any significant difference in thermal expansion is due to a difference in temperature. Cyclic sliding of the interface could wear the materials and increase friction over time, eventually causing them to stick. For the hard anodised surface the friction increases with total sliding on the order of 10 m [212]. As a worst-case analysis, assume that thermal cycling of 40 °C occurs sequentially for the stages. The finite element analysis in Section 4.4.4 shows that the worst case displacement of the interface is 12 µm, which for a 90 min orbit cycle would require over 70 years to produce significant wear.

4.3.2 Electronics

The staging electronics perform three main tasks: routing signals and power to the stages, activating the exposed stage to operate, and providing the energy to operate the HDRM. To ensure the stages separate cleanly, a specific “break and make” sequence is enforced:

1. All hold-down wires separate (<0.5 mm separation).
2. The connections to the released stage break (c. 1 mm separation).
3. The newly exposed stage is activated (c. 2.5 mm separation plus 5 s delay).

During the HDRM wire fusing sequence the stage moves as the wires thermally expand and therefore some compliance is required by the interstage connectors. Spring-loaded pogo-pin connectors were selected and configured to allow at least 1 mm of vertical movement of the stage before disconnecting; ensuring the wires break first. Miniature connectors with a pitch of 1.3 mm were chosen conserve space, and for the high-voltage connections intermediate pins were removed to give sufficient clearance. Two independent interstage connectors are installed on opposite corners as seen in Figures 4.11 and all signals except for the thruster channels are routed through both for redundancy. Each interstage connector has 20 contacts: four high-voltage thruster pins, two thruster extractor pins, five ground pins, three fuse

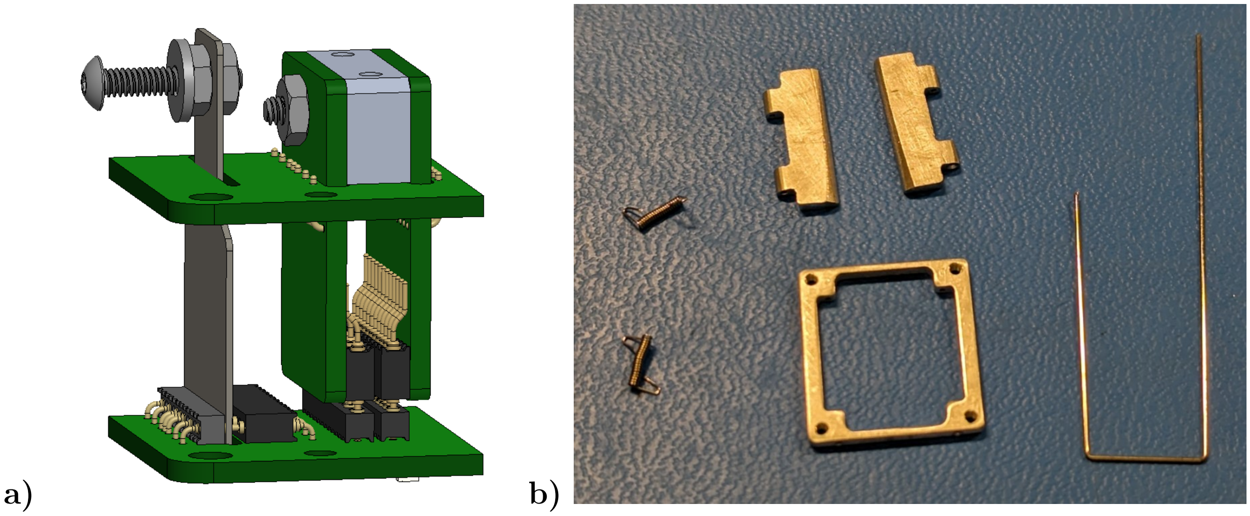

Figure 4.15: Details of the interstage system and shield door. a) The interrupter sheet and connector besides the daughterboards with the interstage connector. b) Parts prepared for shield door assembly.

current pins, and six control signals and is shown in detail in Figure 4.15a. Multiple pins (six in total) are used for the fuse current because the connectors are rated to 3 A each but 14 A is required by the HDRM. The sideways movement of the pins are limited to no more than 0.5 mm by the mating cone angle to remove the risk of cross-connections and short circuits during separation. Each pin has a preload of 0.25 N and a spring rate of 250 N/m, therefore the 40 pins add a combined 20 N of separation force as a small "kick" when separation begins. Small spring-loaded doors shown in Figure 4.15b allow the interstage connectors to pass through the shield and close after separation to block the ambient plasma.

The electrical circuits are routed as a continuous "bus" from the fixed stage up though all stages, and each stage is physically inhibited from operating by the presence of a stage above. The high-voltage thruster connections and an activation signal pass through a connector dubbed the interrupter, shown in Figure 4.15a, that is held open by the stage above. An insulating sheet is added between the spring-loaded pins of the interrupter connector that is removed with the stage above during separation, allowing the contacts to mate. To ensure that the subsequent stage HDRM is not inadvertently actuated a 5 s delay is built in to the stage activiation circuit and the HDRM output power is only enabled for 1 s. Only the physical motion of the stage separation controls the stage activation, making the system "invisible" to the thusters and PPU and also allowing any number of stages to be added, as requirements 1 and 3 demand. The sheet extends 2.5 mm below the connector to guarantee that the deployed stage is disconnected before the newly exposed stage is activated. The interrupter design was selected to minimise the staging penalty height at the

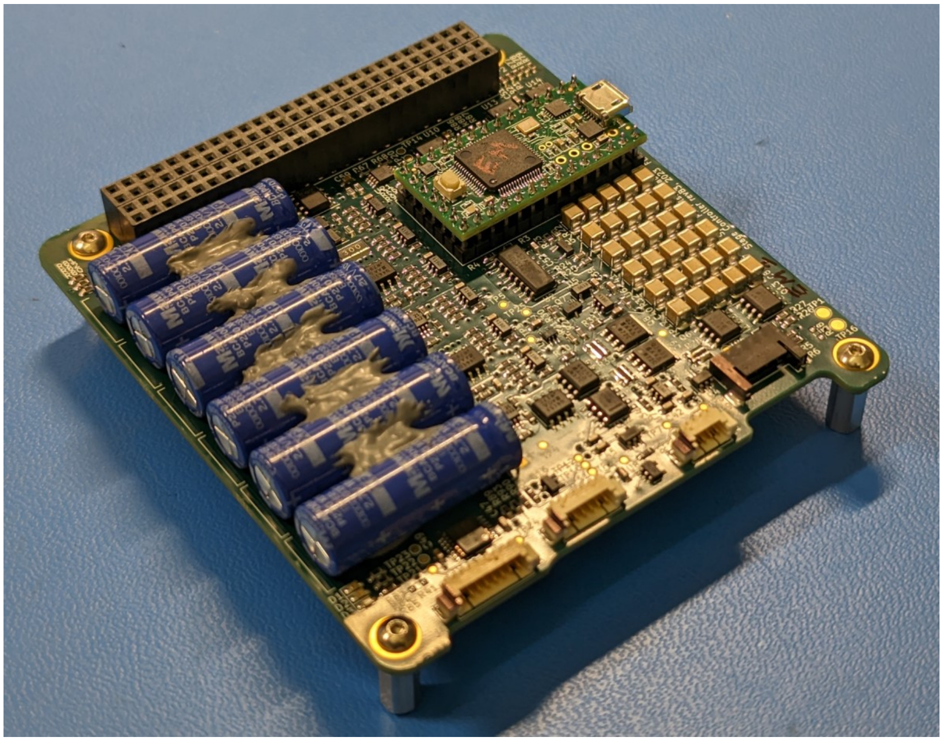

Figure 4.16: Photograph of the staging controller in PC104 format. The main supercapacitor bank is left and the small pulse test capacitor bank is on the right.

expense of penalty area because the former parameter is critical according to the sensitivity analysis. The alternative considered was to use a small button for the activation signal and a latching relay* for each thruster on the back side of the PCB, that would approximately halve the area used by the electronics but add 6 mm to the penalty height. (If the relays were placed on the front side of the PCB, they would not add to the penalty height and use approximately the same area as the interstage does.) The interrupter isolation sheet is 0.5 mm thick and the desired material characteristics are high breakdown voltage, low friction, vacuum compatibility, and toughness. Initially, PTFE was selected because of its ductility and low friction, however, material creep was evident when a sample was left for six months in an interrupter, forming indentations under the pins and increasing the pullout force. The interrupter was changed to polyetheretherketone (PEEK) which did not show any creep and has similar dielectric strength, but increased the initial friction. The complete interstage system weighs c. 20 g and occupies c. 12 cm^2 of area on each stage. The total clamping force of the seven pins of the interrupter is estimated to 2.6 to 3.5 N for each interrupter sheet and the friction coefficient is assumed to be 0.2 to 0.8 for the drag calculation in Table 4.6.

---

*Omron model G6K, which are used in the STEP-1 PPU to control the individual thruster channels.

The power and control signals for the HDRM are provided by a staging controller shown in Figure 4.16 that adds 80 g and 100 cm^3 to the base mass and volume of the propulsion system. The controller stores the energy required to actuate the HDRM in a bank of supercapacitors to allow the staging system to operate without drawing the 14 A current directly from the CubeSat battery. Maxwell model BCAP0010-P270-X01* supercapacitors are used as they offer high energy density, low equivalent series resistance (ESR), and have been qualified for spaceflight [213, 214]. The maximum voltage is derated to 2.2 V per the qualification recommendations and the worst case capacitance and ESR are 8.1 F and 43 mΩ respectively [214]. A bank of six capacitors in a 2-series-3-parallel configuration charged to 4.4 V can supply a constant current of 14 A for 1 s into a 200 mΩ external load which meets the HDRM output requirement. An overvoltage protection circuit was implemented in hardware that automatically isolates the offending series string if the voltage of either capacitor reaches 2.6 V and software protections will halt charging. A passive balance network keeps the supercapacitor voltages equal and dissipate their charge in less than 24 h after charging is disabled. A set of light-emitting diodes (LEDs) indicate if there is charge on the capacitors to meet requirement 8.

The staging controller records telemetry and implements several features to guarantee the safety of the staging system. A small ceramic capacitor bank can output a brief pulse of current to measure the resistance of the hold-down wires and therefore confirm the integrity of the HDRM to meet requirement 6. The HDRM is naturally redundant because two separate fuse sequences must be performed to release both pairs of hold-down wires, meeting requirement 5. In addition, an arming signal must be provided by the spacecraft bus to enable the output from the supercapacitors. Note that the staging controller can not supply sufficient current to fuse all four wires at the same time. An identification resistor with a unique value is placed on each stage so that the active stage(s) can be identified from telemetry.

4.3.3 Managing cold welding

Cold welding is a phenomena where clean metals merge when pressed together at room temperature, causing a strong bond at the interface [215]. In spacecraft this can cause mechanisms to seize because the natural oxide layers that protect metals are not reformed and fretting (repeated small impacts from vibrations) wear away the natural or added surface coating [216]. In the STEP-1 structure there are two areas of metal-to-metal contact that must separate during operations to consider: the mechanical interface that transfers the

---

*Previously known as Nesscap ESHSR-0010C0-002R7UC.

loads between the stages, and the electrical interface that transfers the power and signals required to operate the stages.

The mechanical interface consists of hard aluminium alloys that may be forced together with significant pressure as they are a part of the load-bearing structure of the satellite. Additionally, the conical shape of this interface worsens the cold welding probability by facilitating sliding of the surfaces. Fortunately, in this application the cold welding problem is easily solved by hard-anodising both sides. Anodised surfaces have been shown to be highly resistant to cold welding, even if the coating is cracked or flaking from applied forces [216]. All parts of the mechanical structure are hard anodised with a thickness of 50 µm.

The electrical interface uses spring-loaded pins and pads made from brass coated with 0.25 µm gold over 2.5 µm nickel* to create a durable stage-to-stage connection that allows some relative motion. In this case anodisation is not an option as the coating is non-conductive. The force pressing the contacts together is less than 1 N, however, gold is a soft metal known to easily cold weld in space applications [217]. Gold is a common contact material in low power applications due to its low contact resistance ($1.8 \times 10^{-5}\,\mathrm{m\Omega\,cm^2}$ for 0.3 µm gold over nickel on copper with itself [218]) and protection against oxidising [219]. Due to the surface roughness only a small area is in contact between the pins and pads, given by the contact force F and hardness of the softer material H as $A_c = F/H$ [218]. Assuming the pin has a hardness similar to nickel at 638 MPa [220] and a typical contact force of 0.6 N the contact area is $9 \times 10^{-6}\,\mathrm{cm^2}$ and the contact resistance is 2 mΩ.† Two main strategies are available to manage the electrical interface cold welding concern: add a material to separate the gold contacts, i.e. a conductive grease or a hard coating, or demonstrate that even if cold welding occurs it does not degrade the operations.

Consider that there are are 40 electrical contacts between the stages and four separation springs producing a total initial force of 7.2 N. If we assume the worst case, that the full contact area of all contacts have cold welded, the separation force per contact will be 180 mN or a stress of 200 MPa. This is comparable to but more than gold's tensile strength of 137 MPa [220], thus the cold welds should rip apart even in the worst case. Repeated damage from this process is not a concern since the connectors are only separated once in flight. This strategy was used on the LISA Pathfinder mission, where experiments showed that the test mass release mechanism consistently cold welds to the test mass with a force of 5 to 15 mN required to separate the bond [217].

If testing shows that the cold welding is stronger than predicted a hard coating will be applied to the pads. Using conductive grease is not preferred as it may be difficult to

---

[*] Model 854 pogo-pins and model 856 concave targets from Mill-Max.

[†] The manufacturer specifies the maximum contact resistance to 20 mΩ.

apply consistently or contaminate other parts of the system. Conductive ceramic coatings are popular in many applications, especially for producing transparent conductive surfaces, and are not able to cold weld [221]. Indium-tin-oxide (ITO) is a common material with a contact resistance of 10 to $1000\,\mathrm{m\Omega\,cm^2}$ to metals [222] and titanium-nitride and titanium-carbide have relatively low contact resistances of 4 to $5\,\mathrm{m\Omega\,cm^2}$ to carbon [223]. However, these resistances are several orders of magnitude higher than gold and not suitable for the application. A few pure metals are not able to cold weld with gold: beryllium, cadmium, iron, tin, titanium, and tungsten [215]. Cadmium and tin (along with zinc) sublimate and/or grow whiskers in vacuum and are therefore prohibited by NASA electronics standards [224]. Titanium has high contact resistance of $57\,\mathrm{m\Omega\,cm^2}$ to carbon due to strong oxide growth [223]. Iron will also oxidise quickly and beryllium is expensive. Tungsten is readily available, can be sputter coated, and provides a contact resistivity of $1.2 \times 10^{-4}\,\mathrm{m\Omega\,cm^2}$ [225].* The contact resistivity for tungsten is an order of magnitude higher than for gold, but the resulting resistance of $13\,\mathrm{m\Omega}$ is acceptable for the application.

4.3.4 Stage thermal control

For a deep-space journey the thermal environment is driven by the distance to the Sun: operations in the asteroid belt will be colder than near Earth because the intensity of sunlight has fallen off by a factor of approximately six (2.5^2). The STEP-1 technology demonstration is performed in a low Earth orbit where the thermal environment cycles as the spacecraft passes through eclipse each orbit. Major components of the stage separation mechanism form part of the external structure of the satellite and are therefore directly exposed to the thermal environment. The system could be actively maintained at a desired temperature but to reduce power and complexity the thermal management of the staging system is entirely passive. The analysis in this section motivates why the stages require insulating coatings and that a worst-case thermal cycle of 40 °C is reasonable to assume for the demonstration. More detailed thermal modelling and design is outside the scope of this thesis.

To estimate the thermal cycling of the stages, assume the stages are a block of black anodised aluminium with a mass of $m = 200\,\mathrm{g}$ and heat capacity of $c_p = 900\,\mathrm{J/(kg\,K)}$, where the five sides exposed to space have an emitting area of $A_e = 180\,\mathrm{cm^2}$. This structure is radiatively coupled to the Sun and Earth via an average projected area of $A_p = 30\,\mathrm{cm^2}$ with absorptivity in visible light of $\alpha_{\mathrm{vis}} = 0.8$ and an emissivity in infrared of $\epsilon_{\mathrm{IR}} = 0.8$.† Assume the stages interact with the host spacecraft temperature of T_s through a thermal conductivity

---

[*] The probe material was not specified in this paper, so pure copper with a hardness of 343 MPa [220] was assumed. If the probe was harder, the actual contact resistivity is lower.

[†] Absorptivity and emissivity are two names for the same property, the separate names are historical.

k and that the PCB on the bottom of the stage has an infrared emissivity of $\epsilon_{\mathrm{PCB}} = 0.8$ and is radiatively coupled to the spacecraft with a mutual area of $A_s = 100\,\mathrm{cm}^2$. The total contact area of the stages' mating interface is $140\,\mathrm{mm}^2$ with hold-down pressure around 2 MPa. At this contact pressure the conductance between polished aluminium samples with one side 50 µm hard anodised and the other side raw is $4 \times 10^3\,\mathrm{W/(m^2\,K)}$ [226]. In this case, both sides are anodised and not polished, so assume a contact conductance of $1 \times 10^3\,\mathrm{W/(m^2\,K)}$, giving $k = 0.14\,\mathrm{W/K}$. The stages have negligible internal heat generation except for the thruster thermostat that is not operated unless firing. By combining all heat fluxes into an energy balance the rate of change in temperature T of the stage over time t is given by:

$$mc_p \frac{\mathrm{d}T}{\mathrm{d}t} = A_c I_{\mathrm{sun}} \alpha_{\mathrm{vis}} + A_c I_{\mathrm{earth}} \epsilon_{\mathrm{IR}} - A_e \epsilon_{\mathrm{IR}} \sigma T^4 + A_s \epsilon_{\mathrm{IR}} \epsilon_{\mathrm{PCB}} \sigma \left(T_s^4 - T^4\right) + k(T_s - T) \quad (4.34)$$

where $I_{\mathrm{sun}} = 1368\,\mathrm{W/m^2}$ and $I_{\mathrm{earth}} = 239\,\mathrm{W/m^2}$ [227] are the intensity of sunlight and Earth radiation respectively, and $\sigma = 5.67 \times 10^{-8}\,\mathrm{W/(m^2\,K^4)}$ is the Stefan-Boltzmann constant. Assume a 90 min orbit with an eclipse duration of 40 min in the cold case and no eclipse in the hot case and let $T_s = -10\,^\circ\mathrm{C}$ in eclipse and $T_s = 20\,^\circ\mathrm{C}$ in sunlight. Table 4.7 gives the expected temperature ranges, which is significantly colder than the host spacecraft's controlled temperature. To improve the temperatures the stages are insulated with aluminised tape on the sides and a chromate conversion coating instead of anodisation on the plasma shield. The coatings cover 80% of the structure with $\alpha_{\mathrm{vis}} = 0.2$ and $\epsilon_{\mathrm{IR}} = 0.05$, yielding an effective $\alpha_{\mathrm{vis}} = 0.32$ and $\epsilon_{\mathrm{IR}} = 0.2$ for the coated stages and increased temperatures, see Table 4.7. With the insulating coating the stage temperature is within a few degrees of the controlled spacecraft temperature.

Table 4.7: Steady-state temperature cycle on orbit for a stage that is black anodised compared to case where major areas have been coated for high $\alpha_{\mathrm{vis}}/\epsilon_{\mathrm{IR}}$ (e.g. aluminised tape).

Surface	α_{vis}	ϵ_{IR}	Eclipse	T_{min}[°C]	T_{max}[°C]
Anodised	0.8	0.8	40 min	**-24**	7
			0 min	8	**8**
Coated	0.32	0.2	40 min	**-12**	16
			0 min	18	**18**

4.4 Finite element analysis

Finite element analysis (FEA) was used to validate the design of the propulsion unit structure before environmental testing and the final model and its calibration are presented here. Similar models, methods, and test cases were used to evaluate and improve the design during development, including selecting the hold-down wires' dimensions and tension. Additionally, modelling results showed that the PCBs alone were too flexible to carry the hold-down wire loads and that the shield would likely fail, leading to a redesign. The design was tested to exceed a safety factor of two with an applied static load of 320 N and a random vibration load of 14g RMS from 20 to 2000 Hz according to the NASA GEVS standard. The static load corresponds to the force exerted on a satellite with a mass of 4 kg accelerating at 8g and applies as a distributed load on the structure from either the lateral (X or Y) or longitudinal (Z) direction as the spacecraft launch orientation is not known. All analyses were performed in *Solidworks 2023*.

A simplified version of the payload CAD model where structurally insignificant features and components were excluded was used for the FEA and is shown in Figure 4.17. Distributed masses were added to each circuit board to compensate for the excluded components and match the weight of the the engineering model assemblies. The hold-down wires were not directly modelled, instead, spring elements were added between the hold-down wire blocks where the spring constant was tuned to correspond to a given wire diameter and preloads were added to simulate the effect of tensioning the wires. Each part was meshed adaptively with element sizes of 2 to 10 mm and at least eight nodes per cylinder, with a finer mesh size of 1 mm applied on the stage mating interface. Runs were performed with a halved mesh size to validate that sufficient detail was reached, with results within a few percent of the initial mesh size. Three materials are used in the model: aluminium 6061-T6, stainless steel 304, and a "PCB" material for the circuit boards. The default material properties in the software package were used for the two former materials except the density of the aluminium that was refined by weighing the manufactured parts. The PCB material attributes were experimentally calibrated, see Section 4.4.1, yielding the properties in Table 4.8.

Table 4.8: Material properties CTE = Coefficient of thermal expansion.

Material	Density	Elastic modulus	Poisson ratio	Strength	CTE
Al 6061-T6	2740 kg/m^3	69 GPa	0.33	275 MPa	2.4×10^{-5}/°C
Stainless 304	8000 kg/m^3	190 GPa	0.29	205 MPa	1.8×10^{-5}/°C
PCB (370HR)	2200 kg/m^3	23 GPa	0.17	425 MPa	1.3×10^{-5}/°C

4.4.1 Model stiffness calibration

The printed circuit boards (PCBs) are stacks of several materials with complex patterns bonded together, resulting in unknown combined material properties. For simplicity and cost, a typical PCB design with four copper layers and a total thickness of 1.6 mm was used in the payload, however, to maximise the dielectric separation between each layer a custom stackup with 0.46 mm of dielectric between each copper layer was specified. *Isola 370HR* fibreglass was selected as the dielectric material as this is a common material with good thermal stability suitable for spaceflight applications. The manufacturer specifies that this material has an in-plane (XY) elastic modulus of 24 GPa, Poisson ratio of $\nu = 0.17$, and coefficient of thermal expansion of $1.3 \times 10^{-5}/°\text{C}$. Due to a lack of data in the out-of-plane (Z) direction and the load case on the circuit board being almost pure bending, the material is assumed to be isotropic for the FEA. As the stage PCB has its low-voltage power plane and ground plane on the top and bottom copper layers it may act as a sandwich structure with a copper skin cladding a fibreglass core. The sandwich structure effect could increase stiffness significantly, however, to allow mounting of components the sheets do not completely cover the surface and the effect may be diminished. For a sandwich structure the effective flexural modulus E_f is [228]:

$$E_f = E_c\gamma^3 + E_s(1 - \gamma^3) \tag{4.35}$$

where $E_c = 24\,\text{GPa}$ and $E_s = 110\,\text{GPa}$ are the moduli of the fibreglass core and copper respectively and $\gamma = 0.913$ is the ratio of core thickness to total thickness with 70 µm skins. For the PCB these values yield $E_f = 45\,\text{GPa}$, thus if the PCB acts as a sandwich structure its stiffness is nearly double that of the core material.

The actual PCB elastic modulus was calibrated by tuning the model properties to match the experiment described in Section 4.5. The FEA model for PCB calibration consists of four 0.5" tall stainless steel standoffs bonded at the mounting holes of the PCB, with the bottom of the standoffs fixed. The manufactured PCB was weighed to 30.3 g giving the density of $2200\,\text{kg/m}^3$ used for the FEA. After tuning the elastic modulus to 23 GPa the first mode is at 387 Hz, shown in Figure 4.18a, and matches the experimental value. The fifth mode, shown in Figure 4.18b, is the second lowest mode in the model with significant displacement in the centre of the PCB and occurs at 1407 Hz, within 6% of the experimental result. The tuned elastic modulus of 23 GPa is similar to the specified value for the fibreglass material but significantly below the prediction of the sandwich model, so the effect of the copper appears to be small.

The FEA model of the stage assembly was calibrated and validated before the full propulsion unit analyses were performed as the stages make up the external structure of the payload

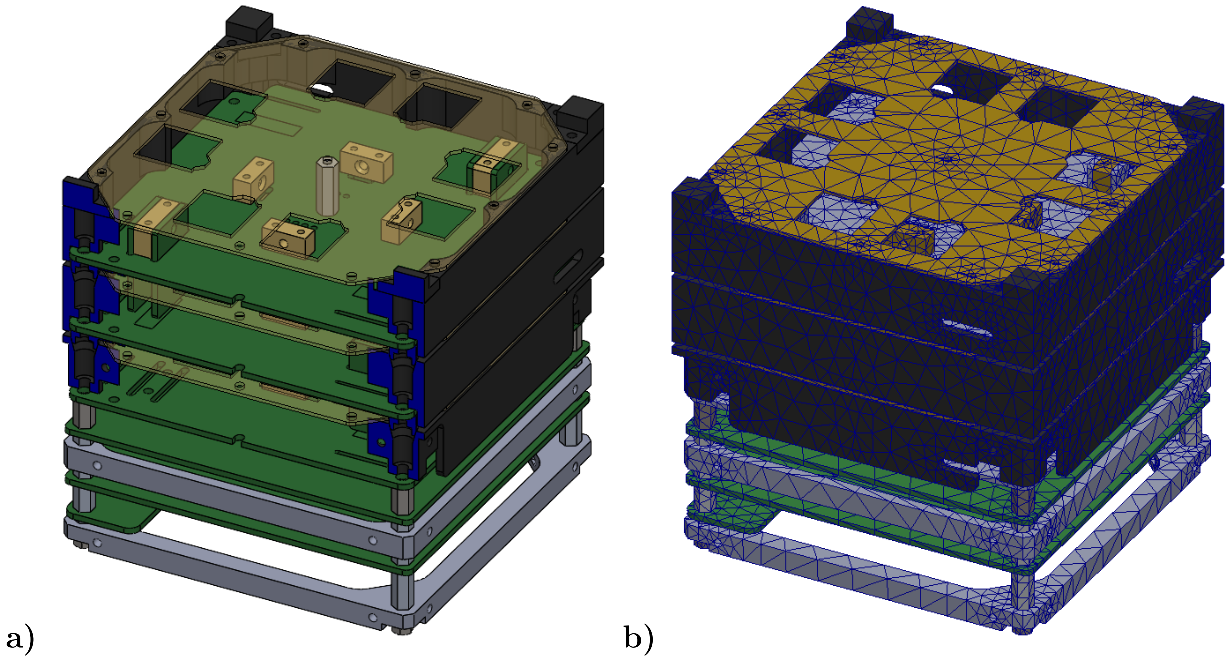

Figure 4.17: Views of the CAD model used for FEA. The green parts are “PCB” material, and all other parts are “Al 6061-T6” except for the standoffs between the bottom stage to the PPU and the threaded rods holding the PPU stack together that are “Stainless 304”. a) Cutaway model. b) FEA mesh.

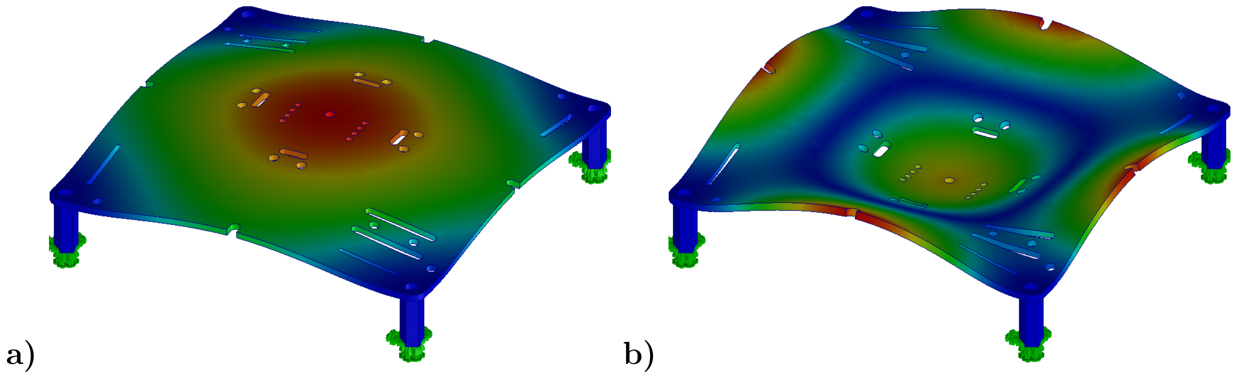

Figure 4.18: FEA of PCB modes after stiffness calibration. a) First mode at 387 Hz. b) Fifth mode at 1407 Hz.

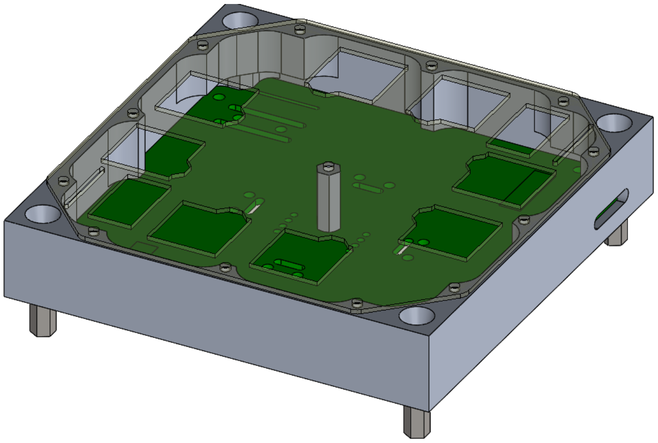

Figure 4.19: CAD model of the simplified stage assembly used for FEA calibration, consisting of only the most critical components. The shield is transparent for visibility.

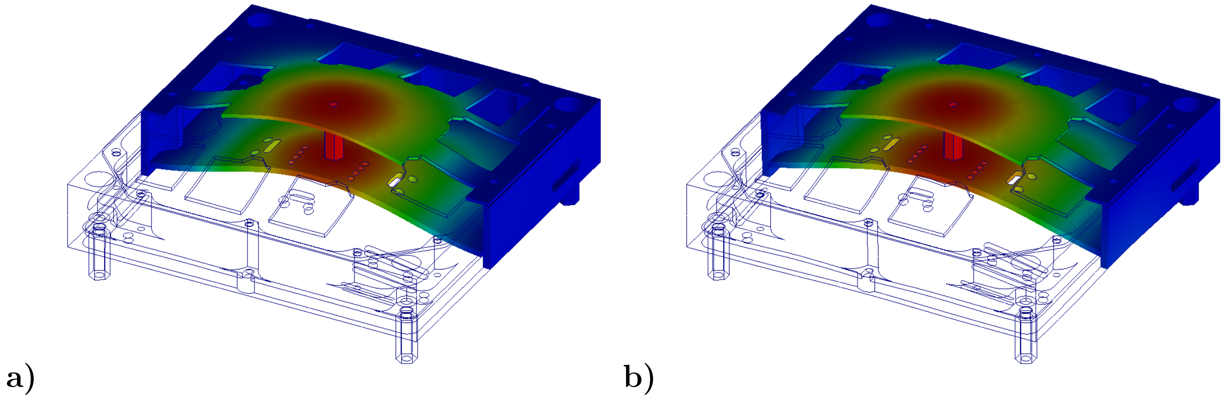

Figure 4.20: FEA of the first mode of the stage assembly. a) Bonded structure at 831 Hz. b) Structure with tuned PCB-frame interface at 710 Hz.

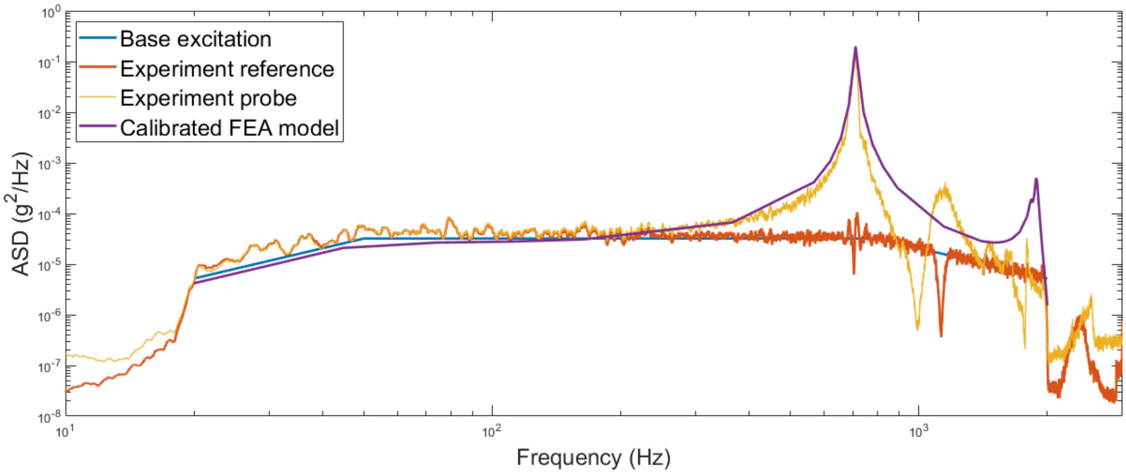

Figure 4.21: Acceleration spectral density (ASD) response for the calibration experiment and the FEA model. The simulated data show relative acceleration while the measurements show absolute acceleration. The test fixture has a known resonance mode around 1100 Hz.

and provide the paths for all external and internal (i.e. hold-down wire tension) loads. Calibration was performed using a simple but representative stage assembly consisting of the frame, PCB, shield, and the standoff that joins the PCB and shield. The CAD model for the validation and tuning is shown in Figure 4.19 and the corresponding experimental method and results are described in Section 4.5. When all parts of the model are bonded together the piston mode of the structure, shown in Figure 4.20a is at 831 Hz, 17% higher than the experimental result for the same structure. The lower stiffness in the real structure is likely due to how the parts are connected together, especially the connection between the PCB and the frame. The frame is relatively rigid so when the PCB and shield deform they apply a shear load on their interfaces to the frame. The shield resists the shear through 12 countersunk screws along its perimeter, but the PCB is not connected as rigidly to the frame. Four large fasteners in each corner clamp the PCB to the frame securely and four small fasteners attach the edges of the PCB to the frame walls, however the latter are unlikely to restrict the inward pulling of the PCB. Therefore, instead of bonding the PCB and frame, the model was improved by joining the PCB to the frame with rigid pins at the corner mounting holes and a spring element that is stiff in vertical motion but allows free horizontal motion at the small screw mounting holes. The spring element's vertical stiffness was tuned to 2×10^7 N/m to give a first mode of 711 Hz shown in Figure 4.20b, matching the experimental results. To finalise the calibrated FEA model, random vibration simulations were performed to compare the acceleration spectra with the experiments, shown in Figure 4.21. As the model gives accelerations relative to the fixed base but the experiments measure absolute accelerations they are only directly comparable where the values are significantly larger than the base excitation. The calibrated model's mode damping was tuned to 1% to match the the measured peak amplitude. The simulated and experimental results after calibration match closely, validating the model accuracy, and giving confidence to proceed with the full propulsion unit analysis.

4.4.2 Static load analysis

Static load analysis was used to dimension the structural components and determine the hold-down wire tensioning for the three-stage stack. Nonlinear node-to-surface contact was applied at the conical mating surfaces to allow free separation and the calibrated model from the previous section was used for the stages. The bottom stage mounting holes were fixed and the PPU was excluded from this analysis as it is not an external member subject to static loads.

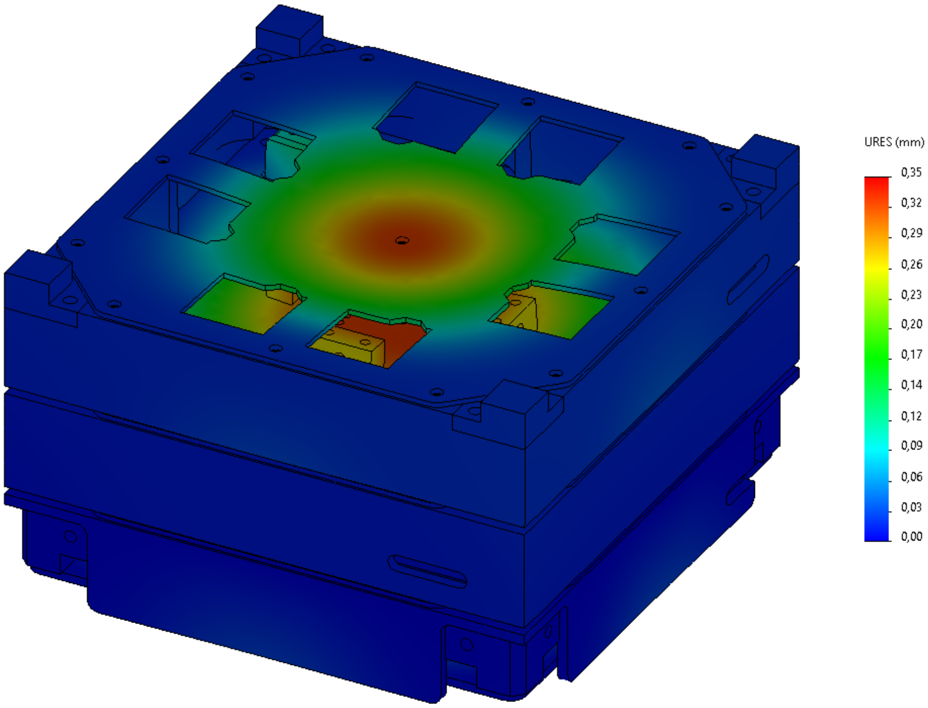

Figure 4.22: Deformation (exaggerated by a factor of 10) of the stage stack due to the wire tensioning without any external load.

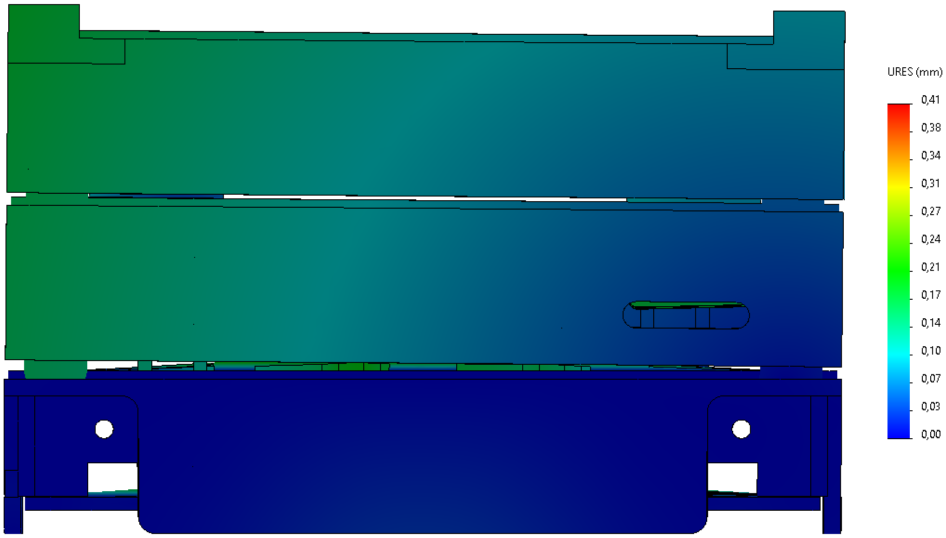

Figure 4.23: Deformation (exaggerated by a factor of 5) of the stage stack due to a 320 N distributed load applied from the left on the sidewalls of the top and middle stages.

Figure 4.22 shows that the peak stress and deformation without external loads are around 50 MPa and 0.35 mm when the hold-down wires are preloaded to 30 N. With the static load test case of 320 N applied from the side a slight gap opens up between the second and third stages as shown in Figure 4.23. The gap was 0.16 mm and the maximum tension in the hold-down wires were 42 N when 0.25 mm diameter stainless steel hold-down wires with a stiffness of 600 kN/m were used. 0.25 mm wire with a strength of 105 N was the smallest readily available diameter giving a safety factor greater than two and was selected as the final dimension. The peak stress on the structure was approximately 100 MPa, located at the mating interface, which is significantly less than the surface hardness of 4.5 GPa [212] and gives a safety factor above two for the material strength. If the wire preload is reduced the gap opens up more under load (e.g. 0.27 mm at 25 N), whereas at higher preload the stress on the wire increases; the selected tension is a compromise. Static load applied vertically has negligible effect on the structure, except for possible concerns of sticking as discussed in Section 4.3.1.

In the first version of the stage design the shield was non-structural and made from thinner material. Static load simulations showed that the shield material between the thruster cutouts would fail and the deflection of the structure was approximately double the value for the final design. By making the shield structural through increasing its thickness and switching from a low (3003) to a high (6061) strength aluminium alloy the results were improved with a penalty of approximately 10 g and 1 mm additional mass and height per stage. Strategies for improving stage stiffness with less penalty may be considered for future derivatives of this work.

Table 4.9: Wire tension in newton at each step of the assembly as calculated from the FEA model. The number in bold shows the value needed to set the new wire pair at each step.

	Middle stage hold-down		Top stage hold-down	
Assembly step	X wire pair	Y wire pair	X wire pair	Y wire pair
Mid tension X wires	**23.3**	-	-	-
Mid tension Y wires	13.6	**13.6**	-	-
Mid final with shield	16.4	16.4	-	-
Top tension X wires	30.8	19.6	**40.7**	-
Top tension Y wires	26.7	26.7	24.0	**24.0**
Top final with shield	29.7	29.7	30.9	30.9

Tensioning the wires during assembly requires care as the load on each wire changes as the other are tensioned and the stiffness of the structure changes when components (i.e. the shields) are added. Ideally, all four wires on each stage would be tensioned at once to guarantee even load, however, due to space constraints it is only possible to tension the wires in pairs. There are thus three steps to mounting each stage where the tension changes: tensioning the first pair of wires, tensioning the second pair of wires, and adding the shield. To find the tension required at each step of the procedure the FEA model was used and walked "backwards" through the assembly steps, recording the wire tensions at each stage as shown in Table 4.9. The smallest and largest tensions required during assembly for the structure to settle at 30 N in all wires are 13.6 N and 40.7 N respectively. In general, the results show that the first pair of wires on each stage needs to be tensioned 70% higher than the second pair and the middle stage needs to be tensioned to half of the final value to even out the tension.

4.4.3 Vibration load analysis

Random vibration simulations were used to verify the propulsion unit's resilience to random vibration loads and to further validate the FEA model. Two types of simulations were performed: vibration in all three axes at once to find peak loads, and vibration in each axis separately for comparison to environmental testing results. For this analysis the PPU stack was included and the total mass of the FEA model is 759 g which corresponds well to the total measured mass of the engineering model. The stage mating interface was bonded to linearise the model and the impact of this simplification is discussed in the comparison to environmental testing data in Section 5.3.2.

The three-axis total stress case is shown in Figure 4.24, where all six mounting holes on each side were fixed which ensures the measured modes correspond only to the internal structural movement, though this may be a poor approximation to how the propulsion unit behaves when attached to the satellite bus structure. The peak RMS stress on the stages were 15 MPa in the shield with a corresponding deformation of 0.13 mm in centre of the stage. At 3σ this gives a safety factor of 9.3 and a peak deformation of 0.74 mm including the static deformation caused by the wire tensioning. For the PPU the RMS stress was 18 MPa with 0.33 mm deformation and a 3σ safety factor of 7.9. The model shows stress concentrations at some discontinuities in the model (i.e. holes and sharp corners) up to approximately 100 MPa, however, as fatigue is not a concern for the applications the stress concentrations are accepted without further investigation. To better understand the motion of the structure during random vibration, pure X and Z vibration simulation were performed (due to symmetry, Y is skipped), with acceleration spectra shown in Figure 4.25. The response was probed in locations that are easily available to measure during environmental testing to guide the interpretation of those results. The X axis test shows a single mode at 1850 Hz for all stages, indicating an overall rocking motion where the motion of the top

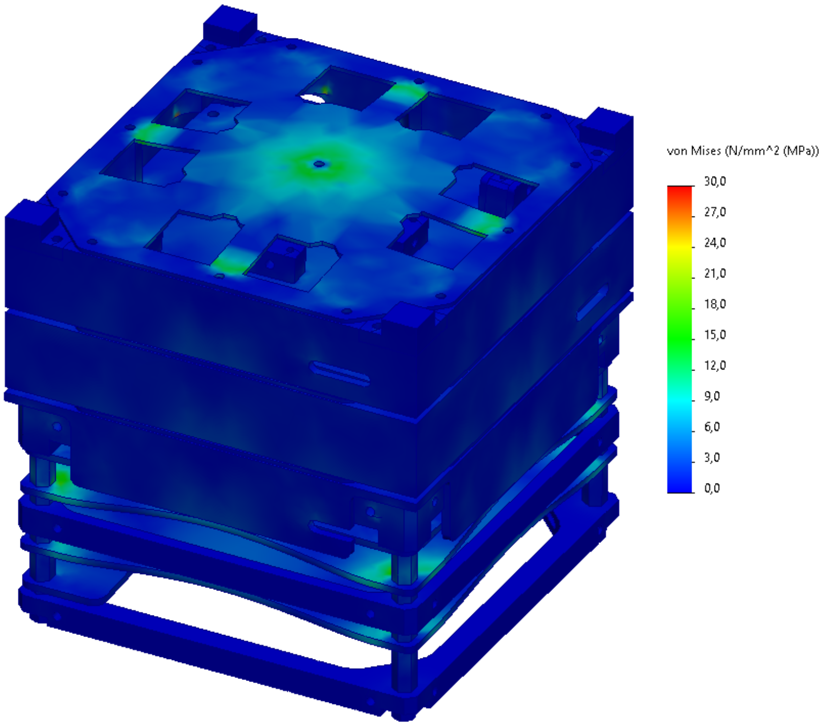

Figure 4.24: Total RMS stress in the structure exposed to 14g RMS random vibration in three axes simultaneously. The deformation is exaggerated by a factor of 30.

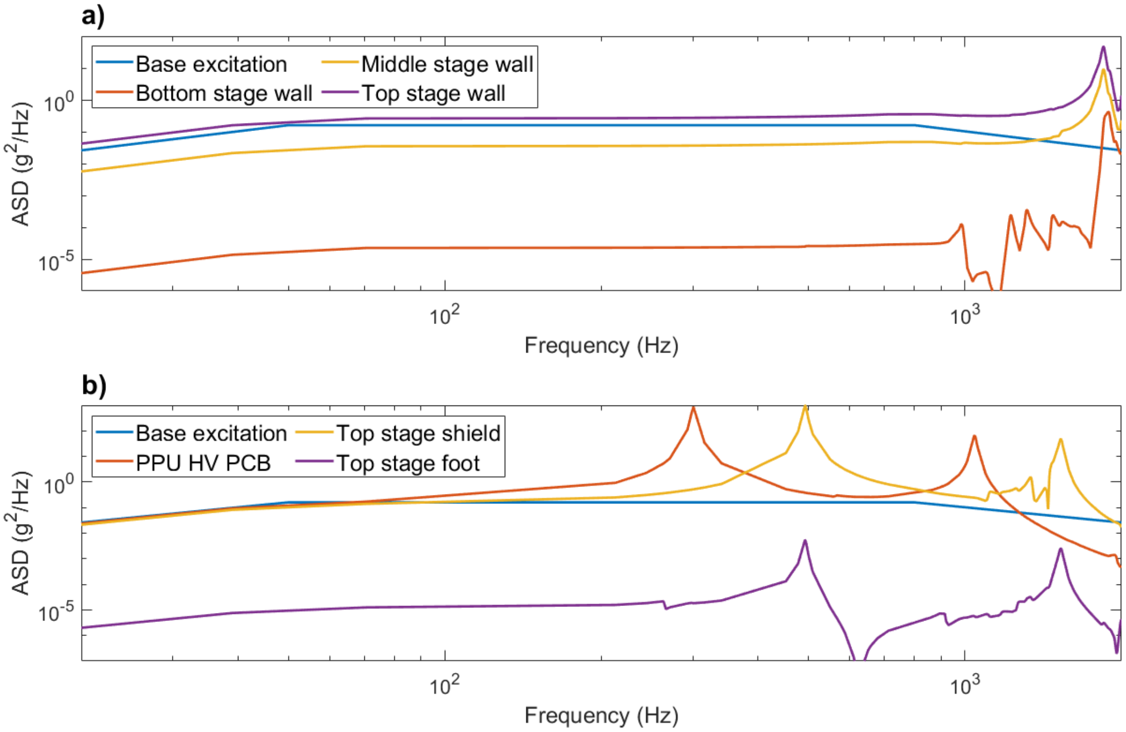

Figure 4.25: Acceleration spectral density (ASD) for single-axis random vibration of the propulsion unit with fixed mounting holes. a) X-axis, b) Z-axis.

stage is the largest. In the Z axis test there are independent piston modes excited for the PPU HV board and stage piston mode at 301 Hz and 493 Hz respectively, with overtones at 1044 Hz and 1529 Hz and no other significant movement in the structure.

Vibration testing of the actual structure is unavoidably affected by the mounting fixture and therefore simulations were performed where the fixture was incorporated. The testing fixture consists of a 9.5 mm thick baseplate and two 3.2 mm thick walls attaching the propulsion unit mounting holes to the baseplate that allows three testing dimensions on a single-axis vibration table as shown in Figure 4.26. The mounting fixture was designed with input from the FEA mode analysis to ensure no pure mounting fixture modes were observed within the testing range. The bottom of the fixture's baseplate was fixed in the simulation and the acceleration spectra for pure X and Z vibration are shown in Figure 4.27. Comparing the X axis results with and without the test fixture (Figures 4.27a and 4.25a) the first mode is shifted down to 1215 Hz but otherwise does not affect the shape or amplitude significantly. The Y axis results (Figures 4.27b and 4.25b) are practically unaffected by the fixture.

4.4.4 Thermal expansion of mating interface

Thermal expansion causes the stage mating interface to grow and shrink during the orbit temperature cycles and wears the mating surfaces. Figure 4.28 shows a worst-case scenario where the temperature of adjacent stages differ by 40 °C and result in sliding of approximately 12 µm. This result is used in Section 4.3.1 to show that the cyclic wear on the interface is negligible.

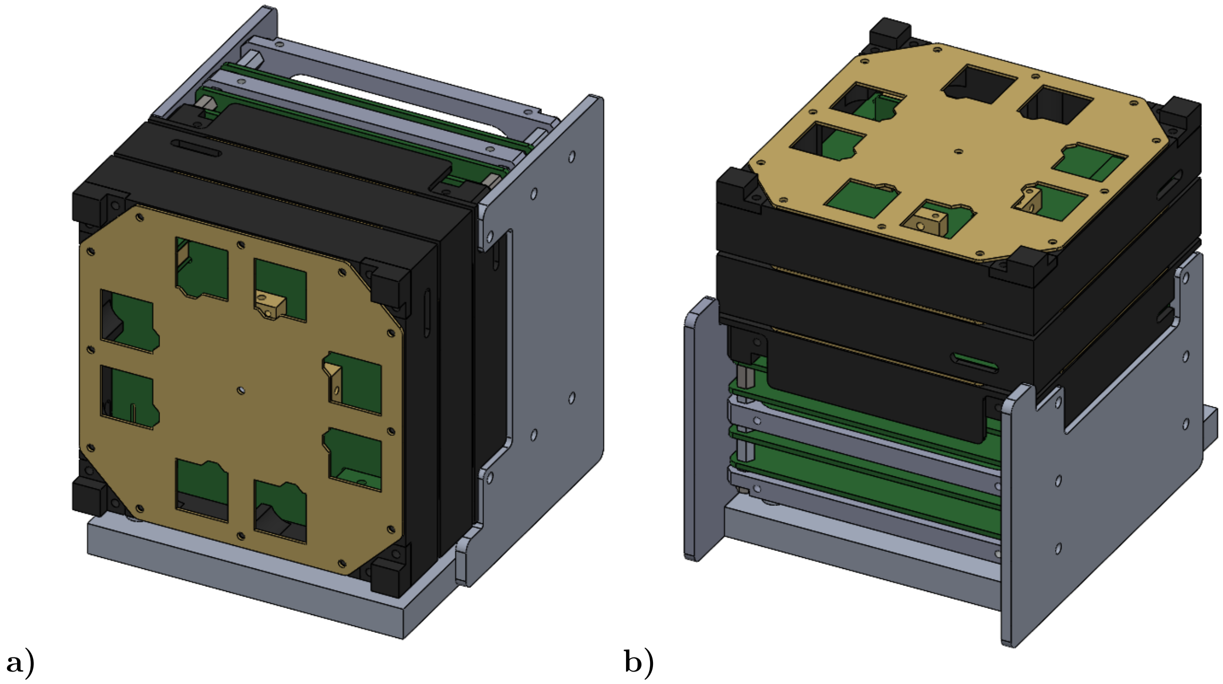

Figure 4.26: Simplified CAD models of the propulsion unit mounted in the vibration testing bracket. a) Oriented for X-axis testing. b) Oriented for Z-axis testing.

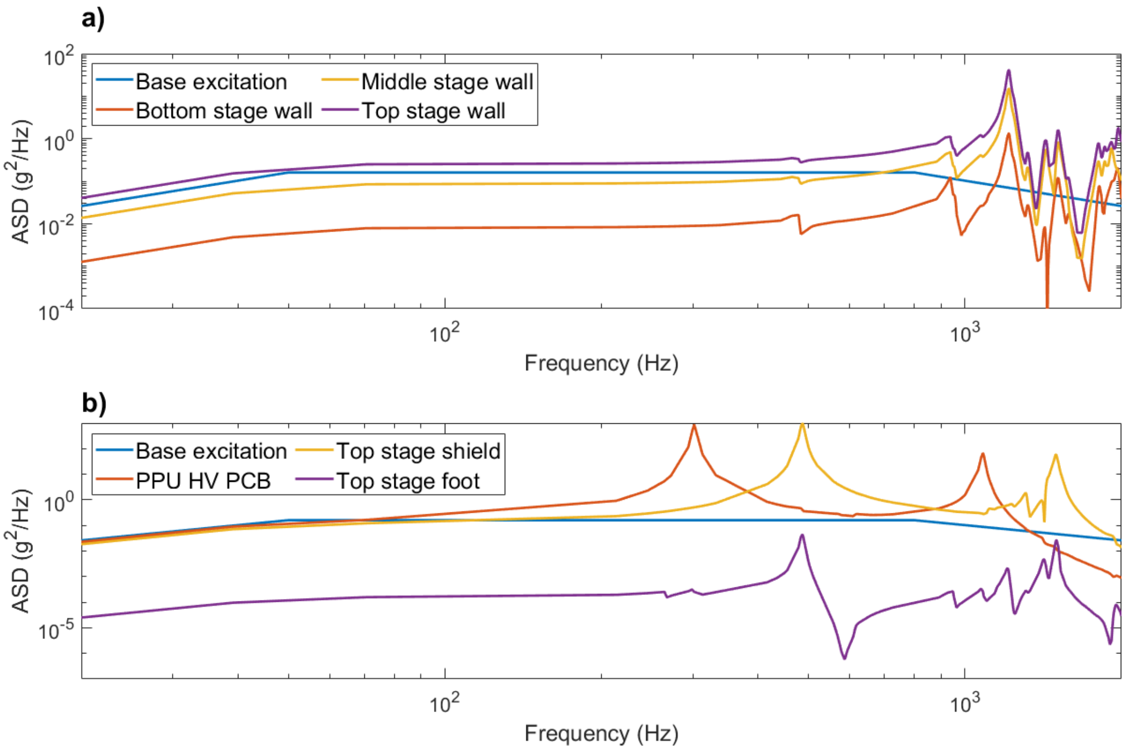

Figure 4.27: Acceleration spectral density (ASD) for single-axis random vibration of the propulsion unit mounted in the test fixture. a) X-axis, b) Z-axis.

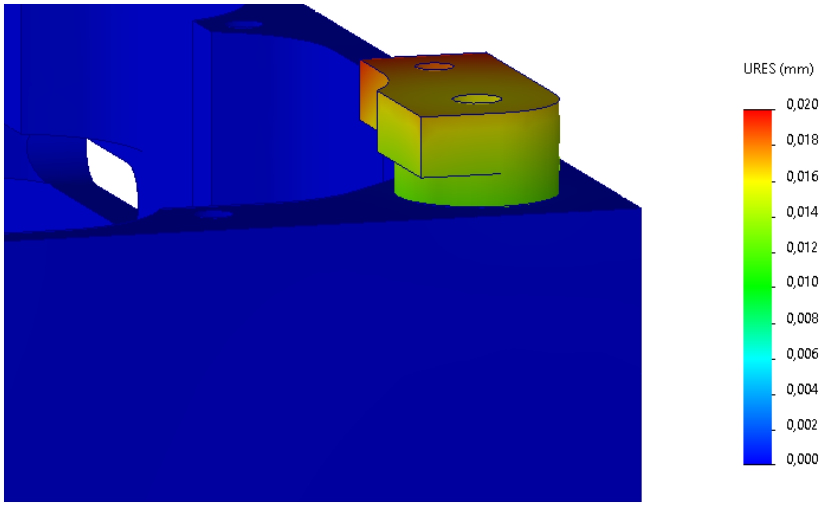

Figure 4.28: Acceleration spectral density (ASD) for single-axis random vibration of the propulsion unit mounted in the test fixture. a) X-axis, b) Z-axis.

4.5 Experiments to inform analysis and design

During the technology development in this thesis several small experiments were performed to inform the analysis, design, and manufacturing of the propulsion unit of which two were important enough to include. These experiments reduce the risk of failure during testing or operation and give confidence to the analysis results. The tests here are generally simple in nature; sufficient to move forward with design without necessarily meeting the rigour of the qualification testing in Chapter 5.

Measuring PCB and stage stiffness

To create an accurate FEA of the propulsion unit the stiffness of the PCB material and stages were calibrated. No components were mounted to the circuit board to simplify the testing and model calibration process. See Section 4.4.1 for how these results were incorporated in the model. The vibration testing hardware was the same as presented in Section 5.2.2.

A base plate with 0.5" tall stainless steel standoffs was mounted to the vibration platform together with a stiffening ring to increase the natural frequency of the vibration platform itself to above 1000 Hz. The test articles were bolted to the standoffs, as shown in Figure 4.29, and the component assembly and screw torquing were performed according to the engineering model integration manual. The ASD for this test was based on the NASA GEVS standard scaled down to $0.2g$ RMS intensity and the test ran for 60 s of which the middle 40 s were averaged.

The test of the PCB alone was set up as shown in Figure 4.29a with the results in Figure 4.30a. Two peaks are clear at 392 Hz and 1322 Hz for the test accelerometer placed in the middle of the PCB. The test of the assembled stage was set up as shown in Figure 4.29b with the results in Figure 4.30b. A single peak at 709 Hz is seen for the accelerometers in the middle of the stage and the PCB and shield are perfectly coupled for all frequencies below 1600 Hz. In both tests there are anomalies in the data around 1100 Hz due to the lowest mode of the vibration table itself, which was confirmed by running the test with the fixtures alone.

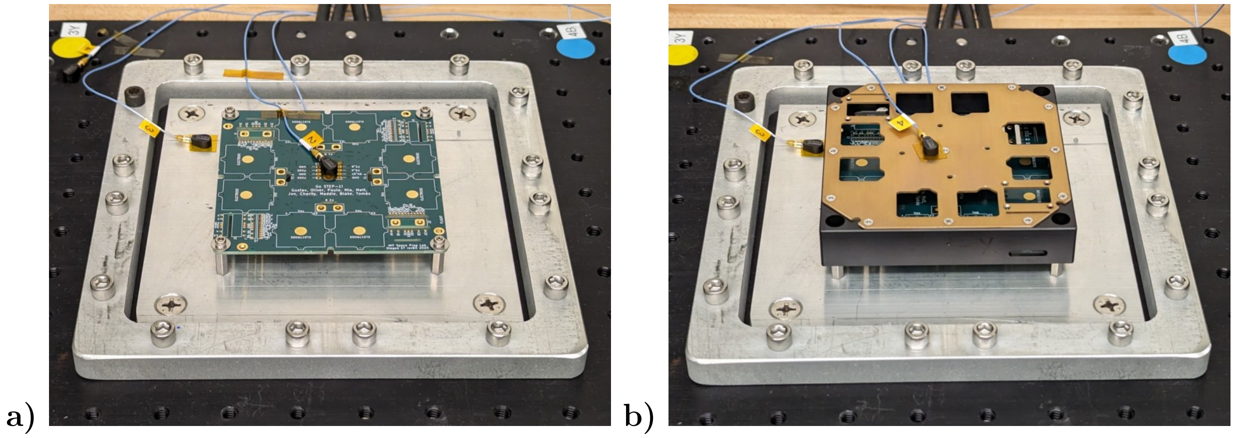

Figure 4.29: Vibration testing setups to calibrate the FEA. In both cases a reference accelerometer is mounted in the middle of the base plate under the test article (not visible). a) The bare PCB supported with standoffs in each corner with an accelerometer in the middle of the board. b) The complete stage structure mounted with standoffs in each corner with an accelerometer in the middle of the PCB (not visible) and in the middle of the shield.

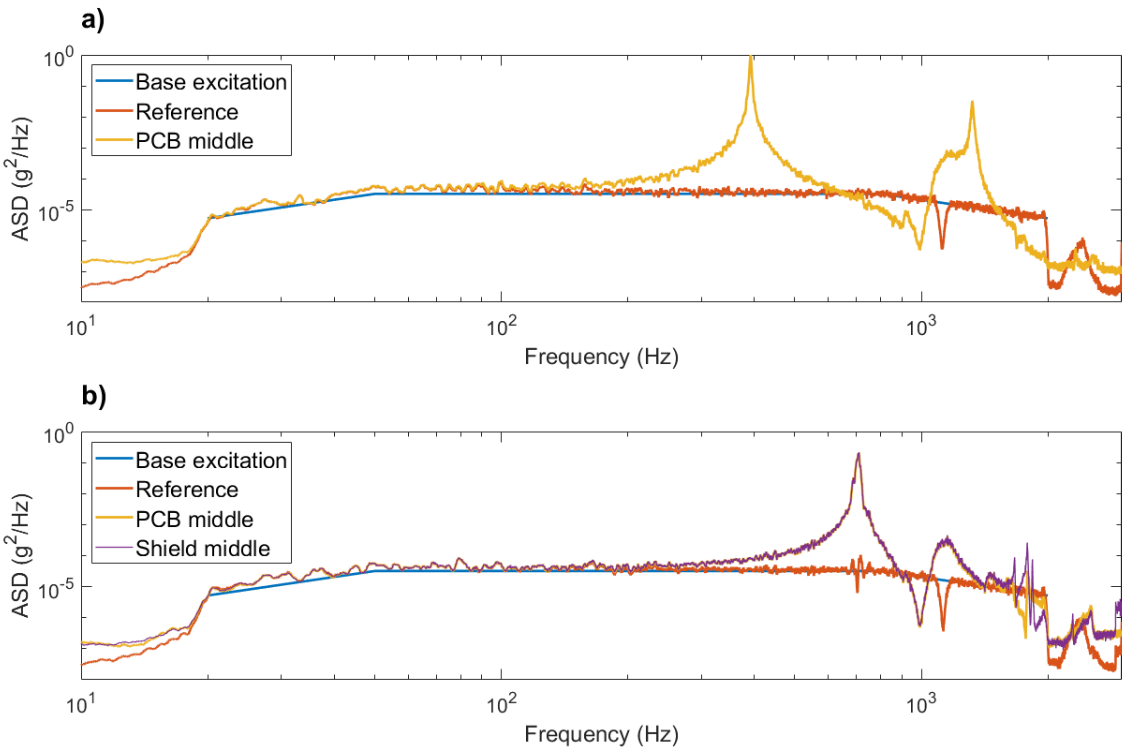

Figure 4.30: Acceleration spectral density (ASD) data for calibrating the FEA model. The base excitation is the target for the vibration table and the reference is an accelerometer placed on the base plate. The test fixture has a known resonance mode around 1100 Hz causing a phantom mode in both scenarios. a) For the PCB alone supported with standoffs in each corner. b) For the complete stage mechanical assembly.

Determining interface coefficient of friction

The actual coefficient of friction between the manufactured hard-anodised parts was measured using the inclined plane method to assess the sticking risk discussed in Section 4.3.1. Testing was performed with a small and large part to compare any effect of interface pressure. The testing setup slowly increased the angle of a frame piece with a test part atop, acting as the plane and sliding object respectively, as shown in Figure 4.31. The angle of the plane was measured to an accuracy of ±0.5° when the sliding object had moved at least halfway across and testing was performed to the right and left to cancel any incline in the table surface.

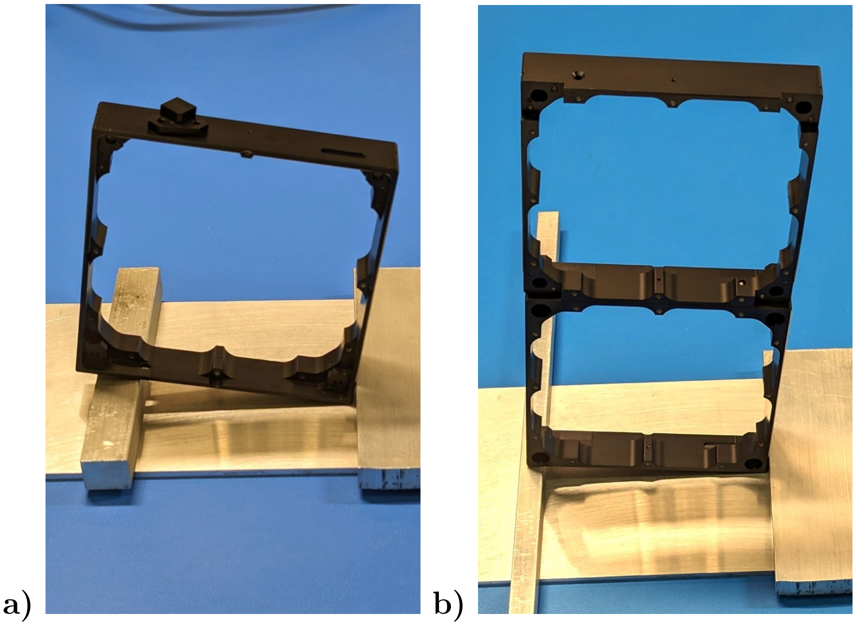

Figure 4.31: Inclined plane test setup to measure coefficient of friction between the final manufactured parts. a) CubeSat “foot” on stage frame. b) Stage frame on stage frame.

Table 4.10: Measurements of the critical angle when the sample slides and the calculated coefficients of friction.

Test setup	No. measurements	Critical angle	Friction coefficient
a) Foot on frame	32	$(14.2 \pm 2.2)^\circ$	0.25 ± 0.04
b) Frame on frame	16	$(9.6 \pm 1.8)^\circ$	0.17 ± 0.03

Table 4.10 presents the measured coefficients of friction with the sample standard deviation used as uncertainty. Notably, the friction measured here is slightly higher than the expected range of 0.1 to 0.2 assumed in the design phase. Due to the low forces in this test and the large difference between the two tests it is possible that the sliding object catches on small imperfections that would not affect the mating interface.

Chapter 5

Raising Technology Readiness of Staged Electrospray Propulsion

Table 5.1: High-level definition of Technology Readiness Level (TRL) by NASA [104].

1	Basic principles observed and reported
2	Technology concept and/or application formulated
3	Analytical and experimental critical function and/or characteristic proof-of concept
4	Component and/or breadboard validation in laboratory environment
5	Component and/or breadboard validation in relevant environment
6	System/subsystem model or prototype demonstration in a relevant environment
7	System prototype demonstration in a space environment
8	Actual system completed and "flight qualified" through test and demonstration
9	Actual system "flight proven" through successful mission operations

5.1 Overview

Technology readiness is a measurement of maturity that indicates the level of risk associated with including a certain technology in a system design. NASA's Technology Readiness Level (TRL) scale shown in Table 5.1 is frequently used in the space industry and beyond to consistently classify the maturity of technologies. By using the TLR scale, the benefits of new technologies can be balanced against realistic risk assessments to nurture innovation and progress new space missions [104].

This chapter serves to demonstrate that the staged electrospray propulsion technology for deep-space CubeSats meets TRL 6; a significant step forward from TRL 4 before this work. Prior work by Jia-Richards et al. developed modelling and a proof-of-concept demonstration in a laboratory environment, see [30, 31, 33], to reach TRL 4. The Staged Electrospray

Pathfinder 1 (STEP-1) propulsion system is designed to meet the requirements of TRL 6, representing a scaled-down system prototype. In this chapter, STEP-1 is demonstrated to operate as designed in a relevant environment and key scaling and life-limiting effects are discussed. Thruster emulators that closely mimic the mechanical and electrical characteristics of electrospray thrusters are used in place of real thrusters, permitting operation in atmosphere and without special handling to simplify the testing setups. Since electrospray thrusters without staging already reach at least TRL 6 [229] the use of emulators does not limit these results. The performance and maturity of electrospray thrusters themselves is generally outside the scope of this thesis. The work in this chapter also serves as a part of the qualification for the flight demonstration of the homonymous STEP-1 CubeSat mission that is expected to bring deep-space staged electrospray propulsion to TRL 7 and will fly an identical propulsion system with real electrospray thrusters on-orbit. A test-as-you-fly philosophy is followed in this chapter by configuring the propulsion system in its flight configuration and performing all testing using the flight interfaces.

To meet the requirement of testing in a relevant environment several aspects of deep-space flight must be considered:

1. The loads during launch.
2. Operation in vacuum and without gravity.
3. The thermal environment in space.
4. Effects of spacecraft charging.
5. Several sources of radiation.

The first three environmental aspects are covered directly in this chapter. The launch loads were tested by performing static load and vibration testing on the propulsion unit followed by functional testing. The thermal and vacuum environment testing was performed in a thermal vacuum chamber by thermal cycling and functional testing at hot and cold temperatures. As the stage separation dynamics are highly dependent on gravity, all functional testing was performed with gravity offloading.

The effects of spacecraft charging and radiation are not covered in this chapter. Previous work by Mier-Hicks and Lozano has shown that spacecraft charging induced by electrospray thrusters operated in a bipolar configuration is bounded and can be modelled accurately [163]. A bipolar configuration is assumed for the staged electrospray systems discussed in this thesis and therefore no additional work is necessary on spacecraft charging. Radiation tolerance primarily applies to electronics and marks a significant difference between operations in different orbital regimes. The low Earth orbit environment and most deep-space destinations are relatively benign and can be handled by commercial off-the-shelf electronics with careful selection or shielding, however, trapped charged particles around e.g. Earth and Jupiter can cause significant radiation damage [109]. As discussed in the literature review Section 2.3.2, a variety of techniques are available to build CubeSats with the necessary radiation tolerance based on mission environmental requirements and is not covered here.

The scaling effects of the system are driven by the number of stages, the number of individually controllable thrusters per stage, and the amount of propellant stored on each stage that drives their size and mass. See Section 4.1 for details on how the system is planned to scale. STEP-1 has three stages, but was designed such that the middle stage can be repeated any number of times to scale from two to an arbitrary number of stages. STEP-1 provides eight individually controllable thruster channels per stage to enable bipolar operation of four thruster groups (to manage accumulated angular momentum) and is sufficient for full-scale systems as well. The amount of propellant per stage on STEP-1 is purposefully kept low ($<10\,\mathrm{g}$) to reduce the cost of development by using small and light stages at approximately $10\times10\times2\,\mathrm{cm}^3$ and 200 g that allow testing in a 3U CubeSat form-factor. In the full-scale target system for a 6U CubeSat, the stages are instead $22\times10\times3\,\mathrm{cm}^3$ and weigh 810 g, of which almost half is propellant (see Table 4.3). Larger stages on heavier spacecraft affect the hold-down wire loads and require additional structural stiffening to keep the natural frequencies acceptable during launch loads. The stages will remain smaller than a CubeSat, and therefore there is abundant experience available to optimise the mechanical design. As the hold-down wire melting is strongly dependent on wire diameter it is preferable to increase the number of wires instead of their size, e.g. to four pairs of hold-down wires instead of STEP-1's two pairs. Using more hold-down wires of the same size avert any significant changes to the staging controller electronics by instead extending the duration of the separation sequence. Finally, by using a "tabbed" version of the 6U or larger CubeSat standard [230] the design loads on the structure may be reduced as the satellite is securely held in place during launch and the relative motion of the stages is restricted by the deployer.

The staging system is dormant for the vast majority of the mission and the mechanical parts are only used once, therefore the lifetime limiting factors are simple ageing. To meet radiation tolerance on long missions the electronics may need to be shielded or updated, but this is a straightforward task. The supercapacitors were sized for the worst case performance measured at the end of ESA's qualification testing where 800 specimen were held under vacuum at 55 °C for 625 days without any failures and therefore should have plenty of life margin. Creep of the plastic interrupter sheet could place an upper limit on the lifetime of the staging system and would require further testing. Wear of the mechanical interfaces due to thermal expansion cycling was shown to require decades for any effect in the worst case and is not of concern.

A secondary camera payload is included in the testing in this chapter as it is a part of the STEP-1 CubeSat mission payload suite and thus required in a test-as-you-fly process. The camera payload has two identical halves for redundancy, each with a Raspberry Pi Zero 1.3 single-board computer and an 8 megapixel camera module. The purpose of the camera payload is to record the stage separations on orbit at a high frame rate to confirm success, evaluate dynamics, and support outreach. When stowed for launch the cameras view out the sides of the spacecraft, however, once in orbit mirrors are extended and pivot to redirect the view of both cameras towards the propulsion unit.

5.2 Methods

5.2.1 Functional testing and separation dynamics

Functional testing was performed on the complete STEP-1 engineering model (EM) payload suite: the propulsion unit, the staging controller, and the camera payload. The propulsion unit consists of three thruster stages and the power processing unit (PPU), which generates the high-voltage power supply to the thrusters. In accordance with the test-as-you-fly philosophy, the payloads were integrated using their respective flight electrical and mechanical interfaces as shown in Figure 5.1. The propulsion unit uses custom interfaces while the staging controller and camera use the standard PC104 CubeSat form factor and data bus interfaces. A harness connects the stages and PPU to the staging controller for data and power. To operate the payloads, an interface adapter board was developed that can read from and write to the payloads' data interfaces and supplies the individual voltage channels required by the payloads. Testing was performed through a graphical user interface that was developed where payloads can be powered on and off, commands can be sent manually or programmed as macros, and housekeeping data is continuously recorded and displayed from the payloads.

Gravity offloading is necessary to characterise the separation dynamics of the stages during functional testing and to ensure the testing represents operation in the orbital environment. The gravity offloading system was designed to reduce the effect of gravity to at most $\pm 0.05g$ and not impart significant force on the separation mechanism through the requirements listed in Table 5.2. To enable functional testing during thermal vacuum testing the gravity offload system was designed fit inside the MIT Space Systems Laboratory 2-foot thermal vacuum chamber and allow a complete test-as-you-fly procedure to be performed without opening the chamber.

Table 5.2: Requirements on the gravity offloading system.

1 Reduce the net gravity on deployed stages to no more than 5% of the value on Earth.
2 Impart horizontal forces of no more than 5% of the separation spring force of 7.2 N.
3 Meet the force requirements for at least the first 40 mm of stage movement.
4 Mount all STEP-1 payload components in their flight configuration.
5 Allow both stages to deploy in sequence without user intervention.
6 Fit inside a 50 cm cube (to go inside the 2-foot thermal vacuum chamber).

An offloading strategy where only the deployable stages are suspended while the rest of the propulsion unit is fixed in place was selected. This does not capture the separation dynamics as well as a fully suspended system would (see e.g. [231]) but simplifies the imple-

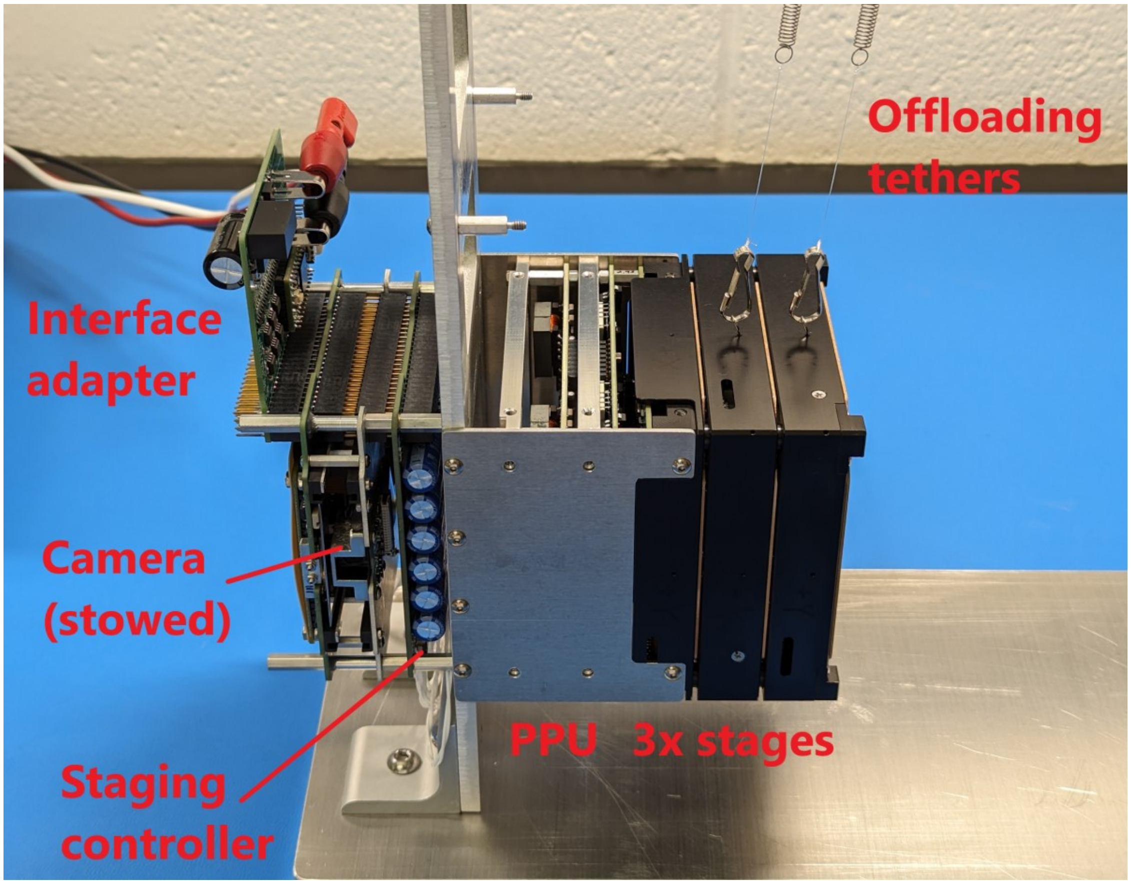

Figure 5.1: The test-as-you-fly configuration of the engineering model for testing. The propulsion unit consists of the three stages and the PPU, and the staging controller provides the signals and power to release the stages. The camera is a secondary payload to record stage separation on orbit and the interface adapter converts the flight data and power interfaces to a single serial connection and 5 V supply.

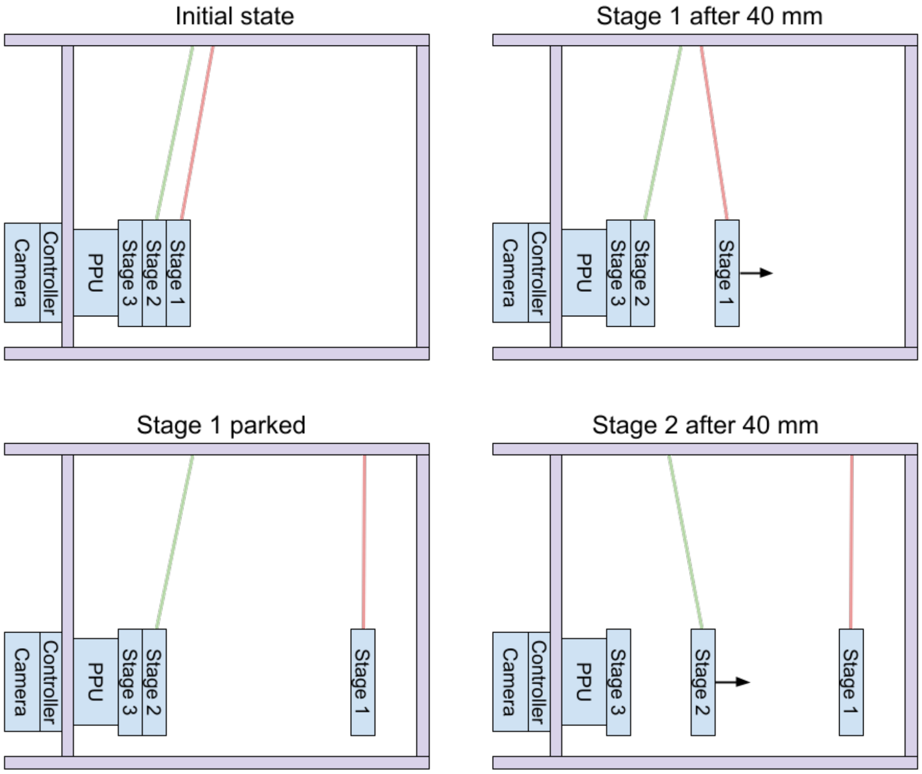

Figure 5.2: Conceptual drawing of the gravity offload system.

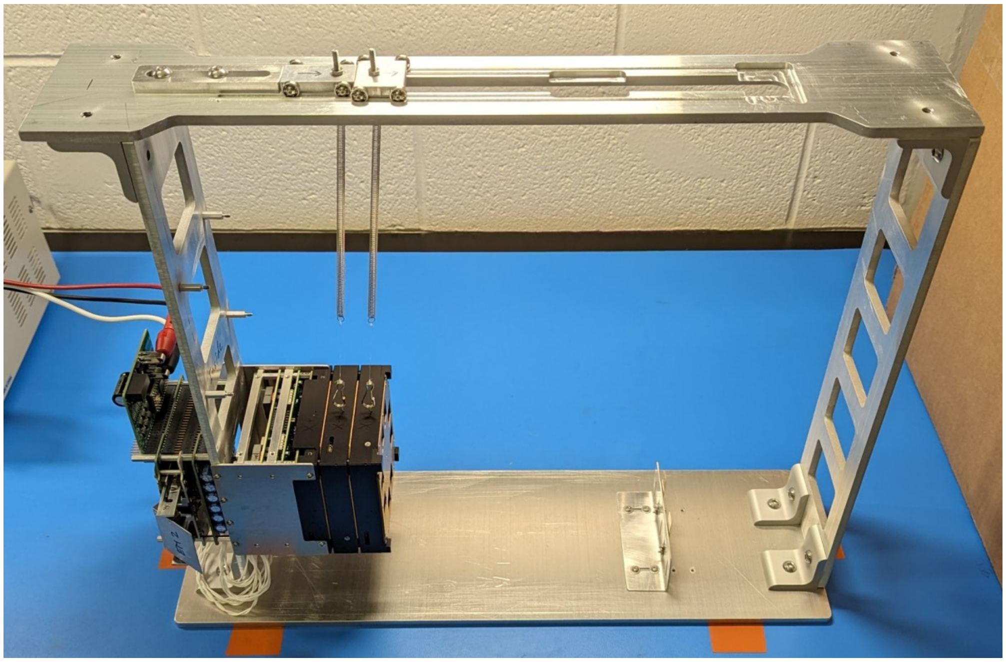

Figure 5.3: Overview image of the gravity offloading system. The STEP-1 flight configuration engineering model is mounted on the left. Two tethers attached to "skateboards" that ride in the top plate compensate for gravity on the deployable stages. In this picture the camera payload is in the deployed state, where mirrors are extended to view the propulsion unit.

mentation, especially as two separations must be performed in sequence. Since the mass of the deployed stage is only approximately 5% of the satellite's mass the reaction on the satellite can be neglected during testing. Figure 5.2 shows a conceptual drawing of the gravity offload system where the propulsion unit is mounted horizontally in its flight configuration with tethers offloading the weight on the stages from their initial position through a 40 mm "swing", meeting requirements 1-3. After the testing swing, the stage tethers' top pivot points automatically move forward to park the stages away from the remaining components of the propulsion unit to meet requirement 5.

The offloading system was inspired by [232], where long soft springs as seen in Figure 5.3 were used to provide a near-constant offloading force. The selected spring has a rate of 0.016 N/mm and a length of approximately 190 mm when holding the weight of one stage. One end of the spring was attached to an adjustable screw to tune the length of the tether while a short segment of string attached the stage to the opposite end of the spring. The tethers' lengths were adjusted such that the deployable stages rest within ±1 mm of the height of the fixed third stage and the attachment points on the stages were adjusted until the stages hung plumb. The tops of the offloading tethers were attached to small "skateboards" that can roll freely with ball bearings along the gravity offloading system's top plate and rest against a stop that places the top pivot 25 mm forward of the bottom pivot. The change of length due to the tether's angle and height adjustment tolerance leads to a total gravity offloading error of no more than 0.037 N or 2% of g. The horizontal force imparted by the tether's angle is no more than 0.21 N or 3% of the separation spring force. The effect of atmospheric drag is less than 0.01 N at the maximum separation speed of 1 m/s and is therefore negligible. When a deployed stage has moved through the testing swing, its momentum will roll the skateboard forward until it drops into a pocket; parking it out of the way.

The separation dynamics were captured using an external motion-tracking camera, shown in Figure 5.4a, at 120 Hz with an exposure time of 0.2 ms to minimise motion blur through an 85 mm $f/2$ lens. Know dimensions of the propulsion unit were used to establish a calibrated pixel coordinate system and the top corners of the stages were manually tracked as shown in Figure 5.4b for approximately 100 mm or until the top plate of the gravity offloading rig blocked the view. Recording from the top instead of the side is less influenced by vertical movement (due to residual effective gravity) or tipping (due to the horizontal force) of the stages that the gravity offload rig may cause. The motion-tracked data were converted into forward and crosswise (up and right respectively in Figure 5.4b) velocities by a linear fit though all data points between 16 to 40 mm separation, corresponding to when the separation springs stop making contact and the end of the testing swing respectively. This was performed independently for the left and right corners, and the total separation velocities

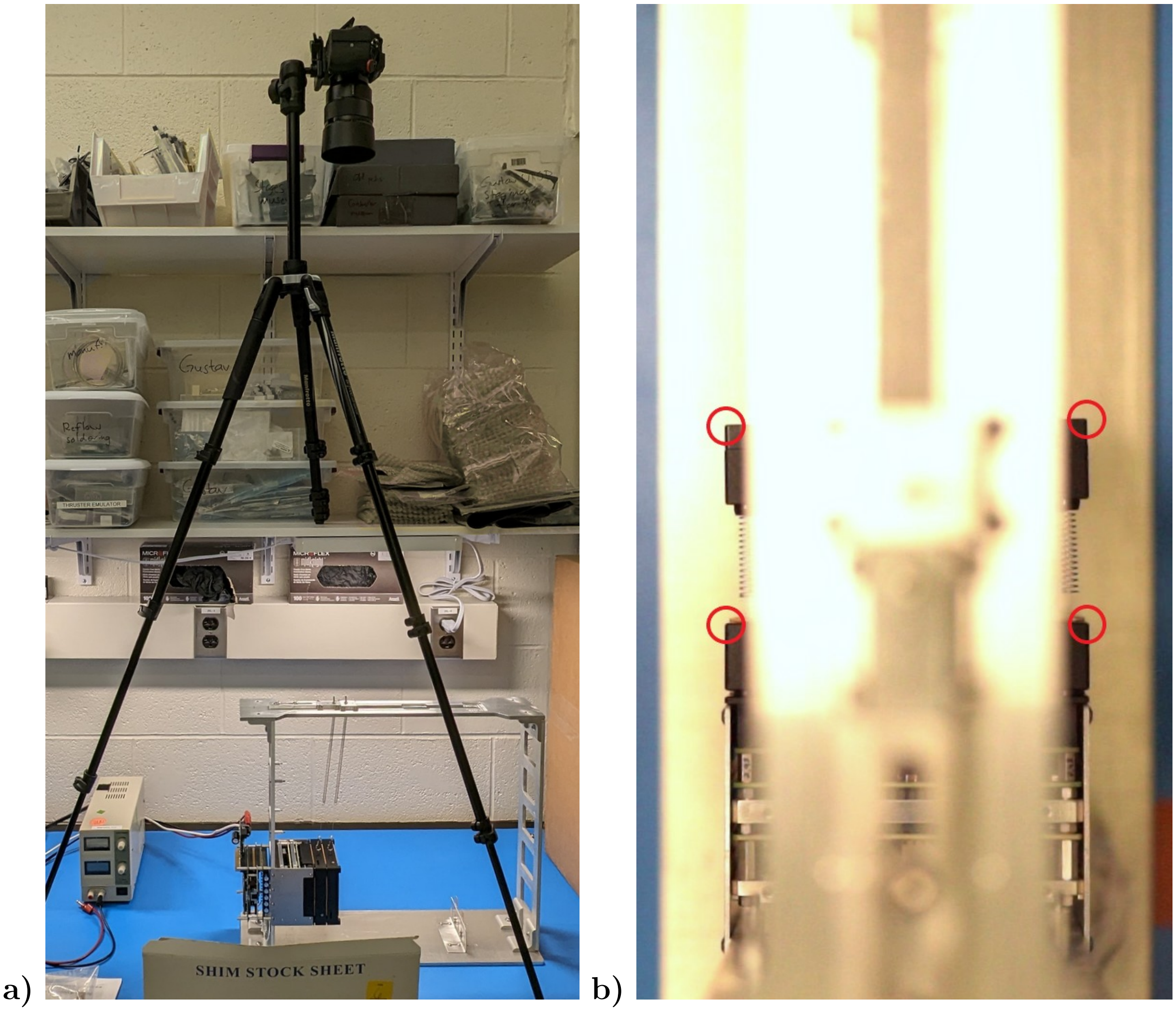

Figure 5.4: The motion-tracking setup for stage separation dynamics. a) Camera positioned 1.2 m above the stages. b) View from the camera with the tracked edges circled in red, after the first stage has separated by approximately 30 mm.

were taken as the average, while the difference in left and right forward velocities were used to calculate the tip-off rate.

Four functional testing sets were performed on the stages of which the dynamics were recorded for the first three. First, a complete test-as-you-fly functional test including operating the camera payload was performed. Subsequently, two functional test were performed after vibration testing and static load testing on the propulsion unit respectively. Finally, functional testing was performed during thermal vacuum testing, however, no external separation dynamics tracking was available inside the thermal vacuum camber.

5.2.2 Vibration testing

Random vibration testing was performed on the assembled propulsion unit in three axes, testing for changes in spectral response before and after each run, and functionality after all axes were tested. The testing followed the NASA GEVS acceleration spectral density (ASD) shape, but scaled down from $14g$ RMS to $4g$ RMS due to unexpected unavailability of higher power facilities during the test campaign. The mounting fixture and expected results through finite element analysis are discussed in Section 4.4.3. A *Controlled Vibration EDP-1212L-8* vibration platform was used with its four corner actuators driven from the same signal by two *Crown DSi 1000* amplifiers. The propulsion unit was mounted to the middle of the platform as shown in Figure 5.5, with a stiffening ring around it to increase the natural frequency of the vibration platform itself to above 1000 Hz. A closed-loop feedback controller shaped the input noise signal to generate a specified test ASD at a reference accelerometer, and three sample accelerometers recorded the propulsion unit's response. The accelerometers were *PCB Piezotronics* model *352C22* with a *482C15* signal conditioner recorded at 10 kHz with a *National Instruments USB-6002* data acquisition card.

Each test started with a 30 s hold at $0.1g$ RMS to record the initial spectral response, then gradually ramped up to $4g$ RMS for a 70 s testing hold, and ramped down for a second 30 s hold at $0.1g$ RMS to record the post-test spectral response. The data was averaged for the respective holds to create three spectra: pre-test, peak load, and post-test. The pre- and post-test spectra were compared to ensure nothing had come loose or shifted in the payload, and the peak load spectra was compared to the FEA predictions. After all three axes were tested the propulsion unit was subjected to a complete functional test.

The staging controller and camera payload were tested separately in a similar manner to $5g$ RMS and functionally tested afterwards, without any noticeable effects.

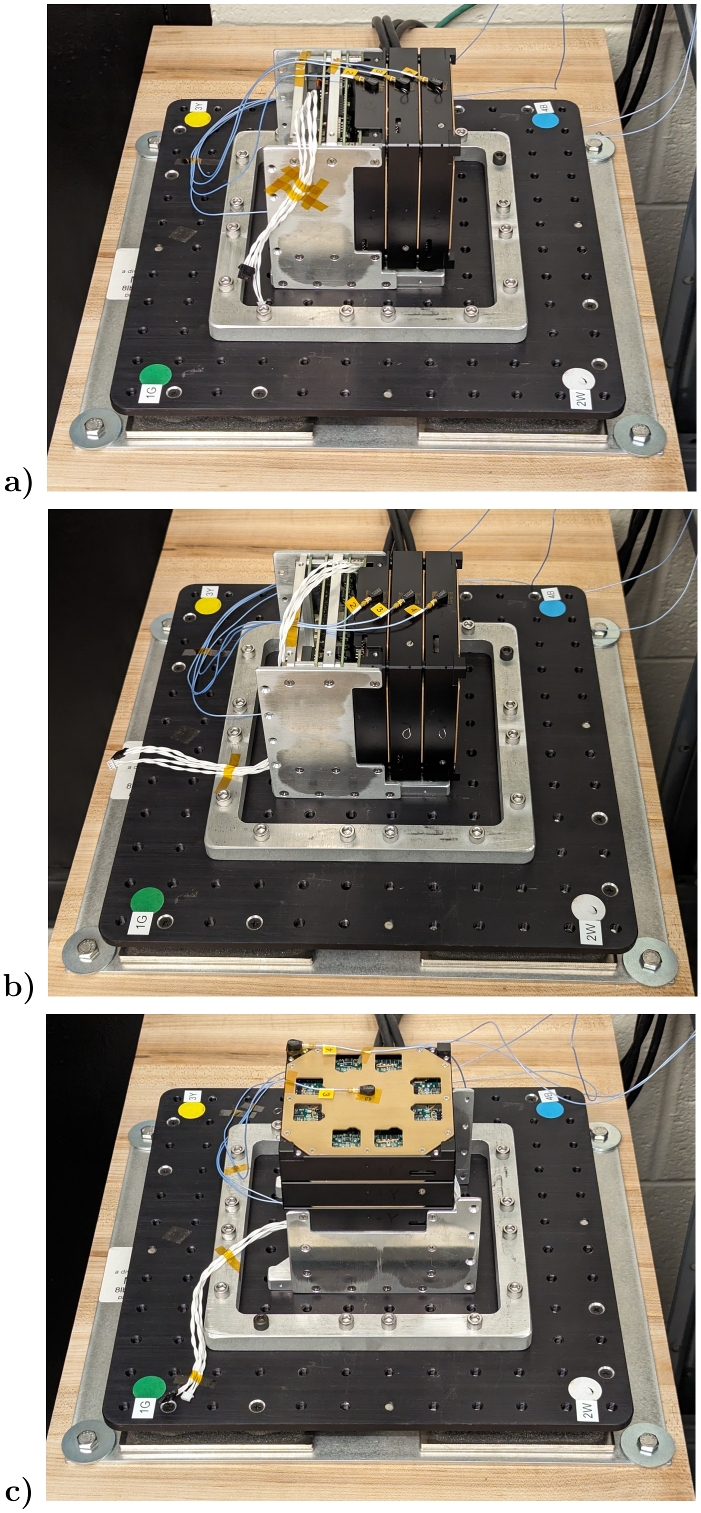

Figure 5.5: Vibration testing setup with the propulsion unit in its fixture and the platform stiffening ring. a-b) For X and Y axis testing respectively with one accelerometer on each stage. c) For Z-axis testing with one accelerometer on the top stage shield, one on the corner “foot”, and one on the PPU HV circuit board (not visible).

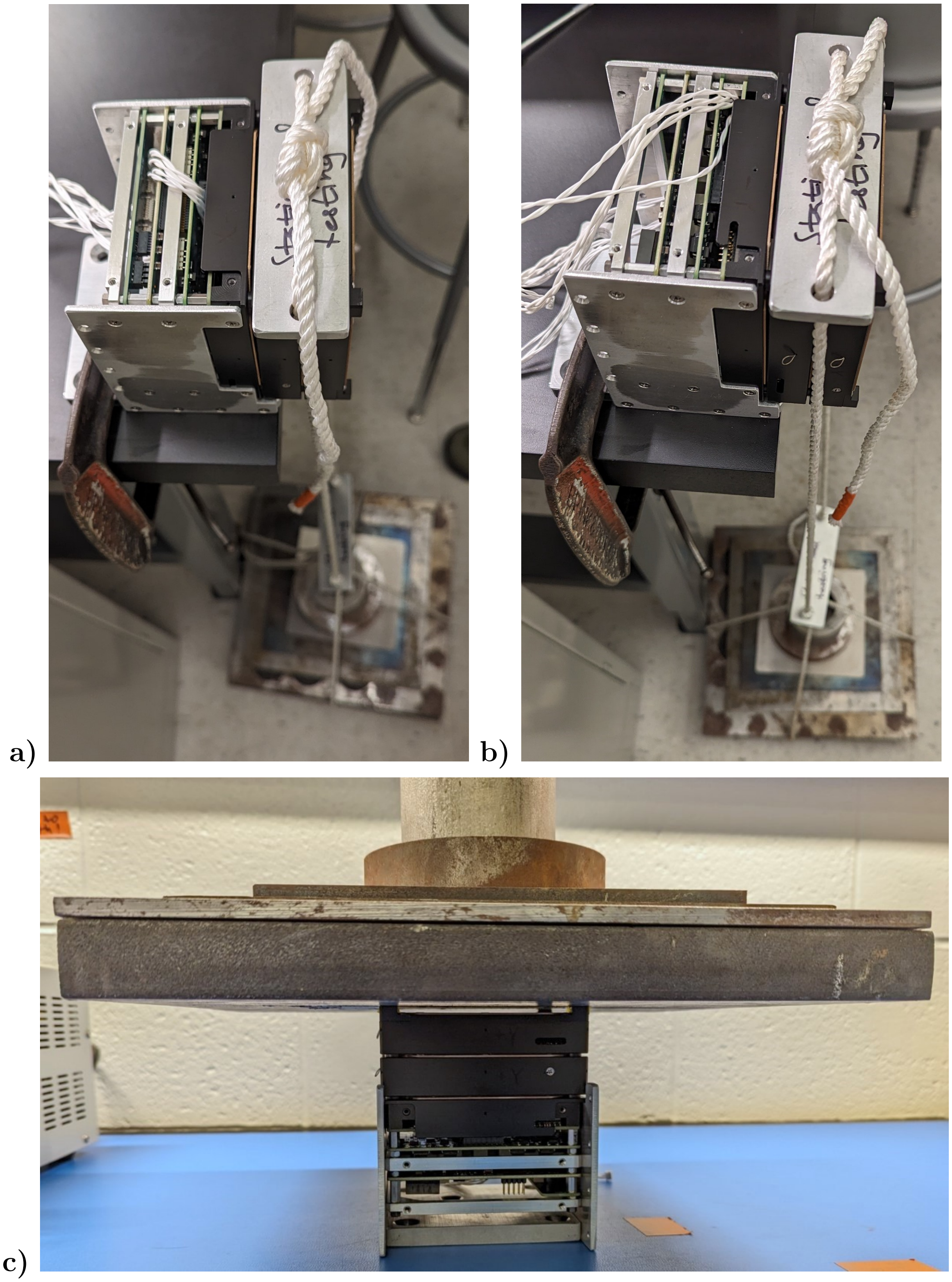

Figure 5.6: Static load testing setup. a) On $-X$ side. b) On $-Y$ side. c) On $+Z$ side.

5.2.3 Static load testing

Static load testing was performed on the assembled propulsion unit in three axes. The static load testing is necessary as the propulsion unit is a part of the satellite's external load-bearing structure. The propulsion unit was designed to take a worst-case load of 320 N, corresponding to the satellite's total weight at $8g$, entirely on the deployable stages with a safety factor of two as discussed in Section 4.4. A stack of scrap steel with a total mass of 32.6 kg was used to load the stages as shown in Figure 5.6. A $13{\times}3.5$ cm^2 flat plate and ropes (weighing c. 0.3 kg) were used to apply the loads from X and Y while the stages were cantilevered off the edge of a table.

During static loading the deformations on the structure were measured and functional testing was performed after all axes were tested. To account for the potential cone sticking concerns discussed in Section 4.3.1 the Z-axis test was performed last and handling was minimised when setting up for the functional test, such that any potential cone sticking would be in the worst-case state.

5.2.4 Thermal vacuum testing

The 2-foot thermal vacuum chamber in the MIT Space Systems Laboratory was used for testing. The chamber was evacuated with a turbomolecular pump capable of an ultimate pressure of c. 1 mPa backed by a mechanical roughing pump. The walls of the chamber are polished stainless steel that remain at room temperature while a large insulated base plate is cooled or heated to a desired temperature. Cooling is performed by feeding liquid nitrogen though pipes bonded to the bottom of the base plate, with closed-loop feedback to hold a desired temperature. Heating is achieved by electric heaters bonded to the top of the base plate dissipating up to 130 W that are controlled manually to ramp or hold temperature. The peak temperature ramp rates of the payload were approximately 0.5 °C/min when cooling and 0.2 °C/min when heating, limited by the thermal coupling of the payload to the chamber base plate and the heater power respectively.

Thermal vacuum testing was performed on the complete test-as-you-fly configuration of the STEP-1 system as shown in Figure 5.7 with all components configured identically to the functional testing case described in Section 5.2.1. Thermal insulation (aluminium on polyimide tape) was added to the stages and the bracket that mounts the propulsion unit to the offloading rig to recreate a typical bus thermal envelope. Six external temperature sensors were added to the test structure and payloads, located at: 1) the chamber cooling/heating base plate, 2) the propulsion unit's mounting location on the offloading rig, 3) the propulsion unit's PPU, 4) the propulsion unit's bottom stage, 5) the camera secondary payload, and 6)

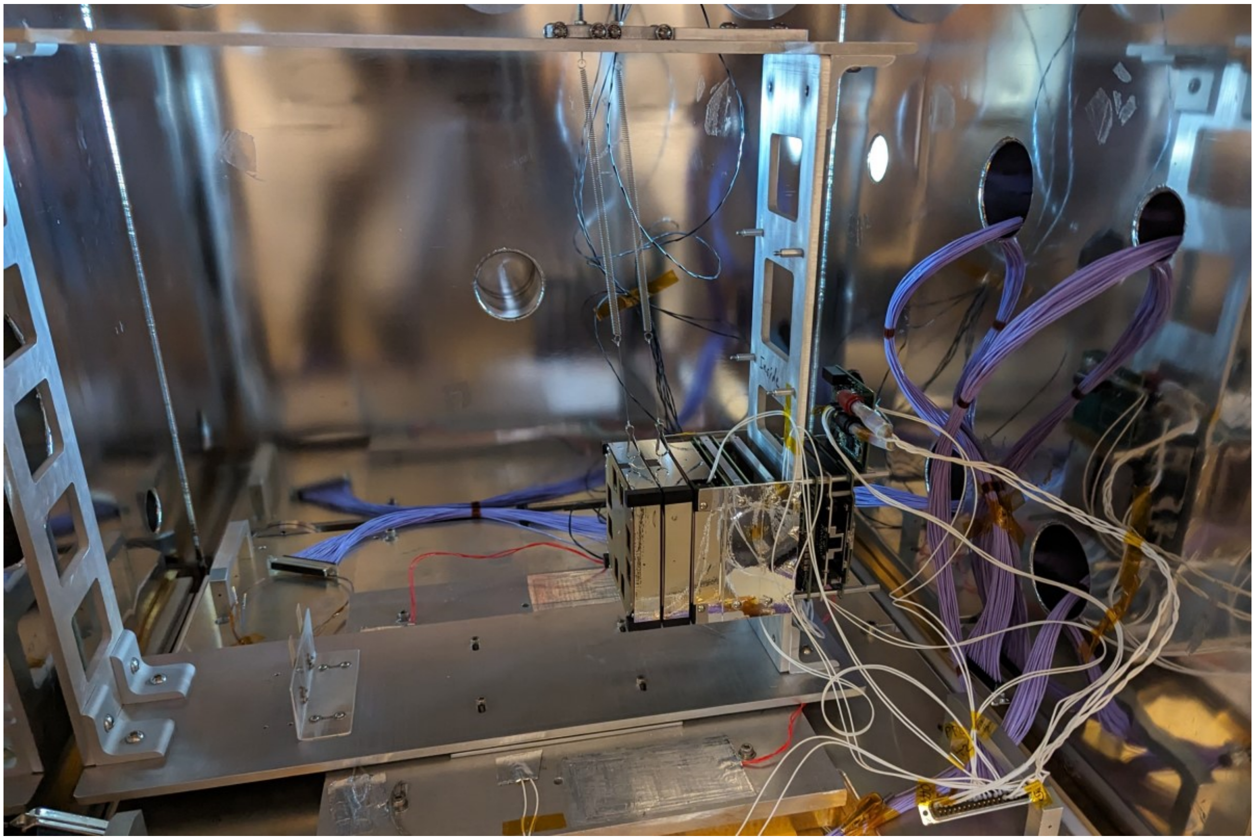

Figure 5.7: Picture of the thermal vacuum chamber setup before starting the test.

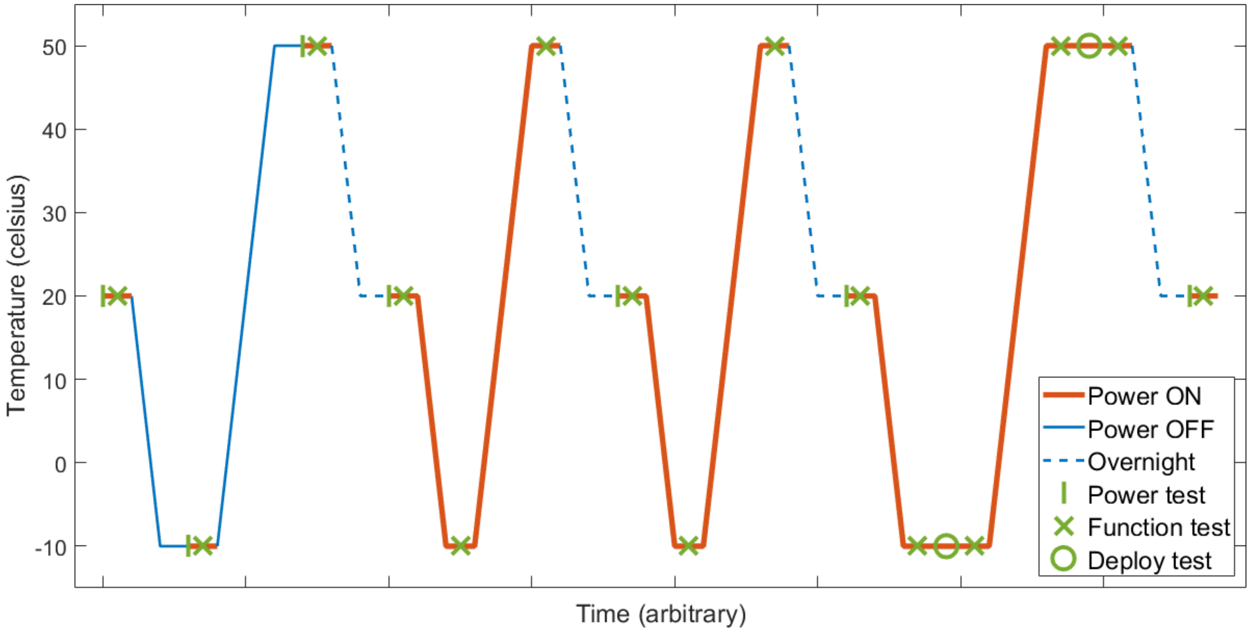

Figure 5.8: Overview of the thermal vacuum test plan. The test includes power on at cold and hot, thermal balance at cold and hot, four thermal cycles, and deployment testing at cold and hot.

the interface adapter board. The reference temperature during the test was the average of the PPU, bottom stage, and camera temperature sensors. *Laird Tpli 220* thermal interface pads were used between the chamber base plate and the offloading rig and under the L-brackets in the offloading rig to improve the thermal coupling of the system.

The test proceeded according to the plan shown in Figure 5.8. The temperature range of −10 to 50 °C was selected because it is the operational temperature limit of the PPU. High vacuum (<10 mPa) was reached before the testing began and was held throughout the duration of the testing. Four thermal cycles were performed with cooling followed by heating across four days of testing, where the system was left overnight after heating. In the first cycle the system was powered off during ramping and allowed to equilibrate at the extremes to determine the passive thermal balance of the complete system and functional tests were performed at the cold and hot temperatures. For the remaining three cycles the system was powered on during the entire test, with functional testing at the extremes. In the fourth and final cycle the cold and hot temperatures were held for an extended functional test that included deploying one stage at each temperature extreme to demonstrate the hold-down and release mechanism's operating range. A last functional test was performed after bringing the system to room temperature the following day.

Videos of the stage separations in the thermal vacuum chamber were recorded with the secondary camera payload while a flashlight illuminated the inside of the chamber through a small viewport.

5.3 Results

5.3.1 Functional testing and separation dynamics

All eight stage separations during functional testing proceeded nominally, with pictures shortly after separation shown in Figure 5.9 for the six motion-tracked tests and Figure 5.16 for the test in thermal vacuum. The measured separation velocities and tip-off rates from motion-tracking are shown in Table 5.3, with the raw data and linear fits plotted in Figure 5.10. The separation velocities were 0.47 to 0.70 m/s, which is similar to but lower than the prediction of 0.59 to 0.89 m/s in Section 4.3.1 and matches the scaled results from early prototype testing of 0.64 m/s [233]. Assuming the satellite bus has a mass of 4 kg, the linear impulse on the bus is negligible at 0.02 to 0.04 m/s, i.e. the orbit of the spacecraft itself is preserved.

The stage separation may cause the satellite to tumble due to the tip-off rate of the stage that was up to 53 °/s (0.93 rad/s or 6.8 s/revolution or the crosswise velocity of up to

0.088 m/s. The moments of inertia around the X and Y axes of the stages are approximately 170 kg/mm^2 and therefore the maximum measured angular momentum of a deployed stage was 0.16 mN m s. The crosswise velocity of a released stage imparts additional angular momentum on the host spacecraft, where a 3U CubeSat with a centre of mass in the geometric centre is assumed. The worst measured crosswise velocity would impart 2.6 mN m s of angular momentum to the CubeSat, giving a worst case total angular momentum of less than 3 mN m/s. The angular momentum is less than a typical CubeSat reaction wheel's storage capacity, but depending on the available wheel torque and responsiveness of the attitude control system it may be sufficient to cause tumbling. The maximum tumble rate depends on the satellite's moment of inertia, which for a 3U CubeSat of 4 kg is around 32.000 kg/mm^2 around the X or Y axis, resulting in a tumbling rate around 5 °/s should the attitude control system be unable to respond immediately.

The cause of the tip-off rate and crosswise separation velocity is likely inconsistent drag when the interrupter sheets are pulled out during the first few mm of travel. As seen from the separation velocities in Figure 5.10b, the early acceleration is not synchronised between the left and right sides, causing the large crosswise velocity. The uneven separation is worse on the EM version than the final prototype and measurements show that the EM interrupter connectors are preloaded approximately 0.2 mm more, supporting the interrupter as the root cause. With a more careful control of the interrupter preload during manufacturing the crosswise separation velocity can be reduced significantly.

Table 5.3: Stage separation dynamics recorded for six separations during the testing campaign.

Test	Stage	Forward vel.	Crosswise vel.	Tip-off rate
During functional testing	First	0.57 m/s	0.008 m/s	9.5 °/s
	Second	0.70 m/s	−0.042 m/s	53 °/s
After vibration testing	First	0.47 m/s	−0.088 m/s	−39 °/s
	Second	0.63 m/s	0.019 m/s	34 °/s
After static load testing	First	0.62 m/s	0.024 m/s	−9.6 °/s
	Second	0.68 m/s	0.002 m/s	52 °/s

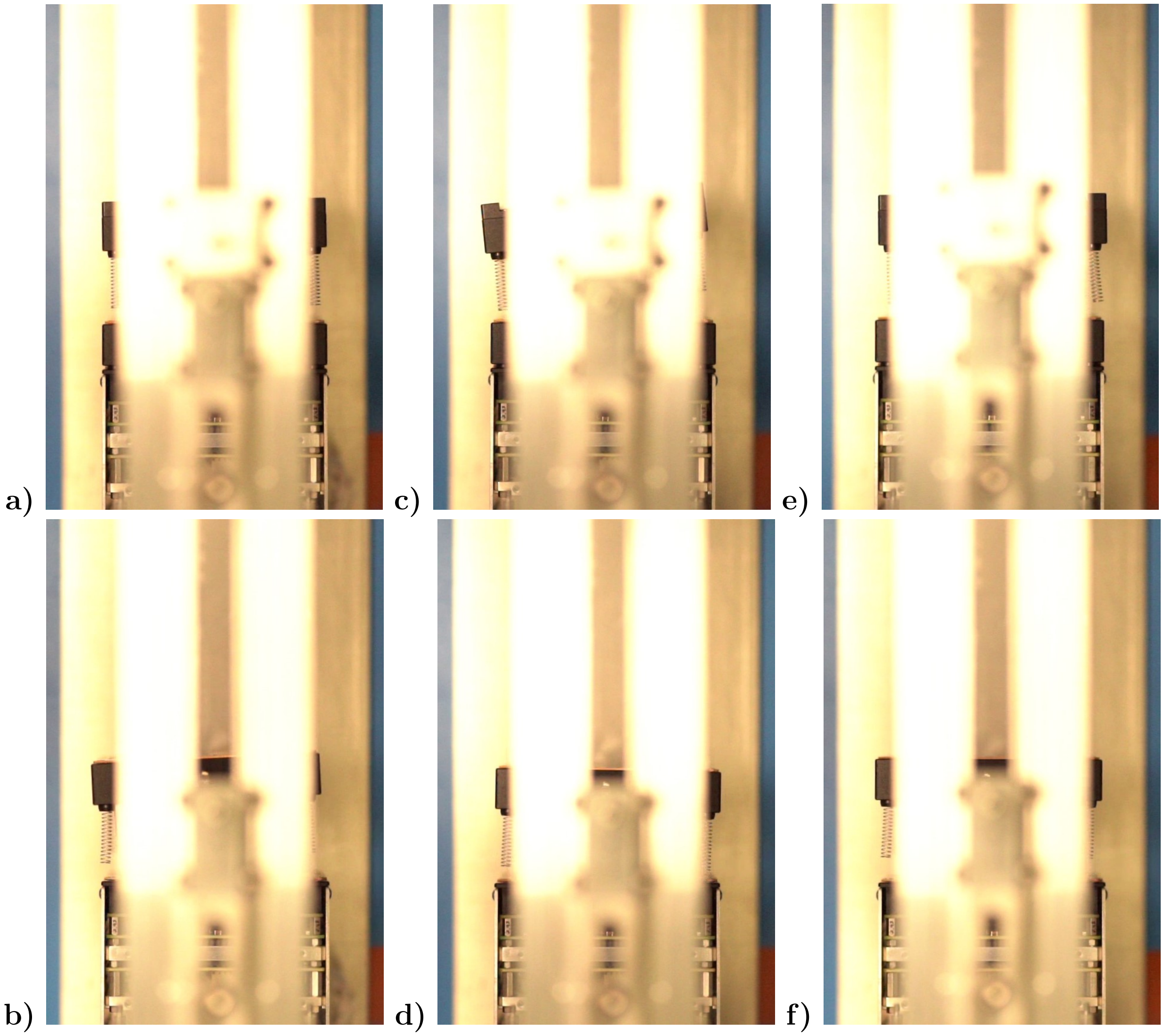

Figure 5.9: Images of the stage separation after approximately 30 mm of motion for all six tests. a-b) First and second stage during functional testing. c-d) First and second stage after vibration testing. e-f) First and second stage after static load testing.

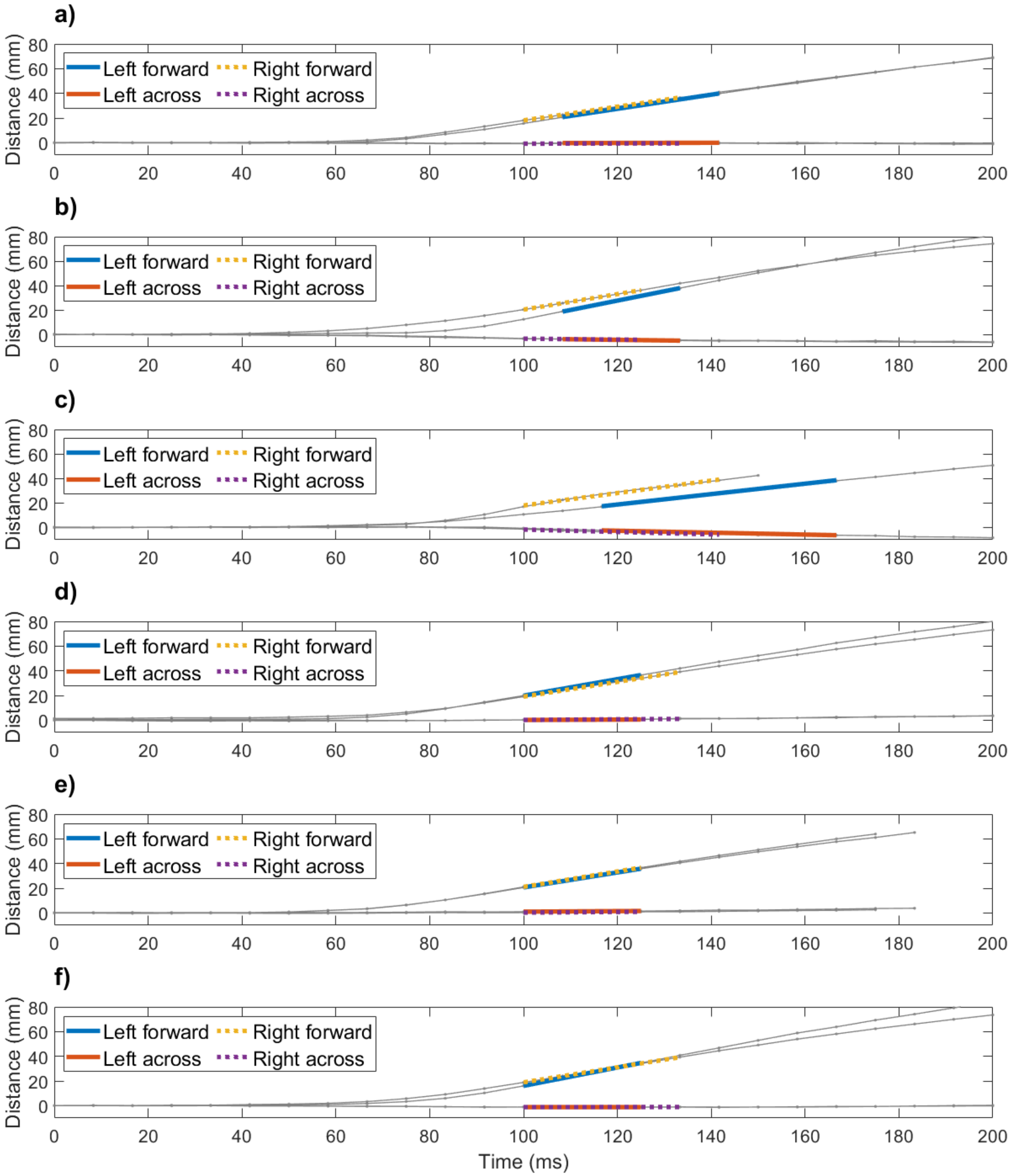

Figure 5.10: Motion tracking data for stage separation dynamics testing. The thin lines show the raw data and the thick lines show the linear fits used to find the separation velocities. a-b) Top and middle stage during functional testing. c-d) Top and middle stage after vibration testing. e-f) Top and middle stage after static load testing.

5.3.2 Vibration testing

The spectral responses from vibration testing in each axis are shown in Figures 5.11 through 5.13. In all cases the responses before and after testing were similar, verifying that no structural changes occurred during the test. In all of the test cases the vibration table struggled to drive the base plate to the target excitation at frequencies above the lowest mode of the test articles. The deviation of the base plate's ASD from the target excitation, as measured by reference accelerometer, means that the high-frequency spectral features may be unreliable. The X and Y axis test results are nearly identical as expected from the symmetrical structure.

In the X and Y testing the lowest frequency was around 470 Hz in both axes, which is less than half of the model results in Section 4.4.3 at 1215 Hz. The lower frequency in the experiment compared to the model is expected as the mating surfaces between the stages were bonded in the model, whereas the actual stages are held together with the thin hold-down wires. The lowest mode showed a stable frequency and amplitude between the $0.1g$ RMS mode studies and the $4g$ RMS maximum intensity studies, demonstrating that the higher intensity does not cause clattering between the mating interfaces. A limitation of these results is that the absence of clattering could not be verified at the planned full $14g$ RMS test intensity due to unexpected unavailability of facilities.

The Z axis testing results align well with the expected results from the modelling in Section 4.4.3. The lowest mode observed is the piston mode of the PPU HV circuit board at 373 Hz, followed by the piston mode of the stages moving together at 636 Hz, which are both around 25% stiffer than the model predictions. No significant differences are seen between the $0.1g$ RMS mode studies and the $4g$ RMS maximum intensity study, except for distortions in the base plate target excitation. The PPU HV circuit board shows a smaller second mode at 635 Hz that may be the resonance of the adjacent circuit board of the PPU transferred though their board-to-board connectors.

Following the three axes of random vibration testing successful functional testing was performed as shown in Section 5.3.1.

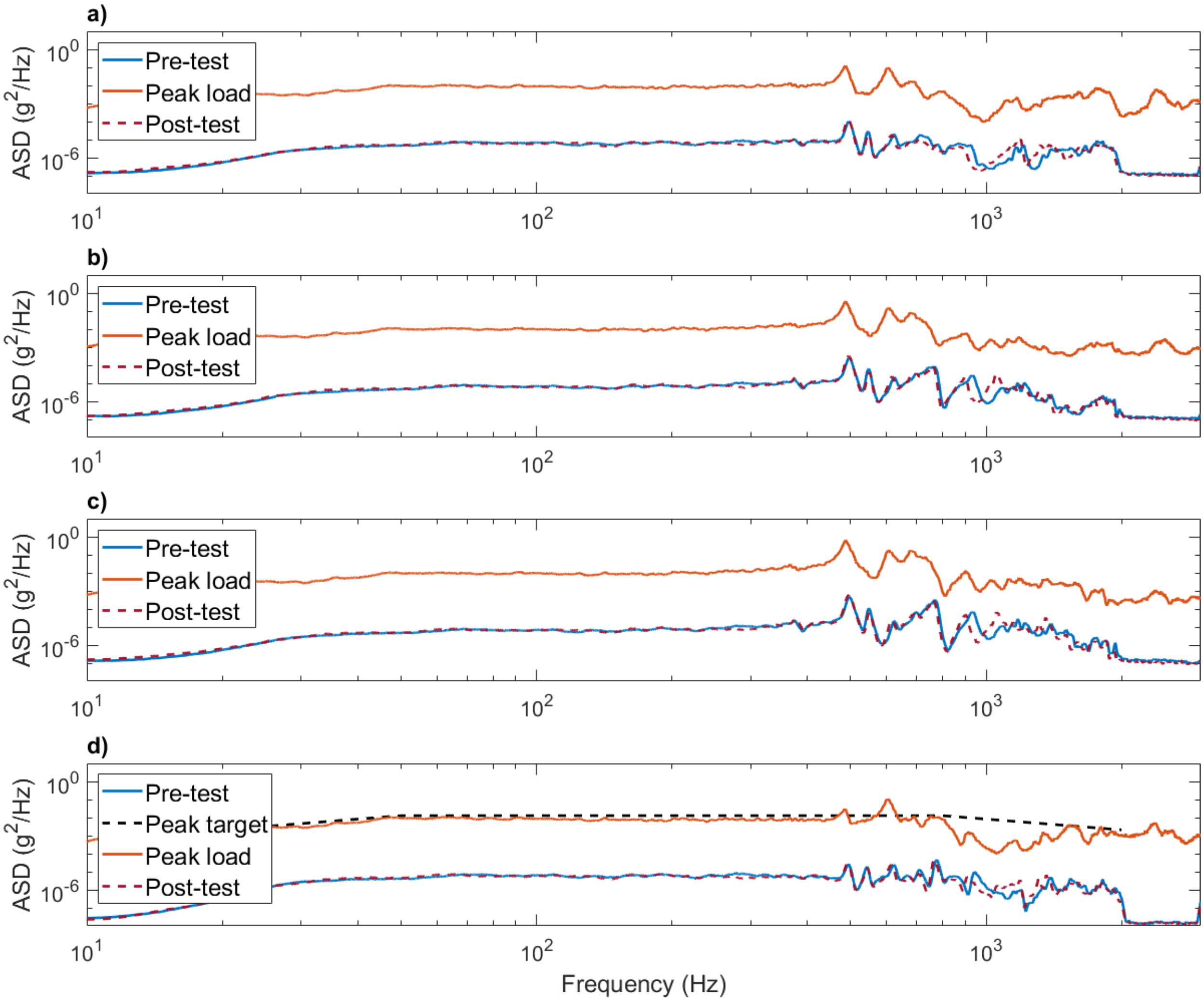

Figure 5.11: Acceleration spectral densities (ASD) measured during X-axis random vibration testing. A $0.1g$ RMS mode study was performed before and after the testing hold at $4g$ RMS for 70 s. a) Accelerometer on the bottom stage side wall. b) Accelerometer on the middle stage side wall. c) Accelerometer on the top stage side wall. d) Reference accelerometer on the fixture base plate shown with the target base excitation.

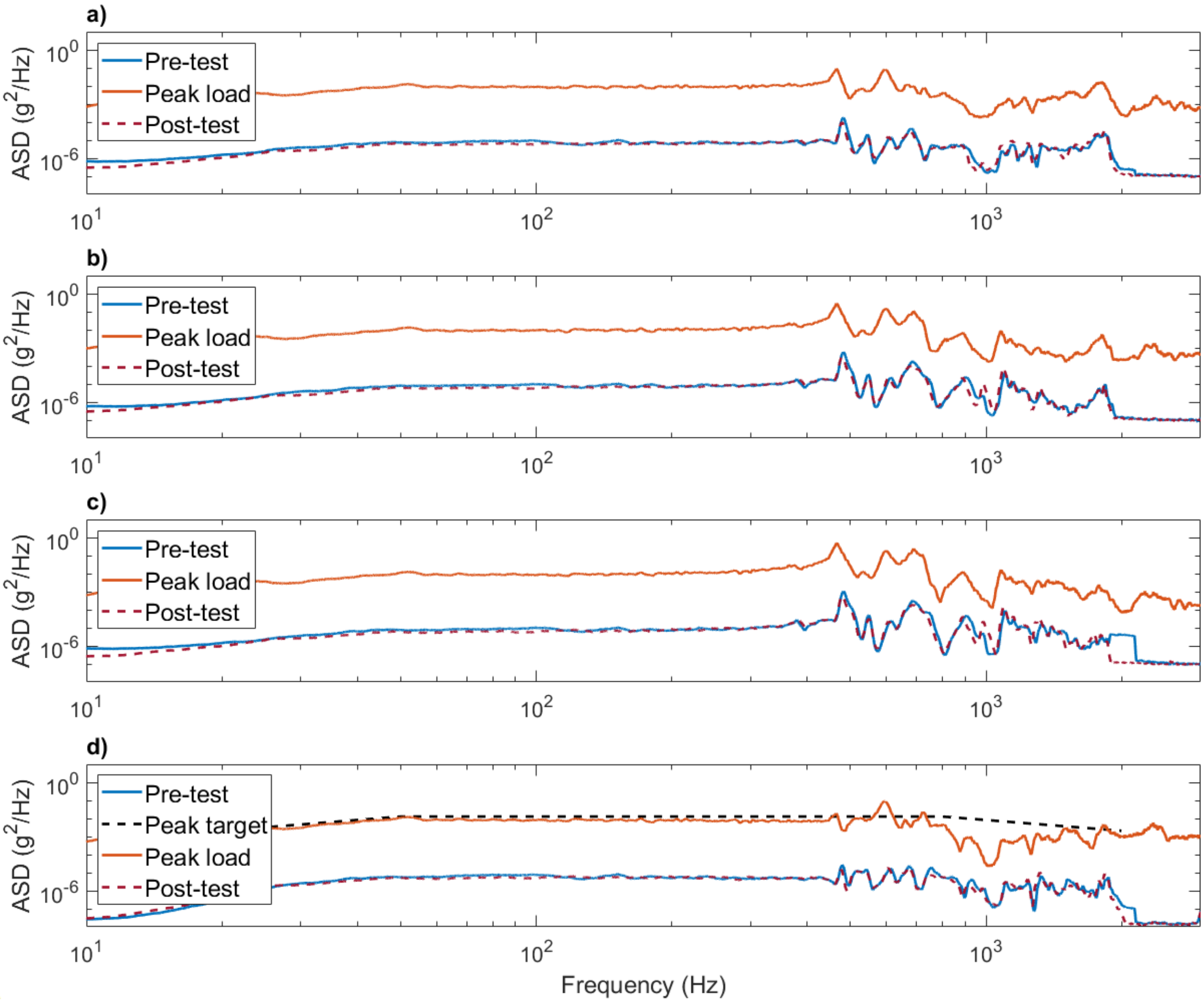

Figure 5.12: Acceleration spectral densities (ASD) measured during Y-axis random vibration testing. A $0.1g$ RMS mode study was performed before and after the testing hold at $4g$ RMS for 70 s. a) Accelerometer on the bottom stage side wall. b) Accelerometer on the middle stage side wall. c) Accelerometer on the top stage side wall. d) Reference accelerometer on the fixture base plate shown with the target base excitation.

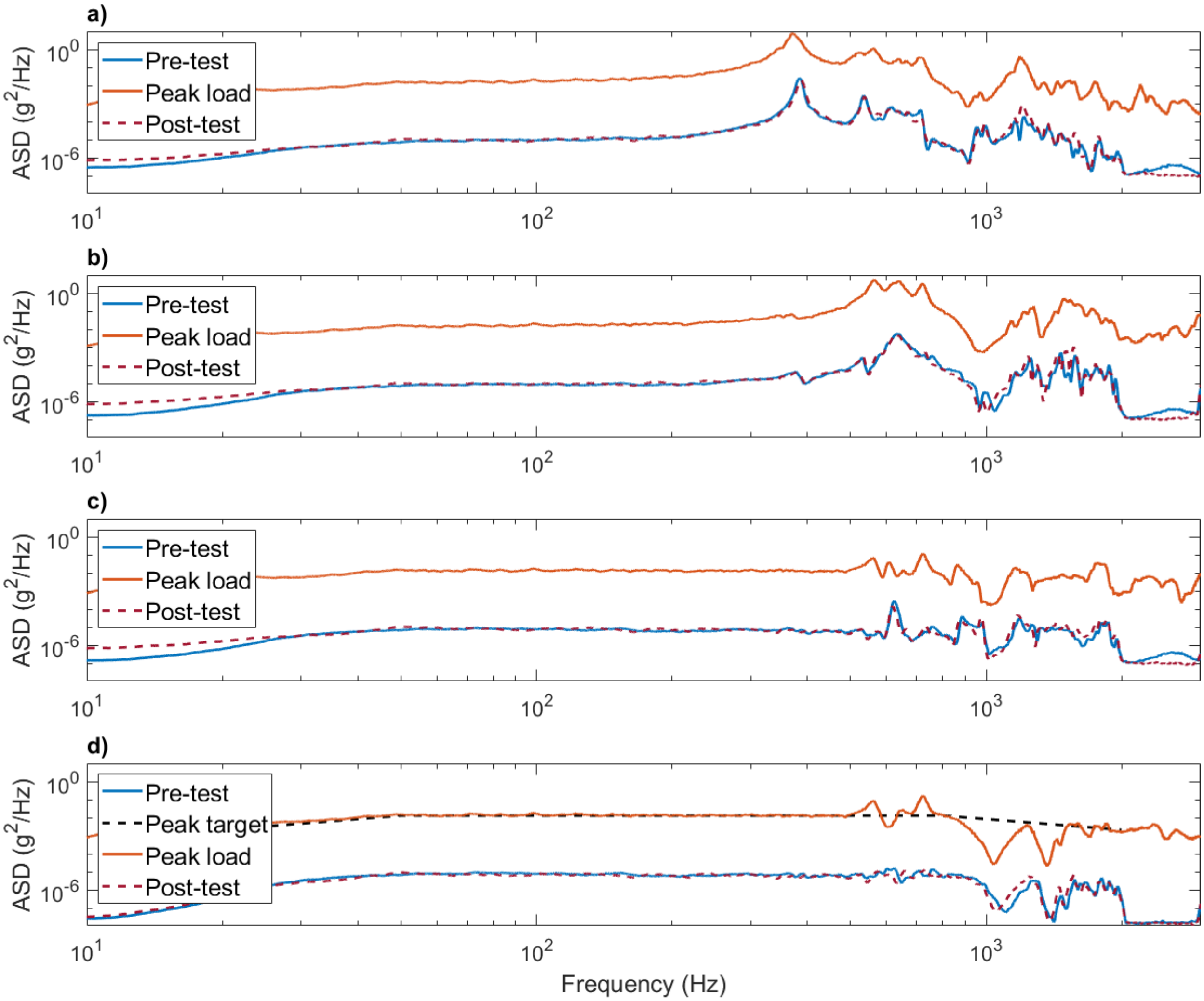

Figure 5.13: Acceleration spectral densities (ASD) measured during Z-axis random vibration testing. A $0.1g$ RMS mode study was performed before and after the testing hold at $4g$ RMS for 70 s. a) Accelerometer on the PPU HV circuit board. b) Accelerometer on the top stage shield. c) Accelerometer on the CubeSat “foot”. d) Reference accelerometer on the fixture base plate shown with the target base excitation.

5.3.3 Static load testing

The static load of approximately 320 N was applied, in order, on the $-X$, $-Y$, and $+Z$ faces of the top and middle stages. During the $-X$ and $-Y$ loading, small gaps in the mating interface of 0.54 mm and 0.66 mm respectively opened up. These gaps were larger than the predicted value of 0.16 mm from FEA (see Section 4.4.2). After the $-X$ and $-Y$ loading the stages settled back to their nominal positions but the hold-down tension was noticeably lower, i.e. less force was required to open a gap again but the maximum gap was consistent. The reduced tension indicates yield in the hold-down wires or structure which may explain the larger than predicted gap. $+Z$ loading was uneventful, with no apparent effect on the structure.

After static load testing the payload underwent successful functional testing as demonstrated in Section 5.3.1 and the stage mating interfaces did not have any visible damage.

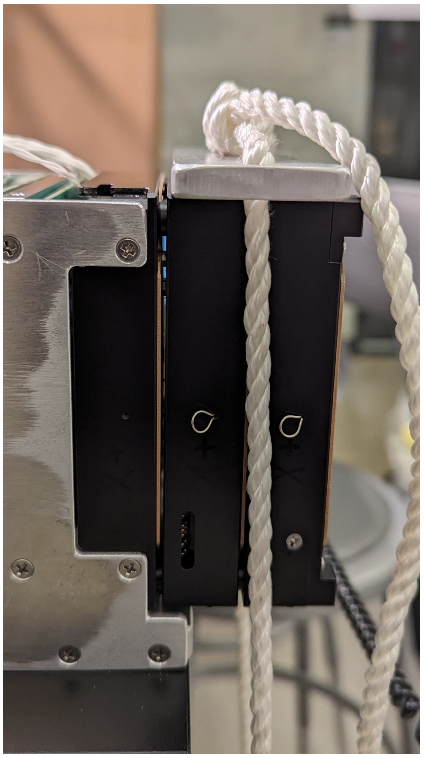

Figure 5.14: Picture of the 0.66 mm gap caused by the static load from $-Y$ side.

5.3.4 Thermal vacuum testing

The temperatures during the four thermal vacuum testing cycles are shown in Figure 5.15. All functional tests during the testing proceeded nominally, including a final test at room

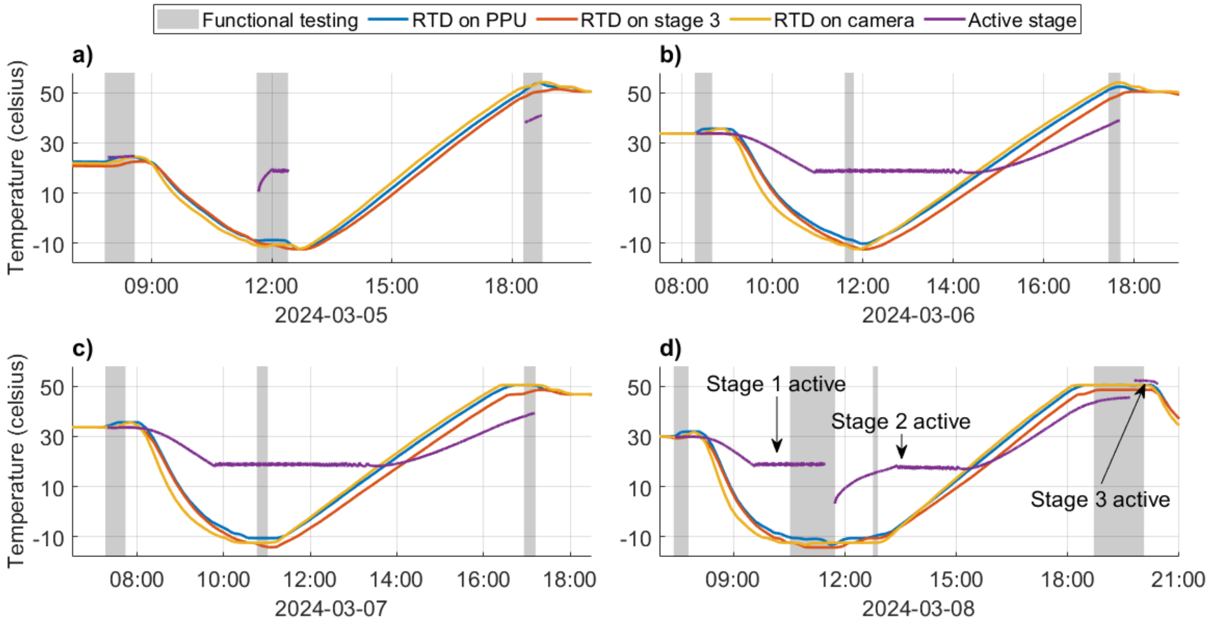

Figure 5.15: Temperature logs for the four thermal vacuum cycles. a) First cycle where the system was off during ramping and allowed to settle before powering on. b-c) Second and third cycles when powered on. d) Fourth cycle when powered on and deployment of the stages were performed at cold and hot temperatures.

temperature the morning after the fourth cycle. The active stage data shows the temperature of the active (i.e. outermost) stage as reported by telemetry and is only available when the payload is powered on. As seen in Figure 5.15a, the first stage was at approximately 10 °C when it was powered on after the rest of the system had settled to −10 °C, confirming the poor thermal transfer to the stages. The thermostat controlled thruster heaters increased the first stage temperature above the 18 °C set point within 20 min. The system was powered off again and brought to settle at 50 °C before powering on, where the stage showed an initial temperature of 40 °C. It is clear that the active stage temperature had not yet settled as it continued to increase in temperature. The two subsequent thermal cycles while powered on were uneventful and it is clear that the stage thermostat works as designed.

The stage deployment at −10 °C is shown in Figure 5.16a and was performed in a cycle where payload had been powered on and therefore the thruster heater kept the first stage board temperature above 18 °C, as would be the case on orbit. The second stage automatically activated as designed and was at a temperature of 3 °C. The second stage was allowed to warm up to 15 °C before functional testing as this corresponds to the minimum thruster operating temperature. The second stage deployment is shown in Figure 5.16b and was performed at 50 °C when the second stage temperature was 46 °C. The third stage was 52 °C when it activated and functional testing was performed immediately following deployment.

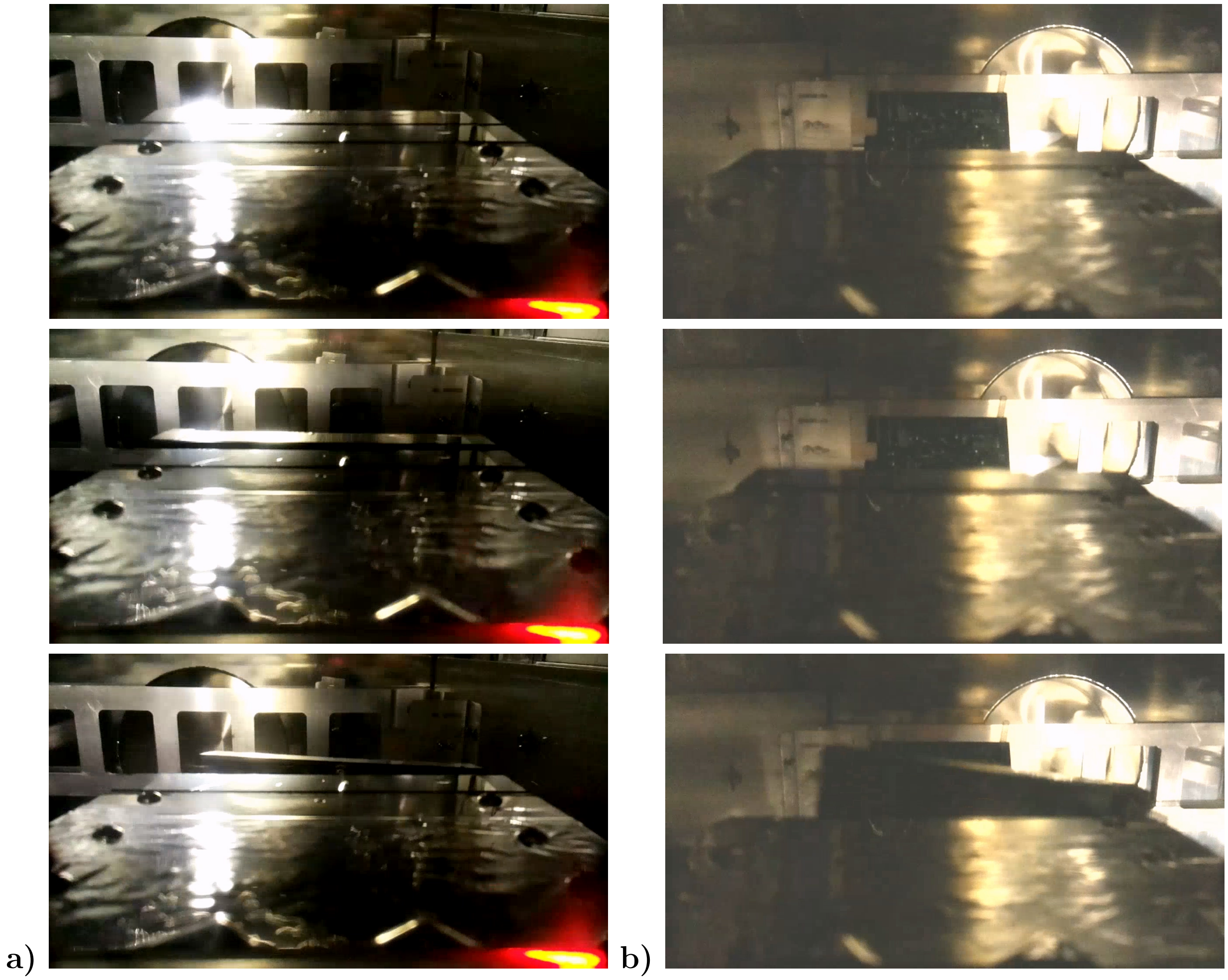

Figure 5.16: Frames from the secondary camera payload's stage separation recordings during testing in the thermal vacuum chamber. a) First stage separation at $-10\,°\mathrm{C}$ from the $-X$ side camera. b) Second stage separation at $50\,°\mathrm{C}$ from the $+X$ side camera (with poor focus due to thermal expansion).

Chapter 6

Conclusions and Future Work

We are living in exciting times for CubeSats as they begin to venture into deep-space and show off new capabilities for exploring our solar system. The oft lamented lack of capable propulsion may finally be resolved with the introduction of the Busek BIT-3 gridded ion thruster and similar systems, where several km/s of Δv in a 6U CubeSat could become commonplace. In near-Earth applications, including to the Moon and near-Earth Asteroids, we are poised for a revolution that will spur the imagination of mission designers and motivate further technology improvements. Thanks to CubeSats the swarm mission concept can finally be implemented and at least two swarm missions to the main asteroid belt can be scientifically motivated, as demonstrated in this thesis. In the main asteroid belt, and other locations far away from the Sun, systems like the BIT-3 are infeasible to operate due to their high power needs, but staged electrospray systems can fill the gap convincingly. A weakness of high Δv ionic liquid electrospray systems (staged or not) is that the lower density of the propellant compared to the solid iodine and indium used in COTS gridded ion and FEEP thrusters leads to physically larger systems, so an investigation of denser ionic liquid is an interesting topic for future work. For all CubeSat electric propulsion the development of larger and lighter solar arrays is important to continue increasing the reach of CubeSats in deep-space.

The staging system designed in this thesis works well and adds manageable penalties in mass and volume compared to a hypothetical single-stage system. The analysis showed that the most important parameters to improve overall performance are thruster specific impulse, lifetime, and propellant packaging efficiency. Because the same parameters are fundamental to advance single-stage systems the staged electrospray system will improve for “free” over time, which validates the initially restrictive requirement that the staging system be an “invisible” addition for modularity and flexibility. The physical interrupter sheet that isolates the stages before they are exposed to space works and adds minimal penalty to the stages, but turned out to have some practical drawbacks. Inserting and securing the interrupter sheets during assembly is difficult and the drag they cause during separation is inconsistent, leading to unnecessarily large tip-off rates. Future technology development of staged electrospray propulsion should focus on three aspects to maximise their potential: 1) mature the core thruster technology with more attention on lifetime testing and improvement; 2) fly the STEP-1 CubeSat and use the lessons learned to build a full scale system; and in the longer term 3) consider a new generation staging design where the penalty in mass and height could be reduced further. The core thruster technology includes system-level considerations, such as the propellant packaging and the power electronics. The next generation of electrospray systems should consider the state-of-the-art in high-voltage solid state relays (and/or transistors) to reduce the volume of the (mechanical relay based) power electronics and potentially replace the interrupter with a simpler system.

Communications, navigation, and autonomy are the main remaining technological barriers to implement a CubeSat main belt swarm; echoing the early days of deep-space exploration. For certain missions, in particular those exploring the members of asteroid families, the hurdles are not very tall and the missions can realistically move forward in the next few years. For broader exploration, however, communications will likely be the limiting factor. In this thesis, a radio-based Earth-to-mothership-to-swarm communications strategy was assumed to limit the reliance on Earth resources (i.e. the DSN) and remain at high technology readiness. Two other strategies are important to consider: node networking across the swarm and direct Earth-to-swarm communications. The results in this thesis (see Table 3.17) show that a low-bandwidth mothership-to-swarm link could close at around 0.2 au separation with mature technologies. If a swarm-to-swarm link is assumed with the same technologies, more than 20 dB is lost due to the smaller antenna and lower power of the swarm member (even when the high-gain antenna used as receiver), and the feasible link distance is only 0.05 au. Therefore, 20 CubeSats would be required to fill a single 1 au span to the mothership and the lack of practicality is obvious. On the other hand, direct Earth-to-swarm links are straightforward as MarCO operated at 1 au on X-band and the two doublings in range afforded by switching to Ka-band (or a drop in data rate) would cover the whole asteroid belt with the 34 m DSN antennas. If the original strategy where the mothership acts as a central communications node for the swarm members is retained, new technologies will be required. Optical communications is the natural successor to radio, but how practical it is for the application is unclear as current optical communications experiments (e.g. on CubeSats in LEO and Psyche en route to the asteroid belt) focus on increasing data rates, not increasing range. However, higher data rate and longer range are physically related because both can be reduced to increasing the efficiency with which power is sent from the transmitter to the receiver. Future work that considers CubeSat-scale optical communications in the context of low-bandwidth and long-range operations would therefore be valuable and could, in the best case, conclude that only small modifications are required to adapt current experimental systems to deep-space CubeSats. Investments to expand the DSN to support swarm missions may cost less and shorten the development timeline significantly compared to implementing advanced communications technologies on the swarm members and mothership, although interest in funding the DSN appears wanting.

The cost of deep-space swarm missions based on CubeSats was not estimated in this thesis but will be important to understand to move the concept forward. Based on typical CubeSats the cost of each swarm member should be a few million dollars, assuming that the savings from producing tens of near-identical units roughly cancels out the cost of building deep-space capable systems. The swarm members should have no or minimal redundancy to minimise their size and weight, where some probability of failure is accepted while meeting the mission science objectives. The mothership, however, is a single point of failure and therefore needs to be a fully-fledged traditional large spacecraft. In this thesis the mothership was assumed to be based on Dawn and could be expected to have a similar cost (NASA Discovery class, c. 500 million dollars), meaning that the cost of the CubeSats themselves would be around 10% to 20% of the mission. A bottom-up design of the mothership from the requirements imposed on carrying the CubeSats to the asteroid belt (and optionally acting as communications and navigation relay) is an important next step to understand the cost and feasibility. The Dawn-derived mothership in this thesis can carry up to 355 kg of swarm members at a wet mass of 1349 kg (ecxl. the CubeSats) and therefore only 21% of the launch mass is swarm members. For comparison, the APIES study [76] estimated the mothership wet mass at 540 kg excluding the total mass of the swarm members of 825 kg, i.e. the swarm members made up 60% of the total launched mass. The potentially pessimistic estimates on the mothership in this thesis were intentional to show that it is certainly feasible to build the requisite mothership. The overall cost of the swarm members combined with a smaller mothership should therefore be possible as a NASA Discovery-class mission (the programme which supported NEAR Shoemaker, Dawn, Lucy,[*] and Psyche). After the first swarm mission is implemented the mothership design and lessons learned can be reused to create gradually more ambitious missions and reduce costs.

Refining the missions proposed here with detailed trajectory and operations optimisations where the technological barriers are considered will better determine how much work is needed and where to focus resources. In the next level of trajectory refinement the following aspects should be captured: 1) optimise actual low-thrust trajectories to capture the effects of gravity losses while using the effective specific impulse to account for the total spacecraft

---

[*] A mission launched in 2021 to flyby several Jupiter trojan asteroids.

mass loss, 2) include the trajectory of the mothership, starting with finding realistic launch windows for gravity-assist trajectories to the relevant regions of the main belt, and 3) consider using small mothership burns in the main belt to reduce the propulsion requirements on the CubeSats. Additionally, requirements to support the instrument suite in proximity operations should be considered, which may include limits on the relative velocity in flyby missions.

8U CubeSats were considered as the platform in this thesis and are feasible for a significant set of missions. However, in several cases the volume limit is breached and volume limits are generally challenging for many CubeSat missions. Stepping up to a 12U (total volume c. 16 L) platform is sufficient for all missions proposed in this thesis but requires twice as much area on the mothership to host. Since 32 6/8U CubeSat deployers fit on Dawn we can expect at least 16 deployers for larger CubeSats which is not a major concern as the missions were found to require 10 to 20 swarm members. In the case of 16 12U CubeSats the mass allocation for each would be 22 kg, enough for all but one of the analysed cases. The larger platform also increases the surface area which may help with both power generation and practical instrumentation integration. The upper feasibility limit for the size growth of swarm members is estimated at 36 to 102 kg by assuming a minimal 10-member swarm and the 1704 kg maximum launch mass of the mothership. The range assumes 21% to 60% of the launched mass is swarm members corresponding to the Dawn-derived mothership in this and the the bespoke APIES mothership respectively.

References

[1] A. Sachs *et al.*, "Babylonian observational astronomy," *Philosophical Transactions of the Royal Society of London. Series A, Mathematical and Physical Sciences*, vol. 276, no. 1257, pp. 43–50, 1997. DOI: 10.1098/rsta.1974.0008.

[2] P. T. Metzger *et al.*, "The reclassification of asteroids from planets to non-planets," *Icarus*, vol. 319, pp. 21–32, 2019. DOI: 10.1016/j.icarus.2018.08.026.

[3] N. A. Moskovitz *et al.*, "The astorb database at lowell observatory," *Astronomy and Computing*, vol. 41, 2022. DOI: 10.1016/j.ascom.2022.100661.

[4] P. Michel, F. E. DeMeo, and W. F. Bottke, "Asteroids: Recent advances and new perspectives," in *Asteroids IV*, 2015, pp. 3–10. DOI: 10.2458/azu_uapress_9780816532131-ch001.

[5] F. E. DeMeo *et al.*, "The compositional structure of the asteroid belt," in *Asteroids IV*, 2015, pp. 13–41. DOI: 10.2458/azu_uapress_9780816532131-ch002.

[6] F. E. DeMeo and B. Carry, "Solar system evolution from compositional mapping of the asteroid belt," *Nature*, vol. 505, no. 7485, pp. 629–634, 2014. DOI: 10.1038/nature12908.

[7] National Aeronautics and Space Administration. "The apollo program." (), URL: https://www.nasa.gov/the-apollo-program/ (visited on 04/15/2024).

[8] National Aeronautics and Space Administration. "Mariner program." (), URL: https://science.nasa.gov/mission/mariner-program/ (visited on 04/15/2024).

[9] J. Veverka *et al.*, "NEAR at eros: Imaging and spectral results," *Science*, vol. 289, no. 5487, pp. 2088–2097, 2000. DOI: 10.1126/science.289.5487.2088.

[10] D. K. Yeomans *et al.*, "Radio science results during the NEAR-shoemaker spacecraft rendezvous with eros," *Science*, vol. 289, no. 5487, pp. 2085–2088, 2000. DOI: 10.1126/science.289.5487.2085.

[11] M. H. Acuña *et al.*, "NEAR magnetic field observations at 433 eros: First measurements from the surface of an asteroid," *Icarus*, vol. 155, no. 1, pp. 220–228, 2002. DOI: 10.1006/icar.2001.6772.

[12] M. T. Zuber *et al.*, "The shape of 433 eros from the NEAR-shoemaker laser rangefinder," *Science*, vol. 289, no. 5487, pp. 2097–2101, 2000. DOI: 10.1126/science.289.5487.2097.

[13] J. I. Trombka *et al.*, "The elemental composition of asteroid 433 eros: Results of the NEAR-shoemaker x-ray spectrometer," *Science*, vol. 289, no. 5487, pp. 2101–2105, 2000. DOI: 10.1126/science.289.5487.2101.

[14] R. P. Binzel, V. Reddy, and T. Dunn, "The near-earth object population: Connections to comets, main-belt asteroids, and meteorites," in *Asteroids IV*, 2015, pp. 243–256. DOI: 10.2458/azu_uapress_9780816532131-ch013.

[15] M. Yoshikawa *et al.*, "Hayabusa sample return mission," in *Asteroids IV*, 2015, pp. 397–418. DOI: 10.2458/azu_uapress_9780816532131-ch021.

[16] "Psyche spacecraft." (), URL: https://science.nasa.gov/mission/psyche/spacecraft/ (visited on 03/27/2024).

[17] B. Twiggs and J. Puig-Suari, "Introduction: The history of the CubeSat," in *Cubesat Handbook*, 2021, pp. xxi–xxviii. DOI: 10.1016/B978-0-12-817884-3.09983-5.

[18] A. Toorian, K. Diaz, and S. Lee, "The CubeSat approach to space access," in *IEEE Aerospace Conference*, 2008. DOI: 10.1109/AERO.2008.4526293.

[19] M. Swartwout, "The first one hundred CubeSats: A statistical look," *Journal of Small Satellites*, vol. 2, no. 2, pp. 213–233, 2013.

[20] National Academies of Sciences, Engineering, and Medicine, *Achieving Science with CubeSats: Thinking Inside the Box*. 2016. DOI: 10.17226/23503.

[21] E. Kulu, "Nanosatellite launch forecasts - track record and latest prediction," in *Small Satellite Conference*, 2022.

[22] A. Klesh *et al.*, "MarCO: Early operations of the first CubeSats to mars," in *Small Satellite Conference*, 2018.

[23] A. Freeman, "Exploring our solar system with CubeSats and SmallSats: The dawn of a new era," *CEAS Space Journal*, vol. 12, no. 4, pp. 491–502, 2020. DOI: 10.1007/s12567-020-00298-5.

[24] E. Kulu. "Nanosats database." (), URL: https://www.nanosats.eu/ (visited on 05/13/2024).

[25] K. Lemmer, "Propulsion for CubeSats," *Acta Astronautica*, vol. 134, pp. 231–243, 2017. DOI: 10.1016/j.actaastro.2017.01.048.

[26] D. Krejci and P. Lozano, "Space propulsion technology for small spacecraft," *Proceedings of the IEEE*, vol. 106, no. 3, pp. 362–378, 2018. DOI: 10.1109/JPROC.2017.2778747.

[27] D. O'Reilly, G. Herdrich, and D. F. Kavanagh, "Electric propulsion methods for small satellites: A review," *Aerospace*, vol. 8, no. 1, 2021. DOI: 10.3390/aerospace8010022.

[28] D. Krejci, M. G. Jenkins, and P. Lozano, "Staging of electric propulsion systems: Enabling an interplanetary cubesat," *Acta Astronautica*, vol. 160, pp. 175–182, 2019. DOI: 10.1016/j.actaastro.2019.04.031.

[29] E. Petro *et al.*, "Characterization of the TILE electrospray emitters," in *AIAA Propulsion and Energy Forum*, 2022. DOI: 10.2514/6.2020-3612.

[30] O. Jia-Richards and P. Lozano, "Stage-based electrospray propulsion system for deep-space exploration with CubeSats," in *IEEE Aerospace Conference*, 2019. DOI: 10.1109/AERO.2019.8742094.

[31] O. Jia-Richards and P. C. Lozano, "Laboratory demonstration of a staging system for electrospray thrusters," in *International Electric Propulsion Conference*, 2019.

[32] O. Jia-Richards *et al.*, “Feasibility of a deep-space CubeSat mission with a stage-based electrospray propulsion system,” in *IEEE Aerospace Conference*, 2020. DOI: 10.1109/AERO47225.2020.9172544.

[33] O. Jia-Richards and P. Lozano, “Analytical framework for staging of space propulsion systems,” *Journal of Propulsion and Power*, vol. 36, no. 4, pp. 527–534, 2020. DOI: 10.2514/1.B37722.

[34] A. Johansen *et al.*, “New paradigms for asteroid formation,” in *Asteroids IV*, 2015, pp. 471–492. DOI: 10.2458/azu_uapress_9780816532131-ch025.

[35] D. Jewitt, H. Hsieh, and J. Agarwal, “The active asteroids,” in *Asteroids IV*, 2015, pp. 221–242. DOI: 10.2458/azu_uapress_9780816532131-ch012.

[36] A. Morbidelli *et al.*, “Building terrestrial planets,” *Annual Review of Earth and Planetary Sciences*, vol. 40, no. 1, pp. 251–275, 2012. DOI: 10.1146/annurev-earth-042711-105319.

[37] K. Lodders, “Solar system abundances and condensation temperatures of the elements,” *The Astrophysical Journal*, vol. 591, no. 2, 2003. DOI: 10.1086/375492.

[38] H. Vollstaedt, K. Mezger, and Y. Alibert, “Carbonaceous chondrites and the condensation of elements from the solar nebula,” *The Astrophysical Journal*, vol. 897, no. 1, 2020. DOI: 10.3847/1538-4357/ab97b4.

[39] J. N. Connelly *et al.*, “The absolute chronology and thermal processing of solids in the solar protoplanetary disk,” *Science*, vol. 338, no. 6107, pp. 651–655, 2012. DOI: 10.1126/science.1226919.

[40] C. M. O. Alexander *et al.*, “The formation conditions of chondrules and chondrites,” *Science*, vol. 320, no. 5883, pp. 1617–1619, 2008. DOI: 10.1126/science.1156561.

[41] E. R. D. Scott *et al.*, “Early impact history and dynamical origin of differentiated meteorites and asteroids,” in *Asteroids IV*, 2015, pp. 573–596. DOI: 10.2458/azu_uapress_9780816532131-ch030.

[42] L. Wilson *et al.*, “Hydrothermal and magmatic fluid flow in asteroids,” in *Asteroids IV*, 2015, pp. 553–572. DOI: 10.2458/azu_uapress_9780816532131-ch029.

[43] J. Drazkowska *et al.*, “Planet formation theory in the era of ALMA and kepler: From pebbles to exoplanets - aspbooks.org,” in *Protostars and Planets VII*, 2023. DOI: 10.26624/QIQF3318.

[44] A. Johansen and M. Lambrechts, “Forming planets via pebble accretion,” *Annual Review of Earth and Planetary Sciences*, vol. 45, no. 1, pp. 359–387, 2017. DOI: 10.1146/annurev-earth-063016-020226.

[45] T. Hartlep and J. N. Cuzzi, “Cascade model for planetesimal formation by turbulent clustering,” *The Astrophysical Journal*, vol. 892, no. 2, 2020. DOI: 10.3847/1538-4357/ab76c3.

[46] A. Morbidelli *et al.*, “The dynamical evolution of the asteroid belt,” in *Asteroids IV*, 2015, pp. 493–508. DOI: 10.2458/azu_uapress_9780816532131-ch026.

[47] A. N. Krot *et al.*, “Young chondrules in CB chondrites from a giant impact in the early solar system,” *Nature*, vol. 436, no. 7053, pp. 989–992, 2005. DOI: 10.1038/nature03830.

[48] P. Vernazza *et al.*, “Multiple and fast: The accretion of ordinary chondrite parent bodies,” *The Astrophysical Journal*, vol. 791, no. 120, 2014. DOI: 10.1088/0004-637X/791/2/120.

[49] P. Vernazza and P. Beck, “Composition of solar system small bodies,” in *Planetesimals: Early Differentiation and Consequences for Planets*, 2017, pp. 269–297. DOI: 10.1017/9781316339794.013.

[50] J. Chambers, “Making the solar system,” *The Astrophysical Journal*, vol. 944, no. 2, 2023. DOI: 10.3847/1538-4357/aca96f.

[51] A. Scheinberg *et al.*, “Asteroid differentiation: Melting and large-scale structure,” in *Asteroids IV*, 2015, pp. 533–552. DOI: 10.2458/azu_uapress_9780816532131-ch028.

[52] P. Vernazza *et al.*, “The formation and evolution of ordinary chondrite parent bodies,” in *Asteroids IV*, 2015, pp. 617–634. DOI: 10.2458/azu_uapress_9780816532131-ch032.

[53] A. Johansen *et al.*, “The multifaceted planetesimal formation process,” in *Protostars and Planets V*, 2014. DOI: 10.2458/azu_uapress_9780816531240-ch024.

[54] J. I. Goldstein, E. R. D. Scott, and N. L. Chabot, “Iron meteorites: Crystallization, thermal history, parent bodies, and origin,” *Geochemistry*, vol. 69, no. 4, pp. 293–325, 2009. DOI: 10.1016/j.chemer.2009.01.002.

[55] P. Vernazza *et al.*, “VLT/SPHERE imaging survey of the largest main-belt asteroids: Final results and synthesis,” *Astronomy & Astrophysics*, vol. 654, 2021. DOI: 10.1051/0004-6361/202141781.

[56] W. F. Bottke *et al.*, “The collisional evolution of the main asteroid belt,” in *Asteroids IV*, 2015, pp. 701–724. DOI: 10.2458/azu_uapress_9780816532131-ch036.

[57] W. F. Bottke *et al.*, “The fossilized size distribution of the main asteroid belt,” *Icarus*, vol. 175, no. 1, pp. 111–140, 2005. DOI: 10.1016/j.icarus.2004.10.026.

[58] D. Nesvorný, M. Brož, and V. Carruba, “Identification and dynamical properties of asteroid families,” in *Asteroids IV*, 2015, pp. 297–322. DOI: 10.2458/azu_uapress_9780816532131-ch016.

[59] D. Vokrouhlický *et al.*, “The yarkovsky and YORP effects,” in *Asteroids IV*, 2015, pp. 509–532. DOI: 10.2458/azu_uapress_9780816532131-ch027.

[60] G. W. Wetherill, “An alternative model for the formation of the asteroids,” *Icarus*, vol. 100, no. 2, pp. 307–325, 1992. DOI: 10.1016/0019-1035(92)90103-E.

[61] D. P. O’Brien, A. Morbidelli, and W. F. Bottke, “The primordial excitation and clearing of the asteroid belt—revisited,” *Icarus*, vol. 191, no. 2, pp. 434–452, 2007. DOI: 10.1016/j.icarus.2007.05.005.

[62] K. J. Walsh *et al.*, “A low mass for mars from jupiter’s early gas-driven migration,” *Nature*, vol. 475, no. 7355, pp. 206–209, 2011. DOI: 10.1038/nature10201.

[63] A. Morbidelli *et al.*, “Dynamics of the giant planets of the solar system in the gaseous protoplanetary disk and their relationship to the current orbital architecture,” *The Astronomical Journal*, vol. 134, no. 5, 2007. DOI: 10.1086/521705.

[64] R. Gomes *et al.*, “Origin of the cataclysmic late heavy bombardment period of the terrestrial planets,” *Nature*, vol. 435, no. 7041, pp. 466–469, 2005. DOI: 10.1038/nature03676.

[65] N. A. Kaib and J. E. Chambers, “The fragility of the terrestrial planets during a giant-planet instability,” *Monthly Notices of the Royal Astronomical Society*, vol. 455, no. 4, pp. 3561–3569, 2016. DOI: 10.1093/mnras/stv2554.

[66] M. S. Clement *et al.*, “Mars’ growth stunted by an early giant planet instability,” *Icarus*, vol. 311, pp. 340–356, 2018. DOI: 10.1016/j.icarus.2018.04.008.

[67] T. Lichtenberg *et al.*, "Bifurcation of planetary building blocks during solar system formation," *Science*, vol. 371, no. 6527, pp. 365–370, 2021. DOI: 10.1126/science.abb3091.

[68] National Academies of Sciences, Engineering, and Medicine, *Origins, Worlds, and Life: A Decadal Strategy for Planetary Science and Astrobiology 2023-2032*. 2023. DOI: 10.17226/26522.

[69] A. Golkar, "Distributed CubeSat mission concepts," in *Cubesat Handbook*, 2021, pp. 123–133. DOI: 10.1016/B978-0-12-817884-3.00005-9.

[70] D. Selva *et al.*, "Distributed earth satellite systems: What is needed to move forward?" *Journal of Aerospace Information Systems*, vol. 14, no. 8, pp. 412–438, 2017. DOI: 10.2514/1.I010497.

[71] W. J. Blackwell *et al.*, "An overview of the TROPICS NASA earth venture mission," *Quarterly Journal of the Royal Meteorological Society*, vol. 144, pp. 16–26, S1 2018. DOI: 10.1002/qj.3290.

[72] M. Safyan, "Planet's dove satellite constellation," in *Handbook of Small Satellites: Technology, Design, Manufacture, Applications, Economics and Regulation*, 2020. DOI: 10.1007/978-3-030-20707-6_64-1.

[73] S. Curtis *et al.*, "ANTS for human exploration and development of space," in *IEEE Aerospace Conference*, 2003. DOI: 10.1109/AERO.2003.1235057.

[74] P. Clark *et al.*, "BEES for ANTS: Space mission applications for the autonomous NanoTechnology swarm," in *AIAA Intelligent Systems Technical Conference*, 2004. DOI: 10.2514/6.2004-6303.

[75] M. Hinchey *et al.*, "Modeling for NASA autonomous nano-technology swarm missions and model-driven autonomic computing," in *International Conference on Advanced Information Networking and Applications*, 2007, pp. 250–257. DOI: 10.1109/AINA.2007.93.

[76] P. D'Arrigo and S. Santandrea, "The APIES mission to explore the asteroid belt," *Advances in Space Research*, vol. 38, no. 9, pp. 2060–2067, 2006. DOI: 10.1016/j.asr.2006.09.017.

[77] D. Izzo *et al.*, "Designing complex interplanetary trajectories for the global trajectory optimization competitions," in *Space Engineering: Modeling and Optimization with Case Studies*, 2016, pp. 151–176. DOI: 10.1007/978-3-319-41508-6_6.

[78] A. Blocher, "Alternative mission concepts for the exploration of outer planets using small satellite swarms," Master's Thesis, California Polytechnic State University, San Luis Obispo, 2017. DOI: 10.15368/theses.2018.22.

[79] I. Garrick-Bethell *et al.*, "NanoSWARM: NanoSatellites for space weathering, surface water, solar wind, and remanent magnetism," *Bulletin of the American Astronomical Society*, vol. 53, 2021.

[80] I. Garrick-Bethell *et al.*, "NANOSWARM: A cubesat discovery mission to study space weathering, lunar magnetism, lunar water, and small-scale magnetospheres," in *Annual Lunar and Planetary Science Conference*, 2015.

[81] *CubeSat Handbook: From Mission Design to Operations*, 2021. DOI: 10.1016/C2018-0-02366-X.

[82] B. Yost and S. Weston, "State-of-the-art small spacecraft technology," National Aeronautics and Space Administration, TP—20240001462, 2024.

[83] C. S. Fish *et al.*, "Design, development, implementation, and on-orbit performance of the dynamic ionosphere CubeSat experiment mission," *Space Science Reviews*, vol. 181, no. 1, pp. 61–120, 2014. DOI: 10.1007/s11214-014-0034-x.

[84] A. Klesh, J. Baker, and J. Krajewski, "MarCO: Flight review and lessons learned," in *Small Satellite Conference*, 2019.

[85] A. T. Klesh *et al.*, "INSPIRE: Interplanetary NanoSpacecraft pathfinder in relevant environment," in *AIAA SPACE Conference and Exposition*, 2013. DOI: 10.2514/6.2013-5323.

[86] J. Schoolcraft, A. Klesh, and T. Werne, "MarCO: Interplanetary mission development on a CubeSat scale," in *Space Operations: Contributions from the Global Community*, 2017, pp. 221–231. DOI: 10.1007/978-3-319-51941-8_10.

[87] E. Dotto *et al.*, "LICIACube - the light italian cubesat for imaging of asteroids in support of the NASA DART mission towards asteroid (65803) didymos," *Planetary and Space Science*, vol. 199, 2021. DOI: 10.1016/j.pss.2021.105185.

[88] E. Dotto *et al.*, "The dimorphos ejecta plume properties revealed by LICIACube," *Nature*, vol. 627, no. 8004, pp. 505–509, 2024. DOI: 10.1038/s41586-023-06998-2.

[89] L. McNutt *et al.*, "Near-earth asteroid scout," in *AIAA Space Conference*, 2014.

[90] D. R. Jones *et al.*, "Initial acquisition orbit determination for NEAScout and the artemis i secondary payloads," in *AAS/AIAA Astrodynamics Specialist Conference*, 2023.

[91] A. J. Ricco *et al.*, "BioSentinel: A 6u nanosatellite for deep-space biological science," *IEEE Aerospace and Electronic Systems Magazine*, vol. 35, no. 3, 2020. DOI: 10.1109/MAES.2019.2953760.

[92] J. Fusco, T. Stevenson, and R. Nakamura, "Flight experience and lessons learned from biosentinel: A 6u deep space cubesat," in *Annual AAS Guidance, Navigation and Control Conference*, 2024.

[93] M. I. Desai *et al.*, "The CubeSat mission to study solar particles," *IEEE Aerospace and Electronic Systems Magazine*, vol. 34, no. 4, 2019. DOI: 10.1109/MAES.2019.2917802.

[94] R. Funase *et al.*, "Mission to earth–moon lagrange point by a 6u CubeSat: EQUULEUS," *IEEE Aerospace and Electronic Systems Magazine*, vol. 35, no. 3, 2020. DOI: 10.1109/MAES.2019.2955577.

[95] A. Fujimori *et al.*, "AQUARIUS: The world's first water-based thruster enabled 6u CubeSat to complete lunar flyby," in *Small Satellite Conference*, 2023.

[96] C. Hardgrove *et al.*, "The lunar polar hydrogen mapper (LunaH-map) mission," in *Small Satellite Conference*, 2019.

[97] C. Hardgrove *et al.*, "Lunar polar hydrogen mapper (LunaH-map) CubeSat mission launch, early operations and lunar flyby neutron data collection," in *Lunar and Planetary Science Conference*, 2023.

[98] B. K. Malphrus *et al.*, "The lunar IceCube EM-1 mission: Prospecting the moon for water ice," *IEEE Aerospace and Electronic Systems Magazine*, vol. 34, no. 4, 2019. DOI: 10.1109/MAES.2019.2909384.

[99] B. A. Cohen *et al.*, "Lunar flashlight: Illuminating the lunar south pole," *IEEE Aerospace and Electronic Systems Magazine*, vol. 35, no. 3, 2020. DOI: 10.1109/MAES.2019.2950746.

[100] C. Smith *et al.*, "The journey of the lunar flashlight propulsion system from launch through end of mission," in *Small Satellite Conference*, 2023.

[101] T. Hashimoto *et al.*, "Nano semihard moon lander: OMOTENASHI," *IEEE Aerospace and Electronic Systems Magazine*, vol. 34, no. 9, 2019. DOI: 10.1109/MAES.2019.2923311.

[102] V. Di Tana *et al.*, "ArgoMoon: There is a nano-eyewitness on the SLS," *IEEE Aerospace and Electronic Systems Magazine*, vol. 34, no. 4, 2019. DOI: 10.1109/MAES.2019.2911138.

[103] R. Lane *et al.*, "NASA space launch system cubesats: First flight and future opportunities," in *Small Satellite Conference*, 2023.

[104] W. M. Kimmel *et al.*, "Technology readiness assessment best practices guide," National Aeronautics and Space Administration, SP-20205003605, 2020.

[105] R. L. Staehle *et al.*, "Interplanetary CubeSats: Opening the solar system to a broad community at lower cost," *Journal of Small Satellites*, vol. 2, no. 1, 2013.

[106] T. Imken *et al.*, "CubeSat flight system development for enabling deep space science," in *IEEE Aerospace Conference*, 2017. DOI: 10.1109/AERO.2017.7943885.

[107] A. Freeman and C. Norton, "Exploring our solar system with cubesats and nanosats," in *Reinventing Space Conference*, 2018. DOI: 10.1007/978-3-319-32817-1_1.

[108] R. Walker *et al.*, "Deep-space CubeSats: Thinking inside the box," *Astronomy & Geophysics*, vol. 59, no. 5, pp. 5.24–5.30, 2018. DOI: 10.1093/astrogeo/aty232.

[109] B. K. Malphrus *et al.*, "Interplanetary CubeSat missions," in *Cubesat Handbook*, 2021, pp. 85–121. DOI: 10.1016/B978-0-12-817884-3.00004-7.

[110] "HaWK specifications for comparison," MMA Design LLC. (), URL: https://mmadesignllc.com/specs-table/ (visited on 03/28/2024).

[111] F. de Asís Delgado, P. Hernández, and M. Toso, "MicroSADA-18 development of one axis solar array drive mechanism for small satellites," in *European Space Power Conference*, 2023. DOI: 10.1109/ESPC59009.2023.10412701.

[112] F. C. Krause *et al.*, "Implementation of commercial li-ion cells on the MarCO deep space CubeSats," *Journal of Power Sources*, vol. 449, 2020. DOI: 10.1016/j.jpowsour.2019.227544.

[113] George R. Schmidt, Thomas J. Sutliff, and Leonard A. Dudzinski, "Radioisotope power: A key technology for deep space exploration," in *Radioisotopes - Applications in Physical Sciences*, 2011. DOI: 10.5772/858.

[114] R. E. Hodges *et al.*, "A deployable high-gain antenna bound for mars: Developing a new folded-panel reflectarray for the first CubeSat mission to mars," *IEEE Antennas and Propagation Magazine*, vol. 59, no. 2, pp. 39–49, 2017. DOI: 10.1109/MAP.2017.2655561.

[115] M. M. Kobayashi, M. Shihabi, and J. Taylor, "Mars cube one telecommunications subsystem design," in *DESCANSO Design and Performance Summary Series*, 2021.

[116] NASA Jet Propulsion Laboratory. "Iris v2.2 SmallSat deep space transponder." (2022), URL: https://scienceandtechnology.jpl.nasa.gov/sites/default/files/documents/Brochure_Iris_Transponder_V2.2_SEP_2022.pdf.

[117] R. E. Hodges *et al.*, "ISARA - integrated solar array and reflectarray CubeSat deployable ka-band antenna," in *2015 IEEE International Symposium on Antennas and Propagation & USNC/URSI National Radio Science Meeting*, 2015, pp. 2141–2142. DOI: 10.1109/APS.2015.7305460.

[118] N. Chahat *et al.*, "Deployable one-meter reflectarray for 6u-class CubeSats," in *European Conference on Antennas and Propagation*, 2019.

[119] H. H. Means, "The deep space network: Overburdened and underfunded," *Physics Today*, vol. 76, no. 12, pp. 22–23, 2023. DOI: 10.1063/PT.3.5358.

[120] K.-M. Cheung *et al.*, "Next-generation ground network architecture for communications and tracking of interplanetary smallsats," in *CubeSat Developer Workshop*, 2015.

[121] F. Perez Lissi *et al.*, "Main challenges of cubesat piggyback on an interplanetary mission: The HERA cubesats, a technology demonstration case," in *Small Satellites Systems and Services Symposium*, 2022.

[122] A. Biswas *et al.*, "Deep space optical communications," in *Free-Space Laser Communication and Atmospheric Propagation XXX*, vol. 10524, 2018, pp. 242–252. DOI: 10.1117/12.2296426.

[123] A. Carrasco-Casado *et al.*, "Optical communication on CubeSats — enabling the next era in space science," in *2017 IEEE International Conference on Space Optical Systems and Applications (ICSOS)*, 2017, pp. 46–52. DOI: 10.1109/ICSOS.2017.8357210.

[124] C. Pong, "On-orbit performance & operation of the attitude & pointing control subsystems on ASTERIA," in *Small Satellite Conference*, 2018.

[125] A. Klesh and J. Krajewski, "MarCO: CubeSats to mars in 2016," in *Small Satellite Conference*, 2015.

[126] D. Sternberg *et al.*, "Attitude control system for the mars cube one spacecraft," in *IEEE Aerospace Conference*, 2019. DOI: 10.1109/AERO.2019.8741816.

[127] C. Levit and W. Marshall, "Improved orbit predictions using two-line elements," *Advances in Space Research*, vol. 47, no. 7, pp. 1107–1115, 2011. DOI: 10.1016/j.asr.2010.10.017.

[128] J. Arlas and S. Spangelo, "GPS results for the radio aurora explorer II CubeSat mission," in *AIAA Aerospace Sciences Meeting including the New Horizons Forum and Aerospace Exposition*, ser. Aerospace Sciences Meetings, 2013. DOI: 10.2514/6.2013-123.

[129] D. W. Curkendall and J. S. Border, "Delta-DOR: The one-nanoradian navigation measurement system of the deep space network—history, architecture, and componentry," *The Interplanetary Network Progress Report*, vol. 42, 2013.

[130] T. J. Martin-Mur and B. Young, "Navigating MarCO, the first interplanetary CubeSats," in *Australian International Aerospace Congress*, 2019, pp. 24–28.

[131] E. Turan, S. Speretta, and E. Gill, "Autonomous navigation for deep space small satellites: Scientific and technological advances," *Acta Astronautica*, vol. 193, pp. 56–74, 2022. DOI: 10.1016/j.actaastro.2021.12.030.

[132] E. Andreis, V. Franzese, and F. Topputo, "An overview of autonomous optical navigation for deep-space CubeSats," in *International Astronautical Congress*, 2021.

[133] J. Riedel *et al.*, "Using autonomous navigation for interplanetary missions: The validation of deep space 1 AutoNav," in *International Conference on Low-Cost Planetary Missions*, 2000.

[134] V. Franzese *et al.*, "Deep-space optical navigation for m-ARGO mission," *The Journal of the Astronautical Sciences*, vol. 68, no. 4, pp. 1034–1055, 2021. DOI: 10.1007/s40295-021-00286-9.

[135] S. Casini *et al.*, "Combined optical line-of-sight and crosslink radiometric navigation for distributed deep-space systems," *Scientific Reports*, vol. 13, no. 1, 2023. DOI: 10.1038/s41598-023-43339-9.

[136] S. I. Sheikh *et al.*, "Spacecraft navigation using x-ray pulsars," *Journal of Guidance, Control, and Dynamics*, vol. 29, no. 1, pp. 49–63, 2006. DOI: 10.2514/1.13331.

[137] J. Stupl *et al.*, "CubeX: A compact x-ray telescope enables both x-ray fluorescence imaging spectroscopy and pulsar timing based navigation," in *Small Satellite Conference*, 2018.

[138] M. B. Quadrelli *et al.*, "Guidance, navigation, and control technology assessment for future planetary science missions," *Journal of Guidance, Control, and Dynamics*, vol. 38, no. 7, pp. 1165–1186, 2015. DOI: 10.2514/1.G000525.

[139] S. Speretta *et al.*, "LUMIO: An autonomous CubeSat for lunar exploration," in *Space Operations: Inspiring Humankind's Future*, 2019, pp. 103–134. DOI: 10.1007/978-3-030-11536-4_6.

[140] L. Feruglio and S. Corpino, "Neural networks to increase the autonomy of interplanetary nanosatellite missions," *Robotics and Autonomous Systems*, vol. 93, pp. 52–60, 2017. DOI: 10.1016/j.robot.2017.04.005.

[141] K. Colton and B. Klofas, "Supporting the flock: Building a ground station network for autonomy and reliability," in *Small Satellite Conference*, 2016.

[142] A. Freeman, B. K. Malphrus, and R. Staehle, "CubeSat science instruments," in *Cubesat Handbook*, 2021, pp. 67–83. DOI: 10.1016/B978-0-12-817884-3.00003-5.

[143] T. H. Prettyman *et al.*, "Dawn's gamma ray and neutron detector," in *The Dawn Mission to Minor Planets 4 Vesta and 1 Ceres*, 2012, pp. 371–459. DOI: 10.1007/978-1-4614-4903-4_14.

[144] M. Burks *et al.*, "Measuring the surface abundance of iron and nickel on the asteroid (16) psyche in the presence of large solar particle events," *Planetary and Space Science*, vol. 240, 2024. DOI: 10.1016/j.pss.2023.105832.

[145] T. H. Prettyman *et al.*, "Elemental composition of the lunar surface: Analysis of gamma ray spectroscopy data from lunar prospector," *Journal of Geophysical Research: Planets*, vol. 111, E12 2006. DOI: 10.1029/2005JE002656.

[146] C. Hardgrove *et al.*, "LunaH-map: Revealing lunar water with a new radiation sensor array," in *Small Satellite Conference*, 2022.

[147] H. Goldberg *et al.*, "The juventas CubeSat in support of ESA's hera mission to the asteroid didymos," in *Small Satellite Conference*, 2019.

[148] M. Cardi *et al.*, "The hera milani CubeSat mission," in *Small Satellites Systems and Services Symposium*, 2022.

[149] "JPL MarCO micro CubeSat propulsion system," VACCO Industries. (2015), URL: https://cubesat-propulsion.com/jpl-marco-micro-propulsion-system/ (visited on 03/17/2024).

[150] E. Glenn Lightsey, T. Stevenson, and M. Sorgenfrei, "Development and testing of a 3-d-printed cold gas thruster for an interplanetary CubeSat," *Proceedings of the IEEE*, vol. 106, no. 3, 2018. DOI: 10.1109/JPROC.2018.2799898.

[151] L. M. Littleton, "Assembly, integration, and testing of a green monopropellant propulsion system for NASA's lunar flashlight mission," Ph.D. dissertation, 2021.

[152] D. Krejci *et al.*, “Emission characteristics of passively fed electrospray microthrusters with propellant reservoirs,” *Journal of Spacecraft and Rockets*, vol. 54, no. 2, pp. 447–458, 2017. DOI: 10.2514/1.A33531.

[153] M. Tsay *et al.*, “Twin ion engine demonstration for small spacecraft applications,” in *Small Satellite Conference*, 2022.

[154] D. Rafalskyi *et al.*, “Development and in-flight testing of an iodine ion thruster,” in *Small Satellite Conference*, 2021.

[155] A. Gurciullo *et al.*, “Experimental performance and plume characterisation of a miniaturised 50w hall thruster,” in *International Electric Propulsion Conference*, 2019.

[156] “ENPULSION NANO $\mathbf{r^3}$ propulsion system - enpulsion.” (2021), URL: https://www.enpulsion.com/order/nano-r3/ (visited on 03/17/2024).

[157] P. Lascombes *et al.*, “Lessons learnt from operating the first cubesat mission equipped with a hall thruster,” in *Small Satellite Conference*, 2021.

[158] Exotrail, *Spaceware nano l datasheet*, 2022.

[159] J. R. Brophy, M. D. Rayman, and B. Pavri, “Dawn: An ion-propelled journey to the beginning of the solar system,” in *IEEE Aerospace Conference*, 2008. DOI: 10.1109/AERO.2008.4526264.

[160] I. K. Johnson *et al.*, “100,000hrs of on-orbit electric propulsion and MAXAR’s first electric orbit raising,” in *AIAA Scitech Forum*, ser. AIAA SciTech Forum, 2020. DOI: 10.2514/6.2020-0189.

[161] X. Gallud and P. C. Lozano, “The emission properties, structure and stability of ionic liquid menisci undergoing electrically assisted ion evaporation,” *Journal of Fluid Mechanics*, vol. 933, A43, 2022. DOI: 10.1017/jfm.2021.988.

[162] D. Krejci *et al.*, “Demonstration of the ifm nano feep thruster in low earth orbit,” in *4S Symposium*, 2018.

[163] F. Mier-Hicks and P. C. Lozano, “Spacecraft-charging characteristics induced by the operation of electrospray thrusters,” *Journal of Propulsion and Power*, vol. 33, no. 2, pp. 456–467, 2017. DOI: 10.2514/1.B36292.

[164] I. Romero-Sanz *et al.*, “Source of heavy molecular ions based on taylor cones of ionic liquids operating in the pure ion evaporation regime,” *Journal of Applied Physics*, vol. 94, no. 5, pp. 3599–3605, 2003. DOI: 10.1063/1.1598281.

[165] R. S. Legge and P. C. Lozano, “Electrospray propulsion based on emitters microfabricated in porous metals,” *Journal of Propulsion and Power*, vol. 27, no. 2, pp. 485–495, 2011. DOI: 10.2514/1.50037.

[166] D. G. Courtney, S. Dandavino, and H. Shea, “Comparing direct and indirect thrust measurements from passively fed ionic electrospray thrusters,” *Journal of Propulsion and Power*, vol. 32, no. 2, pp. 392–407, 2016. DOI: 10.2514/1.B35836.

[167] D. G. Courtney, H. Q. Li, and P. Lozano, “Emission measurements from planar arrays of porous ionic liquid ion sources,” *Journal of Physics D: Applied Physics*, vol. 45, no. 48, 2012. DOI: 10.1088/0022-3727/45/48/485203.

[168] M. R. Natisin *et al.*, "Efficiency mechanisms in porous-media electrospray thrusters," *Journal of Propulsion and Power*, vol. 37, no. 5, pp. 650–659, 2021. DOI: 10.2514/1.B38160.

[169] G. M. Pettersson *et al.*, "Performance measurement and propellant testing for the STEP-1 CubeSat elecrospray thrusters," in *International Electric Propulsion Conference*, 2022.

[170] D. Krejci and P. Lozano, "Micro-machined ionic liquid electrospray thrusters for cubesat applications," in *International Electric Propulsion Conference*, 2017.

[171] V. C. Thomas *et al.*, "The dawn spacecraft," *Space Science Reviews*, vol. 163, no. 1, pp. 175–249, 2011. DOI: 10.1007/s11214-011-9852-2.

[172] J. S. Snyder *et al.*, "Electric propulsion for the psyche mission: Development activities and status," in *AIAA Propulsion and Energy Forum*, ser. AIAA Propulsion and Energy Forum, 2020. DOI: 10.2514/6.2020-3607.

[173] C. Steiger *et al.*, "BepiColombo–solar electric propulsion system operations for the transit to mercury," in *International Electric Propulsion Conference*, 2019.

[174] Lee Mohon. "NEA scout status update - NASA." (2022), URL: https://www.nasa.gov/centers-and-facilities/marshall/nea-scout-status-update/ (visited on 03/31/2024).

[175] J. R. Masiero *et al.*, "Asteroid family physical properties," in *Asteroids IV*, 2015, pp. 323–340. DOI: 10.2458/azu_uapress_9780816532131-ch017.

[176] P. Michel *et al.*, "Collisional formation and modeling of asteroid families," in *Asteroids IV*, 2015, pp. 341–354. DOI: 10.2458/azu_uapress_9780816532131-ch018.

[177] L. Prockter *et al.*, "Surface expressions of structural features on eros," *Icarus*, vol. 155, no. 1, pp. 75–93, 2002. DOI: 10.1006/icar.2001.6770.

[178] T. Michikami *et al.*, "Size-frequency statistics of boulders on global surface of asteroid 25143 itokawa," *Earth, Planets and Space*, vol. 60, no. 1, pp. 13–20, 2008. DOI: 10.1186/BF03352757.

[179] D. Nesvorny, *Nesvorny HCM asteroid families bundle v1.0*, in collab. with PDS Small Bodies Node, 2020. DOI: 10.26033/6CG5-PT13.

[180] Thomas H. Burbine *et al.*, "Evidence for differentiation among asteroid families," in *Planetesimals: Early Differentiation and Consequences for Planets*, 2017, pp. 267–362. DOI: 10.1017/9781316339794.

[181] P. Michel, W. Benz, and D. C. Richardson, "Catastrophic disruption of pre-shattered parent bodies," *Icarus*, vol. 168, no. 2, pp. 420–432, 2004. DOI: 10.1016/j.icarus.2003.12.011.

[182] F. Spoto, A. Milani, and Z. Knežević, "Asteroid family ages," *Icarus*, vol. 257, pp. 275–289, 2015. DOI: 10.1016/j.icarus.2015.04.041.

[183] V. Carruba *et al.*, "On the age of the nele asteroid family," *Monthly Notices of the Royal Astronomical Society*, vol. 477, no. 1, pp. 1308–1317, 2018. DOI: 10.1093/mnras/sty777.

[184] T. Mothé-Diniz and D. Nesvorný, "Visible spectroscopy of extremely young asteroid families," *Astronomy & Astrophysics*, vol. 486, no. 2, 2008. DOI: 10.1051/0004-6361:200809934.

[185] B. Novaković, "Portrait of theobalda as a young asteroid family," *Monthly Notices of the Royal Astronomical Society*, vol. 407, no. 3, pp. 1477–1486, 2010. DOI: 10.1111/j.1365-2966.2010.17051.x.

[186] D. Nesvorný *et al.*, "Origin of the near-ecliptic circumsolar dust band," *The Astrophysical Journal*, vol. 679, no. 2, 2008. DOI: 10.1086/588841.

[187] L. A. Molnar and M. J. Haegert, "Details of recent collisions of asteroids 832 karin and 158 koronis," in *AAS/Division for Planetary Sciences Meeting Abstracts*, vol. 41, 2009, p. 27.05.

[188] D. Izzo *et al.*, *Esa/pykep: Optimize*, version v2.6, 2020. DOI: 10.5281/zenodo.4091753.

[189] "Horizons system." (), URL: https://ssd.jpl.nasa.gov/horizons/ (visited on 03/26/2024).

[190] B. Novaković *et al.*, "Asteroid families: Properties, recent advances, and future opportunities," *Celestial Mechanics and Dynamical Astronomy*, vol. 134, no. 4, 2022. DOI: 10.1007/s10569-022-10091-7.

[191] M. Di Martino *et al.*, "Veritas asteroid family: Remarkable spectral differences inside a primitive parent body," *Icarus*, vol. 127, no. 1, pp. 112–120, 1997. DOI: 10.1006/icar.1996.5674.

[192] H. H. Hsieh *et al.*, "Asteroid family associations of active asteroids," *The Astronomical Journal*, vol. 155, no. 2, p. 96, 2018. DOI: 10.3847/1538-3881/aaa5a2.

[193] A. Cellino *et al.*, "Brangäne: A new family of barbarian asteroids," *Monthly Notices of the Royal Astronomical Society*, vol. 485, no. 1, pp. 570–576, 2019. DOI: 10.1093/mnras/stz451.

[194] B. Carry, "Density of asteroids," *Planetary and Space Science*, Solar System science before and after Gaia, vol. 73, no. 1, pp. 98–118, 2012. DOI: 10.1016/j.pss.2012.03.009.

[195] S. Marchi *et al.*, "Small crater populations on vesta," *Planetary and Space Science*, vol. 103, pp. 96–103, 2014. DOI: 10.1016/j.pss.2013.05.005.

[196] "Small-body database query." (), URL: https://ssd.jpl.nasa.gov/tools/sbdb_query.html (visited on 03/25/2024).

[197] "Interplanetary HaWK solar arrays make history on CubeSats," MMA Design LLC. (), URL: https://mmadesignllc.com/first-interplanetary-hawk-solar-arrays/ (visited on 03/27/2024).

[198] Blue Canyon Technologies. "Attitude control systems datasheet." (2024), URL: https://www.bluecanyontech.com/components.

[199] A. Näsilä and T. Kohout, "Miniaturized spectral imaging instrumentation for planetary exploration," in *IEEE Aerospace Conference*, 2020. DOI: 10.1109/AERO47225.2020.9172437.

[200] "HeraMission milani cubesat," Hera Mission. (), URL: https://www.heramission.space/hera-mission-milani-cubesat (visited on 03/30/2024).

[201] M. Amoroso *et al.*, "Italian cubesats for moon and asteroid imaging," in *International Astronautical Congress*, 2022.

[202] J. S. Bennett *et al.*, "Precision magnetometers for aerospace applications: A review," *Sensors*, vol. 21, no. 16, 2021. DOI: 10.3390/s21165568.

[203] "Hera mission juventas cubesat," Hera Mission. (), URL: https://www.heramission.space/hera-mission-juventas-cubesat (visited on 03/31/2024).

[204] V. Marchese *et al.*, "LICIACube mission: The fastest fly-by ever done by a CubeSat," in *Small Satellite Conference*, 2021.

[205] M. A. Barucci *et al.*, "The flybys of asteroids (2867) šteins, (21) lutetia, and (4179) toutatis," in *Asteroids IV*, 2015, pp. 433–450. DOI: 10.2458/azu_uapress_9780816532131-ch023.

[206] J. Taylor, "Dawn telecommunications," in *DESCANSO Design and Performance Summary Series*, 2009.

[207] G. W. Wetherill, "Collisions in the asteroid belt," *Journal of Geophysical Research (1896-1977)*, vol. 72, no. 9, pp. 2429–2444, 1967. DOI: 10.1029/JZ072i009p02429.

[208] William E. Wiesel, *Spaceflight Dynamics*, 3rd ed. 2010.

[209] O. Jia-Richards, "Segmented reconstruction of low-acceleration orbital maneuvers," *Journal of Guidance, Control, and Dynamics*, vol. 46, no. 12, pp. 2290–2299, 2023. DOI: 10.2514/1.G007548.

[210] C. R. Seubert, L. A. Stiles, and H. Schaub, "Effective coulomb force modeling for spacecraft in earth orbit plasmas," *Advances in Space Research*, vol. 54, no. 2, pp. 209–220, 2014. DOI: 10.1016/j.asr.2014.04.005.

[211] B. Huett and C. Willey, "Design and development of miniature mechanisms for small spacecraft," *Small Satellite Conference*, 2000.

[212] C. Soffritti *et al.*, "Dry sliding behavior of an aluminum alloy after innovative hard anodizing treatments," *Materials*, vol. 14, no. 12, 2021. DOI: 10.3390/ma14123281.

[213] B. Buergler *et al.*, "Towards supercapacitors in space applications," in *European Space Power Conference*, 2017. DOI: 10.1051/e3sconf/20171617003.

[214] B. Faure *et al.*, "Qualification of commercial off-the-shelf supercapacitors for space applications," in *Passive Components Networking Symposium*, 2018.

[215] N. Bay, "Cold welding," in *ASM Handbook*, vol. 6A, 2011. DOI: 10.31399/asm.hb.v06a.a0005581.

[216] A. Merstallinger *et al.*, "Assessment of cold welding between separable contact surfaces due to impact and fretting under vacuum," European Space Agency, STM-279, 2009.

[217] D. Bortoluzzi, C. Zanoni, and J. W. Conklin, "On-ground testing of the role of adhesion in the LISA-pathfinder test mass injection phase," *Advances in Space Research*, vol. 59, no. 10, pp. 2572–2582, 2017. DOI: 10.1016/j.asr.2017.02.030.

[218] P. Misra and J. Nagaraju, "Electrical contact resistance in thin ($<$0.5 um) gold plated contacts: Effect of gold plating thickness," *IEEE Transactions on Components and Packaging Technologies*, vol. 33, no. 4, pp. 830–835, 2010. DOI: 10.1109/TCAPT.2010.2060340.

[219] "Electrical contact materials," in *Metals Handbook*, 2nd ed., 1998. DOI: 10.31399/asm.hb.mhde2.a0003157.

[220] G. V. Samsonov, "Mechanical properties of the elements," in *Handbook of the Physicochemical Properties of the Elements*, 1968, pp. 387–446. DOI: 10.1007/978-1-4684-6066-7_7.

[221] L. Zhang *et al.*, "Ceramic nanowelding," *Nature Communications*, vol. 9, no. 1, 2018. DOI: 10.1038/s41467-017-02590-1.

[222] A. C. Rastogi and S. T. Lakshmikumar, "Indium-tin-oxide-metal interfacial resistance and its implication for solar cells," *Solar Cells*, vol. 26, no. 4, pp. 323–328, 1989. DOI: 10.1016/0379-6787(89)90091-4.

[223] K. Takahashi *et al.*, "Reduction of contact resistance on titanium sheet surfaces by formation of titanium carbide and nitride, and its stability in sulfuric acid aqueous solution," *ISIJ International*, vol. 59, no. 9, pp. 1621–1631, 2019. DOI: 10.2355/isijinternational.ISIJINT-2018-787.

[224] "Prohibited materials section," NASA Electronic Parts and Packaging Program. (2001), URL: https://nepp.nasa.gov/npsl/prohibited/index.htm (visited on 10/18/2023).

[225] G. Kotlarski *et al.*, "Electrical contact resistance of tungsten coatings deposited on cu and al conductors," *Journal of Physics: Conference Series*, vol. 1859, no. 1, 2021. DOI: 10.1088/1742-6596/1859/1/012063.

[226] M. A. Lambert, E. E. Marotta, and L. S. Fletcher, "The thermal contact conductance of hard and soft coat anodized aluminum," *Journal of Heat Transfer*, vol. 117, no. 2, pp. 270–275, 1995. DOI: 10.1115/1.2822516.

[227] "Earth orbit environmental heating," National Aeronautics and Space Administration, GD-AP-2301.

[228] A. F. Johnson and G. D. Sims, "Mechanical properties and design of sandwich materials," *Composites*, vol. 17, no. 4, pp. 321–328, 1986. DOI: 10.1016/0010-4361(86)90749-4.

[229] S. Miller *et al.*, "Survey and performance evaluation of small-satellite propulsion technologies," *Journal of Spacecraft and Rockets*, vol. 58, no. 1, pp. 222–231, 2021. DOI: 10.2514/1.A34774.

[230] R. Hevner *et al.*, "An advanced standard for CubeSats," in *Small Satellite Conference*, 2011.

[231] G. Greschik and W. K. Belvin, "High-fidelity gravity offloading system for free-free vibration testing," *Journal of Spacecraft and Rockets*, vol. 44, no. 1, pp. 132–142, 2007. DOI: 10.2514/1.21454.

[232] H. Mao *et al.*, "Deployment of bistable self-deployable tape spring booms using a gravity offloading system," *Journal of Aerospace Engineering*, vol. 30, no. 4, 2017. DOI: 10.1061/(ASCE)AS.1943-5525.0000709.

[233] G. M. Pettersson, O. Jia-Richards, and P. C. Lozano, "Development and laboratory testing of a CubeSat-compatible staged ionic-liquid electrospray propulsion system," in *AIAA SciTech Forum*, 2022. DOI: 10.2514/6.2022-0040.